Exotic Thermal Transport in a Kitaev Magnet

Peter Czajka

A Dissertation
Presented to the Faculty
of Princeton University
in Candidacy for the Degree
of Doctor of Philosophy

Recommended for Acceptance
by the Department of
Physics
Adviser: Nai Phuan Ong

September 2022

Abstract

In 2006, Alexei Kitaev presented an exactly solvable spin model that is capable of exhibiting a novel spin liquid phase with non-abelian Majorana fermion excitations whose physics is strongly relevant to topological quantum computing. At the heart of this model is a unique type of magnetic exchange interaction that can potentially produce the phenomenology of Kitaev's solution as well as other exotic magnetic phases. $RuCl_3$ is currently the most well-known and intensely studied material candidate for realizing this model. In this thesis, we present results from a variety of experiments aimed at studying this material using thermal transport. Transport measurements have long been a key tool for studying excitations in condensed matter systems. Thermal transport measurements are used instead of more traditional electrical ones because $RuCl_3$ is electrically insulating and its excitations are charge neutral. The first major finding presented in this dissertation is the observation of magneto-oscillations in the material's longitudinal thermal conductivity κ_{xx}. Such an effect may imply Landau quantization of charge-neutral quasiparticles and is therefore possibly the strongest piece of evidence yet for the long-sought spinon Fermi surface state. The second major finding is a planar thermal Hall conductivity κ_{xy} with a temperature-dependence consistent with the presence of topological bosonic edge modes at high field. This result is the first clear observation of a topological bosonic quasiparticle in a transport measurement and therefore has substantial implications for both spintronic technologies and topological physics more broadly. We also discuss at length the various technical and materials challenges associated with these notoriously difficult experiments.

Acknowledgements

The first person I need to thank is my advisor Nai Phuan Ong. Phuan is a titan in physics and it has been a thrill to be able to work so closely with him for the last six years. He likes to say that he prefers graduate students over postdocs as he can more easily treat them as a blank slate and mold them according to his own style. Phuan has a highly unique approach to scientific research that, at its heart, is driven by an intense curiosity. Much of modern condensed matter physics research can be somewhat superficial in nature with various efforts being plagued by tunnel vision and inability to look beyond the initial motivation for an experiment. Working with Phuan has taught me to allow myself to be surprised and to not be afraid of puzzles. I believe that the two main experiments presented in this thesis reflect these two motifs quite well. The thermal conductivity oscillations presented in Chapter 2 were something that no one expected to find. In fact, I was prepared to publish the data with a very conservative interpretation before Phuan convinced *me* that they really could be true, fermionic quantum oscillations. The topological magnon model discussed in Chapter 3 was also not arrived at easily. It took many hours of the two of us diving through old papers and "playing theorist" to come up with a suitable quantitative model for our thermal Hall effect data. This kind of task would usually either be outsourced to a theorist or simply omitted entirely. Doing this myself demonstrated for me the benefit being a well-rounded physicist (something else that Phuan encourages in his students) and, for this reason, this project is the accomplishment I am proudest of. I now look forward to adapting Phuan's philosophy to new scientific endeavors.

I also need to thank Max Hirschberger. Max spent his own PhD developing many of the experimental tools used for thermal Hall effect measurements. His thesis has become something of a sacred text for thermal transport experiments in our group and Max has always been willing to answer our many highly specific (and often lengthy) technical questions. Max has also been an amazing mentor to me personally who has happily provided me with personal and professional guidance over the last several years.

The efforts presented in this thesis were not pursued alone. I have had the fortune of collaborating with a number of tremendously gifted young scientists through my work. The first person I must thank is Tong Gao. Tong and I worked together on many of the $RuCl_3$ measurements and I am grateful to have had someone to join me in this frequently frustrating endeavor. I would also like to thank Jiayi Hu, my successor for our group's thermal transport experiments. Jiayi is an incredibly dedicated young scientist and the future of our research is in good hands with her.

The work presented in this thesis would not have been possible without the collaboration with

Oak Ridge National Laboratory's $RuCl_3$ team (Arnab Banerjee, Paige Lampen-Kelley, David Mandrus, and Stephen Nagler) who provided the crystals used for our experiments. I would like to thank Arnab Banerjee (now a professor at Purdue) in particular for the many stimulating discussions and for writing me a letter of recommendation for my postdoc applications. In a similar spirit, I would also like to thank Sanfeng Wu for serving as the second reader for my thesis as well as Ali Yazdani and Frans Pretorius for serving on my thesis committee.

Over the last six years, I have had the pleasure of working with several other graduate students in Phuan's group. These individuals are (not including the ones mentioned above) Wudi Wang, Jingjing Lin, Sihang Liang, Nick Quirk, Stephan Kim, Zheyi Zhu, and Bingzheng Han. We have suffered through helium shortages and the pandemic together and I am grateful for the camaraderie that we have all been able to share during this challenging era. I would also like to thank Stephan specifically for the countless hours he has put into developing the lab's Helium recovery system. As I will emphasize again later, the global Helium situation deteriorated substantially over the course of my six years at Princeton. This necessitated the construction of our own recycling system that was ultimately instrumental for the work presented in this thesis.

On a more personal note, I have also had the incredible fortune of being able to make numerous friends during my time in Princeton. I would first like to thank the various members of Das Creu (my friends from first year) such as James Loy, Veronica Boyce, Oak Nelson, Annie Levine, Vivek Kumar, Fedor Popov, Diana Valverde-Mendez, Sarah Marie Bruno, Steven Li, Kyle Luther, Jim Wu, and Charlie Murphy. Moving to a new place knowing no one is always a bit nerve-wracking so it was quite a relief to have so many great friends appear almost spontaneously in my life. I would also like to thank the many other friends I have made during my time in Princeton (either through the physics department or elsewhere). This includes Christian Jepsen, Himanshu Khanchandani, Damon Binder, Nick Haubrich, Luca Iliesiu, Wayne Zhao, Erin Healy, Zach Sethna, Sam Higgenbotham, Joseph Van der List, Ilya Belopolski, Ben Weiner, Mikhail Mlodik, Ho Tat Lam, Ziming Ji, Nana Shumiya, Tyler Cochran, Songtian Zhang, Trithep Devakul, Link Patrick, Suying Jin, Eric Emdee, and many others.

I now move to my go-to fun fact about my life: my involvement with the DBar. If someone had told me ten years ago that I would be effectively running a bar at night (while still working on a PhD in physics during the day), I definitely would not have believed them. However, on a personal level, it has proved to be an incredibly valuable experience that I will truly miss. I would like to acknowledge my co-czars during this time: Adam Fisher, Zach Hervieux-Moore, Kris Meehan, Cora Betsinger, Andy Alt, Chris Ushay, Eric Franklin, and Connor Way.

My journey in physics began before my arrival at Princeton. I would therefore also like to thank the many teachers, mentors, and friends who helped me get here in the first place. In particular, I would like to single out Cyril Opeil and Andrzej Herczynski who, along with the rest of the Boston College physics department, helped me realize that a career in physics really was the right choice for me.

Between the pandemic, referee battles, and job applications the last couple years have been rather stressful. I would like to thank my girlfriend Huan Yi Low (and our corgi Archie) for helping to keep me sane during this challenging time. I could not ask for a better partner for this next chapter of my life. Finally, I need to thank my family (my sisters Kelley and Catherine and my parents John and Meg) for helping me become the person I am today. I am tremendously fortunate to have parents who have so eagerly supported me at every step of my life.

For my parents.

Contents

Chapter 1

Introduction

1.1 Quantum Spin Liquids

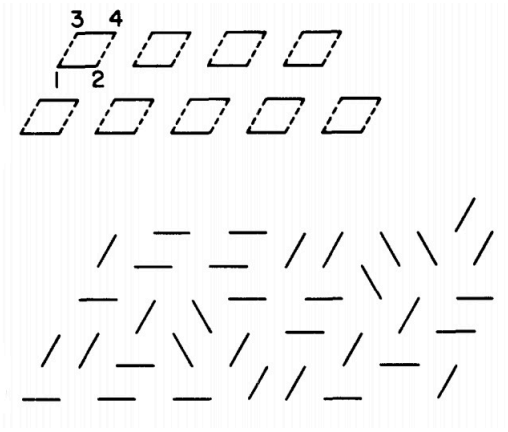

Figure 1.1: Anderson's original proposal for an entangled state as the solution to the spin-1/2 antiferromagnetic Heisenberg model on the triangular lattice. This solution will eventually grow into a genre of quantum states called quantum spin liquids. Figure adapted from [1].

The concept of a quantum spin liquid (QSL) was first proposed by Phil Anderson in 1973 [1]. The original theory focused on the spin-1/2 antiferromagnetic Heisenberg model on the triangular lattice ($H = J \sum_{\langle ij \rangle} \mathbf{S}_i \cdot \mathbf{S}_j$), which Anderson argued could have a 'resonating valence bond' (RVB) state as a low energy solution that also satisfies the Hamiltonian's intrinsic frustration. In this state, the spins form quantum superpositions of different singlet coverings as shown in Fig. 1.1. In the figure, the singlets are indicated by lines between neighboring triangular lattice sites. Anderson's idea has since been extended to a wide variety of lattices and models and the solutions form a new class of states collectively referred to as quantum spin liquids. These states are united by their

common ability for the spins to form long range entangled states instead of magnetically ordered ones.

Interest in QSL states was later catalyzed by the discovery of high temperature superconductivity. Anderson and others proposed that the unusual superconductivity in the cuprate systems could arise from the charge-doping of an RVB-type ground state [2][3][4]. Subsequent theoretical developments let to the identification and categorization of QSL's such as gapped $\mathbb{Z}_2$ and gapless U(1) states.

At this point, the observant reader has likely noticed that the work discussed thus far has been purely theoretical. They may be left wondering what a QSL does apart from permitting a mathematical description that falls neatly into the categorization scheme that has been developed over the last few decades. A major challenge for the physicists who study these systems is that QSLs are typically identified only by what they do not do (namely order magnetically). Theoretical frameworks are able to offer a little more precision (such as the mathematical structure of the nonlocal quantum entanglement[5]), but few of the insights gained from these schemes translate to experimentally visible behaviors. Specific phenomenological signatures are infamously rare. One common theme in searching for such signatures is by exploiting possible quasiparticle fractionalization. The nature of the quantum entanglement in a QSL state permits the excitation's degrees of freedom to effectively fractionalize into separate particles. Additionally, the quasiparticle excitations that result from this fractionalization can show fermionic statistics instead of the bosonic character of conventional magnetic excitations. Efforts to identify QSL behavior in materials have therefore focused on signatures of fractionalization as well as the presence of emergent fermions. An example of how an electron might fractionalize in such a system is shown in Fig. 1.2.

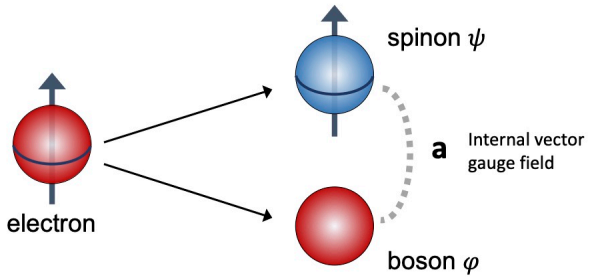

Figure 1.2: Example of effective electron fractionalization that can happen in quantum spin liquids. The electron splits into a a fermionic spin-containing particle (the spinon) and a charge-carrying boson.

Finally, we acknowledge that the introduction to QSLs presented here is only intended to serve as a general primer for the experiments discussed in this thesis. Readers who are interested in learning more about these fascinating systems are encouraged to read some of the many review papers that

have been written about this topic [5][6][7].

1.2 Kitaev Model

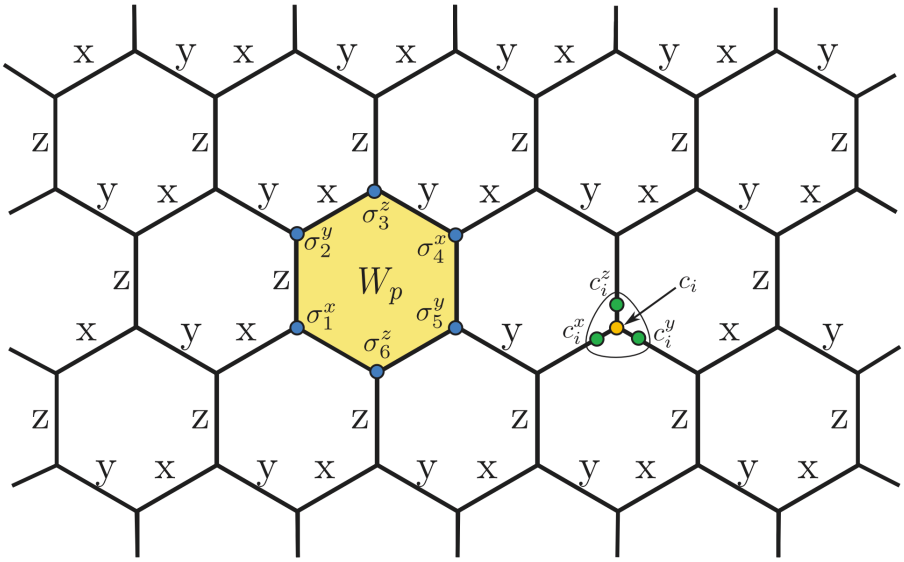

Figure 1.3: Depiction of the Kitaev honeycomb lattice Hamiltonian and its corresponding parton solution. Figure adapted from [5].

In 2006, Alexei Kitaev proposed a now famous model for a new kind of spin liquid [8] with several highly attractive features. Unlike most quantum spin liquid theories, Kitaev's is exactly solvable. At the heart of the model is a unique bond-directional exchange term that has the form:

$$H_K = K_x \sum_{\langle ij \rangle \in x} \sigma_i^x \sigma_j^x + K_y \sum_{\langle ij \rangle \in y} \sigma_i^y \sigma_j^y + K_z \sum_{\langle ij \rangle \in z} \sigma_i^z \sigma_j^z \tag{1.1}$$

where the x, y, and z labels refer to the type of honeycomb bond (see Fig. 1.3) and σ^μ ($\mu = x, y, z$) are Pauli matrices. This model can be solved using a fermionic parton construction. We first define the plaquette operator $W_p = \sigma_1^x \sigma_2^y \sigma_3^z \sigma_4^x \sigma_5^y \sigma_6^z$. W_p commutes with the Hamtiltonian (meaning $[W_p, H] = 0$) so we obtain eigenvalues of either +1 or -1 for each plaquette. This is a local $\mathbb{Z}_2$ symmetry that allows us to simplify the problem by focusing on specific sectors of the Hilbert space. We now turn our attention to the subspace where W_p is the same value for all plaquettes in the system. After this restriction, the degrees of freedom are reduced such that there is one two-level system per unit cell. The problem can then be solved by reexpressing the spins using Majorana fermion operators (c, c^x, c^y, c^z):

$$\tilde{\sigma}^x = ic^x c \qquad \tilde{\sigma}^y = ic^y c \qquad \tilde{\sigma}^z = ic^z c \tag{1.2}$$

Note that the tildes have been added to indicate that the operators act on an expanded 4D Fock space rather than the original one. A real space depiction of these new operators is shown in Fig. 1.3. The new operators represent Majorana fermions because they are there own complex conjugate ($c = c^\dagger$), meaning that they describe fermions that are their own antiparticle.

We now rewrite the Hamiltonian in the following suggestive form:

$$H = \frac{i}{4} \sum_{\langle ij \rangle} \hat{A}_{ij} c_i c_j \tag{1.3}$$

where we define $\hat{A}_{ij} = 2K_{\gamma_{ij}} \hat{u}_{ij}$, $\hat{u}_{ij} = ic_i^{\gamma_{ij}} c_j^{\gamma_{ij}}$, and $\gamma_{ij} = \mu$ if $\langle ij \rangle \in \mu$. Note that the Majorana operators do not act on the same Hilbert space as the original Hamiltonian. More information on how this expanded Hilbert space can be related to the physical subspace via a projection scheme is given in [8]. The reason that the form of Eq. 1.3 is suggestive is that it strongly resembles the a conventional quadratic fermion Hamiltonian. However, there is one important difference. $\hat{A}_{ij}$ is an operator and not a real skew-symmetric matrix (as seen in a tight binding Hamiltonian for example). Some additional work must be done to convert $\hat{A}_{ij}$ into a more appropriate form. We exploit the fact that each $c_i^{\gamma_{ij}}$ appears in H only once. Therefore $[\hat{u}_{ij}, \hat{u}_{kl}] = 0$ and $[\hat{u}_{ij}, H] = 0$. This then permits us to focus the specific eigenvalue sectors with $\hat{u}_{ij} = \pm 1$ (similar to what we just did with the plaquette operator W_p). In fact there is actually a connection between the bond and plaquette operators that can be exploited. Explicitly:

$$W_p = \prod_{\langle ij \rangle \in \partial p} \hat{u}_{ij} \tag{1.4}$$

demonstrating that the bond operators $\hat{u}_{ij}$ are associated with the Z_2 flux operator W_p. $\hat{u}_{ij}$ acts as a scalar within a given sector, which allows $\hat{A}_{ij}$ to be demoted from an operator to a matrix, thereby finally permitting a free fermion description of the c Majorana fermions. This interpretation reveals why the expression of the Pauli matrices σ^μ in terms of Majorana operators c, c^μ was so clever. The c^μ operators are associated with the $\mathbb{Z}_2$ fluxes while the c operators are associated with "matter" fermions.

Now that we have reduced H to the desired form, we can attempt to diagonalize it. The first step is to choose which eigenvalue sector to work in. We opt for the one where $W_p = 1$ for every

plaquette as it was previously shown by Lieb [9] that the ground state of this type of model should be one with no vortices (which would be a plaquette with $W_p = -1$). We can select a set of $\hat{u}_{ij}$ that are equivalent to a no vortex situation. We choose to have $\hat{u}_{ij} = 1$ if i belongs to the A sublattice and $\hat{u}_{ij} = -1$ otherwise. We can then diagonalize H using a Fourier transformation that reduces the problem to the following matrix:

$$i\tilde{A}(\mathbf{q}) = \begin{pmatrix} 0 & if(\mathbf{q}) \\ -if(\mathbf{q})^* & 0 \end{pmatrix} \tag{1.5}$$

with $f(\mathbf{q}) = 2(K_x e^{i(\mathbf{q}\cdot\mathbf{n}_1)} + K_y e^{i(\mathbf{q}\cdot\mathbf{n}_2)} + K_z)$. The energy spectrum for the c fermions is:

$$\epsilon_{\mathbf{k}} = \pm 2|K_x e^{i\mathbf{k}\cdot\mathbf{n}_1} + K_y e^{i\mathbf{k}\cdot\mathbf{n}_2} + K_z| \tag{1.6}$$

with $\mathbf{n}_{1,2} = \left(\pm\frac{1}{2}, \frac{\sqrt{3}}{2}\right)$ and the z bond is taken to lie along the vertical direction. This energy function permits two distinct phases: one where the Majorana spectrum is gapless and one where it is gapped. Which of these two phases is realized depends on the anisotropy of the Kitaev exchange interaction. The spectrum is gapless if the expression $K_x e^{i\mathbf{k}\cdot\mathbf{n}_1} + K_y e^{i\mathbf{k}\cdot\mathbf{n}_2} + K_z = 0$ has solutions. Alternatively, the gapless phase is obtained if the following inequalities are satisfied:

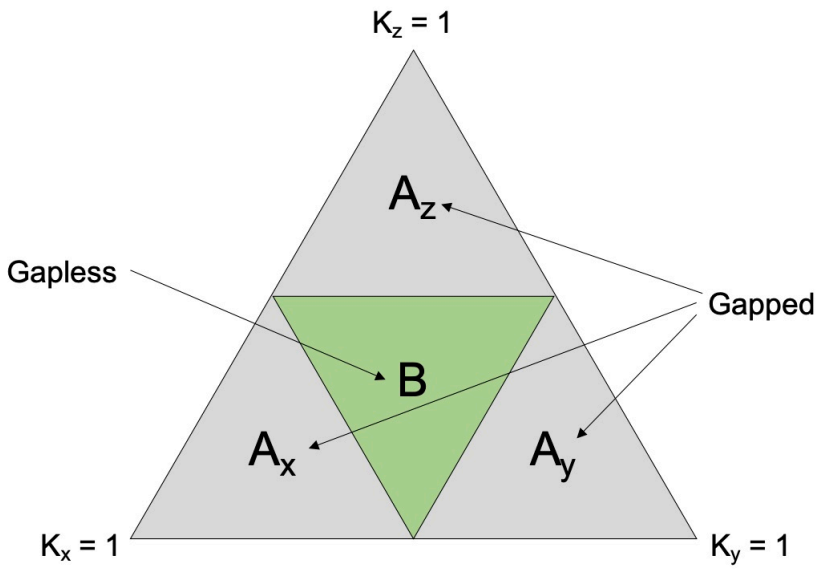

Figure 1.4: The exact solution to Kitaev's honeycomb model permits two different ground states. If the Kitaev exchange interactions are sufficiently isotropic (similar for the x, y, and z bonds), the Majorana spectrum will be gapless. This phase is labeled B in the phase diagram and is shown in green. For strongly anisotropic exchange, the spectrum will be gapped. These regions of the phase diagram are labeled A_x, A_y, and A_z according to which type of interaction is overly dominant.

$$|K_x| \leq |K_y| + |K_z| \qquad |K_y| \leq |K_x| + |K_z| \qquad |K_z| \leq |K_x| + |K_y| \tag{1.7}$$

This is illustrated visually in Fig. 1.4. The gapped phase is a traditional $\mathbb{Z}_2$ spin liquid that hosts abelian anyon excitations and can be mapped to Kitaev's Toric Code model [10]. However, it is the gapless phase that has attracted the most interest. In this phase, the spectrum consists of linearly dispersing Dirac-like cones centered at two different points $\pm\mathbf{q}^*$ within the Brillouin zone (with $\mathbf{q}^*$ depending on the exact values of K_x, K_y, and K_z). This is depicted in Fig. 1.5.

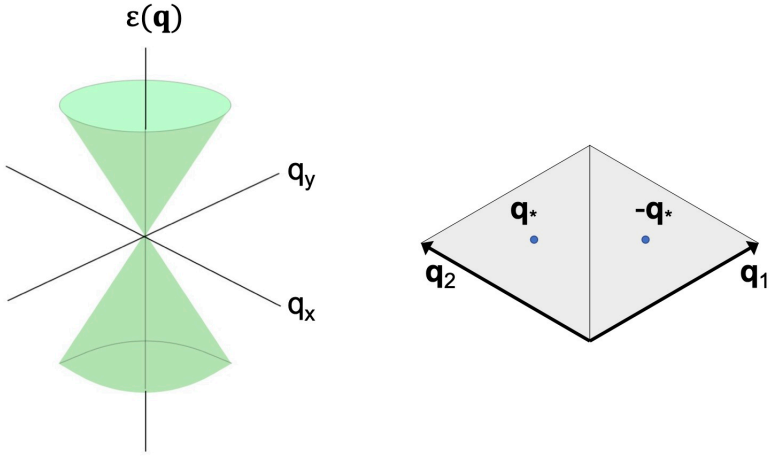

Figure 1.5: In the gapless phase of the Kitaev model, the Majorana spectrum consists of gapless, linearly-dispersing Dirac cone-like states located at $\mathbf{q}^*$ and $-\mathbf{q}^*$.

It is actually not the pure form of this gapless phase that has generated so much interest in Kitaev's model, but rather what happens when a magnetic field is applied. Once a field is applied, the model can no longer be solved exactly. However, its effect can be described perturbatively via the addition of the term

$$V = -\sum_j \left(h_x \sigma_j^x + h_y \sigma_j^y + h_z \sigma_j^z\right) \tag{1.8}$$

where h_x, h_y, and h_z refer to the field component along the Kitaev axes (which relate to the bond labeling), not the Cartesian directions. In this notation, a fully perpendicular field will couple equally to each of the three types of bonds. It can be shown using Green's function methods that one must go to third order in perturbation theory to break time reversal symmetry and open a gap in the Majorana spectrum. This third order term has the form:

$$H_{eff}^{(3)} \sim \frac{h_x h_y h_z}{K^2} \sum_{j,k,l} \sigma_j^x \sigma_k^y \sigma_l^z \tag{1.9}$$

Note that we have chosen $K = K_x = K_y = K_z$ for simplicity. This sum is over spin arrangements of the form:

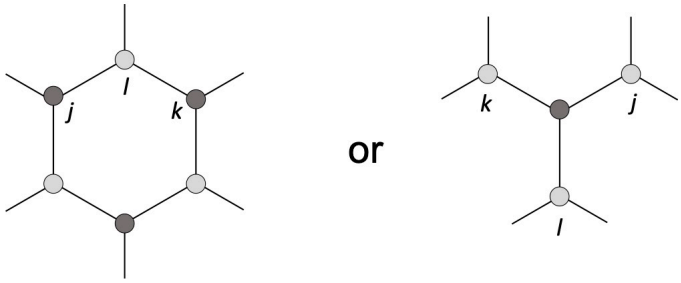

Figure 1.6: Site configurations associated with the perturbative term.

This new Hamiltonian permits an appealing visual interpretation that is shown in Fig. 1.7. The applied field field induces a complex valued hopping amplitude for second nearest neighbors and is reminiscent of Haldane's model for the quantum Hall effect without Landau levels [11]. We find the new spectrum in the same way as before, but now the A matrix has the form:

$$i\tilde{A}(\mathbf{q}) = \begin{pmatrix} \Delta(\mathbf{q}) & if(\mathbf{q}) \\ -if(\mathbf{q})^* & -\Delta(\mathbf{q}) \end{pmatrix} \tag{1.10}$$

Diagonalization of this new Hamiltonian reveals that the Majorana spectrum is now:

$$\epsilon(\mathbf{q}) = \pm\sqrt{|f(\mathbf{q})|^2 + \Delta(\mathbf{q})^2} \tag{1.11}$$

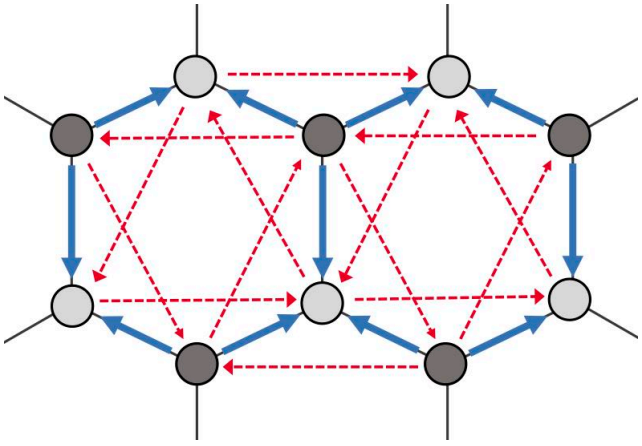

Figure 1.7: The applied field leads to an imaginary hopping amplitude for second nearest neighbors as indicated by the dotted red arrows. The blue arrows represent the sign of the hopping for nearest neighbors, which depends on whether the hopping is from the A sublattice to the B sublattice or vice versa. The alternating light and dark gray circles indicate the two sublattices.

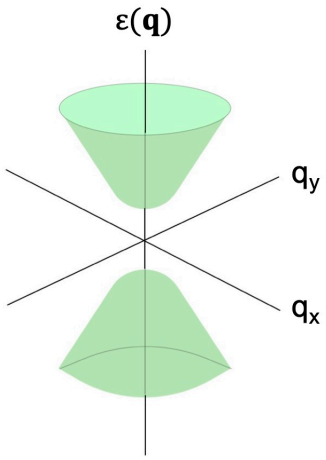

Figure 1.8: The Dirac cone-like Majorana spectrum acquires a bulk gap when a magnetic field is applied (though gapless chiral modes exist at the edge).

with $f(\mathbf{q}) = 2K(e^{i(\mathbf{q},\mathbf{n}_1)}+e^{i(\mathbf{q},\mathbf{n}_2)}+1)$ and $\Delta(\mathbf{q}) = 4\frac{h_x h_y h_z}{K^2}(\sin(\mathbf{q}\cdot\mathbf{n}_1)+\sin(\mathbf{q}\cdot-\mathbf{n}_2)+\sin(\mathbf{q}\cdot\mathbf{n}_2-\mathbf{n}_1))$.

We find that the magnetic field has opened up a gap Δ at q^* of size:

$$\Delta \sim \frac{h_x h_y h_z}{K^2} \tag{1.12}$$

Because we are breaking time reversal symmetry and gapping the spectrum it follows that the bands acquire nontrivial topology. More specifically, each of the two bands is characterized by a integer valued Chern number $\mathcal{C}$ that is equal but opposite in sign for the two bands. There will then inevitably be a gapless chiral edge mode that connects there two bands. Such a system is typically referred to as a Chern insulator [12][13], but the present situation presents some unique peculiarities due to the Majorana nature of the quasiparticles. For this reason, the entire system is usually labeled with a single Chern number $\mathcal{C}$ that refers to the chirality (the direction of circulation) of the resulting edge modes. This quantity is expected to have the following field-dependence:

$$\mathcal{C} = sgn(h_x h_y h_z) \tag{1.13}$$

where again, h_x, h_y, and h_z refer to the field component along the Kitaev x, y, and z axes, not the Cartesian directions. This detail will be made more clear when we discuss the application of Kitaev formalism to real materials in a later section.

The chiral edge modes also lead to one of the most attractive features of Kitaev's model: a true smoking gun for the quantum spin liquid state. Specifically, these edge states should support a half-integer quantized thermal Hall conductivity κ_{xy}. This effect can be theoretically illustrated

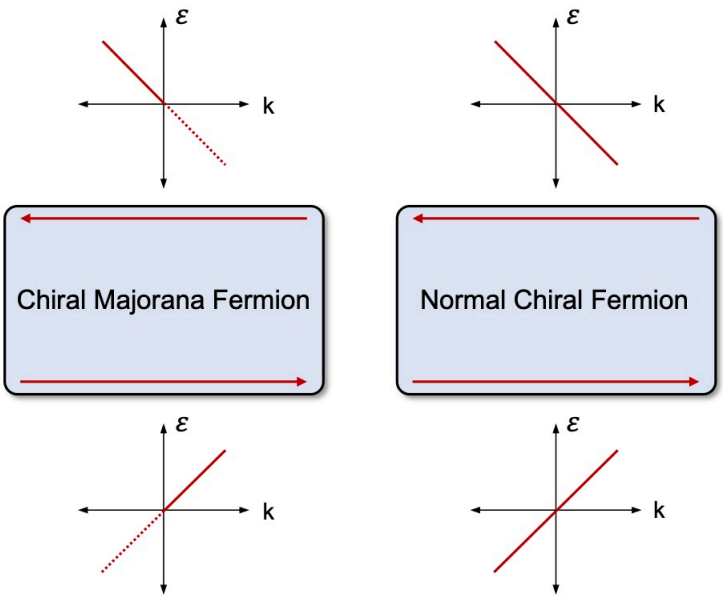

Figure 1.9: Majorana fermions are effectively half of a normal fermion. The nature of this property and its relation to the Majorana fermion's particle-hole symmetry are illustrated here.

in a few different ways. One involves a formal conformal field theory (CFT) and is beyond the scope of this thesis. We only mention that the Chern number $\mathcal{C}$ discussed here is equivalent to the chiral central charge in CFT language. We will instead demonstrate Kitaev's prediction via an explicit treatment of the relevant energy current and thermal transport setup (which will also follows Kitaev's derivation). We consider a 1D chiral Majorana edge mode with energy $\epsilon(q)$ that propagates at velocity $v(q) = d\epsilon/dq$ and whose statistics are governed by the Fermi distribution $n(q)$. The energy current caused by this mode can be calculated as:

$$I = \int_{\epsilon(q)>0} n(q)\epsilon(q)v(q)\frac{dq}{2\pi} = \frac{1}{2\pi}\int_0^\infty \frac{\epsilon d\epsilon}{1+e^{\epsilon/T}} = \frac{1}{2\pi}\int_0^\infty \frac{\epsilon d\epsilon}{1+e^{\epsilon/T}} = \frac{\pi}{24}T^2 \tag{1.14}$$

where we have set all fundamental constants to zero for simplicity. The Majorana nature of the fermions enters the calculation via the integrand of the first expression. For a conventional fermion, we would have to integrate over all possible energies ($-\infty$ to $+\infty$). However, due to the particle-hole symmetric nature of the Majorana fermion, states with q and $-q$ are equivalent. Majorana fermions can therefore be viewed as "half" of a normal fermion. This characteristic is illustrated in Fig. 1.9. This is also reflected in the final value of the energy current carried by the edge mode. Integrating between $-\infty$ and $+\infty$ instead would yield twice as much current. Another key piece of physics that has been demonstrated here is the universality of thermal transport in 1D. This is reflected in the fact that final expression for I contains only fundamental constants, no microscopic details

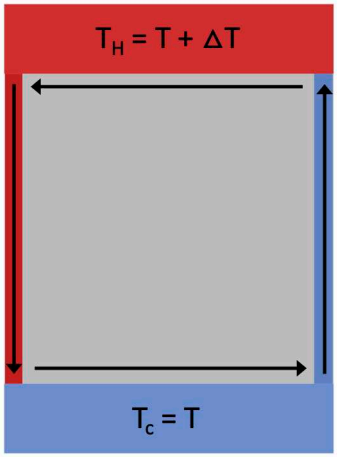

Figure 1.10: The smoking gun for a Kitaev Spin Liquid with chiral Majorana fermion edge states is a quantized thermal Hall effect. The way this occurs via ballistic transport in the edge modes is depicted here.

pertaining to specific characteristics of the edge mode (apart from its chirality/ direction).

One can then show that this feature of 1D physics has a more macroscopic manifestation that is relevant to Kitaev's model. This can be done by considering the application of a temperature gradient to a layer of a material described by Kitaev's honeycomb model as shown in Fig. 1.10. The top edge of the system is heated to a temperature T_H while the bottom edge is kept at T_C. We assume that the chirality is such that the edge states flow in a counterclockwise direction (when viewed as shown in Fig. 1.10). We also treat the edge modes as ballistic so that the effective temperature of the left side of the sample is T_H and temperature of the right side is T_C. The current flowing along the two sides can then be calculated using Eq. 1.14:

$$I_{Left} = I_H = \frac{\pi}{24} T_H^2 \tag{1.15}$$

$$I_{Right} = I_C = \frac{\pi}{24} T_C^2 \tag{1.16}$$

This particular configuration can then be associated with a thermal transport phenomenon called the thermal Hall effect. This unusual effect is a major topic of this thesis so we will leave a more appropriate discussion of it for a later section. The thermal Hall effect refers to the temperature gradient that appears transverse to an applied heat current (or vice versa as described here). Explicitly, this can be related to the Fourier-like expression (the thermal equivalent of Ohm's Law):

$$J_Q = -\kappa_{xy} \nabla T \tag{1.17}$$

The longitudinal heat current density J_Q can be related to the difference between the currents along the two edges calculated in Eq.'s 1.15 and 1.16. Similarly, the transverse temperature gradient can be expressed in terms of the two known temperatures. We then use this knowledge to rewrite Eq. as:

$$\frac{1}{d}\left(I_H - I_C\right) = -\kappa_{xy}\frac{1}{d}\left(T_H - T_C\right) \tag{1.18}$$

The sample width d appears on both sides of the equation and cancels. We can then express the currents explicitly and find:

$$\frac{\pi}{24}\left(T_H^2 - T_C^2\right) = -\kappa_{xy}\left(T_H - T_C\right) \tag{1.19}$$

We now reexpress the temperatures as $T_H = T + \Delta T$ and $T_C = T$:

$$\frac{\pi}{24}\left(\left(T + \Delta T\right)^2 - T^2\right) = -\kappa_{xy}\Delta T \tag{1.20}$$

We take the linear response limit ($\Delta T \to 0$) and perform some algebra to obtain an expression for the thermal Hall conductivity:

$$\frac{\kappa_{xy}}{T} = \frac{\pi}{12} \tag{1.21}$$

We can now reinsert the units to reveal the predicted value that would be the smoking gun for chiral Majorana fermion edge states: $\kappa_{xy}/T = \frac{\pi}{12}\frac{k_B^2}{\hbar}$. This is exactly 1/2 of the expected value for normal chiral fermions and also 1/2 the value of the 1D quantum of thermal conductance K_0/T with $K_0 \approx 9.5 \times 10^{-13}$ W/K^2. This makes sense as the edge modes are quasi-1D. The presence of the fraction $\pi/12$ in Eq. 1.21 highlights the connection to conformal field theory.

We now arrive at the most exotic and potentially technologically impactful feature of Kitaev's model. In his paper, Kitaev demonstrated that the quasiparticles in the field-induced phase are able to exhibit non-abelian statistics. Specifically, the composite excitations formed by the binding of c Majorana fermions to the vortices (plaquettes with W_p = -1) should show non-abelian statistics with each other. In this context, the "non-abelian" label refers to the fact that the particles' statistics are history-dependent. An important consequence of this property is illustrated in Fig. 1.11. By moving the various particles around each other, one can create braid-like structures along the time axis. In addition to making contact with a rich field of pure mathematics, this sort of structure would be incredibly useful in quantum computing. A major challenge for current quantum information platforms is that the information necessary for performing calculations is only stored for tiny fractions of a second, which necessitates elaborate error correction schemes. Information stored

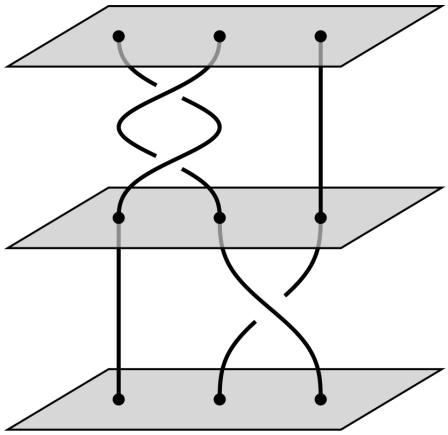

Figure 1.11: Depiction of now non-abelian anyons can be braided to form exotic states that can be used for quantum computation. Each of the three planes shown in the figure represent a different time. Because the particles' statistics exhibit history-dependence, they can form knot-like structures in time. Figure adapted from [14].

in braids like those shown in Fig. 1.11 is topologically protected by the knot-like structure and cannot be destroyed by simple processes (as is the case in current devices). Platforms that utilize non-abelian statistics are therefore referred to as topological quantum computers and are receiving substantial investments from companies like Microsoft.

The lack of a need for error correction presents a clear advantage for topology-oriented computing schemes compared to more conventional ones. However, there is one major caveat. As we have alluded to throughout this section, non-abelian statistics are not commonly observed in nature. In fact, no such effect has ever been conclusively demonstrated in an experiment and recent efforts have been focused on increasingly elaborate material platforms suspected of hosting Majorana fermions [15] [16] [17]. However, the necessity of exotic matter has created a fruitful partnership between quantum information researchers and more traditional solid state physicists. It is in this spirit that we present this thesis.

1.2.1 Jackeli-Khaliullin Mechanism

In this section, we describe the mechanism by which Kitaev-type exchange interactions can arise in real materials. The information presented here is largely adapted from ref. [18] with additional information from [19] and [20].

The first model for realizing Kitaev exchange in real materials was proposed by Jackeli and Khaliullin [21] [22]. In their proposal, one must begin with a J_{eff} =1/2 Mott insulator. Fig. 1.12

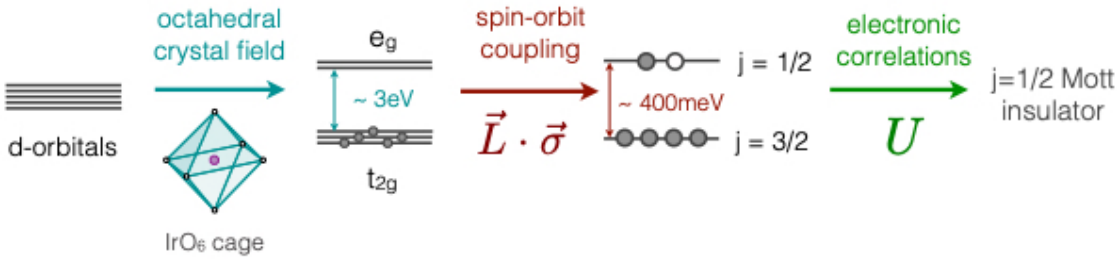

Figure 1.12: Mechanism for creation of $J_{eff} = 1/2$ Mott Insulator state. The degeneracy of the d-orbitals is reduced through crystal field splitting and spin-orbit coupling. Figure adapted from [23].

depicts how such a state arises in a d^5-type atomic state. If the ion is placed in an octahedral crystal field, the levels will split into two separate groups: an empty e_g set and a triply degenerate t_{2g} set containing one hole. Spin-orbit coupling ($H \propto \mathbf{L} \cdot \boldsymbol{\sigma}$) will further split the t_{2g} states into J_{eff} =1/2 and J_{eff} =3/2 states. Finally, if the Coulomb interactions are strong (represented by the Hubbard constant U), then we will be left with a single hole at each site with its only energetically relevant degree of freedom being that of the local J_{eff} =1/2 moment.

Note that the spin-orbit interaction needs to be quite strong to ultimately produce a robust J_{eff} =1/2 state so most materials of interest typically possess 4d and 5d transition metal atoms. The J_{eff} states can be expressed in terms of atomic orbitals in the following way [22]:

$$|j_{1/2}\rangle = \begin{cases} \frac{1}{\sqrt{3}}\left(-|xy,\uparrow\rangle - i\,|xz,\downarrow\rangle - |yz,\downarrow\rangle\right) & \left(m_j = +\frac{1}{2}\right) \\ \frac{1}{\sqrt{3}}\left(|xy,\downarrow\rangle + i\,|xz,\uparrow\rangle - |yz,\uparrow\rangle\right) & \left(m_j = -\frac{1}{2}\right) \end{cases} \tag{1.22}$$

$$|j_{3/2}\rangle = \begin{cases} \frac{1}{\sqrt{2}}\left(-i\,|xz,\uparrow\rangle - |yz,\uparrow\rangle\right) & \left(m_j = +\frac{3}{2}\right) \\ \frac{1}{\sqrt{6}}\left(2\,|xy,\uparrow\rangle - i\,|xz,\downarrow\rangle - |yz,\downarrow\rangle\right) & \left(m_j = +\frac{1}{2}\right) \\ \frac{1}{\sqrt{6}}\left(2\,|xy,\downarrow\rangle - i\,|xz,\uparrow\rangle + |yz,\uparrow\rangle\right) & \left(m_j = -\frac{1}{2}\right) \\ \frac{1}{\sqrt{2}}\left(-i\,|xz,\downarrow\rangle + |yz,\uparrow\rangle\right) & \left(m_j = -\frac{3}{2}\right) \end{cases} \tag{1.23}$$

The strength of various types of exchange interactions can then be calculated by considering the possible hopping processes within this manifold of states. Jackeli and Khaliullin's key insight was realizing that an edge-sharing geometry for neighboring octahedra was crucial for realizing materials with dominant Kitaev exchange. The exchange pathway that is most relevant to this particular calculation is between d orbitals on neighboring honeycomb sites via a ligand p orbital (see Fig. 1.13a). The reason that the edge-sharing geometry is so important is because it allows for hopping

to be done between two possible ligand sites. One must then consider the interference between the possible hopping amplitudes when calculating exchange interactions. Crucially, they find that this leads to constructive interference that enhances Kitaev (anisotropic) exchange and destructive interference that weakens the more conventional Heisenberg (isotropic) exchange. The latter should actually vanish entirely in the idealized case. The ultimate strength of the Kitaev interaction is dictated by the relevant hopping amplitude t and the on-site Hund's coupling J_H (see Fig. 1.13b).

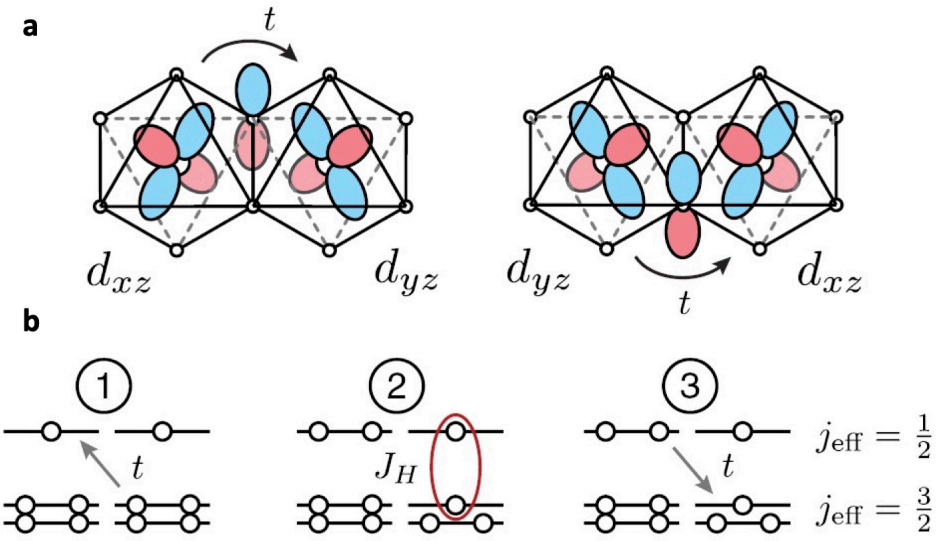

Figure 1.13: Panel (A): Key hopping pathway that gives rise to Kitaev exchange. Panel (B): The strength of the Kitaev exchange interaction is dictated by the hopping amplitude t for the relevant virtual processes as well as the on-site Hund's coupling J_H. Figure adapted from [18].

1.2.2 Extended Kitaev Model

In real materials, there will likely be additional types of exchange interactions that result from other kinds of hopping pathways. It is common to express the full "extended" Kitaev Hamiltonian for neighboring sites i and j in the following way:

$$H_{ij} = J_{ij}\mathbf{S}_i \cdot \mathbf{S}_j + K_{ij}S_i^\gamma S_j^\gamma + \Gamma_{ij}(S_i^\alpha S_j^\beta + S_i^\beta S_j^\alpha) + \Gamma'_{ij}(S_i^\gamma S_j^\alpha + S_i^\gamma S_j^\beta + S_i^\beta S_j^\gamma) \tag{1.24}$$

with $\{\alpha, \beta, \gamma\} = \{y, z, x\}$, $\{z, x, y\}$, and $\{x, y, z\}$ for the x, y, and z bonds. Note that in writing the Hamiltonian in this form, we assume local C_{2h} symmetry of the γ bond between sites i and j. The non-Kitaev terms largely arise from direct (non-ligand assisted) d-d hopping, which was not considered in Jackeli and Khaliullin's theory discussed earlier. The J_{ij} term in Eq. 1.24 is a typical Heisenberg-type isotropic exchange interaction and the K_{ij} term is the Kitaev exchange interaction.

	$d_{i,yz}$	$d_{i,xz}$	$d_{i,xy}$
$d_{j,yz}$	t_1	t_2	t_4
$d_{j,xz}$	t_2	t_1	t_4
$d_{j,xy}$	t_4	t_4	t_3

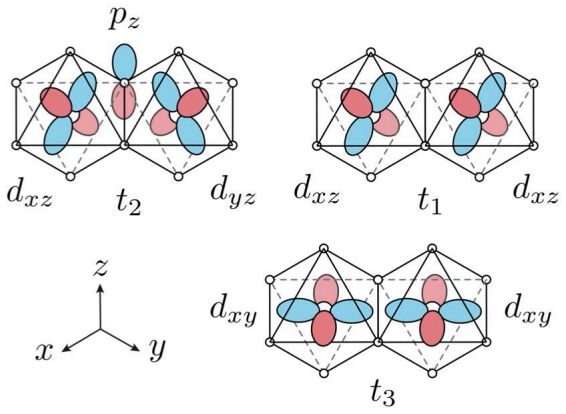

Figure 1.14: Illustration of types of hopping parameters used in calculating exchange terms in the extended Kitaev model. Figure adapted from [18].

The Γ_{ij} and Γ'_{ij} terms are symmetric off-diagonal exchange interactions. These terms are bond-directional in nature which, like the Kitaev exchange, is a consequence of the strong spin-orbital nature of the underlying magnetic moments. Note that the Γ'_{ij} term vanishes if there is perfect O_h local symmetry and even when there are trigonal distortions [24], Γ'_{ij} will still generally be much weaker than Γ_{ij} (although Takikawa et al. argue that Γ'_{ij} may have significant effects on the ultimate Kitaev spin liquid state [25]). Additionally, significant Γ_{ij} is thought to be effectively unavoidable in Kitaev materials [19]. This term has the effect of acting like an antiferromagnetic interaction for spins aligned perpendicular to the 2D plane, but a ferromagnetic interaction for spins aligned within the 2D plane (for $\Gamma > 0$).

As stated above, the non-Kitaev exchange terms can be understood by considering exchange pathways where hopping occurs between d orbitals directly and not through ligand p orbitals. We now describe how the various coefficients in Eq. 1.24 can be calculated from these specific types of hoppings. We adapt the framework and notation from Rau et al. [19] and Winter et al. [20]. The possible d-d pathways can be divided into four distinct categories (labeled t_1 to t_4), which are summarized in Fig. 1.14.

$$J_{ij} = \frac{4A}{9}\left(2t_1 + t_3\right)^2 - \frac{8B}{9}\left(9t_4^2 + 2\left(t_1 - t_3\right)^2\right) \tag{1.25}$$

$$K_{ij} = \frac{8B}{3}\left(\left(t_1 - t_3\right)^2 + 3t_4^2 - 3t_2^2\right) \tag{1.26}$$

$$\Gamma_{ij} = \frac{8B}{3}\left(2t_2\left(t_1 - t_3\right) + 3t_4^2\right) \tag{1.27}$$

$$\Gamma'_{ij} = \frac{8B}{3}\left(t_4\left(3t_2 + t_3 - t_1\right)\right) \tag{1.28}$$

where $A \sim 1/\mathrm{U} >> B \sim J_H/(3U^2)$.

The formalism developed by Jackeli and Khaliullin also helps to clarify the nature of the field-dependent model in a real material. We remind the reader that the applied field should only open up a gap in the Majorana fermion spectrum if it couples to each of the three bond types (x, y, and z and their corresponding Paul matrices σ^μ). Fig. 1.15 illustrates how the edge-sharing octahedra can be assembled to form a honeycomb lattice (for the metal atoms at their centers) and how the cubic Kitaev x, y, and z axes can be defined from this resulting structure. Note that all three vectors point partially out of the honeycomb plane.

These additional types of exchange interactions can also lead to various other non-Kitaev spin liquid ground states. This was investigated early on by Rau et al. [19] who were able to map out the parameter space (of ground states) using exact diagonalization calculations (see Fig. 1.16). The θ, ϕ-based parameterization is also defined in Fig. 1.16. Note that we have only included the phase diagram for $\Gamma > 0$ (as this will prove to be the more relevant scenario). According to the calculations, the Kitaev spin liquid state should be very unstable with even small amounts of other exchange terms leading to magnetically ordered states. The specific types of order identified in Rau

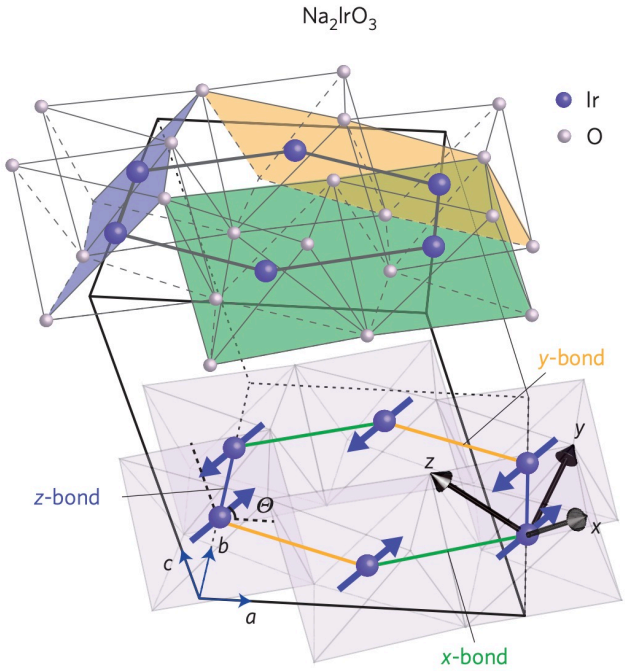

Figure 1.15: This figure illustrates the edge-sharing octahedra-based geometry associated with the Kitaev exchange interactions. It also illustrates how the cubic Kitaev axes (labeled x, y, and z in the figure) relate to the honeycomb lattice and the monoclinic directions (labeled a, b, and c). Note that this specific figure is specifically intended for Na_2IrO_3, but that the various features illustrated here extend to $RuCl_3$. Figure adapted from [26].

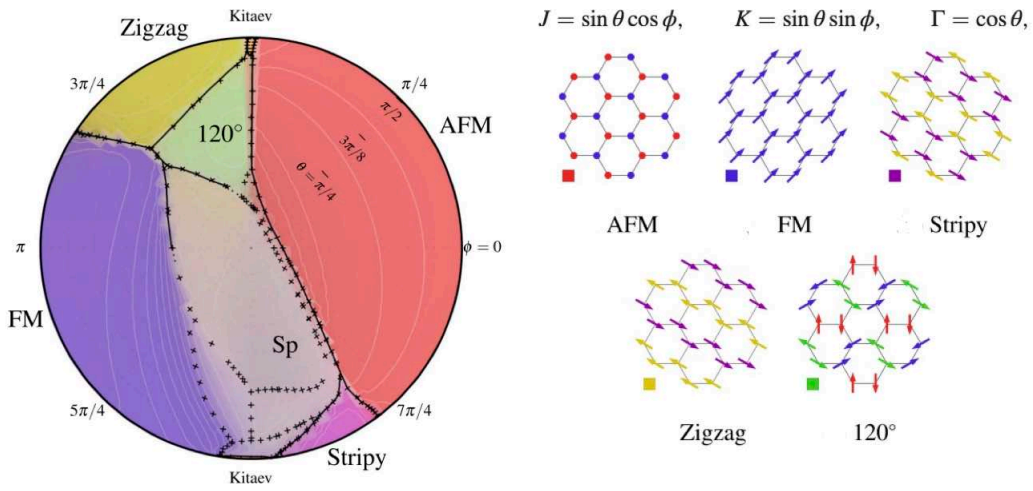

Figure 1.16: Phase diagram obtained from exact diagonalization calculations on Kitaev Magnets. Here, $\Gamma > 0$. The angle-based parameterization scheme is described in indicated in the figure. The numerous possible magnetically ordered ground states are also depicted. Figure adapted from [19].

et al.'s calculations include Neel antiferromagnetic, collinear ferromagnetic, stripy, zigzag, and 120°.

Note that the Hamiltonian discussed above only includes nearest neighbor interactions. Further neighbor in-plane as well as interlayer interactions can be present as well. Winter et al. [27] found that the presence of a third neighbor Heisenberg-type term can help further stabilize the zigzag order (the specific ground state found in $RuCl_3$).

Before concluding this section, we would like to note that the full effects of the off-diagonal exchange interaction are not yet understood. It appears that it may actually help stabilize various spin-liquid states (even if they do not follow the strict Kitaev-type phenomenology) rather than magnetically ordered ones. For example, in the classical limit, a Γ-only model should have a (classical) spin liquid ground state. Additionally, the more relevant $S = 1/2$ K-Γ model has been studied using numerical techniques such as exact diagonalization [28] and Density Matrix Renormalization [29]. These studies strongly suggest that that the competition between the two interactions may ultimately stabilize a different kind of quantum spin liquid ground state whose exact properties are not yet known. As we will emphasize throughout this thesis, many of presented results are highly anomalous in nature. We discuss the uncertainties associated with the effects of the Γ interaction to stress that much about the extended Kitaev model is not yet understood theoretically either. This uncertainty provides ample space for unusual properties to appear.

1.3 $RuCl_3$

Early efforts to study Kitaev magnetism in real materials focused on Ir-based compounds Na_2IrO_3 and α-Li_2IrO_3 [30][31][32][33]. However, difficulties with chemical stability and Ir's neutron-absorbing tendencies [33] made experiments with these materials incredibly difficult. While $RuCl_3$ has weaker spin-orbit coupling than the Ir-based systems (Ru is a 4d element while Ir is a 5d element), it does not suffer from these issues so it quickly became (and remains) the most well-studied Kitaev material [34].

Before moving on, we briefly mention that other promising candidates have since emerged. These include Ir-based materials $H_3LiIr_2O_6$ [35], $Ag_3LiIr_2O_6$ [36], Cu_2IrO_3 [37] and a new class of 3d compounds such as $BaCo_2(AsO_4)_2$ [38], $Na_3Co_2SbO_6$, and $Na_2Co_2TeO_6$ [39]. We believe that the results presented in this thesis bode well for the discovery of other novel Kitaev exchange-derived physics in other systems.

1.3.1 Crystal Structure

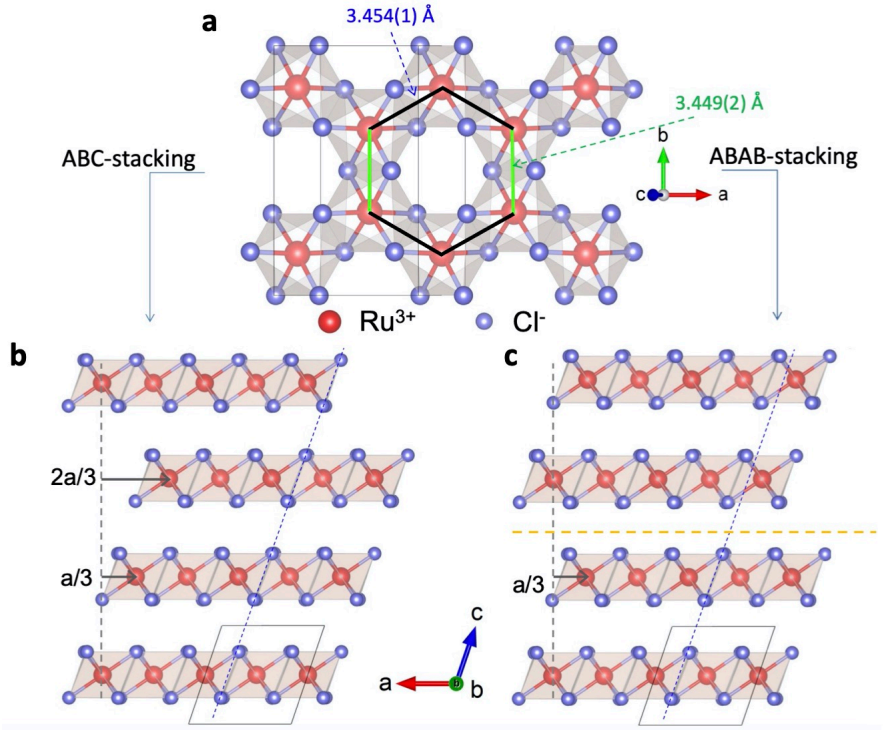

Figure 1.17: Panel (A): Top view of $RuCl_3$'s crystal structure that illustrates the bonding geometry. Ru atoms are shown in red and Cl atoms are shown in blue. Note the edge-sharing geometry of the Cl octahedra. Panel (B): Side view of $RuCl_3$ structure showing three layer ABC stacking seen in high quality crystals. Panel (C): Two layer stacking structure that appears as stacking faults in poor quality $RuCl_3$ crystals. Figure adapted from [40].

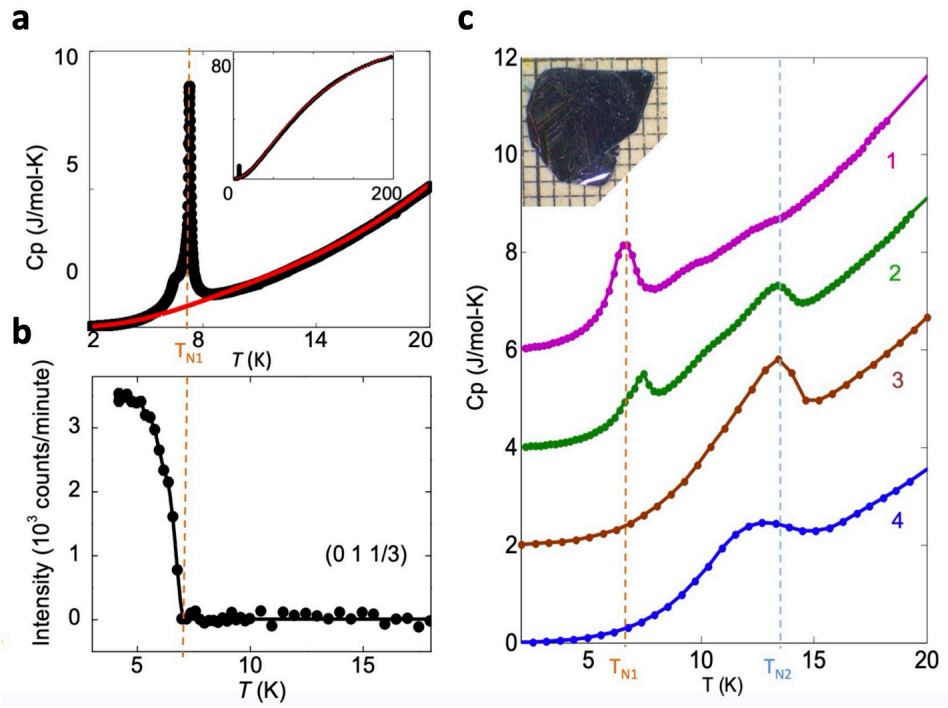

Figure 1.18: Panel (A): Heat capacity vs. temperature. There is a sharp transition associated with the zig-zag antiferromagnetic ordering transition at 7 K. The inset shows the same data over a larger temperature range. The red curve is a 2D Debye model fit. Panel (B): Intensity of the (0, 1, 1/3) magnetic Bragg peak vs. T. This indicates that the magnetic order onsets abruptly at 7 K and has three layer stacking periodicity. Panel (C): Heat capacity vs. T for the crystal used for the measurements shown in the other two panels before and after deformation. As the crystal is deformed more and more, the ordering transition noticeably shifts to higher T's. Figure adapted from [40].

The crystal structure of α-$RuCl_3$ is shown in Fig. 1.17. The Ru atoms form a honeycomb lattice and each Ru atom is surrounded by an octahedral cage of Cl atoms. Crucially, the octahedra connect to each other in an edge-sharing fashion, which is necessary for the generation of Kitaev exchange interactions. The honeycomb layers are bound together by Van der Waals interactions. While these interactions are comparatively weak, $RuCl_3$ is not fully quasi-2D. The material exhibits 3D structure whose unit cell consists of three honeycomb layers stacked in an ABC-type configuration as shown in Fig. 1.17b. The 3D structure was initially thought to be two-layer (AB stacking, which is shown in Fig. 1.17c), but it has since been realized that the AB structure is actually the result of defects [41][40]. Cao et al.'s demonstration of this fact is illustrated in Fig. 1.18. The authors performed T-dependent heat capacity C_p and elastic neutron scattering measurements on a crystal they suspected of being high in quality and found that this crystal showed sharp transitions at 7 K. The neutron scattering measurement also revealed that the magnetic order seen below the 7 K transition shows three layer periodicity (as indicated by the peak in scattering intensity at (0, 1,

1/3)). The authors then deliberately mechanically deformed this crystal and then performed the C_p measurement again. They did multiple iterations of this and found that deformations produced noticeable structure around 14 K, which indicates inhomogeneity in the crystal. Regions with three-layer stacking exhibit $T_N = 7$ K while those with two-layer stacking show $T_N = 14$ K. As the three-layer stacking is the dominant arrangement in high quality samples, the two-layer stacking regions are referred to as stacking faults. These stacking faults have proven to be a major challenge for experiments in $RuCl_3$. Even if a crystal is grown perfectly, stacking faults can be induced in the sample simply by rough handling. Special care must be taken when working with $RuCl_3$ crystals in order to avoid putting any unnecessary stress or strain on the sample.

While it is known that the structure of high quality crystals consists of three layer stacking periodicity, the exact space group has yet to be conclusively determined. Specifically, there is still disagreement about whether the true low temperature space group is C2/m or R$\bar{3}$. These two structures are shown in Fig. 1.19. Numerous experiments have also revealed a weak anomalous breaking of rotational symmetry breaking to C_2 (two-fold) even in crystals with clear evidence for the R$\bar{3}$ space group [43].

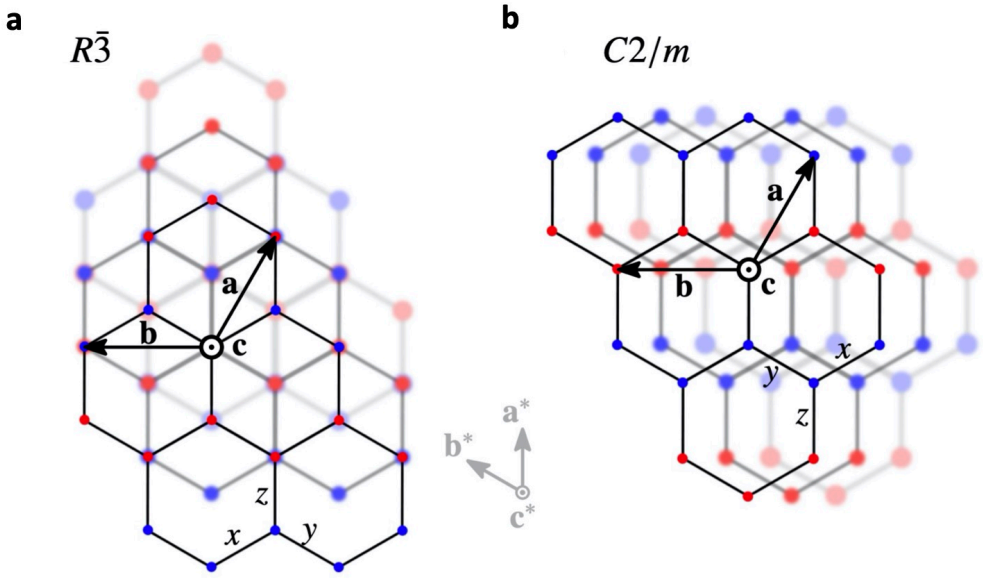

Figure 1.19: It is still unclear whether the full 3D structure of $RuCl_3$ is rhombohedral (space group R$\bar{3}$ shown in Panel (A)) or monoclinic (space group C2/m shown in Panel (B)). Figure adapted from [42].

1.3.2 Hamiltonian

While $RuCl_3$ is certainly a promising candidate for realizing Kitaev's model, it still exhibits numerous deviations from Kitaev's idealized model. The true Hamiltonian is still debated, but is thought to generally consist of equally strong K and Γ terms (with $K < 0$ and $\Gamma > 0$) as well as relatively weak J, J_3 (third neighbor Heisenberg), and $\Gamma^{'}$ [27] [44]. A set of parameters that has now been applied in several studies is $(J, K, \Gamma, J_3) \approx$ (-0.5,-5.0,+2.5,+0.5) meV [45][46][47][27].

As discussed earlier, there is still significant uncertainty regarding $RuCl_3$'s 3D structure and the nature of the system's weak, but non-negligible interlayer exchange interactions. The interplay between these two properties has been explored by Janssen et al. [42]. Interestingly, whether $RuCl_3$ is in an $R\bar{3}$ structure or a C2/m structure has a significant effect on not just the strength of the interlayer interactions, but on their nature as well. Specifically, the bond-directional nature of the in-plane Kitaev and off-diagonal exchange interactions (Γ and Γ') carrier over to the interlayer interactions as well. This is illustrated in Fig. 1.20.

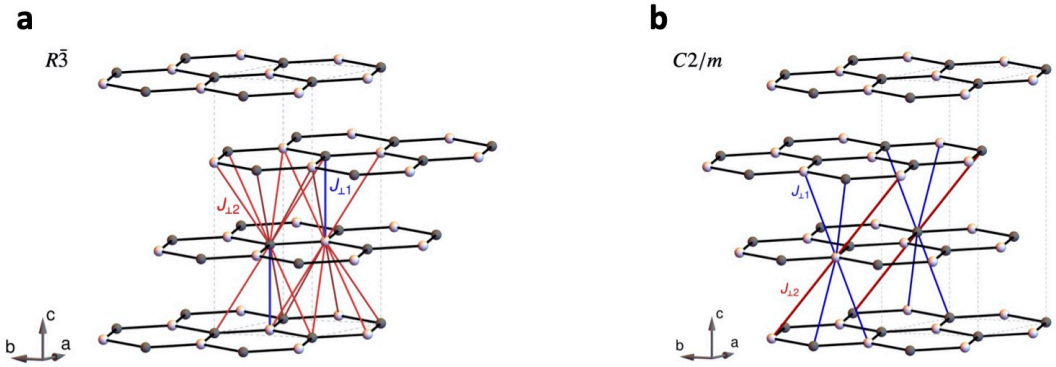

Figure 1.20: The nature of the possible interlayer exchange interactions in $RuCl_3$ depends on the exact space group, which is still not fully known. This figure shows the possible interactions for the $R\bar{3}$ space group (Panel (A)) and the C2/m space group (Panel (B)). Figure adapted from [42].

1.3.3 Phase Diagram

The significant non-Kitaev exchange interactions ultimately lead to an ordered ground state rather than a spin liquid one. At 7 K (in high quality crystals), $RuCl_3$ orders into a zig-zag type antiferromagnetic (AFM) arrangement. Notably, this particular ground state is consistent with the material's suspected Hamiltonian and the calculations done by Rau et al. [19] and Winter et al. [27]. Within a given honeycomb layer, zig-zag order consists of alternating chains of ferromagnets where the chains run along the honeycomb zig-zag direction (typically referred to as the **a** axis in $RuCl_3$). Note that the individual moments do not lie entirely in-plane and that the ordered moment

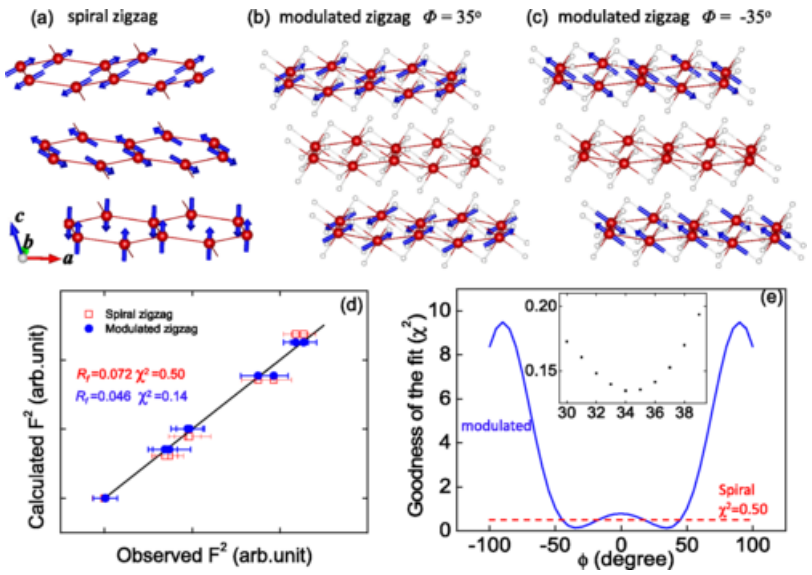

Figure 1.21: Possible 3D ordering configurations form the magnetic moments in $RuCl_3$'s zig-zag antiferromagnet phase. Figure adapted from [40]

is thought to point about 35° out-of-plane (see Fig. 1.21) [40]. Like the 3D crystal structure, the exact 3D magnetic structure is not definitively known. Some possible arrangements are shown in Fig. 1.21. The moments are likely aligned in a collinear fashion with the individual moments lying within the ac plane at a finite angle relative to the **a** axis (the modulated zig-zag states in Fig. 1.21).

$RuCl_3$'s full phase diagram is shown in Fig. 1.22. As we just discussed, the material's true ground state is an antiferromagnetically ordered phase. However, this magnetic order can be destroyed by a fairly weak magnetic field of about 7 T. The precise value of the order destroying field H_c varies depending on the sample and field configuration. Crucially, a 7 T field is not strong enough to fully polarize the magnetic moments in the system. A state that exhibits full polarization (or at least shows properties consistent with a spin-polarized state rather than a disordered one) is not seen until $B > 11$ T. This leaves an intermediate field regime where the moments are strongly disordered and may possibly exhibit spin liquid phenomenology. Evidence of this spin liquid physics will be discussed in the next section. Note that the phase diagram depicted in Fig. 1.22 only applies for **B** directed in-plane (**B** ∥ **a** specifically). Much higher field values are needed to kill the antiferromagnetic order for **B** ∥ **c**. This is due to a combination of local anisotropy and the Γ exchange, which acts as a ferromagnetic interaction for in-plane spins, but an antiferromagnetic interaction for out-of-plane spins. Zhou et al. recently observed that a perpendicular field of 36 T was needed to destroy the magnetic order [50].

We now return to the zig-zag ordered state and elaborate on its field dependence. There is an

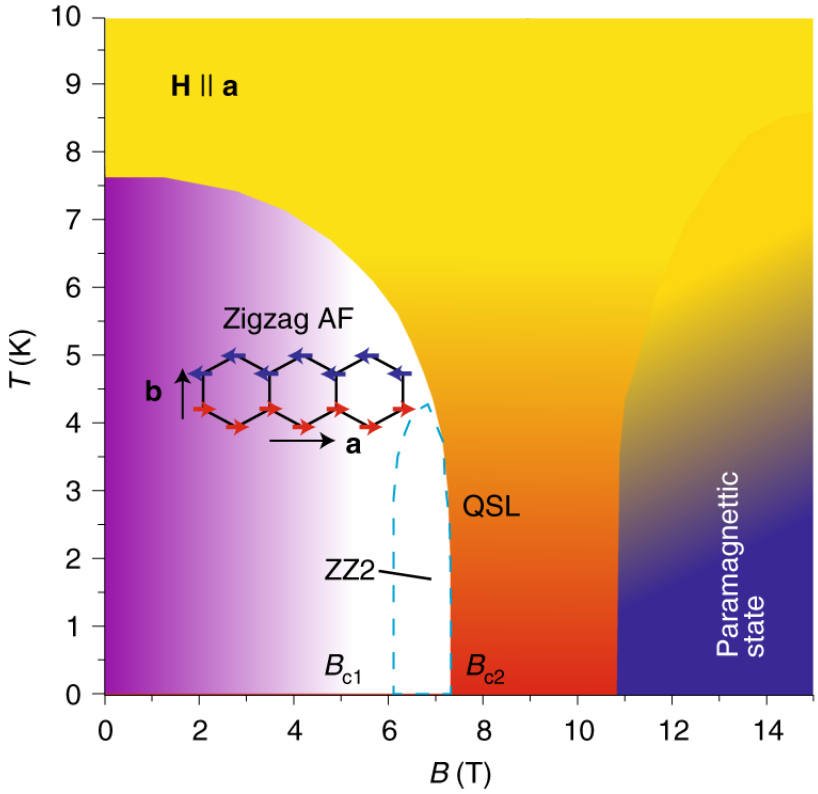

Figure 1.22: The phase diagram showing the QSL phase (shaded red and orange) sandwiched between the zigzag (purple) and polarized states (navy blue) with **H** ∥ **a** (**a** and **b** axes shown in inset). The ZZ2 phase that lies between critical fields B_{c1} and B_{c2} is outlined by the blue dashed curve [48]. The inset shows the zigzag order (red and blue arrows are local moments on Ru sites). Figure adapted from [49].

intrinsic degeneracy to the zig-zag order. The in-plane component of the moment at a particular site must be perpendicular to one of the three bonds connecting that site to its nearest neighbors. This leaves three possible in-plane directions along which the moments are able to point. This degeneracy manifests itself through the appearance of different types of domains. These domains can be seen in neutron scattering measurements where they appear as intensity peaks at two of six possible points in the Brillouin zone as shown in Fig. 1.23 [51]. Note that this degeneracy only holds for $B = 0$. When a field is applied, domains with an ordered moment perpendicular to **B** will be energetically favored. A single domain structure will therefore be seen for $B > \sim 2$ T. **B** ∥ **a** presents a unique case as two of the three possible domains will equally favored.

As shown in Fig. 1.22 there is a transition that occurs within the ordered state. This phase (labeled ZZ2) only occurs for **B** ∥ **a** as shown in Fig. 1.24a. The configuration of the magnetic moments in the ZZ2 phase is depicted in Fig. 1.24c in a manner that emphasizes its contrasts from 1.24b. The first notable difference is that the magnetic unit cell consists of six layers, not three

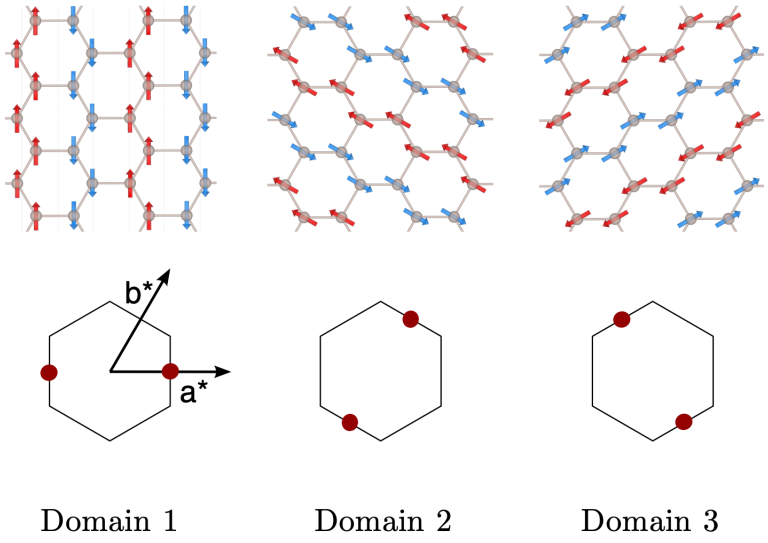

Figure 1.23: In a zig-zag antiferromagnetic ordered state, the moments can point along three different directions. A magnetic field will cause one of the three configurations to be favored. In the absence of such a field, the three ordering directions will coexist as magnetic domains. This figure shows the three possible types of configurations as well as the corresponding locations of the magnetic Bragg peaks in the Brillouin zone. Figure adapted from [51].

like the ZZ1 phase. The moments also exhibit different interlayer alignments. As shown in Fig. 1.24, the close neighbors on separate layers show ferromagnetic alignment, which differs from the antiferromagnetic alignment seen in the low B zig-zag phase. This change in stacking periodicity and magnetic structure implies that interlayer interactions are not insignificant.

Above $\approx$ 7 T, the system loses all magnetic order entirely. This was demonstrated explicitly by Balz et al. [52] who found that that sharp excitations (typically associated with magnon-like excitations) disappear for $7 \leq B \leq 9$ T. Because the system lacks magnetic order, but the applied field is not yet strong enough to fully polarize the spins, it is thought that this field-induced disordered state may be a quantum spin liquid. Specific evidence for this assertion will be discussed in the next section. Balz et al. found that note that sharp magnon-like excitations reappeared for $B > 9$ T, indicating that the system has entered a spin-polarized phase. While this phase is not ordered in the traditional sense (the ferromagnet-like spin configuration has been enforced by the external field, not the intrinsic exchange interactions), the correlations between the individual moments give rise to magnon-like spin wave modes that are visible in neutron scattering experiments. Note that the nature of the transition from the intermediate field disordered phase to the spin-polarized phase is not fully understood. Simple energy considerations would seem to imply a weak crossover at a T-dependent field, but some experiments (including some presented in this thesis) indicate a sharper

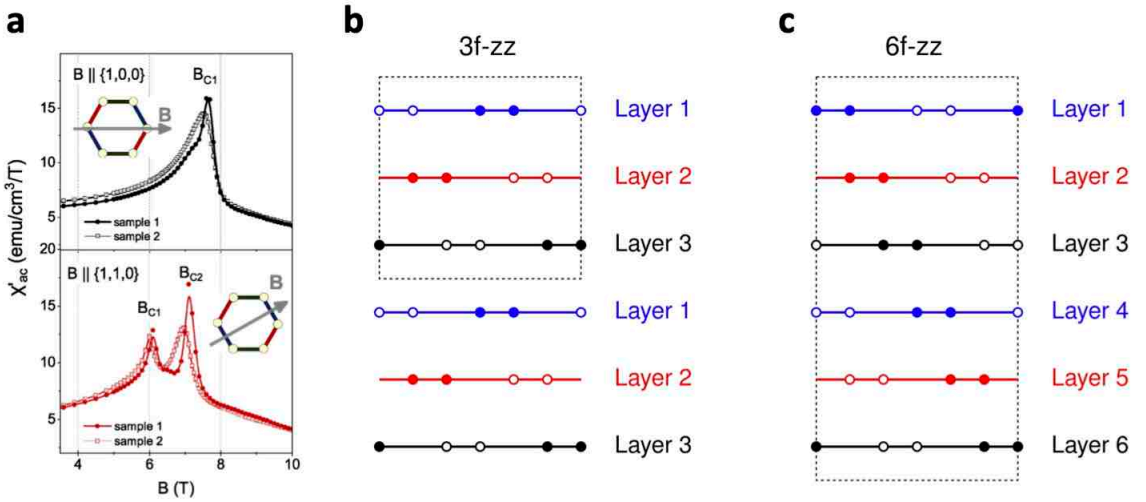

Figure 1.24: $RuCl_3$ exhibits another ordered phase at intermediate field (often labeled ZZ2). Panel (A): As evidenced by AC magnetic susceptibility, the ZZ2 phase only occurs when $\mathbf{B} \parallel \{1, 1, 0\}$ (or equivalently **a**), but not when $\mathbf{B} \parallel \{1, 0, 0\}$ (or equivalently **b**). Panel (B): Illustration of the primary zig-zag ordered phase (often referred to as ZZ1), which has three layer stacking periodicity. Panel (C): Illustration of the ZZ2 order and its six layer stacking periodicity. Open and closed circles are used to indicate the direction of the magnetic moment. Note that spins directly above each other are antiferromagnetically aligned in the ZZ1 phase and ferromagnetically aligned in the ZZ2 phase. Figure adapted from [48].

transition. Similarly, there is some disagreement on where this transition occurs (what value of B). This uncertainty clearly justifies further exploration.

1.3.4 Evidence of Spin Liquid Physics

While $RuCl_3$ does magnetically order, the T_N of 7 K is lower than one should expect based on the energy scale of the exchange interactions ($K \approx 5$ meV ≈ 60 K). This behavior is typically taken as a signature of frustration in QSL candidates. This led many to believe that the system could be thought of as a spin liquid at high energy scales. Early efforts therefore focused on the high T (and zero field) regime where numerous encouraging results were obtained. Specifically, Raman [53] [54] and Inelastic neutron scattering (INS) [41] [55] experiments revealed evidence of a continuum of scattering states that may be consistent with Majorana fermion excitations.

INS data from Banerjee et al. [41] is shown in Fig. 1.25. Above T_N, there is a continuum of scattering states located around Γ (the Brillouin zone center). The fact that the intensity is broad (in contrast to the sharp modes seen for magnons), but still localized to a particular region of energy-momentum space is consistent with fermionic multiparticle scattering. A continuum of scattering intensity is expected for fractional excitations because the neutron used to excite the

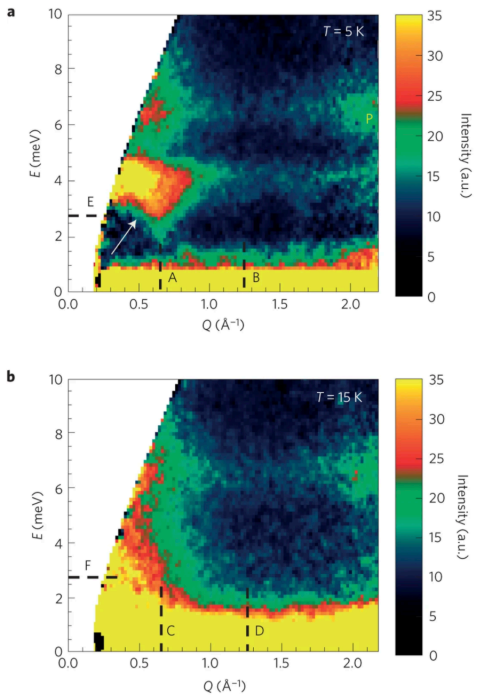

Figure 1.25: Inelastic neutron scattering (INS) spectrum for $RuCl_3$ measured below (top panel) and above (bottom panel) T_N. Figure adapted from [41].

system will generally be unable to excite a single such fermionic excitation and will therefore excite multiple quasiparticles instead. Below T_N, there is a clear rearrangement of scattering intensity. The low energy portion of the continuum disappears and sharp minima are visible at the M points ($Q = 0.62^{-1}$ in this plot). These features are associated with magnon excitations of the zig-zag order. At high energies it appears that the high continuum remains despite the presence of magnetic order.

The Raman experiments also reveal high energy scattering continua at high T, but are able to address the existence of Majorana fermions in a more quantitative fashion. Fig. 1.26a (adapted from Sandilands et al. [53]) shows the Raman scattering spectra for an $RuCl_3$ crystal at 5 K. Sharp phonon-derived modes appear on top of a broad continuum (shown in blue). Nasu et al. [54] later showed that the integrated Raman intensity measured in Sandilands et al.'s experiment could be fit to the function $I \sim (1 - f(\omega_0))^2$ where $f(\omega_0)$ is the Fermi distribution function and ω_0 is some characteristic frequency. The reason that the intensity would be expected to have this functional form is that the Raman processes excited in the experiment should create pairs of Majorana fermions.

More recently, attempts to search for spin liquid physics in $RuCl_3$ have shifted to the intermediate field disordered state ($7 < B < 11$ T). Evidence for spin liquid physics in this field range has been

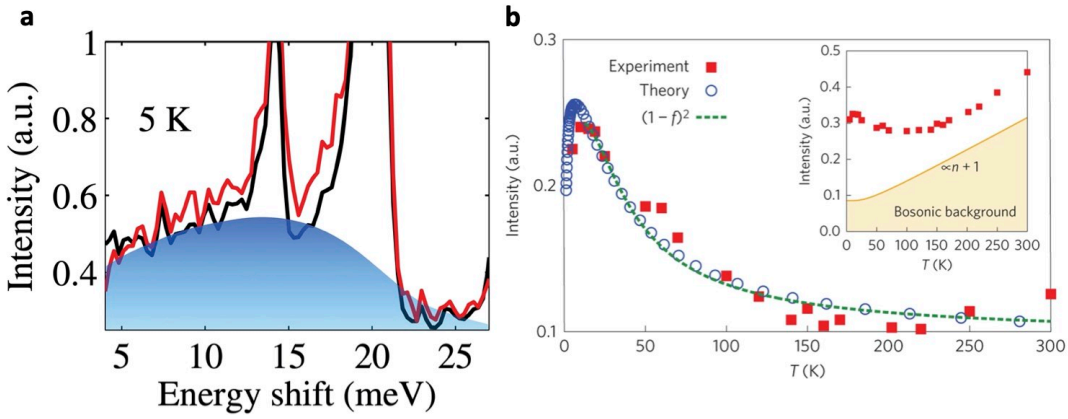

Figure 1.26: Panel (A): Measurement of $RuCl_3$'s Raman scattering spectrum, which consists of sharp phonon modes on top of a broad background continuum (shown in blue). Panel (B): Comparison of the T-dependence of the integrated Raman intensity measured in the experiment (red) and obtained from quantum Monte Carlo simulations (blue) as well as a fitting of the data to the expected distribution function for multi-fermion excitations (green). Figures adapted from [53] and [54].

found in nuclear magnetic resonance (NMR) [57] [58], INS [56] [52], and terahertz spectroscopy measurements [59]. Banerjee et al.'s field-dependent INS experiment is particularly instructive (see Fig. 1.27). At zero field, they observe scattering spectra that are very similar to what was previously reported [55] [41]. Above T_N (Fig. 1.27f) there is a column of scattering intensity centered at Γ that is replaced by sharper modes centered at the M points for $T < T_N$ (although some of the continuum is still visible at high energy). As B increases the apparent excitation gap decreases along with the intensity at the M points. At 8 T, a broad (and seemingly gapless) scattering continuum is observed at Γ while the M point scattering is absent entirely, consistent with the destruction of magnetic order. This spectrum is very similar to what was observed for $T > T_N$, which implies that a magnetic field can reveal a possible quantum spin liquid state. Balz et al. [52] subsequently found that a gapped spectrum was recovered at higher field (8.6 T for the crystal measured in that experiment), meaning the alleged field-induced quantum spin liquid should only exist within a finite field window. It has also been suggested that the scattering continuum may be due to a tendency for multimagnon excitations (caused by the Γ exchange) rather than exotic fractionalization- derived quasiparticles [27].

However, the most notable piece of evidence for Kitaev spin liquid (KSL) behavior at intermediate B is the alleged half-integer quantized thermal Hall conductivity observed by Kasahara et al. [60]. This finding is presented in Fig. 1.28. This specific report is of substantial relevance to this thesis and it (along with the thermal Hall effect in general) will be discussed at length later. For now, we only give a brief summary of the results. As discussed earlier, applying a magnetic field to a

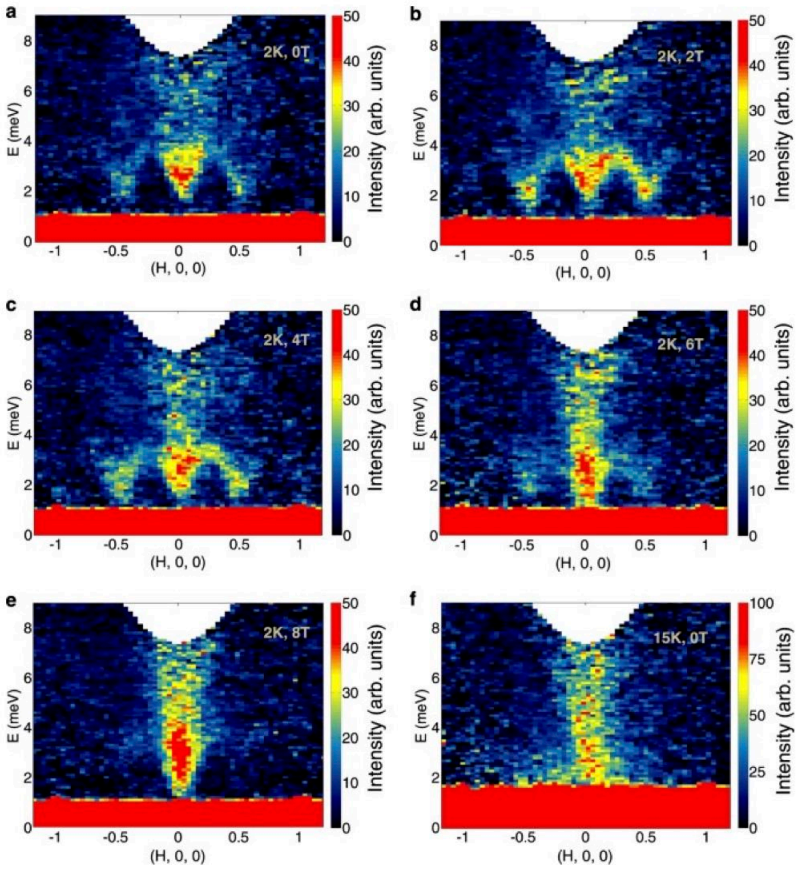

Figure 1.27: Inelastic Neutron Scattering (INS) spectrum at a series of temperatures and magnetic fields. Note that **B** ∥ **a** here. Gapped spin waves are observed at the M points in the ordered phase while a column of scattering centered at Γ is seen for all fields. Figure adapted from [56].

KSL state should gap out the bulk excitations and leave only the chiral Majorana fermion edge modes. This then creates a topological state (depicted in Fig. 1.28a) that is reminiscent of a more conventional quantum Hall state except that the edge current carries only heat, not charge and the quasiparticles possess half of the energy of a regular fermion (due to their Majorana nature). 1.28b shows several curves of the thermal Hall conductivity divided by temperature (κ_{xy}/T) data collected during this experiment, which are then used to construct a phase diagram in 1.28c that demonstrates that the effect is intrinsic to the intermediate B phase. Note that **B** is applied at a finite angle relative to the honeycomb plane. This is because a substantial in-plane field is needed to create the spin liquid phase and it was thought at the time that a perpendicular component was needed to generate the thermal Hall effect. The key observation in this report is the value of κ_{xy}/T within the intermediate B window. The authors found that for a narrow field range, κ_{xy}/T exhibits a plateau-like behavior and the value at the plateau (at least for the curves taken between 3 and 5 K) equals one half of the thermal conductance quantum K_0 (as discussed earlier). We remind

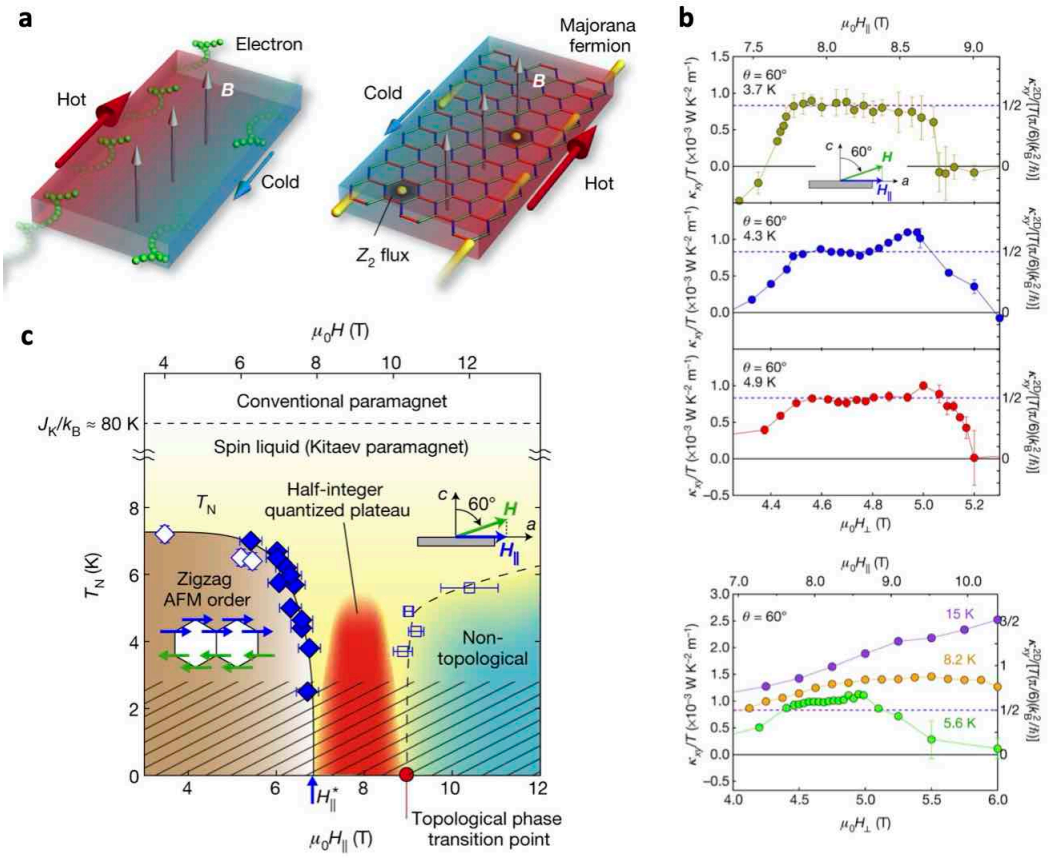

Figure 1.28: Panel (A): Physical depiction of the alleged quantized thermal Hall state claimed for $RuCl_3$ (right) with a particular emphasis on its similarity to the more conventional integer quantum Hall state (left). Panel (B): Thermal Hall conductivity divided by T at a series of different temperatures where $\mathbf{B}$ is directed 60° away from the c axis and $\mathbf{H}_\parallel \parallel \mathbf{a}$. The left axis uses SI units while the right axis is in units of the thermal conductance quantum, K_0. The latter emphasizes that the measured value is half of K_0 as expected for Majorana fermions. Panel (C): T, B phase diagram for $RuCl_3$ showing that the quantized κ_{xy}/T signal is only observed in the intermediate field disordered regime. All figures adapted from [60].

the reader that this is exactly the smoking gun for chiral Majorana fermion edge states that Kitaev originally proposed (though the B values at which the effect is reported are likely far beyond the perturbative regime) so the finding generated significant excitement around $RuCl_3$ and quantum spin liquids in general. However, for reasons discussed throughout this thesis, this finding is still highly controversial and it remains to be seen whether it will truly hold up in the face of significant scrutiny.

Before concluding, we would like to note that the work from Kasahara et al. [60] is not the only such claim of a quantized thermal Hall conductivity (or even half-integer quantization). The Heiblum group at the Weizmann Institute of Science has published multiple reports on quantized thermal transport in fractional quantum Hall states [62][61]. The thermal Hall effect probes chirality,

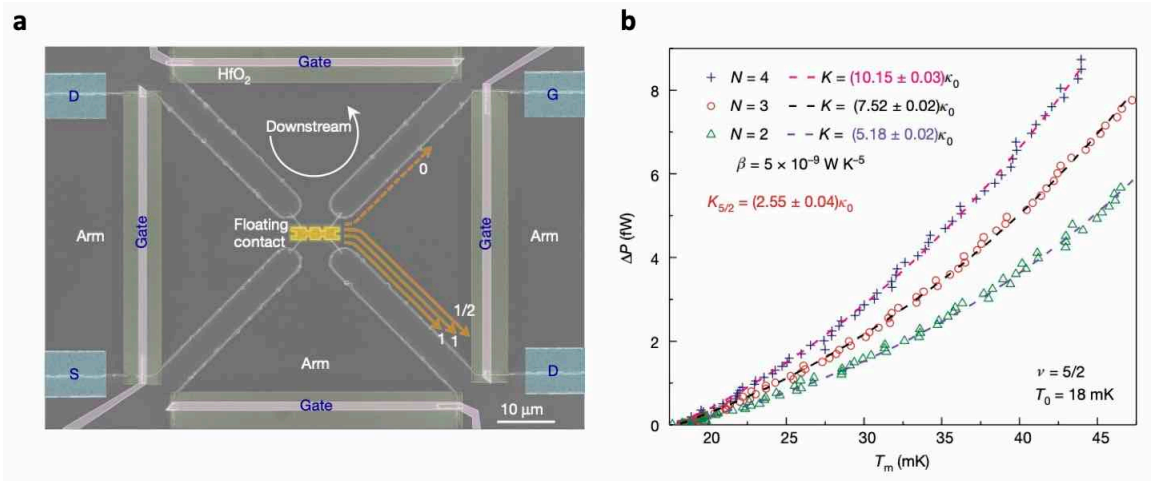

Figure 1.29: Panel (A): An image of the device used to measure quantized thermal transport in quantum Hall states. The yellow arrows indicate the flow of the "downstream" charge modes and the "upstream" Majorana mode. Panel (B): κ_{xy} in the $\nu = 5/2$ state is calculated using temperatures that are obtained by measuring the electrical noise in the edge modes, something that cannot be done for insulating magnets like $RuCl_3$. These figures are adapted from [61].

not just the conductivity of charge-carrying modes. Fractional Quantum Hall states can have highly complex edge states, which may be composed of several different edge modes (each of which can be charged or not, or move "upstream" or "downstream"). The $\nu = 5/2$ filling state is of particular interest due to its predicted ability to exhibit Majorana fermion edge states (though the exact description of this state is still highly controversial). The thermal Hall effect can, in principle, help distinguish between the candidate states, but Banerjee et al.'s measurement has only added added more confusion [63][64][65]. These are highly impressive experiments, but they study a very different physical system and do so in a very different way. Instead of using resistive thermometry, these experiments measure temperature via the electrical noise of the edge modes. While the bulk of these quantum Hall systems may be gapped, the edge state are still intimately related to charge degrees of freedom, which is what makes this noise thermometry possible. Such an experiment cannot be trivially done with magnetic insulators like $RuCl_3$.

1.4 Experimental Details

1.4.1 Sample Preparation

Once a crystal is selected, the first step is to make thermal contacts. We do this by bonding 5 mil (100 μm) Au wires to the crystal with Stycast 2850FT epoxy. Though Ag paint is convenient for attaching the Au wires to the sample, we found that it does not stick well to the smooth surfaces

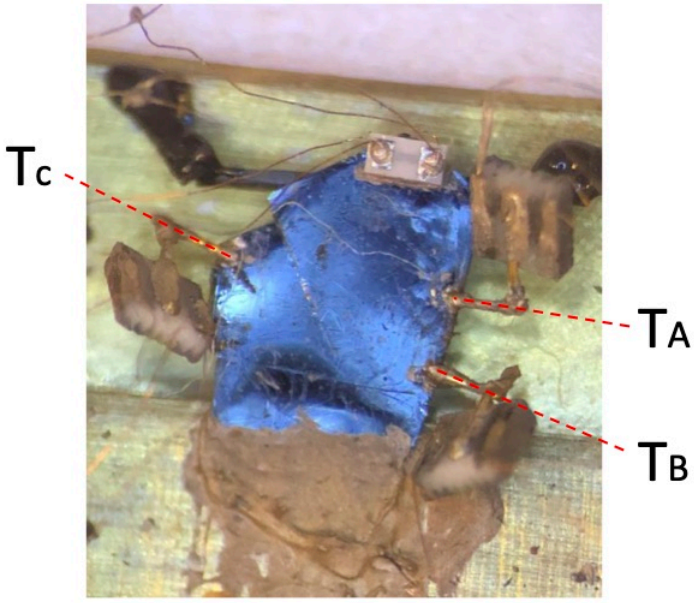

Figure 1.30: Image of mounted crystal (Sample 3) used for thermal transport experiments. A heater is placed at the top of the sample and the three thermometers (T_A, T_B, and T_C) are attached via gold wires. The crystal is mounted onto a brass plate using Ag paint and is mechanically supported at the opposite end with a Delrin post. The reflectivity of the surface indicates smoothness and therefore an absence of creases that might indicate the presence of stacking faults.

of the $RuCl_3$ crystals. Stycast tends to form large contact surfaces, which causes uncertainty in measures of the true dimensions, but the low thermal impedance of the large contacts is more important than the geometric uncertainty. Ag epoxy can also be used, but it needs to be heated to cure correctly and we did not want to risk the heat degrading the $RuCl_3$ crystals. A heater (typically a 1 kOhm 2MCS-1001F resistor from API technologies) is attached to the crystals either directly with Ag paint or through another 5 mil Au wire.

After the epoxy for the Au contacts has dried, one end of the crystal is thermally anchored to brass plate designed specifically for our experimental setups. This anchoring can either be done directly with Ag epoxy (as shown in Fig. 1.30) or though an additional Au wire. In the latter case, Stycast is typically used for the necessary connections as Ag paint does not have sufficient mechanical strength. Before the crystal is mounted onto the brass plate, Nylon posts, with electrical contact pads (made from Ag epoxy) on top, are placed onto the brass plate. Then, thermometers (typically Lakeshore Cryotronics RX102A, which have $R = 1$ kOhm at room temperature) are thermally attached to the remaining Au wires with Ag paint (see Fig. 1.30). Specifically, the Au wires on the sample are connected via a second set of Au wires that are attached to the thermometers using Ag

epoxy. This is done to minimize the mechanical stress placed on the sample during the mounting process. The thermometers are then connected to the contact pads on the Nylon posts using 1-mil phosphor bronze wires (that are typically also added prior to mounting).

Although the crystals are highly flexible, weak stresses on them can produce stacking faults that ruin their quality. We employ special care to minimize the applied stress during the mounting process. Essential support is provided by a Delrin post glued by Stycast to the free end of the crystal (and anchored to the brass plate). The post prevents crystal bending from the torque ($\tau = \mathbf{m} \times \mathbf{B}$) in a strong field. The ultra-low thermal conductivity of Delrin and the large aspect ratio of the post minimize the heat current shunted by the post.

1.4.2 Thermometry

We now provide a brief overview of the various thermometers used in the experiments presented in this thesis.

- **RX102A:** The primary sample thermometer used in the experiments presented in this thesis. $R(T)$ is essentially flat for $T > 40$ K. However, as the temperature is lowered further R vs. T becomes sufficiently steep for the the resistors to be used as thermometers. We find that the RX102A thermometers are the most effective of the commercially available options for thermal transport experiments performed at $T < 15$ K.

- **RX202A:** The RX202A shows substantially weaker magnetoresistance (MR) than the RX102A. It therefore makes an ideal reference thermometer for low T thermal transport experiments in an applied field. The available models are too large to be used as sample thermometers. A cylindrical-shaped RX202A has been inserted into an appropriately-sized hole on the Janis sample stage and held in place using GE varnish. These two features (the hole of matching diameter and the use of the adhesive) are necessary for sufficiently strong thermal contact with the stage. While the RX202A is an effective reference thermometer at low T, its $R(T)$ curve becomes too flat at high temperatures to be used for $T > 40$ K.

- **KOA:** The KOA 1 kOhm resistor (RK73B1HTTC102J from Garrett Electronics) offers a decent alternative to the RX202A as a low MR reference thermometer when spatial considerations on the sample stage do not permit the use of the latter. The KOA is also substantially cheaper. We use the KOA on the ICE Oxford sample stage as its small size (mm scale) allows it to be conveniently placed near the sample itself and held in place using GE varnish.

- **Cernox Thermometers:** The primary advantage of Cernox thermometers over the Ruthenium Oxide- based sensors is that they are able to be used over a much wider temperature range. Their $R(T)$ curves exhibit sufficient curvature that they can be used as diagnostic/reference thermometers up to room temperature, though their utility as sample thermometers is still limited to $T \leq 70$ K as described in [66]. However, the thermometers present significant challenges at low T. While MR is weak enough that they can generally be used without needing to perform field-calibration for $T \geq 10$ K, the MR becomes quite substantial as the temperature is lowered further. Additionally, it has been observed that they can show significant field asymmetry in their MR, which can produce spurious thermal Hall signals. For the experiments presented in this thesis, the primary utility of the Cernox senors is as a secondary reference thermometer that is used to calibrate the low MR thermometer.

1.4.3 Electronics

Figure 1.31: This image depicts a typical electronics setup for a thermal Hall effect measurement. At the top left are the multipin boards and corresponding multipin cables. Also pictured are current source and voltmeter (for exciting and measuring the sample heater) and the various Lakeshore temperature controllers (used to measure the thermometer temperatures).

All thermometers are measured using Lakeshore temperature controllers with the specific model employed being dependent on the thermometer's purpose. A model that utilizes an AC, lock-in amplifier-based technique (such as the LS370 and LS372) is typically preferred for measuring sample

thermometers as they offer substantially higher resolution than the DC-based instruments. These models (the LS336 and LS340) are then used for measuring diagnostic thermometers such as those on the sorb, 1 K pot, and ^{3}He pot. They can also be used for less sensitive measurements such as κ_{xx}, but the AC models are necessary for κ_{xy} due to the small signal size. The primary downside to the AC systems is the cost. Each LS372 costs around $10,000 and can only measure a single thermometer at a time. The LS336 and LS340 models cost around $4,000 and can measure up to four thermometers simultaneously.

The sample heater is excited using a DC current. This current is applied using a current source such as the Keithley 6221 model. This particular model is preferable for low T measurements as DC current sources frequently have current offsets that lead to inaccurate values at low current. For example, we have found that the Keithley 2400 model is not usable for $I < 15$ μA. As the dissipated power in the heater is used to calculate thermal transport quantities, it is best to measure the voltage drop at the 1 kOhm resistor directly. This is done using a K182 or K2182A voltmeter (both from Keithley as well).

1.4.4 Measurement Procedures

In the following sections, we will describe the underlying physical principles that guide our experiments as well as the general procedures used in the measurements. We also provide an extensive discussion of various technical difficulties that arise during the analysis stage. These difficulties are especially apparent in the thermal Hall experiments and the example data shown here is from the experiment presented in Chapter 3.

1.4.4.1 Thermal Transport Tensor

We employ a standard steady-state technique that is analogous to a conventional electrical measurement. We simply replace the Ohm's law-based expression $\mathbf{E} = \rho \cdot \mathbf{J}_e$ with the appropriate thermal transport analogue:

$$\nabla T = \lambda \cdot \mathbf{J}_Q = \begin{pmatrix} \lambda_{xx} & \lambda_{xy} \\ \lambda_{yx} & \lambda_{yy} \end{pmatrix} \cdot \mathbf{J}_Q \tag{1.29}$$

where ρ and λ are the electrical and thermal resistivity matrices. The thermal conductivity matrix κ can be obtained by inverting the resistivity matrix ($\kappa = \lambda^{-1}$). We define our coordinates such that $\mathbf{J}_Q \parallel \hat{\mathbf{x}}$ and $\hat{\mathbf{y}}$ is the transverse (Hall) direction. Typically, one would define $\mathbf{H} \parallel \hat{\mathbf{z}}$, but $\mathbf{H}$ is directed within the transport plane for most of the experiments presented in this thesis. This is

the case even for the thermal Hall effect and is one of the many highly unusual features of $RuCl_3$'s thermal transport physics. We use the fact that $-\nabla T = -\partial_x T\hat{\mathbf{x}} - \partial_y T\hat{\mathbf{y}} = \delta T_x/l_{xx}\hat{\mathbf{x}} + \delta T_y/l_{xy}\hat{\mathbf{y}}$ and Eq. 1.29 to obtain:

$$\lambda_{xx} = \frac{\delta T_x \cdot w \cdot t}{P_H \cdot l_{xx}} \tag{1.30}$$

$$\lambda_{xy} = \frac{\delta T_y \cdot w \cdot t}{P_H \cdot l_{xy}} \tag{1.31}$$

Note that we have used the fact that the sample heater power P_H (measured as VI in the experiment) is related to the heat current density $\mathbf{J}_Q$ using the expression $P_H = |\mathbf{J}_Q|/A$. Here, A is the sample cross sectional area that is calculated as $A = w \cdot t$ above where w and t are the sample width and thickness respectively. l_{xx} and l_{xy} are the distances between the longitudinal and transverse contacts.

As stated above, the thermal conductivity matrix can be obtained by inverting the thermal resistivity matrix. Explicitly,

$$\kappa_{xx} = \frac{\lambda_{xx}}{\lambda_{xx}^2 + \lambda_{xy}^2} \approx \frac{1}{\lambda_{xx}} \tag{1.32}$$

$$\kappa_{xy} = -\frac{\lambda_{xy}}{\lambda_{xx}^2 + \lambda_{xy}^2} \approx -\frac{\lambda_{xy}}{\lambda_{xx}^2} = -\lambda_{xx}\kappa_{xx}^2 \tag{1.33}$$

In the following sections, we provide detailed descriptions of the many technical subtleties associated with accurately obtaining these specific quantities.

1.4.4.2 Experimental Procedures

As just described, at the fundamental level the thermal transport measurements involve applying some known amount of heat current to the sample and then very precisely measuring the resulting temperature gradients as a function of temperature and applied magnetic field. The heat current is applied by running a DC current through a the 1 kOhm heater at the top of the crystal. The total energy loss to heat can be calculated via the known current value and the measured voltage drop across the resistor using the formula $P = IV$. Typical values of P were 225 nW (at a bath temperature of 0.36 K), 1.6 μW (at 0.78K), 6.4 μW (at 1.31 K) and 22.5 μW (at 1.67 K).

Most of the results presented here are performed by fixing the sample stage temperature using a low-MR reference thermometer (such as the RX202A) and sweeping the applied magnetic field. The field can be swept either continuously or in steps. Continuous field sweeps generally take less time than stepscans and the ability to measure the magnetic field over a higher density of values is

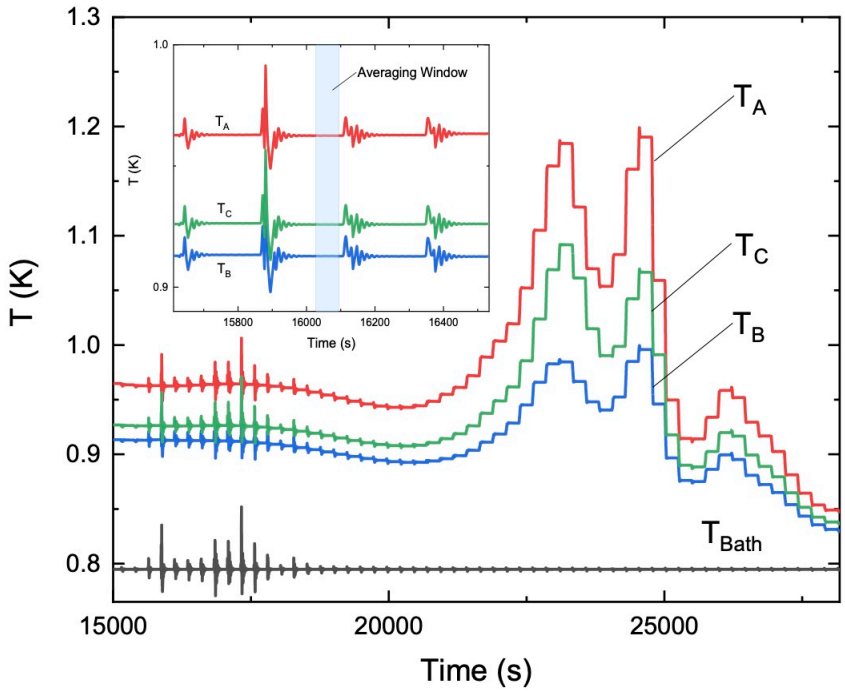

Figure 1.32: Temperatures of the stage thermometer and the three sample thermometers as a function of time. This data is from a stepscan sequence where the T_{Bath} is fixed at 0.8 K. Note how large transient fluctuations appear when the field is swept (that eventually relax after the sweeping ceases). The inset shows the same data, but over a smaller field range around 0 T where the transient effects are particularly strong.

helpful when calculating field derivatives (as we will do frequently for the oscillation data presented in Chapter 2). However, continuous scans can introduce a variety of artifacts that generally make the resulting raw data too noisy to be used for calculating thermal Hall conductivity. These artifacts are mostly associated with transient signals caused by a combination of the changing magnetic field and incomplete thermalisation of the sample. This effect is demonstrated in Fig. 1.32 which shows how the temperatures of the various thermometers (three on the sample and one on the stage) vary with time during a particular stepscan sequence. In this example, B is swept in 0.2 T steps and held at each step for around 180 s. Strong fluctuations appear while B is being swept that eventually relax once B stops changing, a fact that reveals their transient nature. These fluctuations are caused by Eddy currents on the sample stage as well as the magnetocaloric effect in the $RuCl_3$ crystal itself. The latter effect is especially strong near 0 T. The oscillatory-like appearance of these fluctuations is due to the competition between the two effects just described and the stage heater that fights to keep T_{Bath} fixed using a PID algorithm. During the analysis stage, the experimenter identifies a suitable averaging window containing only points after the fluctuations have fully relaxed and then

uses only these points in the analysis. The ability to collect tens of data points at a given field value also helps to achieve a suitable level of resolution for measuring the notoriously small gradients associated with the thermal Hall effect.

1.4.4.3 Thermometer Calibration

The thermometer calibration procedure employed in thermal transport experiments by our group has been developed by various members over many years. Max Hirschberger, in particular, made substantial progress in the application of these and related techniques to thermal Hall effect measurements. As these specific procedures and methods are described in great detail in his thesis [66], I will only give a brief overview of them here.

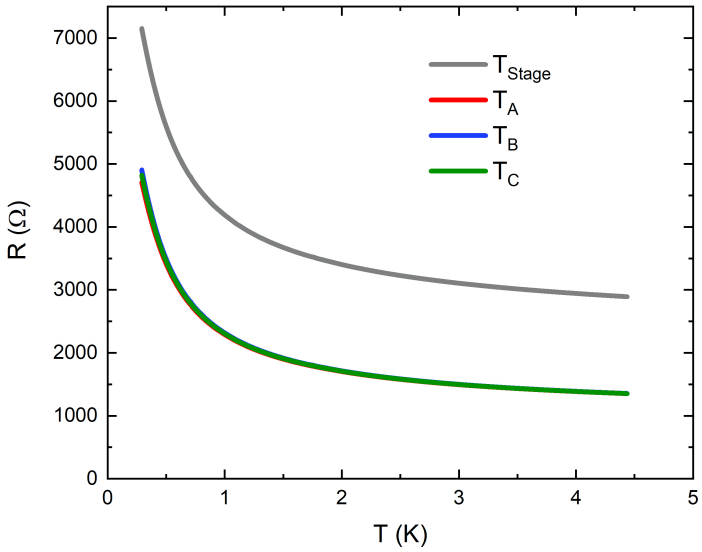

Figure 1.33: The thermometers used in the experiments presented in this thesis are resistors where R varies significantly with T. This figure shows the $R(T)$ curves for the RX202A stage thermometer on the Janis (gray) as well as the three sample thermometers (red, blue, and green).

All thermometers used in the experiments presented in this thesis are resistive thermometers. The temperature can then be obtained by comparing a measured resistance to a known $R(T)$ curve. Example $R(T)$ curves for Janis' RX202A stage thermometer as well as three RX102A thermometers on a $RuCl_3$ crystal are displayed in Fig. 1.33. These curves are measured at zero current excitation. $R(T)$ for the reference thermometer is previously known so at the analysis stage the $R(T)$ curves for the sample thermometers are then fit using Chebyshev polynomials. A similar fitting procedure is used to account for the the thermometers' magnetoresistance using calibration curves collected by sweeping B with zero heater current.

1.4.4.4 Field-Antisymmetrization

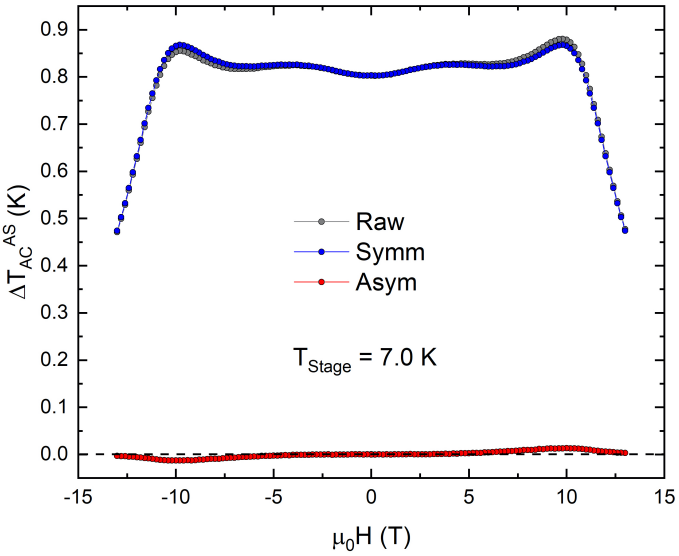

Figure 1.34: Example of temperature gradients measured during a field sweep. The raw data is shown in gray while the field symmetric and antisymmetric components are shown in blue and red respectively.

Owing to a slight, inevitable misalignment of the Hall contacts, the observed signal in the transverse (Hall) channel always includes a fraction of the longitudinal signal $\Delta_x T$ in addition to the intrinsic thermal Hall signal δy. Explicitly, $\Delta_y T$ will have the form:

$$\Delta_y T(H) = \delta_y(H) + \alpha \Delta_x T(H) \tag{1.34}$$

where $\alpha < 1$ measures the contamination caused by Hall contact misalignment. In a typical experiment, the longitudinal contribution will dwarf the transverse one. Conveniently, the two effects show different symmetries in their responses to an applied magnetic field. The Hall effect will change sign with **H** while the longitudinal signal will remain the same. The former is said to be field-antisymmetric and the latter is said the be field-symmetric. These characteristics allow a convenient way to extract the true Hall signal. This is done by measuring at both positive and negative fields and then symmetrizing and antisymmetrizing the data (as is done for electrical for measurements):

$$\Delta T^{sym}(H) = \big[\Delta T(+H) + \Delta T(-H)\big]/2 \tag{1.35}$$

$$\Delta T^{asym}(H) = \big[\Delta T(+H) - \Delta T(-H)\big]/2 \tag{1.36}$$

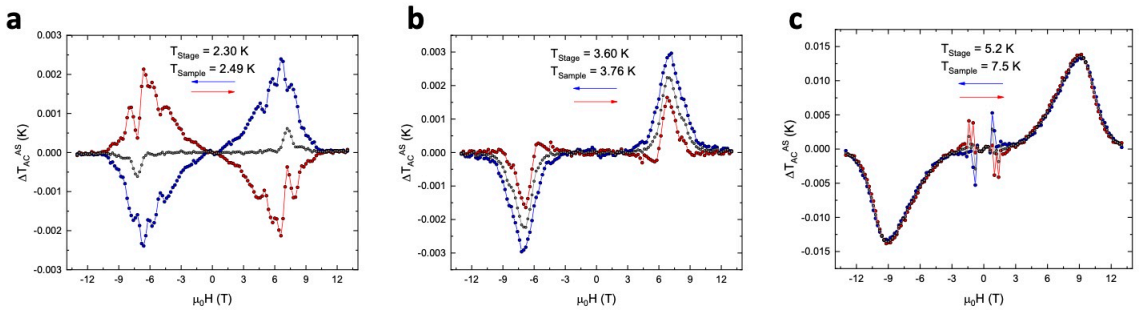

Figure 1.35: Field-antisymmetric temperature difference ΔT measured for sets of field sweeps measured at $T_{\text{Stage}} = 2.3$, 3.6, and 5.2 K. "up"-sweeps (negative to positive field) are shown in red, "down"-sweeps (positive to negative field) are shown in blue and their average is shown in gray. The up and down sweeps differ because of hysteresis that is not present at high T, but gets increasingly strong as T is lowered and eventually dwarfs the intrinsic Hall signal.

An example of this is process is shown in Fig. 1.34. The magnitude of the field-odd signal (red) is smaller than the field-even signal (blue) by more than an order of magnitude. The latter is almost indistinguishable from the raw, unsymmetrized ΔT curve.

Our work on $RuCl_3$ has revealed an additional technical difficulty associated with thermal Hall experiments in the material. We find that the thermal transport exhibits field-induced hysteresis loops (which are notably not observed in more conventional probes like magnetization). The physics of this effect is discussed elsewhere in this thesis and for now we focus only on its relevance to the calculation of the various thermal transport properties. In this context, this effect is highly problematic because it means that the second term in 1.34 will no longer be symmetric in field ($\Delta_x(H) \neq \Delta_x(-H)$). Instead, field-antisymmetrization leads to a "butterfly" loop.

This effect is illustrated in Fig. 1.35. The given examples are measured at fixed stage temperature $T_{Stage} = 2.3$, 3.6, and 5.2 K (with the higher effective sample temperature T_{Sample} indicated in the figure). We plot both the "up"-sweeps (red) and the "down" sweeps (blue) as well as their average (gray). Averaging both directions eliminates the hysteretic component. An alternative technique is to perform the antisymmetrization using the positive H portion of an "up"-sweep and the negative

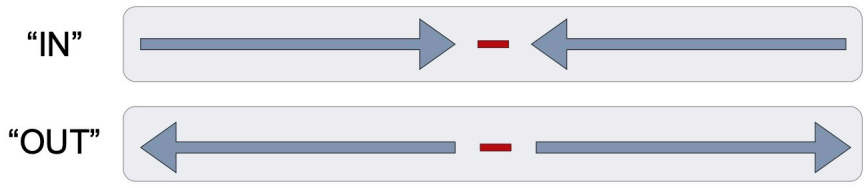

Figure 1.36: To remove the hysteretic contribution to the field-asymmetric signal without averaging two full sweeps, one can instead antisymmetrize segments from different sweeps in the fashion shown here.

H portion of a "down"-sweep (or vice versa). This is illustrated in Fig. 1.36.

As shown in the figure, the hysteresis effect is small at high T, but as the temperature is lowered, it becomes much larger than the true Hall signal. This complicates the analysis as it seems possible that the hysteresis may have more subtle manifestations that are not removed entirely with the techniques described here. This effect therefore merits more attention from the community.

1.4.4.5 Thermal Hall Resistivity: λ_{xy}

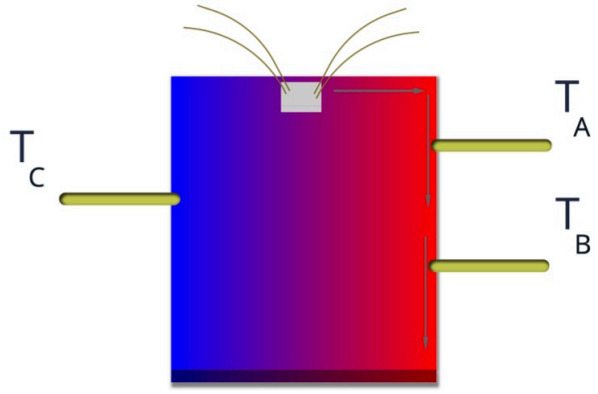

Figure 1.37: The fundamental quantity measured in a thermal Hall experiment is the field-antisymmetric transverse temperature gradient. This is illustrated for a typical sample configuration here where the color represents temperature.

The field-odd antisymmetric transverse gradient that remains after antisymmetrization is analogous to the transverse voltage in an electrical hall effect measurement. Similarly, it can be used to calculate the intrinsic thermal Hall resistivity, λ_{yx} (the thermal transport equivalent of ρ_{xy}):

$$\lambda_{yx} = \frac{\Delta T^{\text{asym}}}{l_{xy}} \frac{wt}{P_H} \tag{1.37}$$

where we have replaced δT_y to indicate its necessary use of field-antisymmetrization to extract the true Hall signal. To quantify the resolution in measurements of the very weak thermal Hall signals, we use the scatter in the $\Delta T^{\text{asym}}(B)$ curves near $B = 0$ T where the thermal Hall signal is either zero or negligibly small. Some examples are shown in Fig. 1.38 where visual inspection reveals noise levels of several μK. The scatter ranges from 5 μK for T_{Stage}= 1.1 K to 30 μK for T_{Stage}= 5.1 K to 120 μK for T_{Stage}= 7.0 K. The lower resolution at high temperatures results from the milder variation of R vs. T in the thermometer above 3 K, and degradation of the stability of ^{3}He cryostat at elevated T.

We note with emphasis that, in virtually all κ_{xy} experiments, the measured quantity is the

thermal resistivity matrix λ_{ij} which is subsequently inverted to obtain the thermal conductivity matrix $\kappa_{ij} = \lambda_{ij}^{-1}$. Although curves of the thermal Hall resistivity λ_{yx} are rarely reported, they are vital for properly assessing the uncertainties in κ_{xy} after the matrix inversion. As discussed below, the inversion process in α-$RuCl_3$ strongly amplifies error bars because i) λ_{yx} is strongly suppressed when B exceeds 10 T at temperatures below 4 K (which yields a very small thermal Hall angle) and ii) κ_{xx} undergoes a steep increase versus B between 7 and 13 T. Together, the two factors amplify uncertainties in measurements of λ_{yx} to produce very larger error bars for κ_{xy} in the regime $B >$ 10 T and $T < 4$ K.

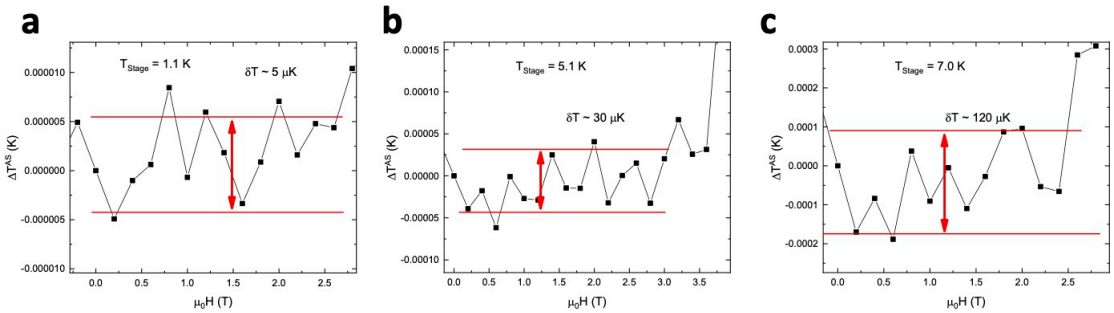

Figure 1.38: Scatter in the field-antisymmetric transverse temperature gradient ΔT^{asym} near zero field can be used as a proxy for experimental resolution. Each panel is labeled with the stage temperature and estimated noise for that particular set of field sweeps.

1.4.4.6 Thermal Hall Conductivity: κ_{xy}

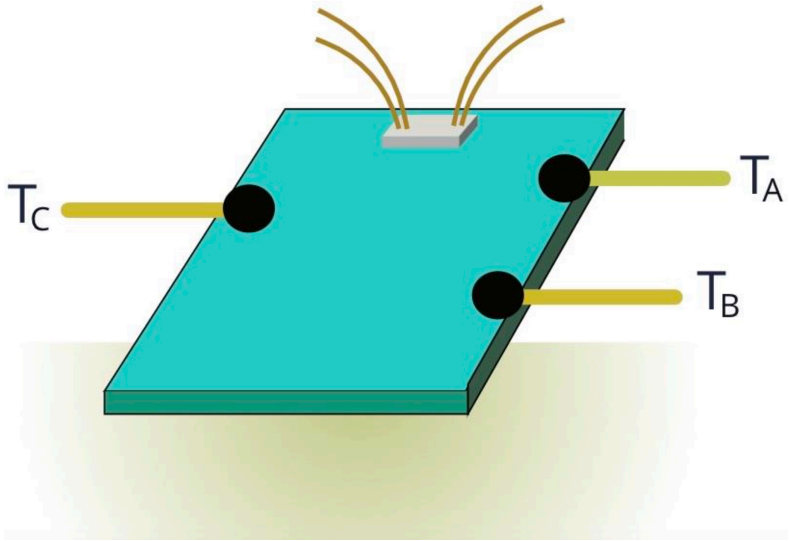

Figure 1.39: Drawing of thermometer configuration used for collecting the data discussed in this section.

Matrix inversion yields the expression $\kappa_{xy} \approx \lambda_{xy}\kappa_{xx}^2$. As shown in Fig. 1.40, λ_{yx} is largest immediately following H_c where the magnitude of κ_{xx} is small. As B is increased above H_c, κ_{xx} grows steeply. For example, between 7 and 13 T, κ_{xx} increases by 20× (or more). Temperature fluctuations of the heat bath are the primary source of noise in these experiments and their amplitude is generally independent of B. This means that the effective noise level in κ_{xy} at 13 T could be 400× larger than at 7 T.

The enhanced noise level is just one of many issues that arises in calculating κ_{xy} in $RuCl_3$ experiments. To illustrate the additional experimental challenges and potential pitfalls, we plot in Fig. 1.40 the following set of traces vs. B (here T_A, T_B and T_C refer to the readings from the three thermometers shown in the Fig. 1.30 and Fig. 1.39):

- The antisymmetric components of the three temperature differences $\Delta T_{AB} \equiv T_A - T_B$ (green), ΔT_{AC} (red), and ΔT_{BC} (light blue).
- The longitudinal thermal conductivity κ_{xx}.
- Curves of κ_{xy}^{AC} and κ_{xy}^{BC} derived from ΔT_{AC} (red) and ΔT_{BC} (light blue).
- The average temperatures T_{AB}^{AVG} (green), T_{AC}^{AVG} (red) and T_{BC}^{AVG} (light blue) inferred from the three thermometers.

This data is from the experiment that will be presented in Chapter 3. We will defer a detailed discussion of the underlying physics till then and will focus only on the technical aspects of the measurement for now. The eight columns report data collected at eight selected temperatures ($2.7 \leq T \leq 6.5$ K). We now describe the key conclusions inferred from this data set.

1. **Significance of transverse thermometer choice:** Measurements of the thermal Hall conductivity require a minimum of three thermometers. This is because a transverse pair is needed to measure the thermal Hall resistivity λ_{yx}, a longitudinal pair is needed to measure the thermal resistivity λ_{xx}, and both quantities are needed to perform the necessary matrix inversion to calculate κ_{xy}. Three thermometers are usually used (instead of four) as one of the longitudinal ones can be used for measuring both temperature gradients. The one transverse thermometer is typically placed directly opposite one of the longitudinal thermometers so that they are at approximately the same temperature at zero field. This helps to ensure that the measured antisymmetric temperature difference ΔT^{asym} is not distorted by artifacts related to other sources of temperature nonuniformity. κ_{xy} is then calculated from this temperature

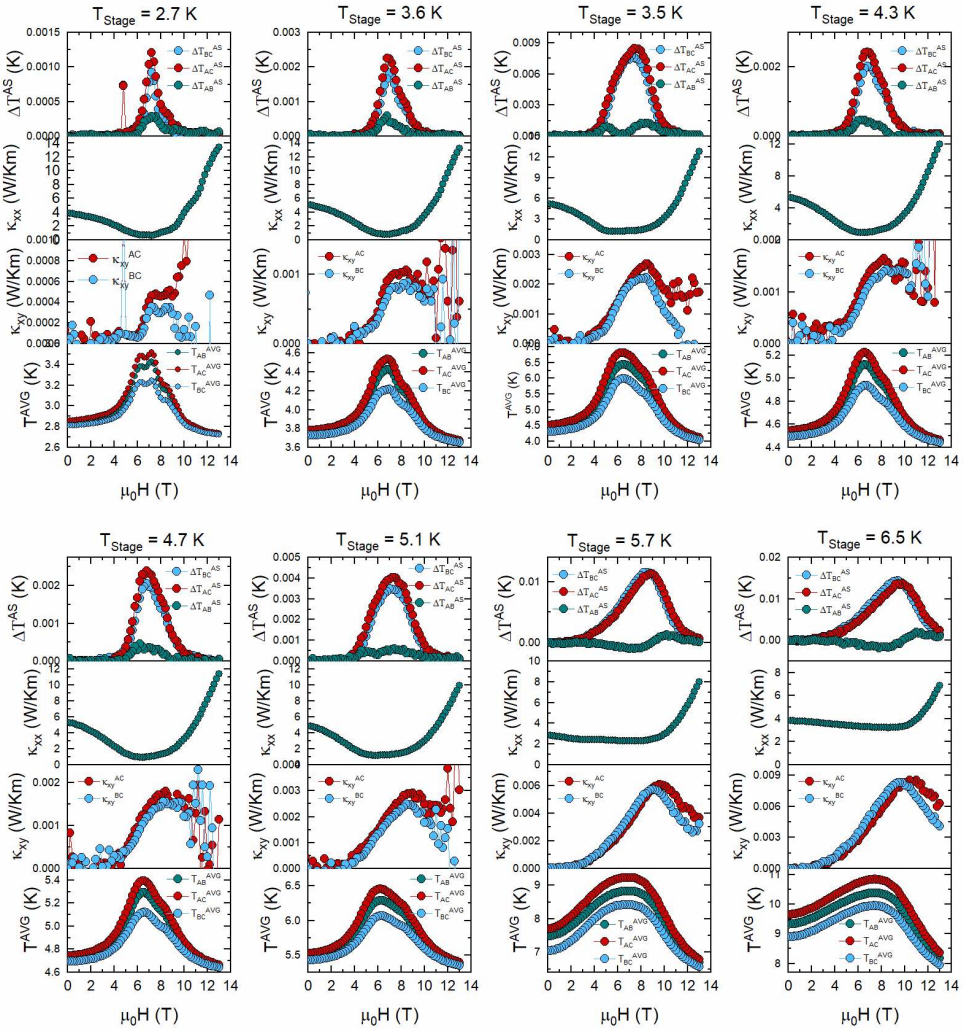

Figure 1.40: Each of the eight columns shows data at the stage temperature $T_{\rm Stage}$ indicated. The four panels in each column (enumerated from the top down) display (panel 1) the antisymmetrized temperature differences $\Delta T^{\rm asym} \equiv \Delta T^{\rm AS}$, (panel 2) κ_{xx}, (3) κ_{xy} and (4) $T^{\rm AVG}$ (4). In panels 1, 3 and 4, we show curves derived from the three measured temperature differences $\Delta T_{\rm AB}$ (green), $\Delta T_{\rm AC}$ (red) and $\Delta T_{\rm BC}$ (light blue). Here $\Delta T_{\rm AB} \equiv T_{\rm A} - T_{\rm B}$ where $T_{\rm A}$, $T_{\rm B}$ and $T_{\rm C}$ are the readings from the three thermometers shown in Fig. 1.30.

gradient and the longitudinal one (and corresponding κ_{xx}) as described earlier. There are two immediate problems with this approach. First, it is essentially impossible to perfectly align the transverse thermometer so as to eliminate distortion caused by the difference in average temperature between the two thermometers. Second, even if the alignment is perfect, effects of nonuniform temperature may still appear via the κ_{xy} calculation. In this idealized scenario, the effective temperature at which κ_{xx} is measured will always be different from the effective temperature at which λ_{yx} is measured. Considering that in these kinds of thermal Hall exper-

iments one needs quantitatively accurate measurements, it is important to be aware of these effects. In our experiment, we have three thermometer temperatures and they are labeled T_A, T_B, and T_C. Figure 1.40 shows how the calculated values of $\Delta T^{\rm asym}$ and κ_{xy} can differ depending on which pair of thermometers is used for the transverse contacts. The differences are not very large, but they are quantitatively relevant. To facilitate meaningful comparisons, we encourage all groups to report similar data sets. Thermometer C is located "above" the other two thermometers on the sample, but in practice $T_{\rm C}$ is actually nearly equal to the average $\frac{1}{2}(T_{\rm A} + T_{\rm B})$. The near coincidence provides a convenient way to ensure that $\Delta T^{\rm asym}$ and κ_{xx} are measured at the same temperature $T_{\rm C}$, which eliminates temperature distortions as described above. For all κ_{xy} data used in quantitative analysis, we used the average of $\Delta T^{\rm asym}_{\rm AC}$ and $\Delta T^{\rm asym}_{\rm BC}$.

2. **How to define T in κ_{xy}/T:** As discussed above, the temperature at which $\Delta T^{\rm asym}$ is measured will differ from the temperature at which κ_{xx} is measured in a three thermometer experimental setup. This is especially important in cases such as this where it is κ_{xy}/T not just κ_{xy} that may exhibit quantization. Because the method used in this experiment (discussed above) allows us to measure $\Delta T^{\rm asym}$ and κ_{xx} at the same temperature, it also makes clear which value to use for T when calculating κ_{xy}/T (we use $T_{\rm C}$ here). We also point out that any value of T used in this calculation should be the temperature of the sample itself and not just the cryostat stage temperature. This is always possible for resistor-based thermometers, but is not the case for thermocouple-based measurements (which only measure temperature differences rather than the absolute temperature).

3. **Difference between λ_{yx} and κ_{xy}:** At each $T_{\rm Stage}$ in Fig. 1.40, the field profiles of $\lambda_{yx} \sim \Delta T^{\rm asym}$ (panel 1, counting from the top) and κ_{xx} (panel 2) illustrate very well the pitfalls and challenges confronting claims of quantization in κ_{xy} (panel 3). Let us consider $T_{\rm Stage} = 4.7$ K for specificity. We see that, as B increases from 10 T to 13 T, λ_{yx} falls extremely steeply towards zero (faster than exponential in B). At the same time, κ_{xx} undergoes a steep 20-fold *increase*. Since $\kappa_{yx} \simeq \lambda_{yx}\kappa^2_{xx}$ the uncertainties in measuring λ_{yx} transform to enormously amplified error bars in κ_{xy} as evident in the third panel. The amplification of error bars is greatest for $3.6 \leq T \leq 4.7$ K (nearly coincident with the temperature window in which half-quantization was reported [60]). We may also note that, to obtain κ_{xy}, the 20-fold increase in κ_{xx} (in the interval 10-13 T) is squared and then multiplied by the steeply falling λ_{yx}. A purportedly quantized κ_{xy}/T (i.e. B independent value) would demand exact cancellation of

these very steep, opposing trends. Hence, to establish the quantization experimentally, one would need to measure the rapidly vanishing Hall signal e.g. $\Delta T_{\mathrm{BC}}^{\mathrm{asym}}$ with exquisitely fine resolution.

4. **Variation of T_{Sample} with field:** An additional consequence of the strong field-dependence of κ_{xx} is that it causes the effective sample temperature T_{Sample} to change with field as well. This is because it is only T_{Stage} that is directly fixed and controlled during the field sweep. The heat applied to the sample is constant so T_{Sample} will change with κ_{xx}. One must therefore be careful with labeling field sweeps with any particular T and should indicate the value of B at which it was measured.

5. **Apparent field-antisymmetric longitudinal signal:** Even though these curves are anti-symmetrized and averaged in a way that should eliminate all hysteresis, a finite antisymmetric signal still appears in the longitudinal temperature difference. The most likely explanation for this is that the small change in T associated with the Hall effect effectively causes the local κ_{xx} on the one edge of the crystal being measured to exhibit this pseudo-field-odd longitudinal signal.

1.5 Cryogenics

1.5.1 Cryostats and Inserts

The experiments included in this thesis were performed in various magnet cryostats and inserts. The magnet systems include a PPMS from quantum design, an Oxford 14 T magnet cryostat, and an AMI 15 T magnet cryostat with the bulk of the data coming from the 15 T system. The measurements were primarily done in two separate ^{3}He inserts, one from Janis and one from ICE Oxford. A custom high vacuum insert designed for the PPMS was used for some early, preliminary experiments.

A typical ^{3}He system is depicted in Fig. 1.41. Roughly speaking, sub-Kelvin temperatures are achieved by condensing the ^{3}He and then pumping on it to lower its temperature further. We now elaborate on precisely how this is accomplished using the components in the figure. At room temperature, the ^{3}He is in a gaseous state and is primarily located in the ^{3}He dump at the top of the probe. However, at low T, the Helium will be drawn towards the lower portion of the probe. Before the ^{3}He can be pumped on, it must be condensed into a liquid state. This is accomplished by lowering the temperature of the 1 K pot to approximately 1.6 K so that it can function as a condensation surface. This temperature is reached by filling the 1 K pot with liquid from the

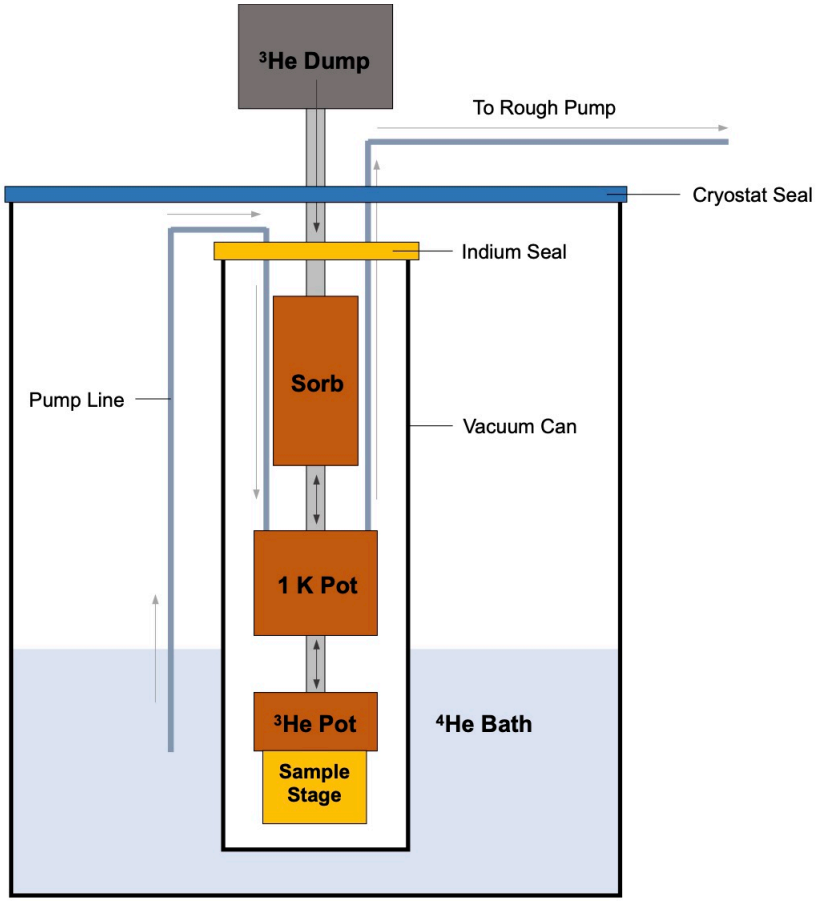

Figure 1.41: Illustration of the components and operation of a typical ^{3}He system (not to scale). The drawing shown here is loosely based on the Janis system used for the thermal Hall experiments presented in this thesis. The arrows indicate the flow of He during experiments with the light-colored arrows being used for He from the cryostat bath (primarily ^{4}He) and the dark-colored arrows representing ^{3}He. Note that the ^{4}He always flows in the same direction while the ^{3}He can move either up or down depending on whether the insert is in condensation or measurement mode.

cryostat's Helium bath (primarily ^{4}He) and then pumping on it to lower its boiling point and with it the temperature. This is accomplished by pumping on the 1 K pot line with a rough pump and then carefully regulating the flow into and out of the 1 K pot using a needle valve and Speedivalve respectively (neither is pictured in Fig. 1.41). The sorption pump (Sorb) is also kept fixed at $T \geq 40$ K to force it to release any absorbed ^{3}He. The Sorb primarily consists of charcoal and its tendency to absorb or release He gas is strongly T-dependent, a feature that is of great utility in cryogenics. Again, as the Sorb and 1 K pot are kept at the appropriate temperatures, ^{3}He will condense on the surface on the ^{3}He line that is in close proximity to the 1 K pot. We emphasize that the ^{3}He itself never leaves the insert and the ^{4}He only affects it via thermal contact. This is in contrast to a dilution refrigerator where the two must mix. As the ^{3}He condenses, it will slide down the ^{3}He line

and collect in the ^{3}He pot as indicated in Fig. 1.41. This process can be monitored via the ^{3}He pot temperature and is complete once it reaches a low, constant value (typically $\approx$ 1.6 K, but can be lower in systems such as the Janis model used for the experiments in this thesis). The condensation process is now complete and the liquid ^{3}He can now be pumped on to lower the temperature even further. This is accomplished by lowering the Sorb temperature, which will cause the Sorb to absorb ^{3}He and thus act as a pump on the liquid. Base temperature ($\approx$ 0.3 K) is achieved by setting T_{Sorb} to about 10 K, but the ^{3}He bath (and therefore the sample stage, which is in direct thermal contact with it) can also be stabilized at higher temperatures by simply setting T_{Sorb} to a higher value. Note that T_{Sorb} is typically only used for coarse temperature control and that a heater and reference thermometer on the sample stage must be used for stabilizing T_{Stage} at precise values. Also note that the cryogenic mechanism discussed here is of the "one shot" variety, which refers to the fact that the amount of liquid ^{3}He decreases as the boil-off is pumped into the Sorb. This fact produces two notable consequences. First, as the amount of liquid ^{3}He decreases over time, the effective cooling power will decrease as well. This will cause the ^{3}He pot temperature to slowly increase, which presents a challenge for thermal Hall effect experiments that must be kept at a fixed T_{Stage} for many hours at a time and where any asymmetry will create an artificial thermal Hall signal. This difficulty can be surmounted by keeping T_{Stage} significantly higher than $T_{^3He}$ using the stage heater. Special care must be taken to ensure that this difference is not so small that T_{Stage} eventually rises as well (thus ruining the measurement). However, the user must also be careful not to make this difference too large as the excess heat put out by the stage heater will cause the ^{3}He to boil at a much faster rate. The second consequence of the "one shot" mechanism is that the liquid ^{3}He will eventually run out, requiring the condensation process to be done again. In practice, we find that it is usually preferable to condense in between field sweeps instead of waiting for the ^{3}He to run out entirely.

We will now provide a brief technical overview of the two ^{3}He inserts with a particular focus on the advantages and disadvantages of the two systems. Note that some procedural information is included as well, but that readers should not interpret this as a replacement for a formal manual. The ICE Oxford system (see Fig. 1.42) is of a modern style and is generally more user-friendly and efficient (from a Helium standpoint) than the Janis system. The system is considered easier to use for a few reasons. First, the distance between the primary O-ring (used to seal the insert inside the cryostat) and the base of the probe is adjustable. The ICE Oxford is a "bottom-loading" system. This label refers to the fact that the samples are manually placed on the stage at the base of the probe. This is in contrast with with a "top-loading" design where the sample can be inserted via the

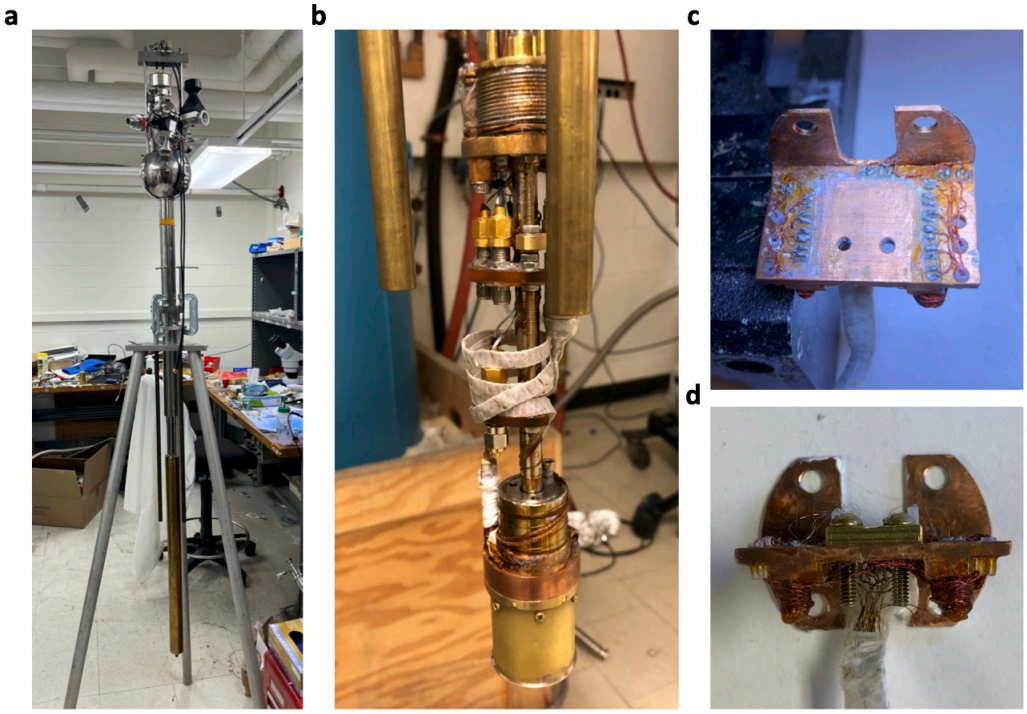

Figure 1.42: The ICE Oxford ^{3}He system. Panel (A): A full view of the ICE Oxford with the vacuum can on. Note the tall, thin structure and the adjustable distance between the cryostat O-ring and the base of the probe. Panel (B): The lower portion of the insert with the vacuum can removed. Shown here are the 1 K pot, ^{3}He pot, and brass radiation shield that was added for this experiment. Panel (C): Removable Copper sample stage. The contact pads around the edges are used to make electrical contacts to the thermometers in the experiment. Panel (D): Removable sample stage with the sample-mounted brass plate attached. The stage can then be attached to the base of the probe using the four screw holes seen here.

top of a probe that is already placed inside the cryostat. In a top-loading system, most of the ^{3}He cryogenic components can be cooled before the sample is added. With a bottom-loading system, the whole insert must be cooled down (from $\approx$ 300 K to 4.2 K) every time a new sample is measured. Typically, this involves directly placing the room temperature insert into the liquid Helium space of the cryostat. The exception would be when the cryostat itself is warm and the ^{3}He system can then be inserted before cooling down both it and the cryostat simultaneously (which is an even more Helium-consuming process than the typical method). The placing of a room temperature object into a 4.2 K liquid Helium bath will cause the liquid to boil incredibly fast. It will boil at such a rapid rate that a substantial amount of the Helium gas will escape via the not yet closed opening through which the user loads the ^{3}He insert. This process can be incredibly stressful to the user due to both the apparent violence of the boil-off and the inevitable release of Helium to the atmosphere. The reason that the adjustability of the ICE Oxford is so attractive is because it allows for the user to place the insert so that the vacuum can initially lies above rather than in the liquid Helium

bath. The absence of direct contact between the ICE Oxford and the liquid significantly lowers the amount of gas produced during this process, thereby creating a far less stressful and costly insertion method. Note that the Helium level in the cryostat may need to be allowed to drop in order for there to be sufficient distance between the liquid Helium and the base of the ^{3}He insert. Once the ICE Oxford has been inserted, it can be slowly lowered over the course of a few hours. The user should be careful to allow it to thermally equilibrate (at least enough that the cryostat pressure is no longer spiking) before the insert is lowered any further. This can be monitored using the Cryomech pressure sensor (more information given about this given later). The insert should be lowered until the orange marker (see Fig. 1.42) lines up with the cryostat O-ring. Note that this marker is placed based on the standard distance between the top of a cryostat and the sample space, but that it is still the responsibility of the user to confirm before every experiment that the sample space does in fact lie in the center of the magnet coil. This is particularly important for thermal Hall effect experiments as any field-asymmetry (even from the sample being off-center in the magnet coil) will appear in the data as a thermal Hall signal.

The internal cryogenics of the ICE Oxford have also been designed to be able to use helium very efficiently. These efforts are reflected in the long cool-down time (evidencing effective thermal insulation) and the small 1 K pot (compared with the older Janis system). These details are reflective of the rapidly rising price of Helium, an increasingly scarce natural resource. Another contemporary design feature included in our ICE Oxford system is a single pump line for both the 1 K pot and Sorb. This is done for convenience as managing one flow rate is simpler than managing two. However, it is our opinion that this is ultimately a disadvantage of the ICE Oxford system. Flow through this line can be controlled using two separate valves. There is a needle valve that regulates the flow of liquid into the 1 K pot and a Speedivalve that controls the pumping of this liquid through the rest of the line (and out to the rough pump). To stabilize the 1 K pot (meaning maintaining the presence of liquid Helium and doing so around 1.7 K), one must carefully tune these two valves. Typically, the 1 K pot is only open a very small amount (start with $\approx 1/8$ turn) and the flow is then optimized using the Speedivalve. The reason that this particular design is ultimately a detrimental feature is that the amount of Helium flow required to stabilize the 1 K pot leads to substantially more cooling power directed to the Sorb than is desirable. A large amount of heat must therefore be applied to the Sorb in order to keep T_{Sorb} constant. The shear magnitude of the heating and cooling power leads to large fluctuations in the Sorb temperature. As T_{Stage} is primarily controlled by the T_{Sorb}, these fluctuations translate to significant temperature instability at the base of the probe as well (and therefore noise in the thermal transport measurements). For this reason, we find

that thermal Hall effect measurements in the ICE Oxford are incredibly difficult so this system is primarily reserved for longitudinal thermal conductivity (κ_{xx}) experiments.

One change that needed to be made to the ICE Oxford system to perform the experiments necessary for this thesis was the addition of a radiation shield for the sample stage. The necessity of the radiation shield was realized when we observed that we were unable to to obtain clean calibration curves for an early $RuCl_3$ $\kappa_{xx}(B)$ measurement. More specifically, we were unable to measure a field sweep at zero applied sample heater current that did not contain oscillation-like features. This indicated that there was still an effective heat source on the sample despite the absence of electrical current in the heater. We concluded that the inhomogeneous absorption of blackbody radiation emanating from the ICE oxford vacuum can (which is in direct contact with the 4.2 K liquid Helium bath) was the likely source of this additional current. We designed and machined a brass radiation shield to block these blackbody photons and prevent them from heating the sample. The radiation shield can be seen at the bottom of Fig. 1.42b.

The Janis ^{3}He system is in many ways the opposite of the ICE Oxford system. It is significantly more difficult to operate and consumes substantially more Helium, but has proved to be capable of producing incredibly high quality thermal Hall data. Sources of difficulty include the lack of a position-adjustable O-ring seal as well as its utilization of an Indium vacuum seal (which is highly time-consuming to prepare). The fixed O-ring requires the system to be inserted directly into the cryostat liquid He bath, producing a huge amount of boil-off (that mostly ends up being directed into the users face and up into the atmosphere instead of into the Helium recovery system). The Janis is also substantially heavier than the ICE Oxford so between the weight and the large amount of helium boil-off, it is generally best to have two or three people present during this process. The boil-off can be minimized by allowing the liquid level to drop to near-zero before inserting the Janis into the cryostat. The level can be monitored using the liquid Helium level meter. Ideally, the level will be under 50% before the insert is placed into the cryostat. Note that the 15 T cryostat is substantially narrower at the base so it will take the level about as much time to go from 50% to 0% as it will to go from 55% to 50% (about one day in both cases if nothing is being reliquefied). More information about the operation of the liquefier will be discussed later, but we will mention one relevant word of caution now. It has been found that if the liquefier is turned off entirely to allow the level to drop so that a ^{3}He system can be inserted, it will often develop a clog before it can be restarted. This can be avoided by simply increasing the pressure setpoint. This increases the cold head heater power output and reduces the liquid production rate in the 15 T to approximately zero. The high Helium consumption is likely due to a large 1 K pot (more liquid must be pumped

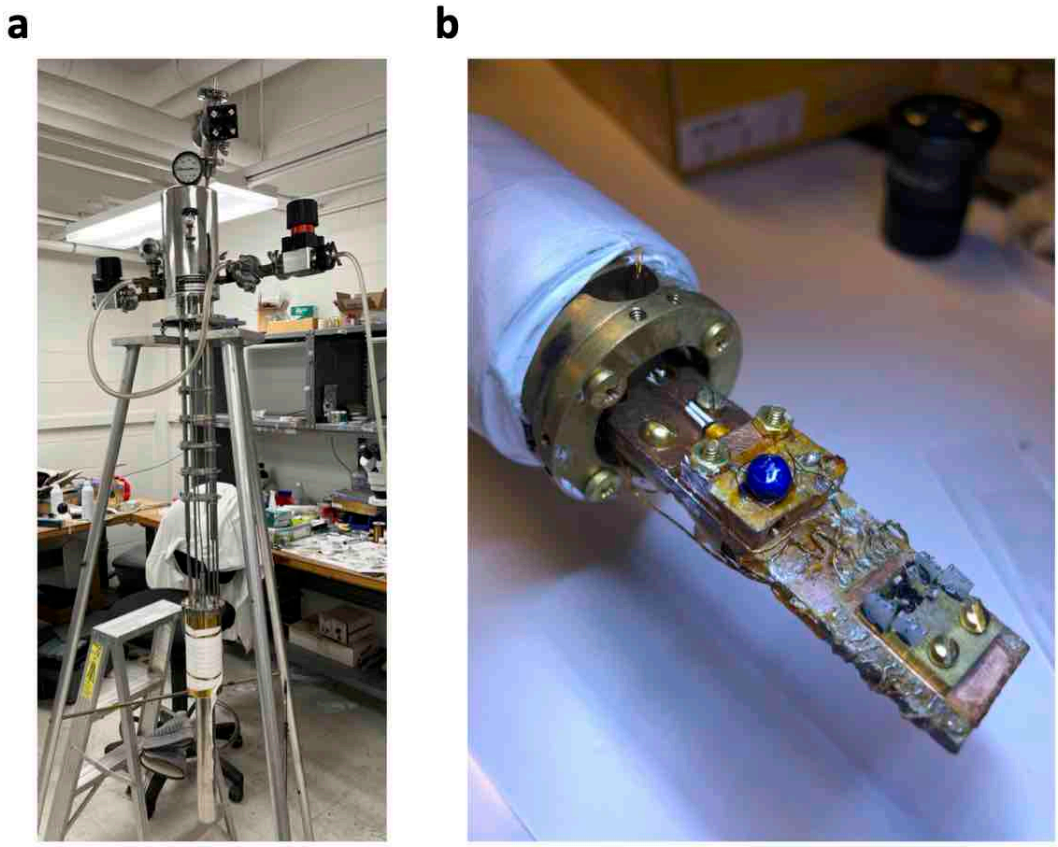

Figure 1.43: The Janis ^{3}He system that is used for high precision thermal Hall effect experiments. Panel (A): Full view of the insert. The midsection is substantially thicker than the vacuum can on the ICE Oxford. The pump lines are also largely outside of the vacuum space, likely weakening thermal insulation. Panel (B): The insert's sample stage with a mounted $RuCl_3$ crystal. This stage cannot be removed easily so the whole insert is usually placed on the lab bench when setting up a measurement.

to keep it full and stable) and somewhat poor thermal insulation. Again, this is an older system and was built in a time when Helium was far less costly. However, it is our opinion that these inefficiencies are (albeit indirectly) what ultimately allow it to produce such clean data. The large 1 K pot (and large matching ^{3}He quantity) and separate Sorb pump line grant the sample stage remarkable temperature stability. This stability is what enables the Janis system to produce such high quality κ_{xy} data.

1.5.1.1 Helium Recycling System

All of the cryostats used for this experiment are "wet" meaning they require liquid cryogens to function. During my time at Princeton, liquid Helium has become increasingly expensive (often prohibitively so) and difficult to obtain due to global shortages. The experiments presented in

this thesis typically require sweeping very strong magnetic fields, which burns helium quite quickly. Because of this, it was not uncommon for us to go through a 100 L dewar of helium in under three days. Five years ago, this was pricey, but still doable. Now; however, it is totally impossible to perform experiments in this manner.

We realized that the only way to make these measurements economically possible would be for the group to acquire its own helium infrastructure and the development of this recycling system has been a major effort for the lab over the last several years. I will now give a broad description of how the current system works with a specific focus on the particular components that have been crucial for obtaining the $RuCl_3$ data presented in this thesis.

Soon after I joined the group, the lab acquired a combined liquid He recycling system and storage dewar (typically referred to as the mother dewar). This system collects the helium that boils off from the various cryostats in the lab and liquefies it into a reservoir that can be used to directly refill the cryostats or indirectly via a movable transfer dewar. This allowed us to significantly reduce the costs associated with the use of the Jadwin recycling system. However, this does not address the frequency with which the cryostats would have to be filled with Helium, which was a particularly significant inconvenience for high field experiments as the field would have to be ramped back down to zero in order to fill Helium.

To address this issue and to further lower Helium costs, we chose to purchase dedicated liquifier systems for the lab's two most technically involved and costly experimental setups: the dilution refrigerator and the 15 T magnet cryostat used for thermal transport experiments. I will now give a brief description of how these two dedicated systems work before providing a more detailed summary of the various procedures used for operating the 15 T magnet system. I would also like to acknowledge Stephan Kim whose extensive research on liquifier systems led to the selection and purchase of these particular setups and ultimately made much of the research presented in this thesis possible.

The dedicated liquefier systems are referred to in this way because they do not have their own liquid dewar like the mother dewar does. They instead use the magnet cryostats themselves to store the liquid He that they produce. They are also generally intended to be used to create an isolated, closed-cycle system for an individual cryostat. However, for reasons that will be described later, the thermal Hall experiments typically necessitate the use of the mother dewar for collecting excess boil-off. Each individual dedicated liquifier system consists of a cold head, a remote motor, and a compressor. In a traditional dewar-based system, the remote motor would be integrated with the cold head. However, the remote motor produces vibrations that can introduce noise in experiments.

For this reason, only the cold head is directly attached to the magnet cryostat while the remote motor is connected to the cold head via special tubing designed to minimize the transmission of vibrational noise. The compressor is kept in a separate room.

We will now provide specific information about the various components of our liquefier system as well as details about their operation. The aim of this section is not just to describe some hyper-specific procedures, but to provide to the reader some level or intuition about the nature of the liquefier system that ultimately will be necessary for dealing with any potential unique, unforeseen scenario that may arise.

1.5.1.2 15 T Cold Head

- **Liquefier Stand:** The liquefier stand is a major component of the system. It holds the cold head in place and is used to move the transfer tube into and out of the 15 T cryostat. While commercial stands are available, there is no model that would conform to the necessary dimensions for our lab space and cryostat system. We therefore opted to design and construct our own. An image of this custom system is shown in Fig. 1.44a. A cable can be hooked onto a tray-like piece that the cold head sits on top of (it is held in place with screws). This tray-like piece lies on a track and can be locked in place when the cold head is not being moved up or down. The cold head is then raised and lowered by turning the crank, which either winds or unwinds the cable.

- **Starting the liquefier:** For small cryostats, it is possible to cool down the cryostat from room temperature using only the liquefier and some He gas, but the cryostat used for our AMI 15 T magnet system is far too large for this so it must be cooled down completely before the liquefier can be used. Once the magnet system is cold and filled to a sufficiently high level (above 55% at least), the process of inserting and starting the liquefier can begin. First make sure that the transfer tube and the cryostat fill port are aligned. This must be done with a pretty high degree of precision as any misalignment will put a large amount of mechanical stress on the transfer tube (and potentially ruin its vacuum thermal insulation). The liquefier stand is on wheels that can be locked in place. I typically first unlock the wheels to move the tube to the roughly correct position (coarse positioning), lock the wheels, and then physically nudge the stand small amounts at a time to obtain a more perfect alignment.

  After alignment, the next step is to purge the inside of the liquefier of atmosphere. This is done my hooking a cylinder of Helium gas up to the liquefier gas inlet. Allow He gas (a pressure

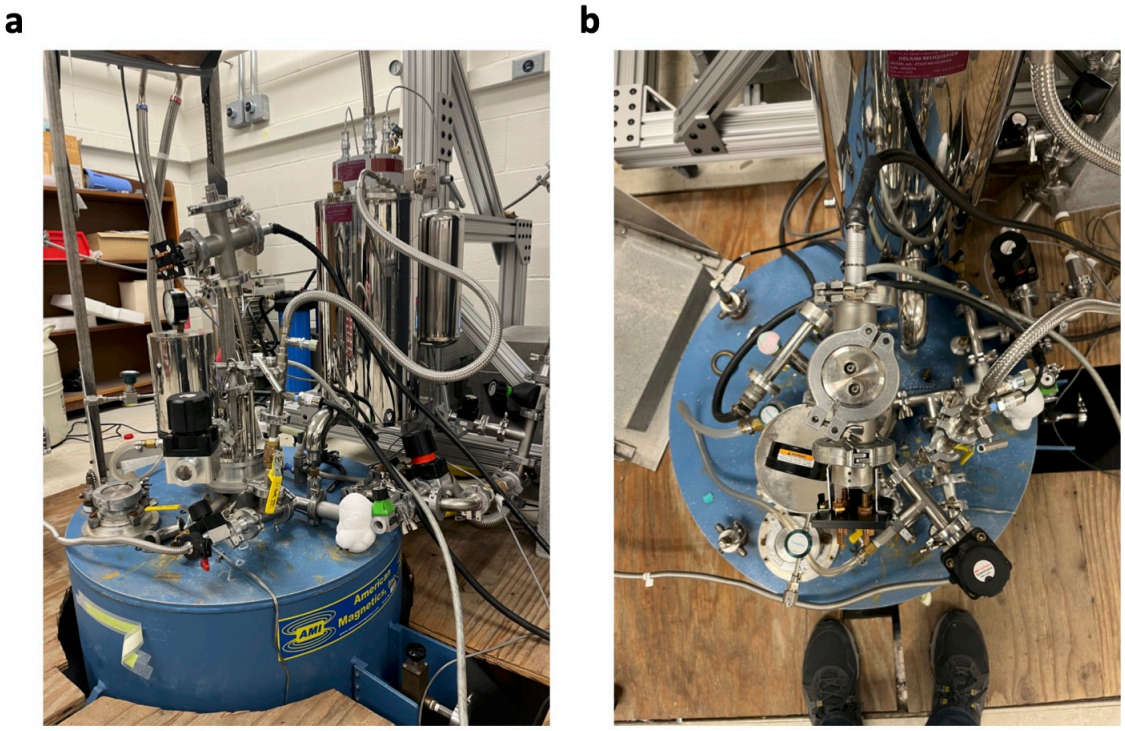

Figure 1.44: Panel (A): The Cryomech liquifier in use during a Janis thermal Hall experiment. Panel (B): Top view of the Janis system in the liquefier. Note that the orientation of the insert must be such that the cold head transfer tube as well as the other cryogenic piping has enough space.

of 1 psi is sufficient) to flow for a few minutes so that only He remains inside the Cryomech. During this time, adjust the He manifold such that the boil-off (and added He gas) is directed towards the Jadwin recovery system and not the mother dewar. This is because the He gas that is typically used is of lower purity than that used for liquid He. After a few minutes, the liquefier can begin to be lowered (though the user needs to continue flowing He gas through it). Use the crank to tighten the line that supports the cold head. Then, turn the brake handles counterclockwise to allow the cold head to move up and down along the track. Open the valve on the 15 T liquid Helium fill port and remove the plug so the transfer line can be inserted into the opening. Slowly begin to turn the crank to lower the cold head. For safety, it is best to have two people present for this process. This allows one person to manually direct the transfer tube into the cryostat liquid He fill port while the other person turns the crank to lower the system. Special care must be taken when the line is approaching the fill port as any sudden drop (sometimes caused by non-ideal winding of the line holding the cold head) could lead to the fragile transfer tube then supporting the full weight of the cold head. Once the tube has been inserted into the fill port, continue to lower the cold head until approximately

Figure 1.45: The Cryomech transfer tube is inserted directly into the liquid fill port of the 15 T cryostat.

one inch remains between the top of the transfer tube and the cryostat fill port (as shown in Fig. 1.45). Finally, tighten the valve at the fill port to lock the transfer tube in place. A heat gun may be necessary for achieving a good seal as the O-ring will likely be cold from the insertion process. Sometimes it is best to do a rough tightening now and a firmer one later once things have stabilized more. As always, do not over-tighten as it will make it difficult to undo later and can actually lead to a weaker seal if the O-ring is stressed in undesirable ways.

At this point, the flow of He gas can be stopped. First close the needle valve on the cold head gas inlet. Then, close the valve on the He cylinder and remove the connecting rubber tubing (via the KF connection). The He gas inlet can then be reattached to the corresponding connection on the cryostat He manifold. In order to avoid a pocket of atmosphere entering the cryostat during this connection, slightly vent the valve on the cryostat before (and during) the attachment process. The local over-pressure of He gas will help minimize contamination of the He environment. Once this is done, allow the cryostat to continue to vent to Jadwin for at least 15 minutes. This will help limit the number of impurities that are ultimately allowed to enter the liquefier during this process.

The next step is to start the liquefier. Close the connection to Jadwin so that the 15 T cryostat is now isolated. Make sure the temperature and pressure sensors are turned on and

are providing realistic numbers. Turn on the compressor (now located in B1) and open the needle valve on the cold head inlet about three full turns. The temperature inside the cold head will begin to drop (from $\approx$ 300 K to $\approx$ 4 K). The amount of time this takes can vary somewhat but typically takes around an hour. Monitor the pressure during this time. If the pressure gets too high (at least 3 psi) the liquefier will not be able to liquefy optimally and the pressure will just increase faster in an avalanche-like effect. If this happens, gently vent the 15 T to the mother dewar. This must be done cautiously so as not to overload the pressure in the mother dewar and lab Helium manifold, which may lead to unwanted He leaks elsewhere such as in the 9 T PPMS (which has over-pressure valves with fairly low threshold values ($<$ 1 psi)). However, one must also be careful to not let the pressure in the 15 T exceed 5 psi as that will trigger the over-pressure valve there and waste Helium. Note that there is another over-pressure valve on the 15 T that begins releasing gas at only 1 psi, but the connection to this valve should be kept closed. This valve's presence was more appropriate before the lab acquired our own Helium recycling system and it was less common to run the system's at higher pressures.

As the cold head temperature approaches 4 K, the temperature may appear to become quite unstable. This is normal and seems to occur due to the beginning of accumulation of boiling liquid He inside the cold head. The pressure should also begin to drop even though the 15 T has been disconnected from any external reservoir. The cold head pressure should be set to around 0.3 psi. Eventually, the system should reach this pressure and heat will have to be applied to the cold head to prevent it from getting too low. More specifically, it is possible for the liquefier to work so well that the pressure inside the dewar actually becomes negative and atmospheric air is sucked in. This should be avoided as this will quickly lead to the build-up of impurities that can clog the system (we discuss this in more detail later). If the system does not appear to be stabilizing in the intended manner, try adjusting the needle valve to allow either more or less gas to enter the cold head.

- **Balancing mother dewar pressure:** In the experiments that are the subject of this thesis, the primary source of Helium consumption and boil-off is typically not the cooling itself. Instead, it is often the magnet system. While the magnet coil itself is superconducting while in use, the leads used to make electrical contact with the coil are not. And while there is thermal insulation between these leads and the Helium space, it is not perfect. Additionally, electrical currents of tens of Tesla are typically required for generating the strong magnetic

fields needed for the experiments. This leads to a significant increase in He consumption via dissipation due to finite resistance when the magnet is in driven mode. When the magnet is in persistent mode, the leads can be de-energized without losing the circulating current in the superconducting coil. Other sources of magnet-related heat load on the Helium space include the switch heater (used to keep the magnet in driven mode) and the Eddy currents induced by a changing magnetic field.

At fields of a few Tesla, the excess He consumption is usually still within the capacity of the liquefier system. However, the $RuCl_3$ experiments often require fields as high as 14 T so other methods must be used to ensure that the magnet pressure does not get too high, that the liquid Helium level remains somewhat constant, and that Helium is not lost. We ultimately decided that the best way to accomplish this was by carefully using the mother dewar to increase the effective capacity of the system. When the magnet is being swept up to fields of more than a few Tesla, we fully open the valve between the 15 T cryostat and the mother dewar such that there are two liquefiers drawing from the lab manifold. The additional capacity of the mother dewar allows for all of the boil-off to be recaptured and liquefied even when the magnet is at fields as high as 14 T. This prevents the runaway pressure effect that we discussed earlier from occurring in the 15 T system. However, the user must also be careful that the amount of Helium that is effectively transferred from the 15 T to the mother dewar is not too large as a decrease in liquid level can lead to poor temperature stability, eventual loss of ^{3}He cryogenic function, and superconducting magnet quenches.

One can prevent this problem by carefully setting the pressure setpoints to direct the flow of Helium gas within the manifold. For example, if one sets the pressure in the mother dewar to 0.3 psi, but 0.25 psi in the 15 T, the mother dewar will apply excess heat in order to attempt to reach that higher pressure. This excess heat will lead to a lower liquid production efficiency inside the mother dewar and ultimately lead to the boil-off from the various cryostats being disproportionately directed towards the 15 T. If we tune the pressure settings in this asymmetric way during a field sweep, then the flow of helium gas from the 15 T to the mother dewar at high field will be compensated for by a flow in the opposite direction at low field. Note that the pressure values given above are only examples. The precise values needed to accomplish the desired balance will vary substantially in practice and depend on a number of factors such as 15 T cold head needle valve impedance (controlled by number of turns), the liquid levels in the two reservoirs, the number of impurities in the two cold heads, and the field

sweep range and frequency.

- **Regenerating cold head:** The mother dewar has its own internal filtering mechanisms to prevent the buildup of impurities, but the 15 T liquefier does not. Therefore, from time to time it will be necessary to "regenerate" the cold head in order to rid it of these impurities. The frequency with which this will need to be done can vary substantially. I have at times been able to go several months without any noticeable drop in liquification capacity, but the identical system used for the lab's dilution refrigerator usually needs to be regenerated every two weeks or so (though the nature of the dilution refrigerator's more complex cryogenics will inevitably lead to the introduction of more impurities). The absence of an internal filtering system (other than the cold trap) will inevitably lead to a need to regenerate the system, but it is sill advised that appropriate precautions be taken to limit the amount of non-Helium gases that are able to enter the Helium space.

  Before giving the regeneration procedure, we describe how the user will be able to tell when it needs to be done. Typically, one will begin to suspect an issue is present when the delicate balance between the 15 T cryostat and the mother dewar begins to tilt increasingly towards the latter (despite the efforts of the user). This will typically happen over the course of days or weeks so there will be ample time for the user to monitor the system before choosing to regenerate the cold head. In the meantime, one can simply increase the pressure setpoint in the mother dewar to compensate for the potential loss in efficiency. It may eventually become impossible to run the 15 T magnet without losing Helium too quickly to be able to restore the level or balance in a timely manner.

  Alternatively, another way that the liquefier may indicate that a regeneration is necessary is if the cold head temperature gets too low (around 3 K instead of 4 K). This likely indicates that there is some sort of clog in the system preventing it from being fed with additional Helium gas. The reason that the temperature is so low is that it applies excess, unnecessary amounts of cooling power to a small, finite amount of liquid. If this occurs while the valve to the mother dewar is closed, one thing that can happen is that the system is simply no longer able to continue filling the cryostat with liquid. However, because the Helium will continue to boil, the pressure will start to build up. Eventually, one may find that the pressure reading is around 5 psi, which indicates that the over pressure valve has been activated. This is highly undesirable as it means that Helium is being lost to the atmosphere and is no longer recoverable. Additionally, this can lead to a safety hazard if the ventilation system in B12 is

not performing as it should. If this happens (and the HVAC system is still functioning), one should first try to stabilize the pressure at a much lower level (such as 0.3 psi or whatever the current setpoint may be). Ideally, this is done by opening the valve to the mother dewar which is able to liquefy the excess Helium gas without increasing the pressure in the manifold too much (again, leaks can occur elsewhere in the system for pressures above 1 psi). If this is not currently possible (or worse, if this valve is already fully open), then the user will have to vent to Jadwin via the typical valve on the 15 T manifold. This should also be done slowly to avoid any unnecessary loss of Helium.

Once the pressure has stabilized, the user should perform some final checks to confirm that the 15 T liquefier is in fact malfunctioning. This is necessary as it can happen that some transient anomaly briefly overloads the liquification capacity and leads to the huge buildup of pressure due to the avalanche effect described above. To evaluate the system's performance, the user should try and see whether they can stabilize the pressure in the isolated 15 T cryostat ("isolated" meaning not vented to Jadwin or the mother dewar) at simply a different needle value setting (try five full turns instead of three for example). In the (likely) event that this or any other adjustment does not lead to a stable pressure, one will need to regenerate the liquefier.

Once the user has determined that regeneration is necessary, they should perform the following procedure to reset the system and rid it of any potential impurities. First, turn off the compressor to stop the liquification process. The next step is to arrange for a constant flow of Helium gas through the cold head during the regeneration process. Like with inserting the liquefier into the cryostat, the constant flow helps to ensure that impurities are unable to enter the system during this process. Close both the yellow valve on the 15 T manifold and the Cryomech needle valve. Attach a Helium cylinder to the KF connection on the needle valve. As always, make sure that the Helium gas is flowing before connecting to the liquefier. Otherwise, the tube connecting the two might be filled with atmosphere that is then injected into the cold head. Open the needle valve to allow the gas to flow. The pressure should start to increase slightly. Next, close the valve to the mother dewar (if it is open) and open the valve to Jadwin. Turn off the pressure monitor to avoid the unnecessary application of heat when the system is open to the atmosphere. The next step is to raise the liquefier. This process is essentially the same as putting it in, except in reverse. First, loosen the valve on the 15 T liquid fill port to allow the transfer tube to move. Next, use the crank on the cold head stand

to tighten the line. Then, loosen the two brake handles to allow the system to slide up and down along the track. Begin turning the crank clockwise to pull the liquefier in the vertical direction. Do this until the bottom of the transfer tube is about two inches above the top of the 15 T fill port. Put the cap back on and tighten the valve to ensure that no Helium gas is able to escape. As before, it may be necessary to use the heat gun to obtain a decent seal.

The final step is to allow the liquefier to warm up. It is best if Helium gas is allowed to continue flowing through the cold head during this process, but the pressure can be kept pretty low to avoid losing too much Helium gas. Control this pressure and flow rate using the Helium cylinder, not the cold head pressure monitor (which should still be off at this point). The temperature can be monitored using the cold head temperature sensor. It typically takes around 3-4 hours for the system to warm to room temperature. Allow Helium gas to flow for at least this long (if not more). To ensure that there are no nooks and crannies for condensation to occur in, it is often best to allow the system to sit overnight if possible. After this time (or whatever is practically feasible), the liquefier can then be re-inserted using the conventional procedure described above.

- **Filling the cold head with liquid He:** Tuning the pressure setpoints in the two liquefiers provides a convenient way to increase the Helium level in the 15 T cryostat without having to fill Helium directly. However, as the boil-off rates in the mother dewar and other cryostats are typically pretty low, this method is inevitably quite slow. If one wants to increase the level faster (such as immediately after putting a ^{3}He insert into the dewar), then it is necessary to transfer liquid Helium directly. Conveniently, this can be done without having to raise the liquefier out of the cryostat. On the top of the cold head, there is a liquid fill port (see Fig. 1.46). The transfer is then done using the conventional method. Note that the liquefier can be kept on during this process.

- **Cold trap for ^{3}He experiments:** The ^{3}He inserts all require pumping on the 1 K pot to condense the ^{3}He and ultimately reach sub-Kelvin temperatures (described above). This is typically done using a rough pump. However, this process can be a source of Helium loss if the outgoing He gas is not recovered. The Janis insert consumes Helium at a particularly high rate due to the size of the 1 K pot. Additionally, the gas cannot be recovered directly as the rough pump can be a major source of impurities. We therefore use a liquid Nitrogen cold trap to effectively clean the gas that has been sent through the pump.

  A cold trap works by forcing gas through a space with a very high impedance. This space is

Figure 1.46: The Cryomech cold head can be filled with liquid Helium directly using the fill port shown here.

placed inside a small liquid Nitrogen dewar so that it is kept at a constant temperature of 77 K. Note that the liquid nitrogen needs to be topped off every 3-5 days. Any impurities with a freezing point above 77 K will then collect inside the cold trap instead of continuing back to the Helium space where they may freeze in a less desirable location and affect the operation of the system's various cryogenic processes. Additionally, as these impurities freeze inside the cold trap, they will block the flow of gas and increase its impedance further. This allows for the monitoring of the quantity of impurities via a pressure gauge on the cold trap.

The cold trap has multiple over-pressure valves to prevent the pressure inside the cold trap from getting too high and potentially becoming dangerous. Empirically, we find that Helium losses via these valves becomes noticeable when the cold trap pressure exceeds 2 psi. Again, Helium losses can be detected by careful monitoring of the liquid level. The system should be sufficiently well-sealed that, when kept isolated from the other reservoirs, it can operate for weeks without any detectable loss in Helium. The frequency with which the cold head needs to be regenerated can vary substantially, but is typically around 1-4 weeks. The exact time will depend on the experimental activity and the extent of the previous regeneration.

Once the pressure exceeds this value, it is best to regenerate the cold trap. This works in a somewhat similar manner to the cold head. Redirect the 1 K pot rough pump output to flow to Jadwin instead of through the cold trap. This can be done by adjusting the two Speedivalves on the top, manifold-like portion of the cold head. The cold head must also be closed off from

Figure 1.47: Image of the liquid Nitrogen cold trap used in our experiments. The ^{3}He insert 1 K pot is pumped using a rough pump and the output can be pumped through the cold trap (the high impedance lower segment is immersed in liquid Nitrogen) to clean the Helium of impurities before recycling it. The flow is directed using the various Speedivalves shown in the picture. The pressure gauge at the top is used to indicate when the cold trap needs to be regenerated.

the 15 T manifold. This can be done using either the corresponding valve on the cold head or the one on the 15 T manifold at the other end of the thin connecting tube. Note that this connecting tube appears to be slightly leaky (though Helium loss appears negligible) so the user should not expect it to be able to hold a vacuum for an extended period of time. Similarly, this tube can also act as a significant heat load on the liquefier system. For this reason, it is advisable to close it off using the 15 T manifold connection valve if the cold head is not in use for more than a few hours.

Once the appropriate valve changes have been made, lift the cold trap out of the dewar. Ice will quickly form around the cold trap due to the low temperature. This is normal and actually provides a way to roughly monitor the cold trap temperature as condensation will cease once it reaches room temperature. The reason that the cold trap needs to be warmed up is that the impurities are frozen at 77 K and need to be warmed up to 300 K to be able to be pumped out as a gas. It will take at least an hour for for the condensation to vanish. However, we have recently found that the cold trap is able to go longer without regenerating if we allow it to fully warm up overnight. If that is not possible, one can (very carefully) use a heat gun to accelerate the warming process. After the cold trap has been allowed to warm up, it must

be pumped. This can be done using either a turbopump or a rough pump though the latter should be done for significantly more time than the former (hours vs. minutes).

After an appropriately long amount of time, the cold trap can be put back into the Nitrogen dewar. This same procedure should be used when putting it in for the first time with the only difference being that is best to let the 1 K pot output flow to the Jadwin system for several minutes if the cold trap is being used for the first time (especially if the 1 K pot is just beginning to run). This helps to ensure that the other areas of the cold trap are flushed out with Helium gas to prevent more impurities from entering. The cold trap will be under vacuum when placed into the Nitrogen dewar, but the valves to the 15 T manifold should be opened immediately after insertion. This prevents the atmosphere from entering if it is left under vacuum. The Nitrogen will boil noticeably faster when these valves are opened as the Helium gas from the manifold will strengthen the thermal link between the liquid Nitrogen bath and the still warm cold trap interior. After several minutes, the 1 K pot can then be redirected to flow through the cold trap instead of to Jadwin.

Chapter 2

Thermal Conductivity Oscillations in $RuCl_3$

This chapter covers content from our report "Oscillations of the thermal conductivity in the spin-liquid state of α-$RuCl_3$" [49]. The key finding in this paper is the observation of magnetooscillations in $RuCl_3$'s longitudinal thermal conductivity κ_{xx}. This report also includes new measurements of the material's planar thermal Hall conductivity. In this chapter, these results are only discussed in terms of their relation to the oscillations in κ_{xx}. The thermal Hall experiments will be covered in greater detail in the next chapter.

2.1 Earlier Measurements

Measurements of the field-dependent longitudinal thermal conductivity in $RuCl_3$ had previously been reported by Leahy et al. [67], Hentrich et al. [68], and Yu et al. [69]. The first such report was from Leahy et al. [68] and revealed a distinct profile for $\kappa_{xx}(B)$ that has been seen in essentially all measurements since (see Fig. 2.1). Upon increasing B from 0, κ_{xx} gradually decreases and then reaches a minimum around 7 T. After this, κ_{xx} increases somewhat rapidly as the field increases and eventually exceeds its value at 0 T. The minimum corresponds to the transition field H_c where the magnetic order is destroyed. The reason that κ_{xx} becomes so low there is that the gap for spin excitations decreases substantially at the transition and they are more able to scatter phonons, which are the dominant heat carrier in $RuCl_3$. The fact that κ_{xx} at high B exceeds its value at 0 T implies that there may be significant spin-phonon scattering at 0 T as well.

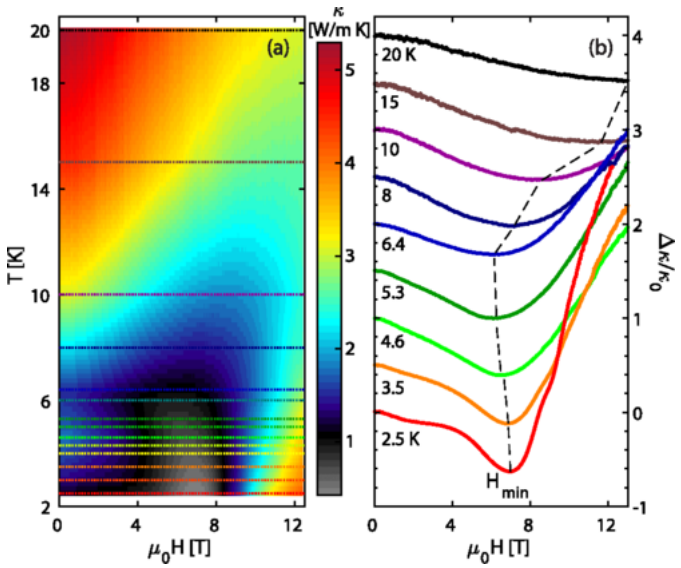

Figure 2.1: Longitudinal thermal conductivity (κ_{xx}) data reported by Leahy et al. [67]. The left panel shows κ_{xx} as a function of B and T as a colormap. The right panel shows the normalized B-dependent component of κ_{xx}. Explicitly, this is defined as $(\kappa_{xx}(H) - \kappa_{xx}(0))/\kappa_{xx}(0)$. Note the broad minimum at the critical field (labeled H_{min} here).

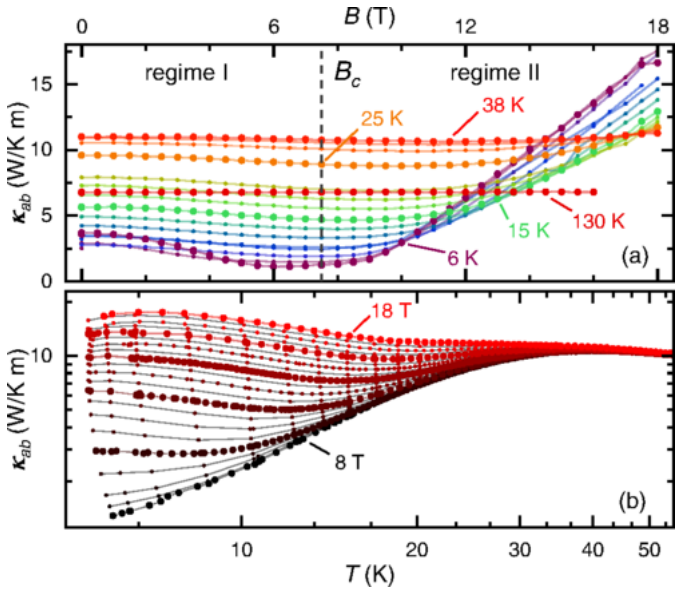

Figure 2.2: Early measurements of field-dependent longitudinal thermal conductivity in $RuCl_3$ evidencing its strong spin-phonon coupling. Top Panel: κ_{xx} vs. B at fixed T revealing the suppression of phonon thermal conductivity at the magnetic phase transition. Lower Panel: κ_{xx} vs. T at fixed B. Figure adapted from [68].

Another early report that we would like to highlight is the one from Hentrich et al. [68]. Here, the authors confirm the profile reported by Leahy et al. [67], but also analyze the results quantitatively. They find that they can fit $\kappa_{xx}(T)$ at high B to a model originally proposed by Callaway [70][71]. From these fits they are able to extract values for the spin gap as a function of B. The values they

obtain are similar to those obtained from a variety of other measurements (more details in next chapter). Additionally, these results help to confirm a key detail of the phenomenology implied by Leahy et al.'s measurements: that the heat is primarily carried by phonons, but is modulated by incredibly strong spin-phonon scattering. Despite the intense interest in $RuCl_3$'s thermal transport physics, data at low temperatures (T < 3 K) had been been surprisingly lacking. In order to remedy this, we measured $\kappa_{xx}(B)$ in a ^{3}He system down to 0.3 K and uncovered several previously unseen effects.

2.2 Oscillations

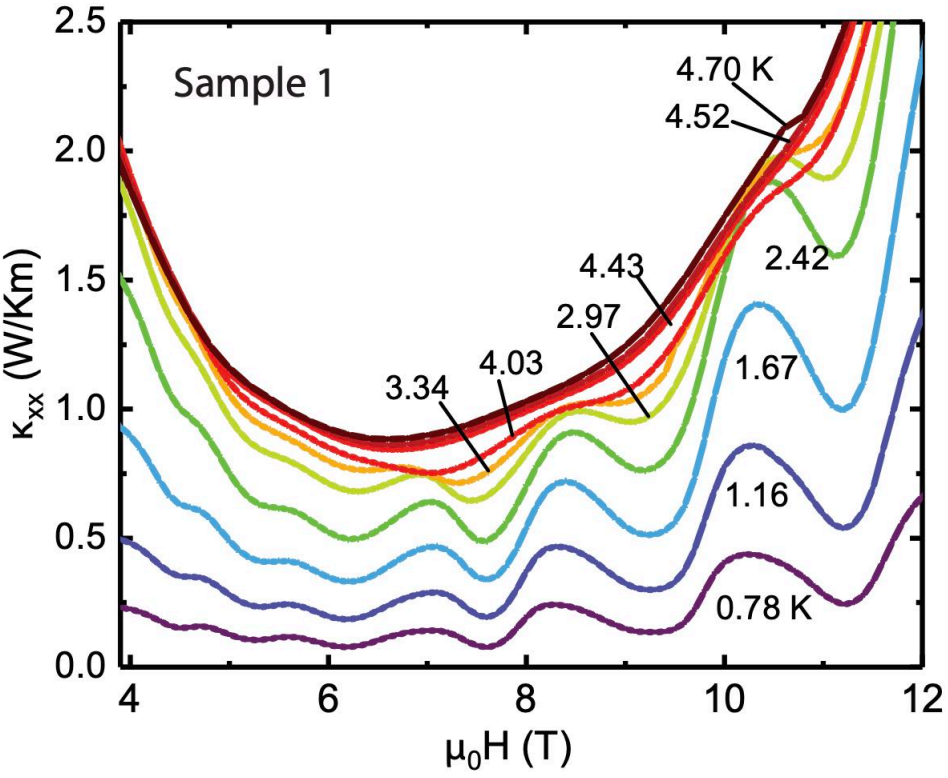

Figure 2.3: Measurements of longitudinal thermal conductivity vs. field. Temperatures range from 0.78 to 4.70 K. Numerous oscillation-like features appear simultaneously around 4.0 K. Data were recorded using the stepped-field technique to correct for magnetocaloric effects (as discussed in Chapter 1). Figure adapted from [49].

Fig. 2.3 shows our measurements of $\kappa_{xx}(B)$ for $0.78 < T < 5$ K. At the highest temperatures (T > 4 K), we observe the same general profile that was previously seen [67]. However, upon lowering T below 4 K, several features appear simultaneously in $\kappa_{xx}(B)$. These features have an oscillatory-like appearance that is strongly reminiscent of Shubnikov de Haas (SdH) oscillations observed in metals.

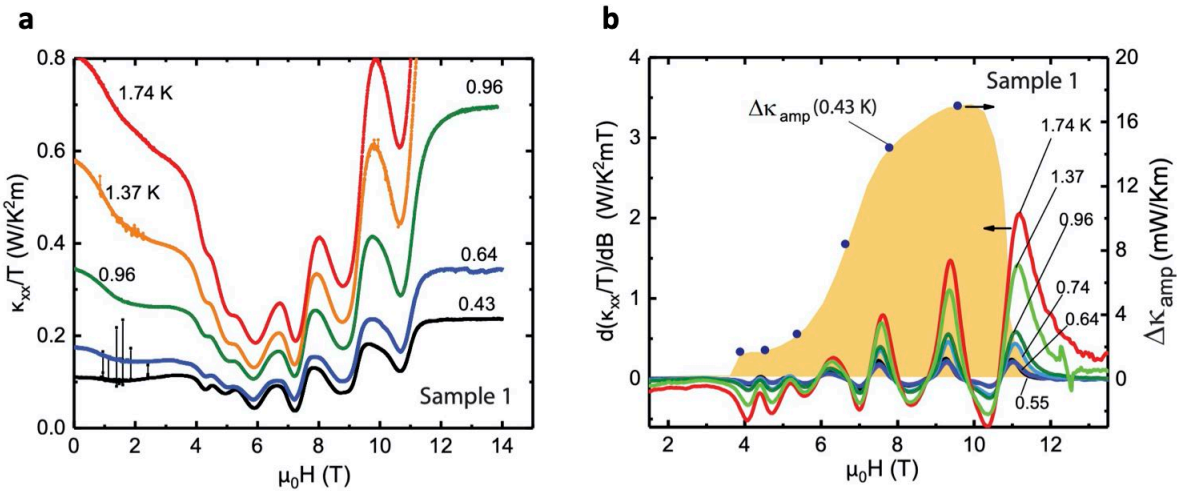

Figure 2.4: Panel (A): The oscillations over the full field range at selected T (colored curves). The data shown here were recorded continuously (in contrast with the field-step procedure employed when collecting the data shown in Fig. 2.3). At around 11 T, κ_{xx} displays a step increase to a plateau-like profile in the polarized state in which oscillations are strictly absent. Panel (B): The derivative curves $\mathrm{d}(\kappa_{xx}/T)/\mathrm{d}B$ for a range of T (colored curves) show that the oscillations onset abruptly at 4 T. The large derivative peak centred at around 11.3 T corresponds to the step increase in κ_{xx}, and is not part of the oscillation sequence. Arrows indicate the relevant axes for the quantity plotted. The amplitude $\Delta\kappa_{amp}$ (solid circles) is strikingly prominent in the QSL state. Its profile (shaded orange) distinguishes the QSL from adjacent phases. A weak remnant tail extends below 7 T to 4 T in the zig-zag AFM ordered state. Figure adapted from [49].

This is surprising because $RuCl_3$ is an incredibly strong electrical insulator (the energy gap is as high as 1.9 eV [72]) and lacks the electronic Fermi surface that is necessary for producing conventional quantum oscillations. This is immediately suggestive of potentially exotic physics being at play.

More information about this striking behavior can be obtained by viewing the data in different ways. The data in Fig. 2.4 was obtained by sweeping field continuously (unlike that in Fig. 2.3, which was measured using a stepscan procedure). Fig. 2.3b shows the field derivatives ($d\kappa/dB$) of the sweeps from Fig. 2.3a. The oscillation-like character is particularly apparent in the $d\kappa/dB$ curves. Also included in Fig. 2.3b is the amplitude of the κ_{xx} oscillation as a function of field for the lowest temperature sweep ($T_{Sample} = 0.43$ K). Depicting the data this way highlights some other important features. For example, the kinks around 4.2 and 5 T are much more apparent in the $d\kappa/dB$ curves. Additionally, the amplitude curve also reveals a structure to the oscillations that is strongly reminiscent to the system's known phase diagram.

Between 0 and 4 T, we observe no oscillations. This makes sense as the system is fully ordered so there is no entanglement or disorder present that may enable more exotic, spin liquid-like physics. For $4 < B < 7$ T, we observe very weak oscillations. This can likely be interpreted as a mixed phase where there is some sort of coexistence between the low B ordered phase and the possible

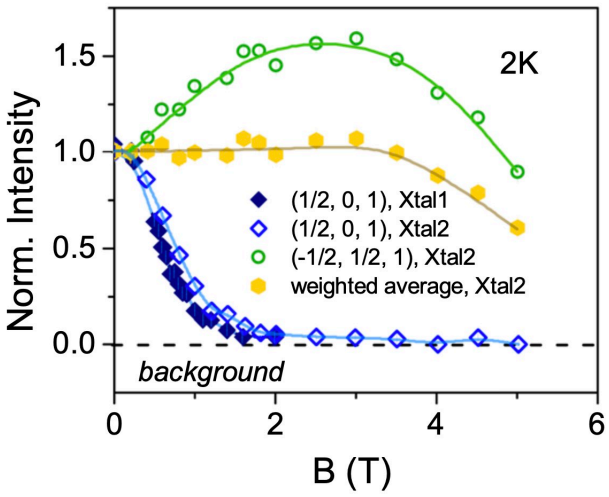

Figure 2.5: Field-dependence of magnetic Bragg peak intensity in $RuCl_3$. As described in Chapter 1, the applied field will favor a particular zig-zag AFM configuration. This is demonstrated by the increasing intensity of the (-1/2, 1/2, 1) peak and the rapidly decreasing intensity at the (1/2, 0, 1) one. The authors also use a weighted average to quantify the overall strength of the AFM order as a function of B (shown in yellow). Notably, the intensity is constant up to around 4 T where it shows a sudden decrease. The field applied along the **a** axis and the measurement is done at 2 K. Figure adapted from [56].

spin liquid state seen at higher B. The existence of the mixed phase was anticipated by neutron scattering measurements performed by Banerjee et al. [56]. The relevant data is shown in Fig. 2.5. The authors track the intensity of various magnetic Bragg peaks as a function of B. As discussed earlier, there are multiple possible arrangements for the zig-zag AFM order. Each of these will have a different signature in scattering probes due to the differing ordering vectors. As B increases, the domains with moments aligned most perpendicular to the applied field will become energetically preferable and will increase in abundance (and therefore intensity in the neutron measurement) while the other types of domains will decrease in population. In this specific experiment, the (-1/2, 1/2, 1)-type order (shown in green) is the preferred direction while the order with intensity at the (1/2, 0, 1) point (shown in light blue) is suppressed by **B**. To measure the overall strength of the magnetic order, the authors calculate a weighted average of the intensity associated with the various directions and obtain the result shown in yellow. Interestingly, the intensity is constant until about 4 T where it exhibits a sudden decrease. This is strikingly reminiscent of what is seen in the κ_{xx} data and suggests that in both cases the magnetic order exists in a weakened form between 4 and 7 T, thereby allowing for spin liquid-like physics to appear concurrently.

For $7 < B < 11$ T, we observe oscillations that are significantly stronger in amplitude than what is seen in for $4 < B < 7$ T. As discussed earlier, this is exactly the intermediate field regime where

the magnetic order has been fully destroyed, but the spins have not yet been fully polarized. It is in this disordered regime where spin liquid physics has been allegedly predicted and observed. Our observation of possible quantum oscillations that are seemingly localized to this field range is therefore consistent with this assumed phenomenology.

Finally, above 11 T, we observe no oscillations. Additionally, we find that for the low T curves, $\kappa_{xx}(B)$ is completely flat. The flatness can be explained in the following way. The changing of κ_{xx} with B can mostly be considered as being due to the modulation of the strength with which phonons (the primary heat carrier) are being scattered by spins (either as well-defined quasiparticles or simply localized moments). At high B, after the alleged field-induced spin liquid phase has been destroyed, the magnetic degrees of freedom form a spin-polarized phase with gapped magnon-like excitations [52]. The size of this energy gap increases with B (eventually linearly) due to the Zeeman effect. Eventually, the thermal population of spin excitations will be so low that it is effectively zero. After this point, the scattering of phonons by spins will therefore stop changing with increasing B so κ_{xx} will cease to exhibit any field-dependence. Such an effect is almost certainly not limited to low T as implied here. Observing this plateau-like effect at higher T will require stronger fields than what can be done with our current setup. We would also like to stress (as we do elsewhere in this thesis) that the value of κ_{xx} at this plateau can be thought of as being that of the pure, intrinsic lattice thermal conductivity of the system and this quantity is likely the best indicator of crystalline quality.

2.3 Reproducibility

We have verified that similar features appear in other $RuCl_3$ crystals. Fig. 2.6 shows similar κ_{xx} vs. B data for another crystal (labeled Sample 3) where $\mathbf{B} \parallel \mathbf{a}$ (as with Sample 1). Superficially, the general profile of κ_{xx} vs. B (colored curves in Fig. 2.6a) may seem somewhat different from what was observed previously. There are clear deviations from a smooth profile, but these deviations have a less oscillatory-like appearance than they do in Sample 1. The features seen within the ordered phase are also much weaker. We also note that the the behavior at high B lacks the characteristic plateau seen previously, but this is most likely due to a technical issue with the field-calibration of the sample thermometers.

The differences from Sample 1 are much less apparent in the derivative curves ($\mathrm{d}\kappa/\mathrm{d}B$ in Fig. 2.6b). The characteristic profile is very similar to what was observed earlier. In particular, the low B features that were difficult to observe in the κ vs. B curves are clearly visible in the $\mathrm{d}\kappa/\mathrm{d}B$ ones.

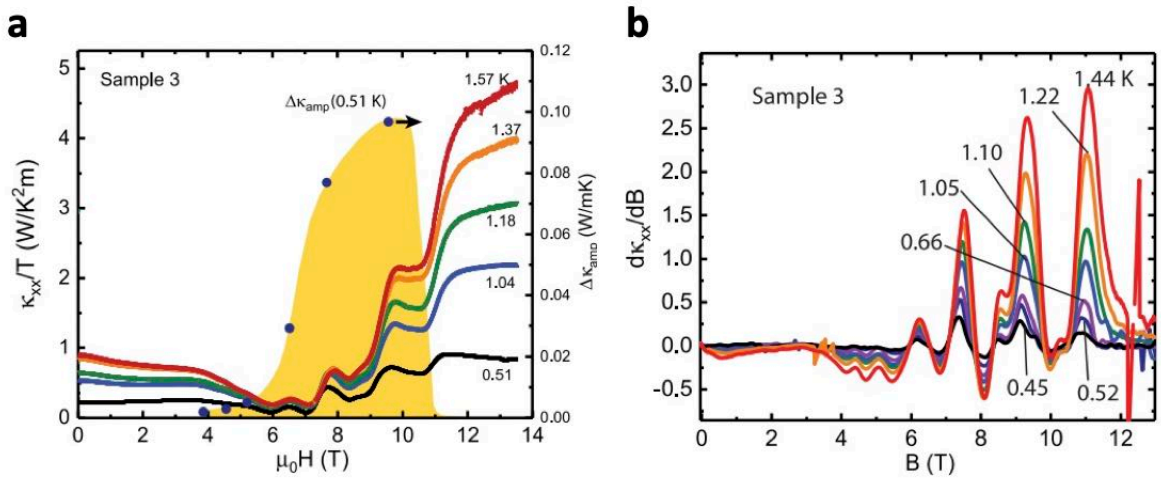

Figure 2.6: Panel (A): κ_{xx}/T vs. T at selected T from 0.51 to 1.47 K for Sample 3 (colored curves and left axis). The black points and yellow area beneath them represent the oscillation amplitude $\Delta\kappa_{amp}$ as a function of B (with the right axis displaying the appropriate units). Panel (B): Derivative curves ($\mathrm{d}\kappa_{xx}/\mathrm{d}B$) of the data shown in Panel (A). Sample 3 clearly displays oscillations as well and the similarities with Sample 1 are especially apparent in the $\mathrm{d}\kappa_{xx}/\mathrm{d}B$ curves. Figure adapted from [49].

Note that Fig. 2.6a also shows the behavior of κ_{amp} at the lowest T measured ($T = 0.51$ K here) and that it appears to be quite similar to what was observed for Sample 1 apart from the features in the ordered phase being weaker.

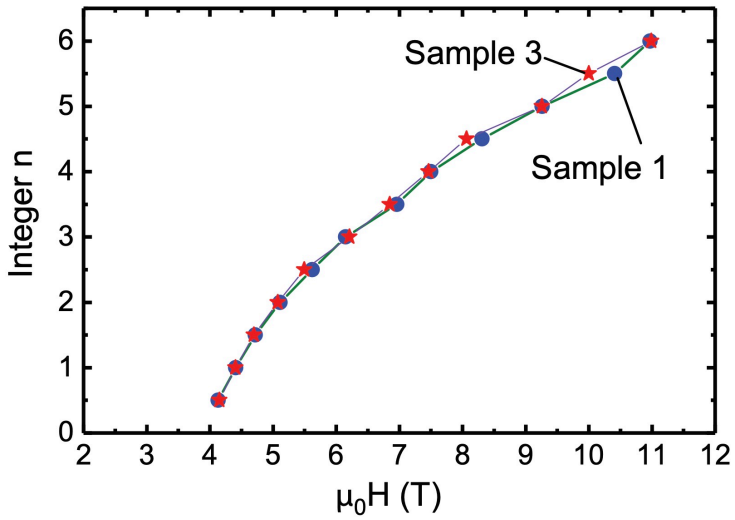

Figure 2.7: Index plot showing the locations H_n of the $\mathrm{d}\kappa_{xx}/\mathrm{d}B$ extrema (identified with integer values n) in Samples 1 (blue circles, green lines) and 3 (red stars, grey lines). In both data sets the slope of the curve monotonically increases as H decreases to 4 T. The narrowing of the spacing between adjacent extrema is strongly incompatible with periodicity versus H. $\mathbf{H} \parallel \mathbf{a}$ for both crystals. Figure adapted from [49].

The similarity between the appearance of this oscillatory-like effect in these two different crystals is even more apparent by tracking the B values at which the features appear. To track the oscillations precisely, we examine the $\mathrm{d}\kappa/\mathrm{d}B$ curves taken at the lowest temperature for both crystals (0.43 K for Sample 1 and 0.45 K for Sample 3). Starting with the first such extremum (a minimum to which we assign an index value of 0.5), we record a new index value for each subsequent extremum. Note that $\mathrm{d}\kappa/\mathrm{d}B$ maxima are given integer valued indices while minima are given have half-integer values. In Fig. 2.7 we plot the values of those indices and the fields at which they occur for both crystals. The two curves agree with each other quite well. This is notable as it strongly suggests that this effect is intrinsic in nature (despite the superficial differences in the appearance of the κ_{xx} vs. B curves).

2.4 Field-angle Dependence

For Sample 1, we also performed measurements with **B** pointed at a finite angle relative to the 2D crystal layers. Crucially, this had to be done without unmounting the crystal. It would be too difficult to remount the sample in a sufficiently gentle way that no stacking faults are induced. The adding of stacking faults between measurements would make a true comparison impossible. This was done by placing a ramp-shaped jig in between the brass plate on which the crystal is mounted and the sample stage of the probe (with all adhesion done using GE Varnish). Using this method, we were able to align the field at angle θ of 39° and 55° relative to the honeycomb plane. Note that it is difficult to align the jig and sample stage precisely so the exact angle can only be determined by visual inspection once the new placement is complete and the GE Varnish is dry.

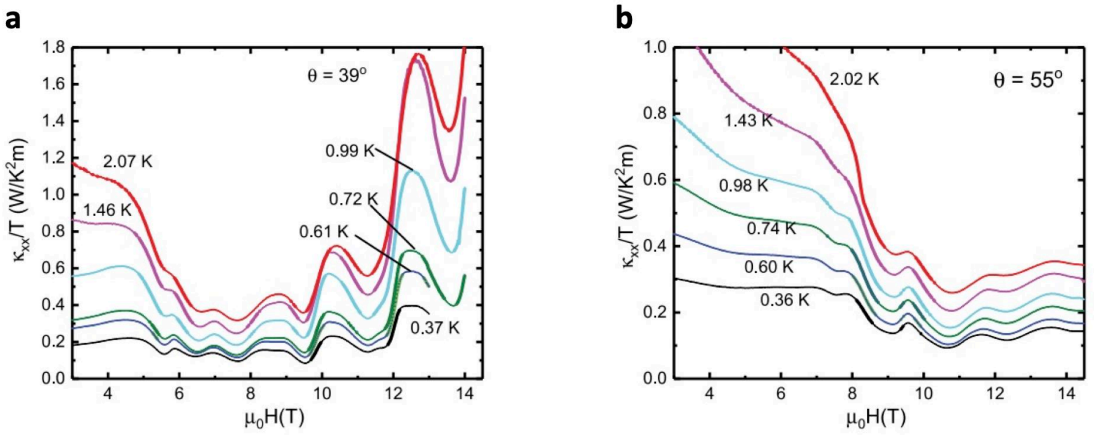

Figure 2.8: Curves of κ_{xx}/T vs. H measured in Sample 1 at tilt angle $\theta = 39°$ (Panel (A)) and $\theta = 55°$ (Panel (B)) with T fixed at the 6 values indicated. Figure adapted from [49].

Fig. 2.8 shows κ_{xx}/T vs. B curves at a series of temperatures ($0.35 < T < 2.07$ K at $B = 0$). For $\theta = 39°$, the profile appears very similar to what is observed for $\theta = 0°$. Note that we are unable to reach a high enough B to observe the high B plateau. For $\theta = 55°$, the oscillatory-like features are still visible, but it appears that the minimum in κ_{xx} that typically occurs when $\mathbf{B}_{\parallel} \approx 7$ T is being stretched to high B and over a wider field range than one would naively expect due to $RuCl_3$'s largely quasi-2D anisotropy. To reiterate, it is typically assumed that $RuCl_3$'s magnetic susceptibility should be so anisotropic that it is only the in-plane component of the applied field ($B_{\parallel}$) that dictates the system's phase diagram and relevant physics (though there are some counterexamples like Kasahara et al.'s tilted field thermal Hall experiments [60]).

We now test the validity of this idea when applied to the thermal transport physics. Fig. 2.9 shows the normalized longitudinal thermal conductivity vs. $B_{\parallel}$ (or equivalently, $\mu_0 H_a$ as shown in the axis label). Here, normalized means that for each field, we divide κ_{xx} at that field value H by the value of κ_{xx} measured at zero field (though we only plot data for $B_{\parallel} > 3$ T). We now highlight some notable features. First, the curves for $\theta = 0°$ and $\theta = 39°$ are remarkably similar. The various local maxima and minima appear at essentially the same field values and the curves exhibit the same general profile consisting of oscillation-like features on top of a broad background with a minimum around $B_{\parallel} \approx 7$ T. The amplitudes differ slightly for some of the oscillations, but this could just be due to differences in T_{Sample} (we remind the reader that we only fix T_{Stage} so T_{Sample} will inevitably vary with κ_{xx} as B is changed).

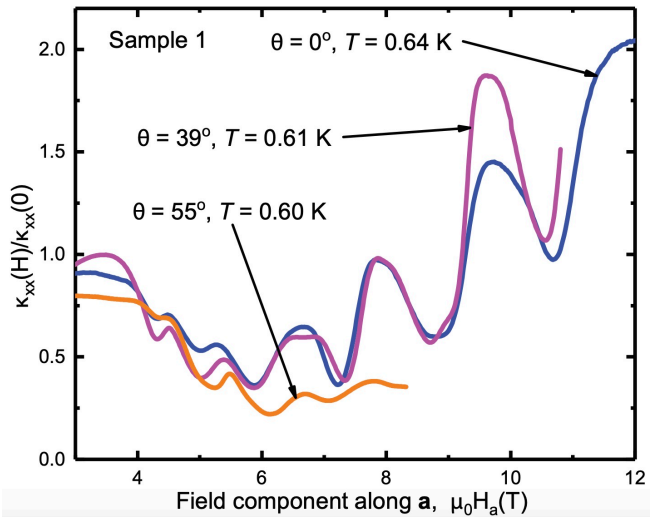

Figure 2.9: The effect of tilting **H** out of the plane by angle θ (relative to the **a** axis) in Sample 1 at T $\approx$ 0.6 K. The curves are measured with $\theta = 0°$ (blue), 39° (purple), and 55° (orange). When they are plotted versus H_a, the periods of the oscillations in κ_{xx} match well for the three angles. Figure adapted from [49].

The situation is somewhat different for $\theta = 55°$. The locations of the oscillations seem to deviate somewhat from the expected values. The oscillations also appear to be much weaker in amplitude than what was observed for the lower values of θ. Additionally, as we mentioned earlier, the profile of the broad background also deviates from what is seen for other angles. Rather than exhibiting a clear minima (after which it increases sharply), κ_{xx} appears that it may continue to show suppressed, rather than enhanced values as B is increased further. These deviations at high angles seem to imply more 3D structure than that consistent with simple field projection, which is not necessarily unexpected given that the system is likely not fully quasi-2D.

2.5 Periodicity

Traditional Shubnikov de Haas oscillations are periodic in $1/B$. Here we show that this is the case for $RuCl_3$'s κ_{xx} oscillations as well. As done earlier when comparing Samples 1 and 3, we use the

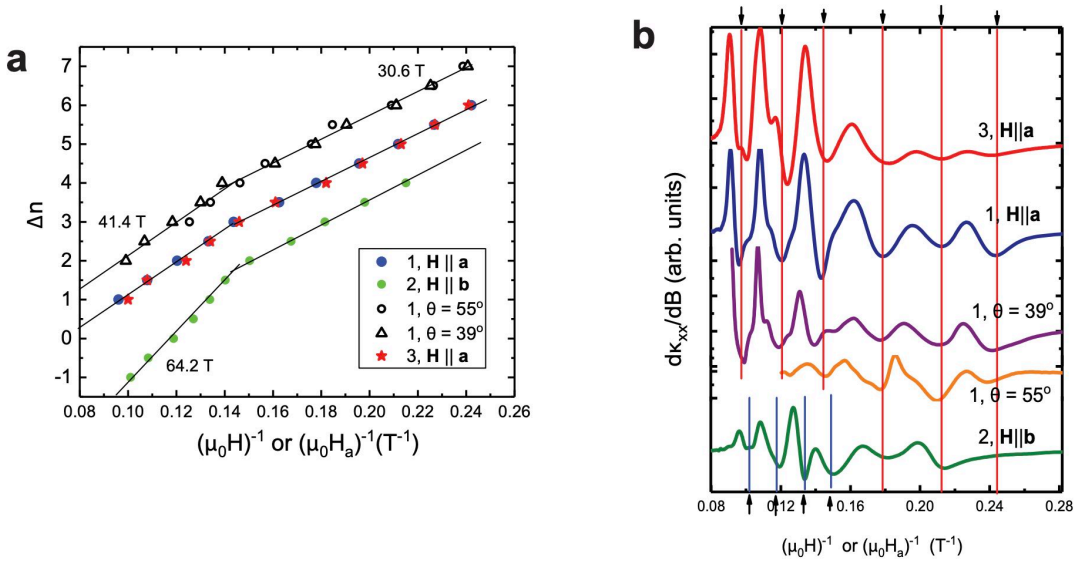

Figure 2.10: Panel (A): The integer increment Δn vs. $1/H_n$ (or $1/H_{n,a}$), where H_n are the fields identifying extrema of the derivative curves $d\kappa_{xx}/dB$ ($H_{n,a} = H_n cos(\theta)$ for tilted **H**). Solid symbols represent data taken with **H** strictly in-plane. The blue circles (Sample 1) and red stars (Sample 3) were measured with $\mathbf{H}_{\|} \parallel \mathbf{a}$, whereas the green circles were measured in Sample 2 with $\mathbf{H}_{\|} \parallel \mathbf{b}$. Open symbols are measurements in Sample 1 with **H** tilted in the a–c plane at angles $\theta = 39°$ (triangles) and $\theta = 55°$ (circles), relative to **a** axis. The points fall on the same segmented curve (comprised of line segments with slope 31 T below 7 T and 41 T above 7 T (solid black lines)). The exception is the high-field slope of 64 T in Sample 2 with $\mathbf{H}_{\|} \parallel \mathbf{b}$. For clarity, the three data sets are shifted vertically by $\Delta n = 1$. Panel (B): Curves of the derivative $d\kappa_{xx}/dB$ vs. $1/H$ (or $1/H_a$) in arbitrary units (a.u.) for Samples 1, 2, and 3 ($H_a = H cos(\theta)$). For Sample 1, we show $d\kappa_{xx}/dB$ measured with $\theta = 0°$, 39°, and 55°. The extrema of $d\kappa_{xx}/dB$ are plotted in Panel (A). Arrows and vertical lines mark the values of $1/H_n$ and $1/H_{n,a}$ read off from the straight-line fits in Panel (A) for integer increments Δn. Figure adapted from [49].

low T dκ/dB curves to identify the locations of the oscillation extrema. Again, derivatives are used because they highlight the local modulations in κ_{xx} vs. B while reducing the effects of the broad background. For this reason, derivative curves are commonly used when analyzing quantum oscillations.

Fig. 2.10a shows the locations of the dκ/dB plotted against $1/B$ for a series of samples and field directions and Fig. 2.10b shows the dκ/dB curves from which those values were extracted. We apply $\mathbf{B} \parallel \mathbf{a}$ for Samples 1 and 3 and $\mathbf{B} \parallel \mathbf{b}$ for Sample 2. For Sample 1, we also performed measurements with $\mathbf{B}$ at a finite angle relative the crystal planes. This was done for $\theta = 39°$ and $\theta = 55°$ (with $\mathbf{B}_{\parallel} \parallel \mathbf{a}$ still). Note that in Fig. 2.10 we plot against $1/B_{\parallel}$.

The index plot (Fig. 2.10a) reveals that the extrema fall on a line as they would for conventional quantum oscillations due to Landau quantization. Note; however, that there is a break in slope around $B_{\parallel} = 7$ T, which roughly corresponds to the B at which the magnetic order is destroyed. The slope of this line is the oscillation frequency. For conventional quantum oscillations, this frequency is proportional to the area of the Fermi surface that is normal to the applied $\mathbf{B}$. We obtain a frequency of approximately 30.6 T for $B < 7$ T for all field directions. Above 7 T, the frequency changes and the new value depends on the in-plane direction of $\mathbf{B}$. For $\mathbf{B}_{\parallel} \parallel \mathbf{a}$ we observe a frequency of 41.4 T while for $\mathbf{B}_{\parallel} \parallel \mathbf{b}$ we obtain a frequency of 64.2 T. It is interesting that there is an apparent anisotropy in the field-induced spin liquid phase, but not in the ordered phase. Similarly, it is notable that the frequencies for the two in-plane directions match even though the oscillations begin at a slightly higher field for $\mathbf{B}_{\parallel} \parallel \mathbf{b}$. This high degree of consistency for various samples and field directions further highlights the strong reproducibility of this effect.

2.6 Relation to Thermal Hall Conductivity

$RuCl_3$'s thermal Hall conductivity will be discussed at length in the next chapter, but here we briefly comment on the κ_{xy} data collected during this experiment and how it might relate to the apparent κ_{xx} oscillations. As shown in Fig. 2.11a we observe a clear planar thermal Hall effect (PTHE) signal. κ_{xy} has a dome-like profile that appears to be mostly associated with the B-induced state immediately above H_c, but bleeds into lower B regions at high T. These characteristics are reminiscent of the alleged quantized signal reported by the Kyoto group [60][73]. However, unlike their results, our measured κ_{xy}/T signal is not quantized and is strongly T-dependent. This T-dependence is shown in Fig. 2.11b. In this same panel, we plot the normalized κ_{xx} oscillation amplitude $\Delta\kappa/\kappa_{bg}$ (more details on how this is calculated will be given later). Note that $\Delta\kappa/\kappa_{bg}$ is

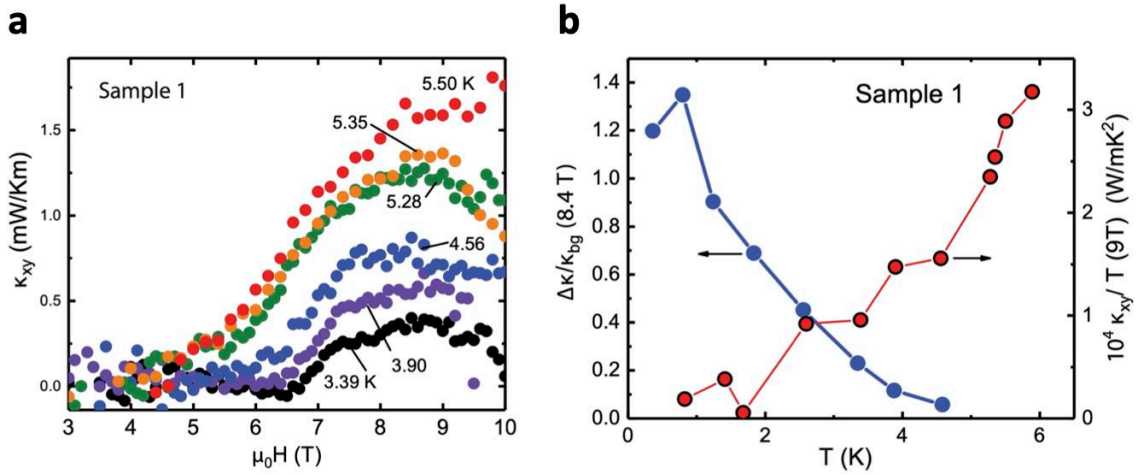

Figure 2.11: Panel (A): Thermal Hall conductivity κ_{xy} vs. B at a series of temperatures. A dome-like planar thermal Hall effect emerges in the B-induced spin liquid phase, but it is not quantized. Panel (B): the normalized κ_{xx} oscillation amplitude (blue points and left axis) and κ_{xy}/T (red points and right axis) vs. T. The two appear to be anticorrelated. Note that $\Delta\kappa/\kappa_{bg}$ is measured at 8.4 T and κ_{xy}/T is measured at 9 T. Figure adapted from [49].

measured at 8.4 T and κ_{xy}/T is measured at 9.0 T. The latter is measured at a slightly higher field to stay in the field regime where κ_{xy} vs. B more clearly shows a plateau/ dome-like profile (and is therefore more likely to be related to the alleged quantization). Notably, $\Delta\kappa/\kappa_{bg}$ and κ_{xy}/T appear to be anticorrelated. This is potentially reassuring from a phenomenological point of view. If the κ_{xx} oscillations do in fact arise from a neutral Fermi surface-like phase, such a state would almost certainly (at least in conventional models) be gapless in nature. This is in contrast with the κ_{xy} signal which, in the Kitaev model, is usually associated with edge states (and a gapped bulk). This anticorrelated T-dependence may therefore imply that two separate states (associated with different T regimes) are responsible for these two seemingly distinct effects. We continue this discussion in the Chapter 3.

2.7 Oscillations in Hysteresis

During our early measurements of $RuCl_3$'s thermal transport properties, we discovered magnetic hysteresis in κ_{xx}. This was unexpected because no such effect had ever been reported in magnetization or any other measurement. As with the κ_{xy} measurements, we will defer a detailed discussion of this phenomenon to a later chapter and will limit this section to commentary on how it relates to the κ_{xx} oscillations.

Fig. 2.12 shows a pair of sweeps measured at $T_{Sample} = 1.31$ K in the same crystal that is used

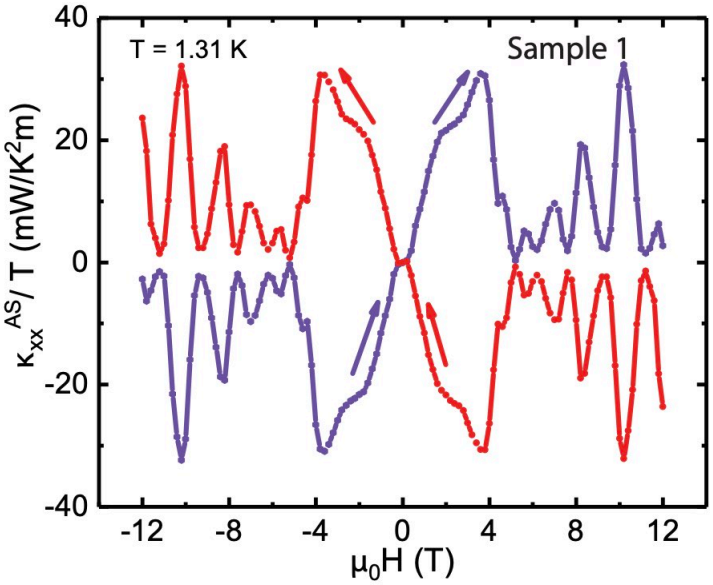

Figure 2.12: The hysteresis in κ_{xx} that can contaminate κ_{xy} if not properly subtracted. The field-antisymmetrized κ_{xx} measured for the "upsweep" (negative to positive field) is shown in purple and the corresponding "downsweep" (positive to negative field) data is shown in red. The measurement is done at fixed T_{Stage} where $T_{Sample}(B = 0\ T) = 1.31$ K. Figure adapted from [49].

for most of the oscillation measurements (Sample 1). We plot the B-antisymmetrized longitudinal thermal conductivity (divided by temperature) κ_{xx}^{AS}/T measured for both "up" (negative to positive B) and "down" (positive to negative B) sweeps. We remind the reader that the antisymmetrized κ_{xx} is calculated in the following way:

$$\kappa_{xx}^{AS}(H) = \left(\kappa_{xx}(+H) - \kappa_{xx}(-H)\right)/2 \tag{2.1}$$

κ_{xx}^{AS} shows a distinct butterfly-like structure consisting of broad hump-like features at low B ($B < 5$ T) followed by a series of spikes where $|\kappa_{xx}^{AS}|$ decreases to close to zero in between the spikes. Interestingly, the $|\kappa_{xx}^{AS}|$ minima occur at the same fields as the minima in κ_{xx}. This fact is illustrated in Fig. 2.13, which shows κ_{xx}^{SY}/T, κ_{xx}^{AS}/T, and $d(\kappa_{xx}^{SY}/T)/dB$. As would be expected, the κ_{xx}^{SY}/T minima occur at the same B values as the zeroes of $d(\kappa_{xx}^{SY}/T)/dB$. Note that this data was collected at a lower temperature than the data shown in Fig. 3.17 to more effectively highlight the indicated correlations. It is tempting to believe that the hysteresis is simply picking up the B-induced modulations in κ_{xx}, but the spike-like profile is so different from what is seen in κ_{xx} that further investigation is warranted. We continue this discussion later.

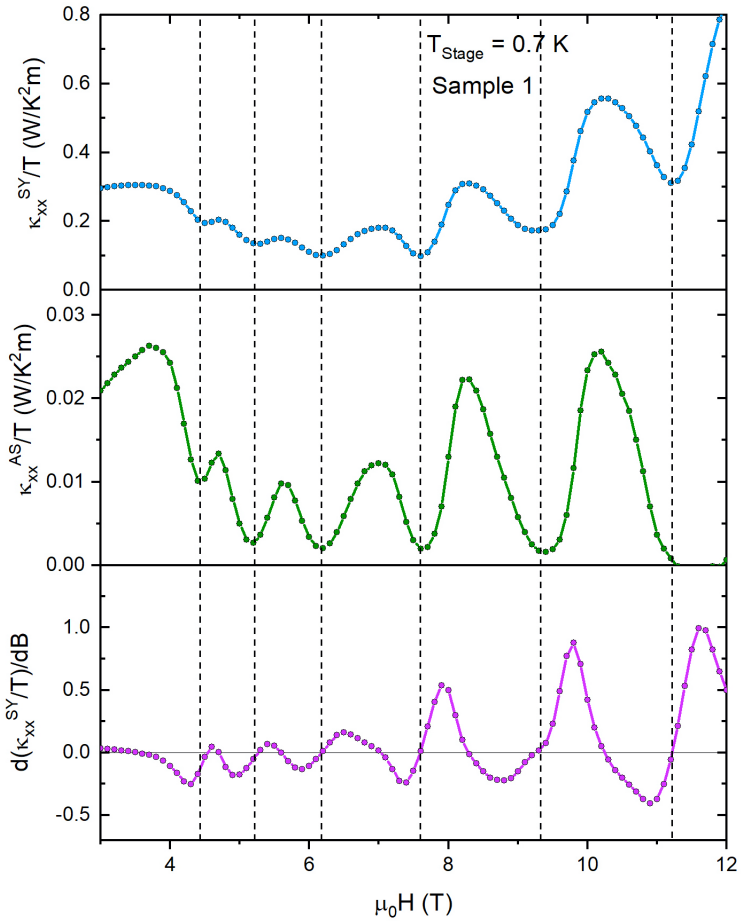

Figure 2.13: Top: Field-symmetrized longitudinal thermal conductivity divided by temperature vs. B measured at fixed T_{Stage} = 0.7 K. Middle: Field-antisymmetrized κ_{xx} measured under the same parameters. Bottom: Field derivative of the longitudinal thermal conductivity (labeled $d(\kappa_{xx}^{SY}/T)/dB$). The extrema of κ_{xx}^{AS}/T occur at the same fields as the extrema in κ_{xx}^{SY}/T (as well as the zeroes of $d(\kappa_{xx}^{SY}/T)/dB$).

2.8 Oscillation Amplitude

The problem of accurately determining the magnitudes of the oscillations is complicated by the strong non-monotonic variation of the curve $\langle\kappa_{xx}(H)\rangle$ (without oscillations) over the entire field interval $0 \rightarrow 14$ T. We adopt the following procedure. First, we find the smooth "background" curve κ_{bg} threading the midpoints between successive extrema of $d\kappa_{xx}/dB$. In Fig. 2.14b, we display the background κ_{bg} as the red curve for T = 0.43K in Sample 1. Assuming that κ_{bg} provides a close approximation to $\langle\kappa_{xx}(H)\rangle$, we obtain the oscillatory component of κ_{xx} as the difference $\Delta\kappa = \kappa_{xx} - \kappa_{bg}$. Its amplitude is called $\Delta\kappa_{xx}$.

For conventional quantum oscillations, quantitative analysis of the data can provide a huge

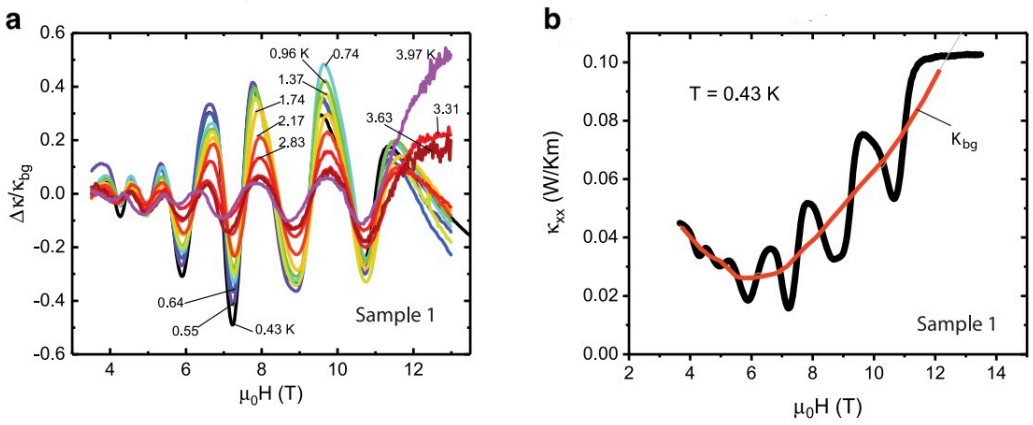

Figure 2.14: Panel (A): The oscillatory component $\Delta\kappa$ divided by the background κ_{bg} measured in Sample 1 at selected T. Panel (B): Depiction of how $\Delta\kappa$ is calculated. κ_{bg} (red curve) is determined from the mid-points between extrema of the measured curve of κ_{xx} (black curve). The difference between κ_{xx} and κ_{bg} gives $\Delta\kappa$. Figure adapted from [49].

amount of information about the material's underlying physics. The T- dependence of the oscillation amplitude can be used to extract the effective mass of the quasiparticles at the Fermi surface producing the oscillations using the Lifshitz-Kosevich equation:

$$\Delta\kappa/\kappa_{bg} = \lambda(T)/sinh\,(\lambda(T)) \tag{2.2}$$

with $\lambda(T) = 2\pi^2 k_B T m^*/\hbar e B$. Remarkably, we find that the κ_{xx} oscillation amplitude in $RuCl_3$ can be fit to Eq. 2.2 as shown in Fig. 2.15. This fitting reveals an effective mass $m^* = 0.67m_e$ for Sample 1 ($B = 8.4$ T) and $m^* = 0.994m_e$ for Sample 3 ($B = 8.0$ T). The latter case is shown in the example (though we acknowledge that the fitting fails for higher fields). Surprisingly, m^* is of the same order as the electron mass m_e despite the absence of charge carriers in the system. However, we also acknowledge that there is some inherent ambiguity into how to quantitatively interpret the $\Delta\kappa$ data. While Eq. 2.2 successfully describes the data if we normalize $\Delta\kappa$ as $\Delta\kappa/\kappa_{bg}$, it is not immediately obvious that this is the correct way to define the oscillation amplitude or that the Lifshitz-Kosevich equation (in its typical form) should apply to thermal conductivity measurements. The presence of phonons (which are usually the dominant heat carriers) introduces an additional level of complexity that may impact the universality of the Lifshitz-Kosevich model.

Similarly, it is not obvious whether a model developed for a conventional Fermi surface of charged particles should apply to one made of more exotic neutral fermions. The Lifshitz-Kosevich model has been shown to apply so some of the other electrical insulators that exhibit quantum oscillations [74], but not to others [75]. We will discuss these other systems more later. Similarly, it has been found

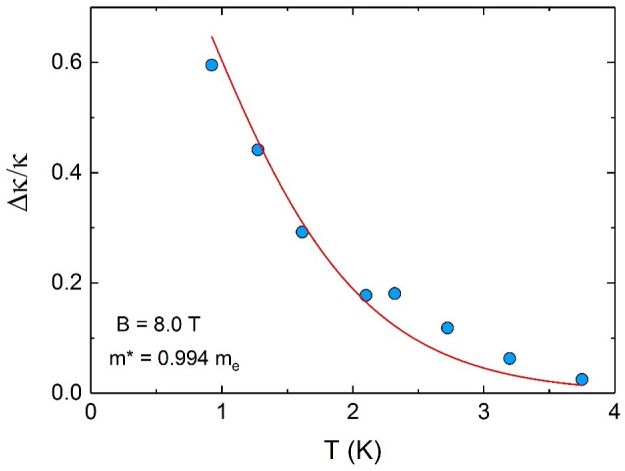

Figure 2.15: Normalized oscillation amplitude $\Delta\kappa/\kappa$ vs. T for Sample 3. Fitting to the Lifshitz-Kosevich formula at 8 T reveals an effective mass of 0.994 m_e.

that Lifshitz-Kosevich formula fails to describe the behavior of $\Delta\kappa$ vs. T in TaAs, a topological semimetal whose strong κ_{xx} oscillations have substantial contributions from collective excitations of the Weyl fermions (this will be discussed further in a later section).

2.9 Additional Measurements

As presented earlier, we have measured κ_{xx} vs. B for a series for a samples. Most of our discussion of the field angle-dependence has focused on Sample 1. However, this is not the only crystal we have measured with **B** directed partially out-of-plane. Data from another such measurement (on a crystal referred to here as Sample 4) is depicted in Fig. 2.16. Also included in this figure are measurements from Samples 1 and 2 for comparison. We remind the reader that $\mathbf{B} \parallel \mathbf{b}$ for Sample 2. As with Sample 1, $\mathbf{B}_{\parallel} \parallel \mathbf{a}$ in the Sample 4 experiment. All data shown in the figure is taken at $T \approx 0.5$ K. The difference between the Sample 4 and the $\theta > 0°$ Sample 1 data is immediately apparent. No oscillations are seen in Sample 4 (where **B** is applied at an angle of 45° relative to the **a** axis). This measurement was actually done before the Sample 1 angled field experiments so it initially led us to believe that an out-of-plane field would kill the oscillations. However, our subsequent experiments revealed that this was not generally the case. There are a few possible explanations for this discrepancy. One is that it is simply another instance of sample variability, a problem that has plagued $RuCl_3$ for years. Another, more interesting possibility is that it is a consequence of the material's (and underlying model's) complex field-angle dependence. Specifically,

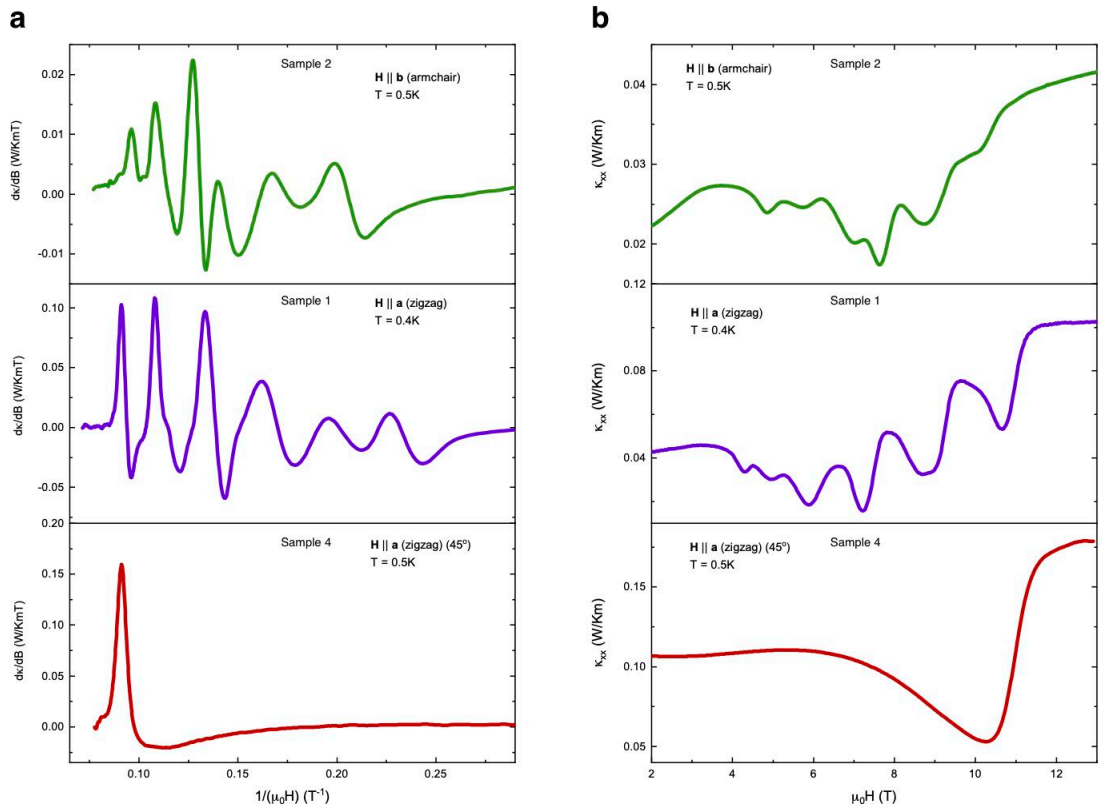

Figure 2.16: Unlike Sample 1, Sample 4 does not show oscillations when **B** is directed partially out-of-plane. This figure shows a low T sweep demonstrating this fact (bottom plots). The upper plots show data from Sample 1 ($\mathbf{B} \parallel \mathbf{a}$) and Sample 2 ($\mathbf{B} \parallel \mathbf{b}$) for comparison. Panel (A): Field derivative of the thermal conductivity plotted against inverse field ($\mathrm{d}\kappa/\mathrm{d}B$ vs. $1/\mu_0 H$). Panel (B): κ_{xx} vs. B. The Sample 4 data also illustrates that the sharp peak at high B seen in all low T $\mathrm{d}\kappa/\mathrm{d}B$ curves is due to the shoulder feature in κ_{xx}.

while consideration of the honeycomb lattice alone cannot explain why directing a field 45° above **a**, would yield different results from applying **B** 45° below **a**. The distinction is apparent when the octahedral cages are incorporated into the analysis. This is the same reason that the ordered moment in the zig-zag AFM phase is subjected to similar restrictions (must point at angle of $\approx +35°$ relative to **a**, not -35°) and the reason for the sign difference in the Chern number for similar changes in field configuration. The former example was discussed earlier and the latter will be discussed in the next chapter.

Another important detail of our data that is further highlighted by the results presented in Fig. 2.16 is the interpretation of the final sharp peak seen in the $\mathrm{d}\kappa/\mathrm{d}B$ curves. Inspection of our oscillation data reveals that this final peak does not follow the expected Landau-like ($1/B$) spacing and the measurements on Sample 4 reveal why this is the case. The reason is that it is not an oscillation. It is instead a reflection of the shoulder-like feature seen in κ_{xx} vs. B. It is notable;

however, that this feature seems to occur at the same raw (non-projected) field value as the one for Sample 1 even though the field is directed entirely in-plane in the latter case. The same seems to be true for Sample 2 (where $\mathbf{B} \parallel \mathbf{b}$) as well. This could imply that the transition to the ordered phase shows more isotropy than is expected from other field angle-dependent measurements. Further experiments with $\mathbf{B}$ directed partially out-of-plane are therefore highly desired.

2.10 Spinon Fermi Surface

As discussed throughout this chapter, the $1/B$-periodic oscillations in κ_{xx} are strongly suggestive of a possible neutral (or spinon) Fermi surface state. Here we present a general overview of what a spinon Fermi surface is, how field induced quantum oscillations can arise in such a state, and how our results could potentially be understood within this context.

Conventional electronic Fermi surfaces arise in metals due to the Pauli exclusion principle. Only one fermion is able occupy a given quantum state so if more fermions are added to the system, they are forced to lie at higher and higher energies. In a condensed matter system, each propagating state is characterized by both an energy and momentum (denoted by the wavevector $\mathbf{k}$) and the quasiparticles that fill up this bath of states are electrons. If the excitation's energy bands are populated in such a way that the topmost occupied level (called the Fermi energy) lies inside one of the electron's allowed excitation bands, then the resulting state will be a metal and will be able to easily conduct electricity. One can also associate a particular 3D geometry to the metal's topmost occupied states via the $\mathbf{k}$'s associated with all possible states at the Fermi energy. This structure is called a Fermi surface. The behavior of conventional quantum oscillations then result from the specific geometry of this surface.

In conventional electrical insulators, all of the relevant excitations are bosonic. Bosons follow different occupation number rules and are not able to form a surface-like structure. Exotic physics is needed for fermions to appear in insulators. As described in Chapter 1, quantum entanglement provides one route by which this can happen. In certain quantum spin liquids, the electron fractionalizes in such a way that the spin and charge act like separate quasiparticles. Additionally, the charge particle will act as a boson while the spin part (called a spinon) will act as a fermion. While the QSL is an insulator from the point of view of the electrical charge, the spinon's fermionic statistics can give rise to some unusual properties. In particular, they are able to form surface-like structures like those in conventional metals. The resulting state in a QSL is typically referred to as a spinon Fermi surface.

We briefly sketch how these charge-neutral fermionic quasiparticles are treated theoretically and how they can produce oscillations in a QSL state. The model presented here is largely adapted from Ref. [76]. In the widely adopted slave-particle approach, the electron operator $c_{i\alpha}$ is decomposed into a charged spinless boson ϕ_i and a neutral spin- 1/2 fermion $\psi_{i\alpha}$, i.e.

$$c_{i,\alpha} = \phi_i \psi_{i\alpha} \tag{2.3}$$

where i is the site index and α denotes the spin polarization.

To describe the insulating QSL state, the charged bosons (called holons) are assumed to be gapped whereas the neutral fermions (spinons) remain itinerant. However, the fermions are strongly correlated. They interact via an internal gauge field $a_\mu = (a_0, \mathbf{a})$, which we motivate as follows.

By Eq. 2.3 the electron operator is invariant under the local gauge transformation

$$\phi_i \to e^{i\theta_i}\phi_i, \qquad \psi_{i\alpha} \to \psi_{i\alpha} e^{-i\theta_i} \tag{2.4}$$

This gauge freedom is implemented by an internal U(1) gauge field a that couples to ϕ_i and $\psi_{i\alpha}$ with opposite gauge charges ± 1.

In addition, the decomposition Eq. 2.3 demands the local constraint

$$\sum_\alpha \psi^\dagger_{i\alpha}\psi_{i\alpha} = 1 \tag{2.5}$$

which is imposed by the Lagrange multiplier a_0. Combining a_0 with $\mathbf{a}$, we have the internal gauge field $a_\mu = (a_0, \mathbf{a})$. The internal field is distinguished from the physical gauge field $\mathbf{A}$ corresponding to the physical magnetic field $\mathbf{B} = \nabla \times \mathbf{A}$.

In the starting Lagrangian $\mathcal{L}$, we describe the fermions (of finite mass m_ψ) as minimally coupled to the internal gauge field $a_\mu = (a_0, \mathbf{a})$. The bosons are also minimally coupled to a_μ but with the opposite sign. In addition, the bosons couple minimally to the external gauge field $\mathbf{A}$. To allow a transition between the gapped phase ($\langle\phi\rangle = 0$) and the condensed phase ($\langle\phi\rangle \neq 0$) which is a metal, we expose the bosons to a field potential described by a Ginzburg-Landau expansion (terms involving $|\phi|^2$ and $|\phi|^4$).

Hence the Lagrangian has the form

$$\mathcal{L} = \psi^\dagger \left(i\partial_t - a_0 - \frac{(\mathbf{p} - \mathbf{a})^2}{2m_\psi} \right) \psi + |(i\partial_\mu + a_\mu - A_\mu)\phi|^2 - w|\phi|^2 - \frac{1}{2}g|\phi|^4 + \cdots \tag{2.6}$$

It bears repeating that the bosons couple to the *difference* field $A_\mu - a_\mu$, whereas the neutral

fermions couple only to a_μ.

As low-lying charge excitations are absent, the bosons are gapped ($\langle\phi\rangle = 0$), and we may integrate them out. The final result is a mean-field expression for the energy density u given by

$$u(b, B) = n\epsilon_\psi(n, B) + \frac{1}{2}\chi_\psi(B - b)^2 + \frac{1}{2}\chi B^2 \tag{2.7}$$

where ϵ_ψ is the fermion energy, n the fermion density, and $\mathbf{b} = \nabla \times \mathbf{a}$ is the internal field. As noted, the energy of the gapped bosons increases with applied field $\mathbf{B}$, but in the form $\frac{1}{2}\chi_\phi(B - b)^2$ (with χ_ϕ the susceptibility). By way of comparison, other (spectator) filled bands indifferent to the decomposition of $c_{i\alpha}$ contribute as $\frac{1}{2}\chi B^2$ (the third term in Eq. 2.7).

In analogy with 2D electrons (with quadratic dispersion), quantization in the internal field $\mathbf{b}$ leads to Landau levels (LLs) of degeneracy $g = b/2\pi$ and uniform spacing ω_c (we set $\hbar$ and e to 1). Writing the filling factor $\nu = n/g$ as $\nu = \nu_i + \nu_f$ where ν_i and ν_f are its integer and fractional part, respectively, we readily find the total energy of the fermions to be

$$E_\psi(n, b) = \frac{1}{2}g\omega_c\nu_i^2 + g\left(\nu_i + \frac{1}{2}\right)\omega_c\nu_f \tag{2.8}$$

Here the first term is the energy of ν_i filled LLs and the second is the energy of the highest, partially-filled level. We then obtain for $\epsilon_\psi(n, b) = E_\psi(n, b)/n$

$$\epsilon_\psi(n, b) = \frac{\pi n}{m_\psi}\left(1 + \frac{\nu_f(1 - \nu_f)}{\nu^2}\right) \tag{2.9}$$

As a function of b, $\epsilon_\psi(n, b)$ displays a scalloped profile with deep, cuspy minima occurring whenever all occupied LLs are fully filled ($\nu = \nu_i$).

At a fixed $\mathbf{B}$, we minimize $u(b, B)$ by allowing b to vary. From Eq. 2.7, b selects the nearest value $b_p = 2\pi n/p$ at which exactly p levels are filled ($p \in \mathbb{Z}$). The cuspy profile of the minima in ϵ_ψ ensures that b remains pinned to b_p in the face of slight field increments ΔB. However, for large enough ΔB, the term $\frac{1}{2}\chi_\phi(B - b)^2$ tips the global minimum to the next cusp, causing b to jump to b_{p1}. Hence, sweeping B continuously leads to a hysteretic, staircase profile for b, which produces sharp oscillations in observable quantities. The staircase behavior of the internal field was first found by Motrunich [77].

Finally, before returning to our discussion of $RuCl_3$ data, we would like to note that $RuCl_3$ is not the first electrically insulating system where possible quantum oscillations have been observed. Similar effects have been observed in Kondo insulators SmB_6 [75] and YbB_{12} [74], monolayer WTe_2

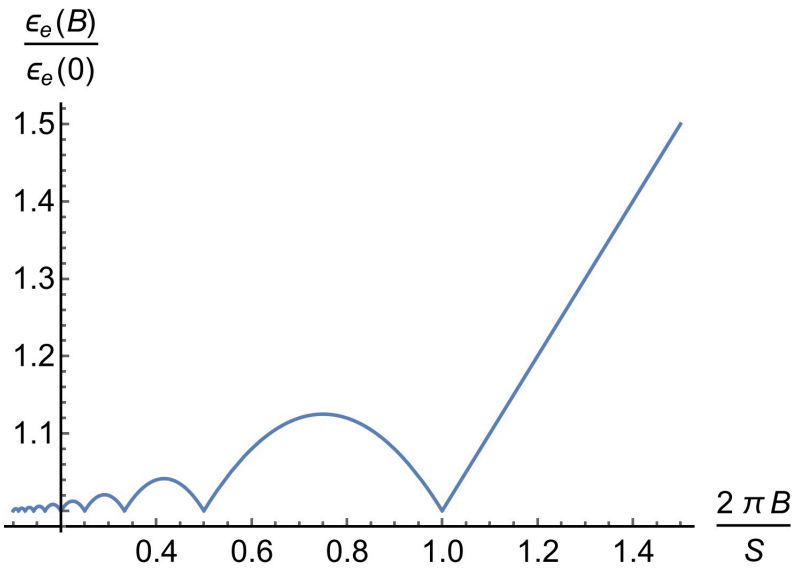

Figure 2.17: Scalloped-shaped field-dependence of the energy function in the spinon Fermi surface stated studied in [76]. Figure adapted from [76].

[78], and InAs/GaSb quantum wells [79][80]. However, while these systems are technically classified as insulators (the Fermi energy lies inside an energy gap rather than inside an energy band), the charge degrees of freedom are not suppressed to the point of irrelevancy as they are in $RuCl_3$. For example, the value of the energy gaps in these systems (typically several meV) are smaller than those proposed for $RuCl_3$ (on the other of 1 eV) by multiple orders of magnitude. This detail is manifested experimentally in the fact that the oscillations in these other materials can be measured using electrical resistance. In $RuCl_3$, the charge gap is so large that electrical resistance cannot even be measured (something I have verified personally).

Because the electrical degrees of freedom are still highly relevant to these systems' physics, many of the theories that have been proposed to explain the oscillations in these systems are very different from entanglement-based phenomenology associated with quantum spin liquids. For example, many of these theories lean heavily on exciton-derived physics [81][82][83]. It seems highly unlikely that the physical mechanism at play in these materials is related to the one that produces κ_{xx} oscillations in $RuCl_3$, meaning that the latter is a truly novel phenomenon despite any superficial similarities.

2.10.1 Possible Neutral Fermi Surface in $RuCl_3$

We now discuss a few additional features revealed in this analysis that we believe are worth highlighting. First, the presence of oscillations for $\mathbf{B}$ directed within the honeycomb plane is unexpected given that $RuCl_3$ is usually treated as a quasi-2D system. This strongly suggests that the still

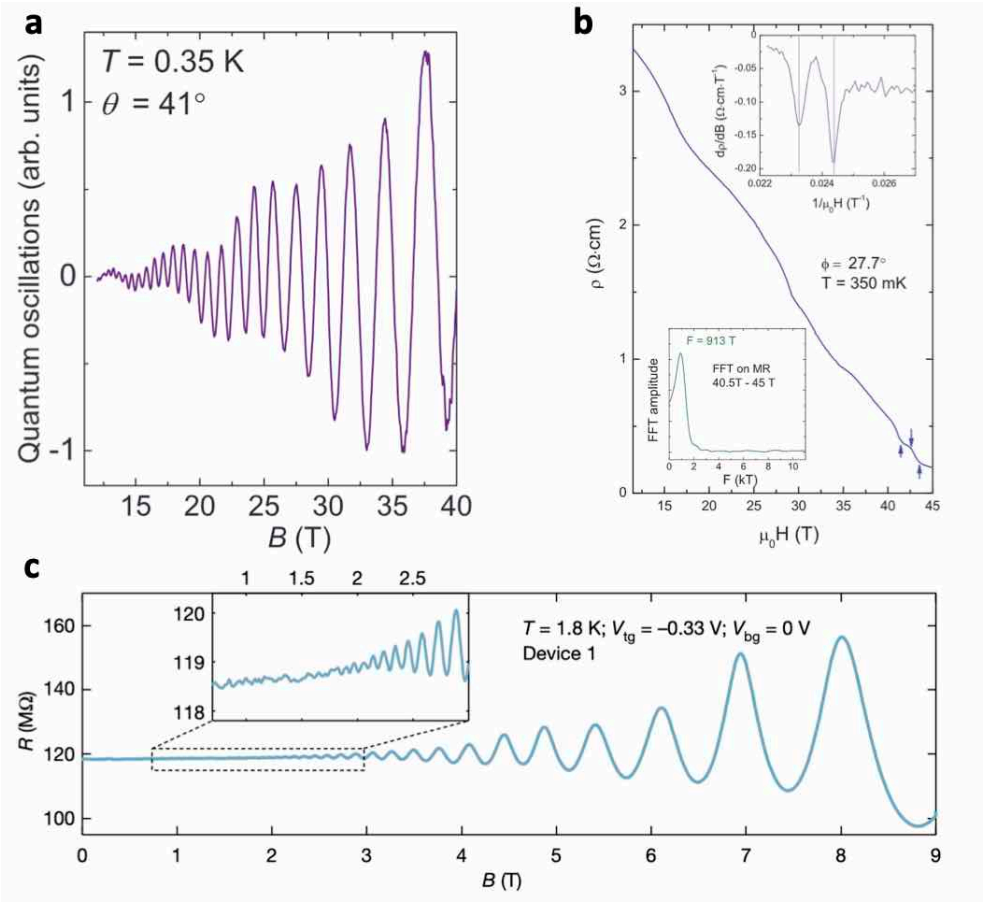

Figure 2.18: Panel (A): Strong quantum oscillations seen in electrical resistance ρ vs. B in the Kondo insulator SmB_6 [75]. Panel (B): ρ vs. B in the Kondo insulator YbB_{12} [74]. Oscillation-like features are seen at high field and are indicated with arrows. The upper right inset inset highlights the oscillations by plotting the data in derivative and Landau-like form (specifically $d\rho/dB$ vs. $1/\mu_0 H$). The bottom left inset shows the Fourier transform spectrum of the oscillation data, which reveals that 913 T is the dominant frequency. Panel (C): Apparent quantum oscillations in R vs. B seen in the supposedly insulating bulk of monolayer WTe_2 [78].

poorly-understood interlayer coupling is crucial for generating this state and its novel physics. An alternative view is that the underlying theory differs from that of the more conventional Fermi surface we have just described. Perhaps the emergent magnetic field that Landau quantizes the spinon Fermi surface points out-of-plane even though the applied field is directed in-plane. A recent theory that explores this possibility will be discussed shortly.

We would also like to stress that the indices in Fig. 2.10a have been chosen arbitrarily. Conventional quantum oscillations will cease once the system enters the lowest Landau level. However, here they stop well before the index analysis suggests they should (they do not trend towards zero). This implies that the transition to the spin-polarized state is abrupt. It could also be that the physics at play here simply differs from the more conventional description.

We now comment on some smaller features that are present in the oscillation data. Superficially, our analysis of the index plot slopes suggests that only a single Fermi surface is present. It is of course quite common in conventional metals for multiple such surfaces to exist and there is no obvious reason for this to differ for spinon Fermi surfaces. Unfortunately, the low number of oscillations that are resolved in the experiment make it difficult for analysis techniques such as a Fourier transform to be used to search for additional structure. However, the possibility of multiple pockets cannot be ruled out. One piece of evidence for this is the small additional wiggle that can be seen in a couple of the $\mathrm{d}\kappa/\mathrm{d}B$ curves (2.10b) around 0.11 T^{-1}. We observed this in Sample 3 and while we initially assumed that it was an artifact we later observed a similar feature in the Sample 1 data where $\mathbf{B}$ is directed at an angle $\theta = 39°$ away from the $\mathbf{a}$ axis. The reproducibility of this small feature suggests that it is an intrinsic effect that may originate in a more 3D Fermi surface structure. More study will be needed before any definitive statements can be made though.

A new theoretical model to explain the oscillations was recently proposed by Inti Sodemann Villadiego [84]. This theory adapts a conventional spinon fermion surface model to $RuCl_3$ by incorporating some of its unique symmetries, leading to a new type of spin liquid state he calls a

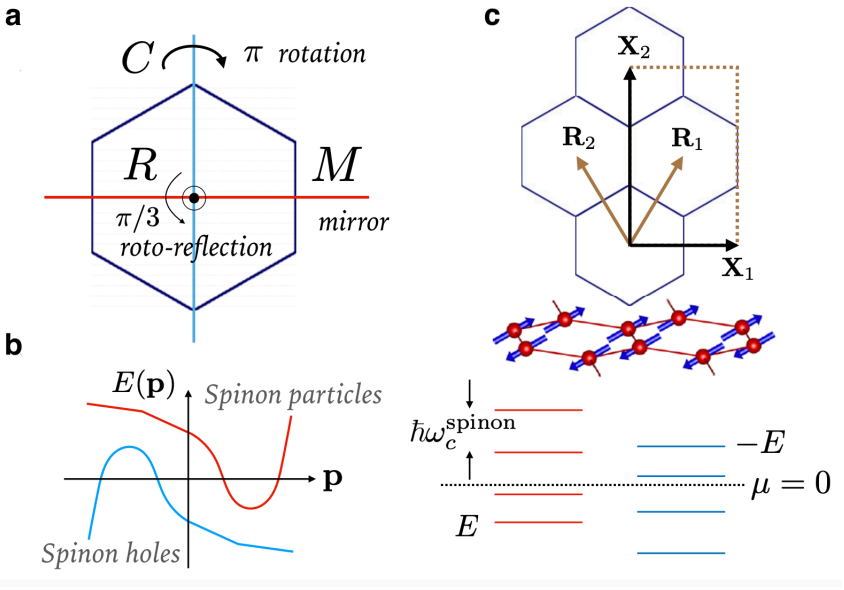

Figure 2.19: Panel (A): Sodemann Villadiego's pseudoscalar spinon Fermi surface model exploits some of $RuCl_3$'s unique point group symmetries, which are illustrated here. Panel (B): The pseudoscalar spinon Fermi surface is reminiscent of a compensated semimetal with both particle and hole-like pockets. When a magnetic field is applied, these pockets can form Landau levels (due to a second, emergent magnetic field). Panel (C): Bravais lattice vectors (labeled $\mathbf{R}_{1,2}$) for the honeycomb lattice and the magnetic Bravais vectors (labeled $\mathbf{X}_{1,2}$) for the zig-zag antiferromagnetic ordered state. Figure adapted from [84].

pseudoscalar U(1) spin liquid. We now briefly summarize this new model and how it may help explain some of $RuCl_3$'s most anomalous behaviors.

The symmetries of focus are the mirror reflection M that takes $\mathbf{b} \rightarrow -\mathbf{b}$ and the π rotation that sends $\mathbf{a} \rightarrow -\mathbf{a}$ (see Fig. 2.19). The primary novelty of this model is the nature of the emergent magnetic field that acts on the spinons to produce quantum oscillations. In a traditional spinon Fermi surface state, the emergent magnetic field is a pseudoscalar (or alternatively, a pseudovector vector pointed along the $\mathbf{c}$ axis) and the spinons experience the emergent field in the same way that electrons do a regular magnetic field. In this new theory, the emergent field is a scalar under the mirror and π-rotation symmetries. These unusual transformation laws can be reconciled with an emergent U(1) gauge structure if the spinon particle number acts as a pseudoscalar under these same symmetries (hence the name of the model). Alternatively put, these symmetries act on the spinons as particle-hole conjugation.

Extending this idea to our $RuCl_3$ thermal transport data logically leads to a physical picture like the one shown in Fig. 2.19. The spinon Fermi surface is like that of a compensated semimetal with equal populations of particle and hole-like spinon excitations. A physical magnetic field applied in-plane leads to an emergent out-of-plane field that acts to Landau quantize the spinons. Due to underlying symmetry, there will be quantum oscillations for all in-plane directions of the applied field, but there will not be a finite thermal Hall signal for $\mathbf{B} \parallel \mathbf{b}$ as is observed in our experiments (this will be discussed further in the next chapter).

Notably, the emergent magnetic field that appears in this pseudoscalar theory does not point along the same direction as the applied physical magnetic field. This would explain the seemingly 3D nature of the oscillation physics in a supposedly quasi-2D material. Other unique features of the κ_{xx} oscillation data that can be explained using this theory are the coexistence of the "mixed" phase observed for $4 < B < 7$ T (including the lower oscillation frequency) as well as the fact that no κ_{xy} signal appears for $\mathbf{B} \parallel \mathbf{b}$ even though κ_{xx} oscillations are present.

2.11 Reproducibility by Other Groups

As stated earlier, we were not the first group to attempt to measure $RuCl_3$'s B-dependent longitudinal thermal conductivity. While the novelty of our observation can be partially attributed to the lower T's in our experiments as well as the use of continuous field sweeps, we feel it is worth elaborating on the other factors that may be at play as well as the relevance of results from other groups.

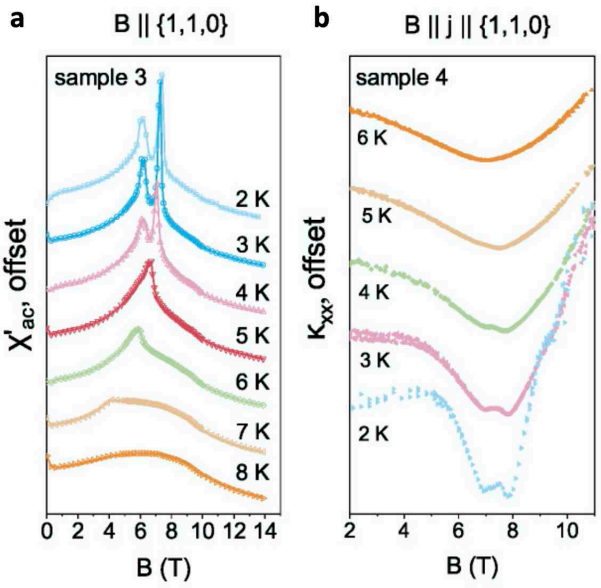

Figure 2.20: Panel (A): AC magnetic susceptibility vs. B at a series of fixed T's. Panel (B): Early measurement of $RuCl_3$'s longitudinal thermal conductivity from Balz et al. [48]. The two sharp minima at intermediate B appear to correspond to the two peaks in χ'_{ac}. This was the first measurement to show more structure than the single minimum around 7 T. Possible oscillation-like features are seen at high B. This figure is adapted from [48].

We begin with the reports that predate the posting of our manuscript [49]. The only early experiment performed at sufficiently low T and high B density to observe the κ_{xx} oscillations was the one from Leahy et al. [67] (Fig. 2.1). While it was not noticed at the time, a more thorough examination of the curve taken at 2.5 K reveals additional structure at high field that can possibly be interpreted as a weaker form of the oscillations seen in our measurements. The relative weakness of these high B features is likely due to lower sample quality (as implied by the lack of a clear maximum in κ_{xx} vs. T around 5 K). Another early κ_{xx} measurement that bears some resemblance to our data is that reported in Ref. [48] (see Fig. 2.20). Note that while this manuscript was not formally published in *Physical Review B* until 2021, the data was posted on arXiv years earlier and was shared with us before then. The curve taken at 2 K shows more structure than the single minimum observed at higher T. The double-minimum structure was interpreted as evidence of the B-induced ordered phase (often referred to as ZZ2). As discussed elsewhere in this thesis, we observe a similar effect in our data though it is not clear whether this feature is more related to the alleged phase transition, the oscillations, or some combination of the two. Additionally, it appears that some additional structure may be visible at higher B (as with Leahy et al.'s data) though the poor resolution makes it impossible to make any definitive statements about it. Note that this data was collected using a commercial thermal transport measurement setup that lacks both the precision

and accuracy that are achievable with custom systems such as ours.

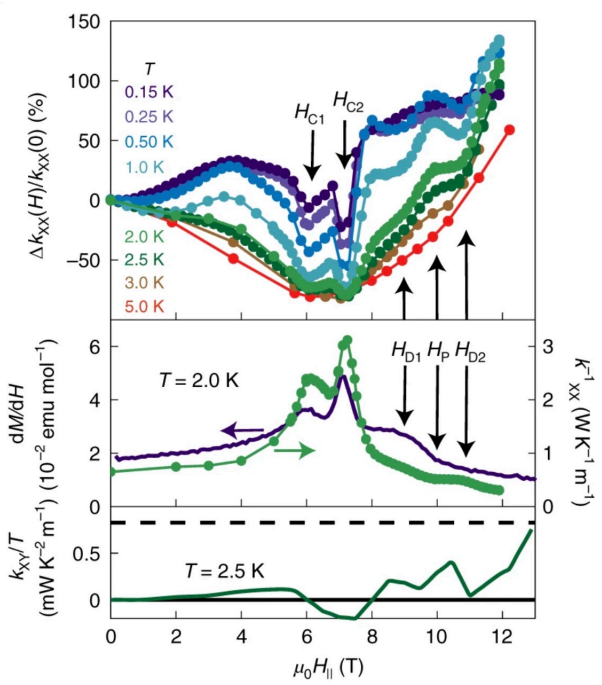

Figure 2.21: Bruin et al. have (partially) reproduced the κ_{xx} oscillations. However, they offer a different interpretation which they illustrate in this figure. The top panel shows the normalized field-dependent component of the longitudinal thermal conductivity ($\Delta\kappa_{xx}(H)/\kappa_{xx}(0)$). The middle panel shows both the field derivative of the magnetization dM/dH (left axis) as well as the thermal resistivity (labeled κ^{-1} on the right axis). The bottom panel shows the thermal Hall conductivity (κ_{xy}/T). The authors also label various anomalies at high field (H_{D1}, H_p, and H_{D2}) that they claim coincide with features in κ_{xx}. However, this correspondence is not so obvious under a more objective examination. Figure adapted from [85].

Since the publication of our report, several other groups have attempted to reproduce the findings. While it is increasingly clear that the appearance of additional features in κ_{xx} vs. T at low T is a highly ubiquitous effect, other groups have proposed alternative explanations in response to our claims. We now briefly summarize these more recent results and claims. Note that the ongoing debate over the κ_{xx} oscillations is happening in parallel with a related one regarding the system's thermal Hall conductivity. Here, we primarily focus on the oscillations and will leave a more detailed discussion of the allegedly quantized κ_{xy}/T for the next chapter. The first such report is from Bruin et al. [85]. These authors do not observe any of the low B ($B < 6$ T) features and argue that the additional structure seen at high B is related to the presence of impurities (more likely stacking faults). The relevant data from this report is shown in Fig. 2.21. The top panel shows κ_{xx} vs. B, but is plotted in a different manner from how we typically do. Instead of simply showing κ_{xx} as a function of B, they calculate the difference between κ_{xx} at a given B (hence the $\Delta\kappa_{xx}$ label)

and then divide this by the zero field value of κ_{xx}. This is done in order to more directly highlight how κ_{xx} changes with B rather than its raw value. This is not necessarily wrong (though it may highlight distortions caused by inevitable changes in T_{Sample} with B), but is mentioned to explain why the low T curves look so different from our data. In the middle panel, the authors plot the field derivative of the measured magnetization and in the bottom panel they plot κ_{xy}/T vs. B. The authors assert that the same features that appear at high B in κ_{xx} also appear in the other two measurements and that this means that all are due to impurity states for reasons that seem inspired by an early report from Kubota et al. [86]. Before we explain and respond to this logic, we would like to point out that the features in κ_{xx} simply do not line up with the weak structure seen at high B in $\mathrm{d}M/\mathrm{d}H$. The way in which the authors have added arrows to indicate otherwise is highly misleading and merits further scrutiny. Additionally, the authors are correct that the features in κ_{xx} coincide with ones seen in κ_{xy}/T. However, this is likely due to incomplete removal of hysteresis artifacts from κ_{xx} when calculating κ_{xy}, which we remind the reader is obtained from the expression $\kappa_{xy} \approx \lambda_{xy}\kappa_{xx}^2$.

In their report, Kubota et al. observed additional features in Magnetization (more specifically $\mathrm{d}M/\mathrm{d}H$) and heat capacity beyond the more ubiquitous ones associated with the ordering transition. These various anomalies are indicated with arrows in Fig. 2.22. At the time of publication, it was known that crystals frequently exhibited ordered behavior at higher T's (closer to 14 K). The authors therefore interpreted the new features seen at high field as being associated with these higher T features. More specifically, they interpreted all of these anomalies as being intrinsic phase transitions that originate from competing energy scales and use the T- and B-dependence of these anomalies to construct an elaborate phase diagram (see Fig. 2.22). As discussed in Chapter 1, it was later realized that these high T transitions are associated with stacking faults, meaning that whatever features they produce in the data are extrinsic behaviors that should not be seen in truly pure crystals. We remind the reader that the crystals being studied in 2015 were of substantially lower quality than the ones grown now, meaning that anyone attempting to use older results such as these to guide contemporary analysis should do so with tremendous caution. The authors of Ref. [86] themselves have publicly admitted that these crystals would not pass standard quality tests today. Another error we believe was made in their report was to claim that any weak feature should be interpreted as a phase transition. In many cases, this assumption represents quite a leap that lacks sufficient evidence. $RuCl_3$ is a highly complicated system so it is not surprising that its magnetism would show some additional field-dependence in thermodynamic probes. It is our view that Bruin et al. have simply taken the inappropriate assumptions and claims in this older report

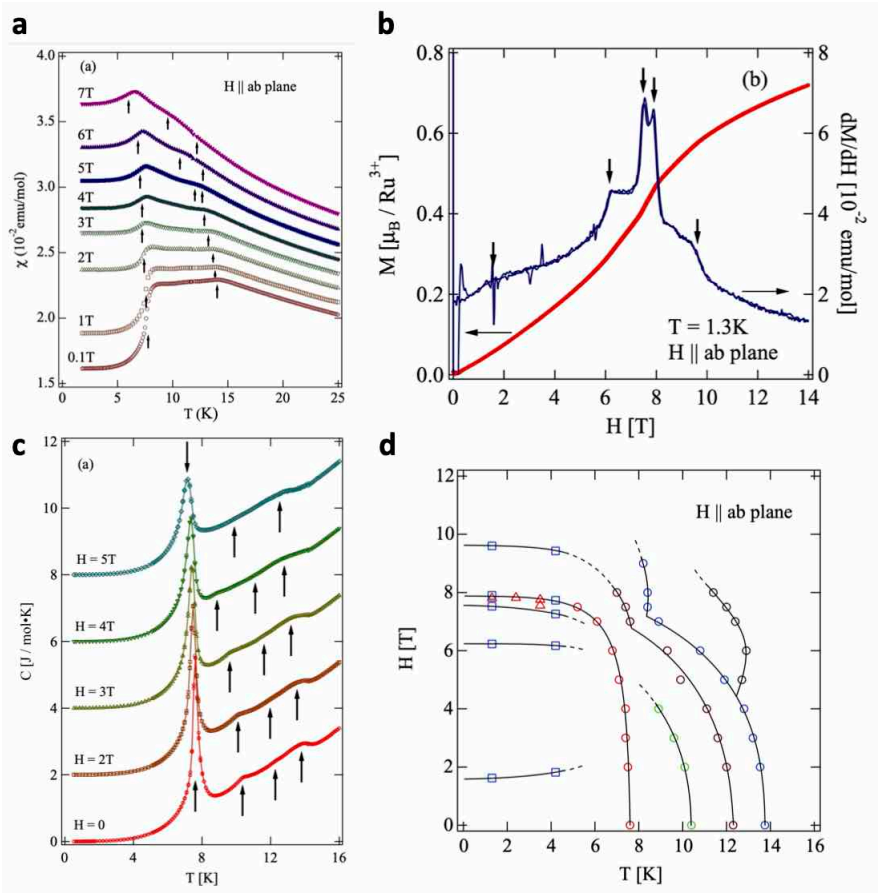

Figure 2.22: Panel (A): Magnetic Susceptibility χ vs. T for a series of fixed B. Panel (B): Magnetization vs. B (red curve and left axis) as well as its derivative $\mathrm{d}M/\mathrm{d}H$ (blue curve and right axis) measured at 1.3 K. Panel (C): Heat capacity C vs. T at several fixed B's. Various anomalies in χ, $\mathrm{d}M/\mathrm{d}H$, and C (panels (A), (B), and (C)) are indicated with arrows. Panel (D): The authors argue that all of the anomalies indicated with arrows are phase transitions, which they then track as a function of T, B and then use them to construct a phase diagram. Note that **B** is directed in-plane, but no effort was made to apply it along any specific axis (such as **a** or **b**). Figure adapted from [86].

and extended them to our data and (somewhat puzzling) their own to argue that any features at high B (in basically any measurement) should be interpreted as indicators of poor sample quality. Under this assumption, the huge oscillations seen in κ_{xx} should be seen as physically equivalent to the weak shoulder-like feature in $\mathrm{d}M/\mathrm{d}H$ despite the substantially different intensities of the two effects and the fact that they do not occur at the same B values.

The other major recent report that presents an alternative interpretation of the κ_{xx} oscillations in $RuCl_3$ is from Suetsugu et al. [87]. Like Bruin et al., they find that additional features appear at high B, but not at low B (though one could argue that they are weakly present in the curve taken at 1 K). However, the authors of this report provide a somewhat different explanation for these

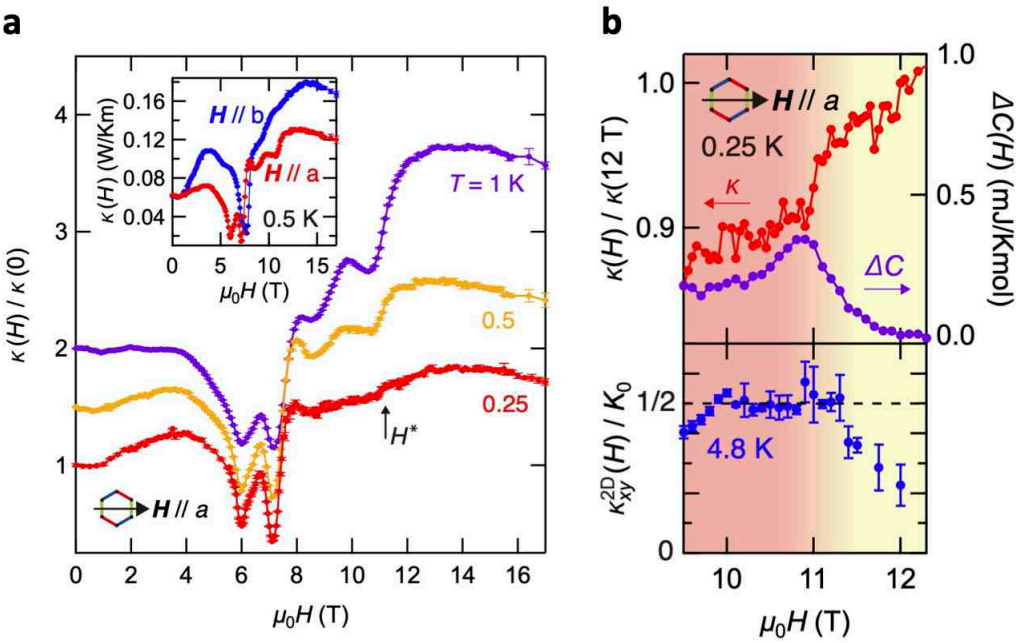

Figure 2.23: Panel (A): Normalized longitudinal thermal conductivity ($\kappa_{xx}(H)/\kappa_{xx}(0)$) vs. magnetic field at 0.25, 0.5, and 1.0 K for $\mathbf{H} \parallel \mathbf{a}$. Suetsugu et al. observe features at high field that strongly resemble the oscillations in our data (though they significantly decrease in intensity at low temperature). The inset compares the normalized κ_{xx} for $\mathbf{H} \parallel \mathbf{a}$ and $\mathbf{H} \parallel \mathbf{b}$, both at 0.5 K. Panel (B): The longitudinal thermal conductivity (now normalized using the value at 12 T, not 0 T) is compared with the estimated magnetic heat capacity ΔC, and the thermal Hall conductivity (in units of the quantum of thermal conductance K_0). Quantization is allegedly lost at the same field where κ exhibits a sudden increase and ΔC peaks. Figures adapted from [87].

features. They argue that these are intrinsic features and are not caused by impurities as suggested by Bruin et al. [85]. The higher B feature around 11 T is the primary focus of the paper for reasons that we now describe. Representative data is shown in Fig. 2.23. Fig. 2.23a shows κ_{xx} vs. B taken at three different T's: 0.25 K, 0.5 K, and 1.0 K ($\mathbf{B} \parallel \mathbf{a}$ for all three curves). Note that this data has been normalized such that the plotted data is the value of κ_{xx} at the given B divided by the zero field value. The inset compares results obtained for $\mathbf{B} \parallel \mathbf{a}$ and for $\mathbf{B} \parallel \mathbf{b}$ ($T = 0.5$ K for both). The high B features are weaker when $\mathbf{B} \parallel \mathbf{b}$. κ_{xx} is also higher than what is seen when $\mathbf{B} \parallel \mathbf{a}$. Fig. 2.23b compares the normalized κ_{xx} measured with the extracted value of the magnetic heat capacity (defined as $\Delta C(H) = C(H) - C(12T)$) and the alleged half-integer quantized κ_{xy}, all measured in the same crystal. Note that ΔC and κ_{xx} are measured at 0.25 K while κ_{xy} is measured at 4.8 K (though it is not entirely clear what exactly these T values refer to). The authors observe that κ_{xx} exhibits a step-like increase and ΔC exhibits a peak at the same B (approximately 11 T) where κ_{xy} begins to deviate from its quantized value. They then claim that this implies that there is a first order (topological) phase transition at 11 T. Reasons for skepticism include the drastically higher T

of the κ_{xy} measurement and the fact that a peak in C is expected to accompany a minima in κ_{xx} as the former will likely lead to enhanced phonon scattering.

Suetsugu et al. also comment on features seen at other fields. Like us, they observe another local minimum closer to 8.5 T. The authors speculate that this feature may be due to short range antiferromagnetic order and point to some older reports where anomalous features appear in the B-dependence of various physical properties of other quantum magnets [88][89]. However, they do not offer any evidence other than superficial similarities and the issue is mostly ignored. We would also like to highlight that the authors place significant weight on the κ_{xx} feature at 11 T being a phase transition, but then claim that the one at 8.5 T is not. It is not at all obvious why these two anomalies would have such different origins. Another feature in their data that differs from ours is the behavior of κ_{xx} vs. B at the highest fields measured. We remind the reader that we consistently observe a perfectly flat profile in this field range ($B > 11$ T for $T < 1$ K) and that this can be explained by the absence of thermally available phonon-scattering spin excitations in the spin-polarized phase. The Kyoto group instead observes a gradual suppression of κ_{xx} that continues up to the highest B's measured. The authors use this detail to argue that the system does not transition to a spin-polarized phase around 11 T, but actually remains in a spin liquid phase for all fields measured. This claim is in stark contrast with prior studies of $RuCl_3$. We believe that this discrepancy can possibly be explained by improper thermometer calibration. As discussed in Chapter 1, the thermometers used for these experiments are thin film resistors. These resistors can (and do) exhibit magnetoresistance (MR) that can be substantial at low T and can lead to substantial distortions of the calculated thermal transport quantities if not accounted for correctly. The Kyoto group has yet to state publicly how they account for thermometer MR so it is impossible to say for sure whether or not field-calibration is being done correctly. We remind the reader that the method employed by our group has been discussed in great detail in [66]. We will note; however, that the Kyoto group has previously admitted to using Cernox thermometers in these experiments [60][73] and that these thermometers can exhibit enormous (and anomalously B-antisymmetric) MR at low T [66]. This detail provides another reason for skepticism.

Finally, we briefly comment on one similarity between the reports from Bruin et al. [85] and Suetsugu et al. [87]. Both groups find that the amplitude of the κ_{xx} features (other than the ones around 6 and 7 T) actually decrease with T. These experiments go down to lower temperatures than is possible with our thermal transport setup (such low temperatures require a dilution refrigerator while our setup uses a ^{3}He cryostat). Because of this, I am unable to say definitively whether we observe the same effect. Interestingly, it was recently suggested that the spinon Fermi state may be

unstable to non-entangled states at low temperature due to nesting instabilities of the Fermi surface [90]. This would be a somewhat exotic mechanism for the decreasing amplitude. It could also simply be that the spin-phonon coupling becomes too weak to substantially affect phonon transport at low T.

We close this section by noting that while our interpretations of certain aspects of $RuCl_3$'s thermal transport physics may differ from those of other groups, the fundamental effect at the heart of our report [49] has now been reproduced [85][87]. Efforts to reconcile smaller differences between our results and those of other groups are now focusing on sample differences rather than experimental procedures.

2.12 Alternative Explanations

We now discuss a few other recent reports that, while not directly related, could help to guide future investigation of $RuCl_3$ and are therefore worthy of mention. One interesting possibility that has not been explored is that the oscillations arise from some kind of collective mode rather than the individual quasiparticles. Such an effect was recently observed in the Weyl semimetal TaAs [91][92]. Specifically, the large κ_{xx} oscillations in TaAs arise from chiral plasmon-like collective modes made

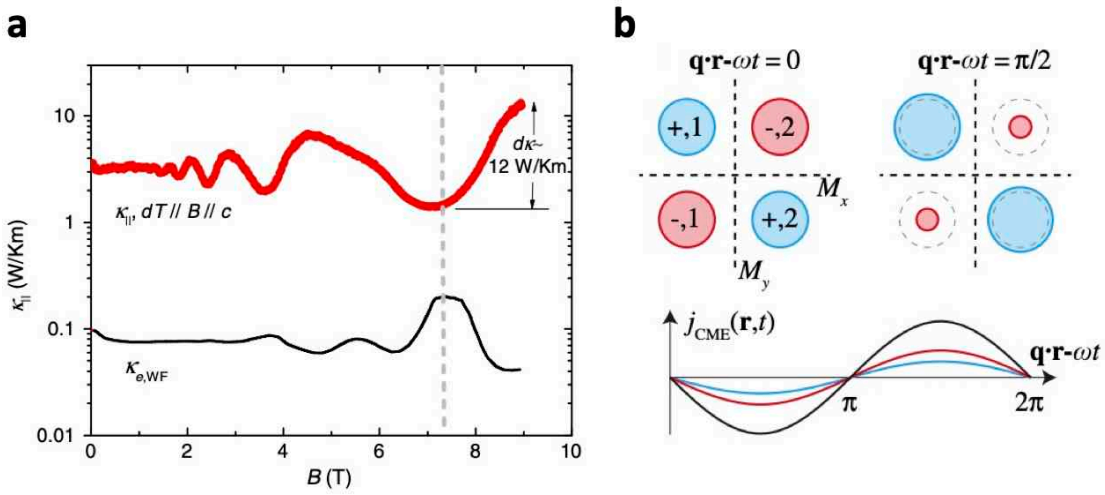

Figure 2.24: Panel (A): The longitudinal thermal conductivity, κ_{xx}, as a function of magnetic field. The red curve shows shows the full value measured in the experiment while the black curve is the electronic component estimated from the Wiedemann–Franz law. **B** is applied parallel to the measured temperature gradient to excite chiral anomaly physics. The fact that the electronic component is out of phase with the full κ_{xx} is suggestive of another significant contribution. Panel (B): The large, non-electronic component of the κ_{xx} oscillations results from collective modes made up of Weyl fermions in pockets of different chiralities. Panel (A) is adapted from [91] and Panel (B) is adapted from [92].

up of the Weyl fermions in the material. The nature of this effect is depicted in Fig. 2.24. Fig. 2.24a shows both the full thermal conductivity as well as the electronic contribution (TaAs is a metal, not an insulator) estimated via the Wiedemann–Franz law ($\kappa = LT\sigma$ where L is the Lorenz number $L = 2.44 \times 10^{-8} V^2 K^{-2}$ and σ is the electrical conductivity) [93]. The separate contribution of the zero sound mode is evidenced by the fact that the total κ_{xx} and the estimated electronic component are out of phase. Fig. 2.24b illustrates how the zero sound mode arises from the collective oscillations of the density of Weyl fermions at the various Weyl points.

We now comment on a few other similar effects that have been identified in the theory literature. One example comes from the work of Takikawa et al. [25]. As discussed earlier, Kitaev's original model is only exactly solvable in the so-called "pure" limit, meaning that the Kitaev exchange interaction is the only term in the Hamiltonian. Even the applied magnetic field can only be incorporated via perturbation theory. In their paper, Takikawa et al. extend Kitaev's perturbation analysis to include other magnetic exchange terms, namely the off-diagonal exchange interactions (the Γ and Γ' terms in Eq. 1.24). They find that these other terms should produce several important effects. One is that these other terms should increase the size of the bulk Majorana energy gap, which would make the alleged quantized κ_{xy}/T visible up to higher temperatures (as quantization will be lost once bulk carriers are excited). The second effect is intriguingly similar to what we observe in our experiment. They find that the coexistence of the Kitaev spin liquid state with the zig-zag AFM ordered phase should produce an emergent internal magnetic field and cause the Majorana fermions to form a Fermi surface of finite area (as opposed to the Dirac-type point like Fermi surface in the pure model). As explained earlier, a finite Fermi surface area is necessary for quantum oscillations to appear so Takikawa's model therefore presented a new way in which such a state could be generated in the Kitaev honeycomb model, which is typically associated with a different genre of spin liquid phenomenology (underlying gauge theory is of $\mathbb{Z}_2$ rather than U(1) type). Additionally, the existence of a mixed phase (evidenced by weak κ_{xx} oscillations for $4 < B < 7$ T) is one of the key observations in our report and it is notable that Takikawa's theory places this feature at the heart of the model. We also note that a subsequent report [94] clarified that the emergence of a finite chemical potential (and corresponding Fermi surface) is possibly a more ubiquitous effect. Specifically, any inversion symmetry breaking in the Kitaev spin liquid phase should produce this phenomenon, not only the coexistence with the QSL state of one with magnetic order. $RuCl_3$ is a highly complicated material so there are numerous potential avenues by which inversion symmetry breaking could arise. In particular, Chari et al. propose that electrical fields be used to generate and tune the Fermi surface state. This could be a promising avenue of study for monolayer $RuCl_3$ crystals.

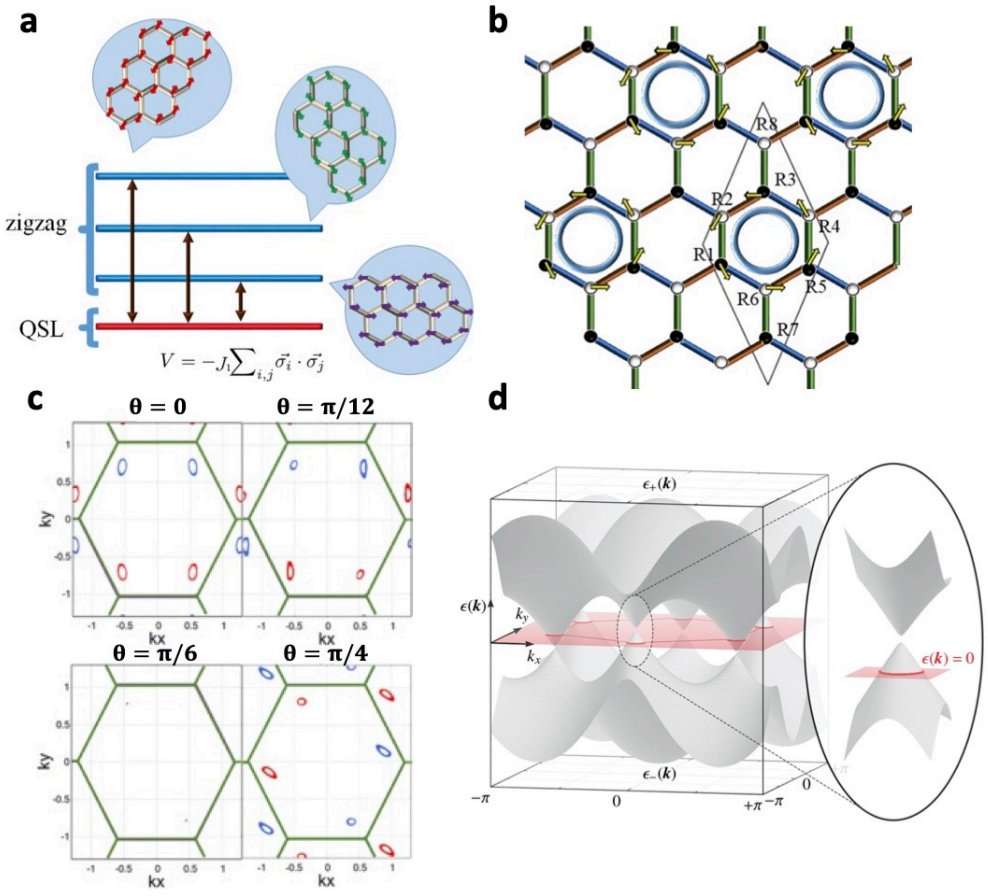

Figure 2.25: Panel (A): The coexistence of a Kitaev Spin Liquid state with various zig-zag antiferromagnet configurations is necessary for stabilizing the Majorana Fermi surface state in Takikawa et al.'s model [25]. Panel (B): The coexistence of spin liquid and ordered phases can give rise to an internal magnetic field via the depicted mechanism. Panel (C): The Majorana fermions form Fermi surfaces with the exact configuration changing with the direction of the applied field. Here, the magnetic field is defined as $\mathbf{H} = H(cos(\theta), sin(\theta))$ where θ is the angle of the applied $\mathbf{H}$ relative to the $\mathbf{a}$ axis. Panel (D): Depiction of how the emergence of a Fermi surface of finite area results from Dirac-type point shifting either up or down in energy depending on the specific pocket in k-space. Panels (A), (B), and (C) are adapted from [25] and Panel (D) is adapted from [94].

We also note that a the U(1) QSL state possibly implied by our results is not entirely divorced from the Kitaev spin liquid phenomenology despite the highly different gauge theory description. In fact, it has been pointed out in several theoretical studies that an external magnetic field could in fact cause a KSL state to transform into a more traditional spinon Fermi surface one [95][96][97], though the mechanism by which this occurs is not as clear in these reports as in the one from Takikawa et al. [25]. This possibility therefore merits further theoretical as well as experimental exploration.

Finally, we note that other mechanisms for Landau-level like states in insulators have been proposed. These include strain-induced Landau levels [98] as well as the exciton-based the theories

that have been proposed for the oscillation-exhibiting Kondo insulator systems discussed earlier [81][82][83].

Chapter 3

Thermal Hall Conductivity of $RuCl_3$

This chapter discusses my measurements of $RuCl_3$'s thermal Hall conductivity. The presented results are primarily from [99] with some additional κ_{xy} data from [49].

3.1 Thermal Hall Effect in Magnetic Insulators

The electrical Hall effect in conductors was first discovered by Edwin Hall in 1879 is still used as materials characterization tool today. The effect can generally be understood as the result of a Lorentz-type force on the charge carriers. While measurements typically focus on charge degrees of freedom, a thermal analogue (the thermal Hall effect) can be measured as well. The measurement is not often done as it is notoriously challenging (for the reasons discussed in Chapter 1) and does not typically provide new information beyond what can be learned from electrical transport (with some notable exceptions [100][61]). However, thermal Hall experiments can be a powerful tool for studying insulators where electrical measurements are not possible.

It is not immediately obvious why a material with no charge carriers would exhibit a Hall effect as the excitations are unable to exhibit a Lorentz force. However, other possible mechanisms for the effect do exist. It can occur if the excitations possess some intrinsic chirality (such as chiral edge states) or Berry curvature. Of course, due to bulk-boundary correspondence, these two characteristics are not mutually exclusive, but are listed separately here as they usually associated with different types of systems in practice.

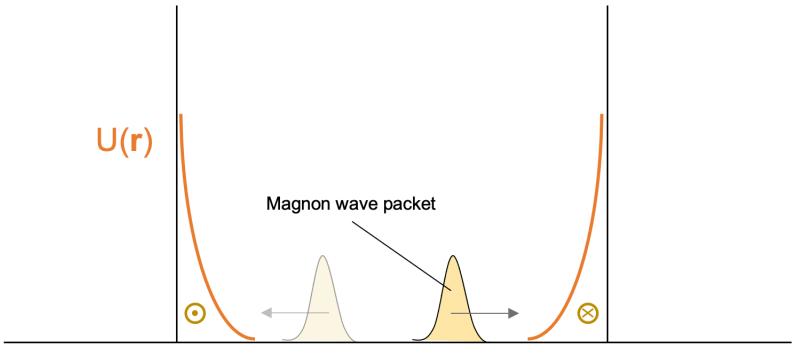

Figure 3.1: The edge potential $U(\mathbf{r})$ will cause the magnon wave packet to circulate around the edge of the sample.

The Berry curvature mechanism in magnetic insulators is a more recent development and offers a more general approach. A quantitative theory for this effect was first proposed by Katsura et al. [101], but was later corrected and expanded upon by Matsumoto and Murakami [102], [103], [104], [105]. We now provide a brief overview of this theory. We consider a wave-packet subject to Berry curvature $\mathbf{\Omega}(\mathbf{k})$ and the force $-\nabla U$ exerted by the wall potential $U(\mathbf{r})$ [105]. The semiclassical equations of motion are:

$$\dot{\mathbf{r}} = \frac{1}{\hbar}\frac{\partial \epsilon_{n,\mathbf{k}}}{\partial \mathbf{k}} - \dot{\mathbf{k}} \times \Omega(\mathbf{k}) \tag{3.1}$$

$$\hbar\dot{\mathbf{k}} = \nabla U(\mathbf{r}) \tag{3.2}$$

The anomalous velocity $\mathbf{v}_A = -\nabla U \times \mathbf{\Omega}(\mathbf{k})$ drives a circulating thermal current around the edges. A thermal gradient $-\nabla T \parallel \hat{\mathbf{x}}$ unbalances the excitation density between the warm and cool edges ($\parallel \hat{\mathbf{y}}$), which leads to a net thermal current $\mathbf{J}_\mathrm{Q} \parallel \hat{\mathbf{y}}$. Crucially, the reversal of $\mathbf{\Omega}$ induced by reversing $\mathbf{B}$ leads to an Onsager planar thermal Hall current. One then finds that the thermal Hall conductivity κ_{xy} can be calculated (see [66][105] for details) as a weighted sum of the Berry curvature $\Omega_{n,z}(\mathbf{k})$ throughout the Brillouin zone:

$$\kappa_{xy} = \frac{k_B^2 T}{\hbar V}\sum_{n,\mathbf{k}} c_2\left(\rho^B(\epsilon_{n,\mathbf{k}})\right)\Omega_{n,z}(\mathbf{k}) \tag{3.3}$$

where the weighting factor c_2 is a function of the boson distribution function ρ^B and will be discussed in greater detail later. An analogy to the more familiar electrical anomalous Hall effect is made clear by the form of Eq. 3.3 [106].

The first observation of a κ_{xy} signal in an insulator was reported by Onose et al. [107] who found

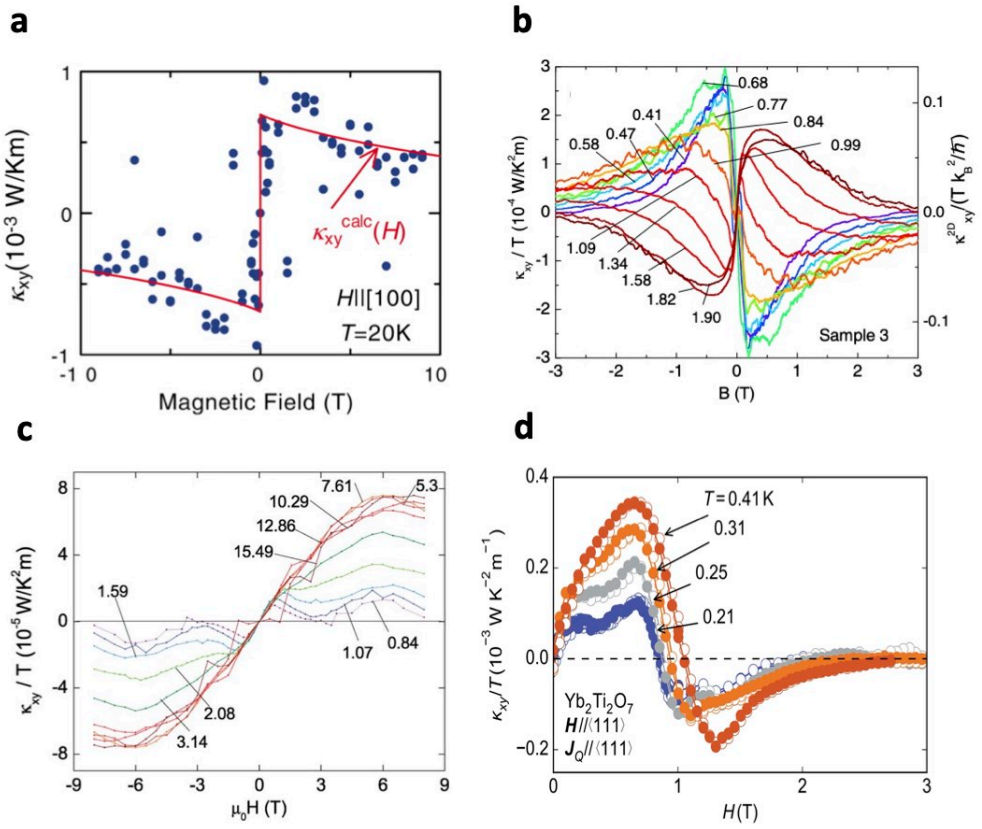

Figure 3.2: Thermal Hall conductivity vs. field measured in $Lu_2V_2O_7$ (Panel (A)) [107], Cu(1-3, bdc) (Panel (B)) [108], $Tb_2Ti_2O_7$ (Panel (C)) [109], $Yb_2Ti_2O_7$ (Panel (D)) [110].

that the pyrochlore ferromagnet $Lu_2V_2O_7$ exhibited the effect within its ordered state ($T < T_C$). This effect was attributed to a sizable Dzyaloshinskii–Moriya interaction as well as the unique symmetries of the pyrochlore lattice. Hirschberger et al. subsequently observed nonzero κ_{xy} signals in $Tb_2Ti_2O_7$ (a nonmagnetic pyrochlore material with evidence of spin liquid physics) [109], Cu(1-3, bdc) (a Kagome ferromagnet where κ_{xy} was observed both above and below T_C) [108], and $Yb_2Ti_2O_7$ (another pyrochlore system where a record thermal Hall angle of 2% was reported) [110]. There have also been reports of nonzero κ_{xy} in $RuCl_3$ for $\mathbf{B} \parallel \mathbf{c}$ [111][112][113] (as well as an attempt to model the effect [114]). Note that the fields used in these experiments are not strong enough to destroy the magnetic order so they are only able to probe the zig-zag AFM ordered state, not the potential field-induced spin liquid.

Finally, we note that other mechanisms for the thermal Hall effect in insulators have also been proposed. It has been argued that a more Lorentz-like effect may occur for fermionic excitations in quantum spin liquids [101][115]. Additionally, it has recently been suggested that the phonon thermal Hall effect may be capable of producing very large κ_{xy} values[116] [117][118][119].

3.2 Alleged Quantization of κ_{xy}/T

As discussed in Chapter 1, one of the most attractive features of Kitaev's model is that there exists a clear smoking gun for its exotic excitations, something that is not the case for most spin liquids. That smoking gun is a half-integer quantized thermal Hall conductivity. More specifically, κ_{xy}/T should equal exactly 1/2 of the quantum of thermal conductance K_0. That specific signal was reported for $RuCl_3$ by the Kyoto group first for diagonal fields (45° and 30° degrees out-of-plane) [60] and later for an in-plane field [73] (discussed in next section). The effect has yet to be convincingly reproduced (although some have claimed to [120] [85]).

In our earlier report [49], we observed that κ_{xy}/T was lower than the predicted quantized value, but was still clearly nonzero. Additionally, the signal was strongly temperature-dependent, which is

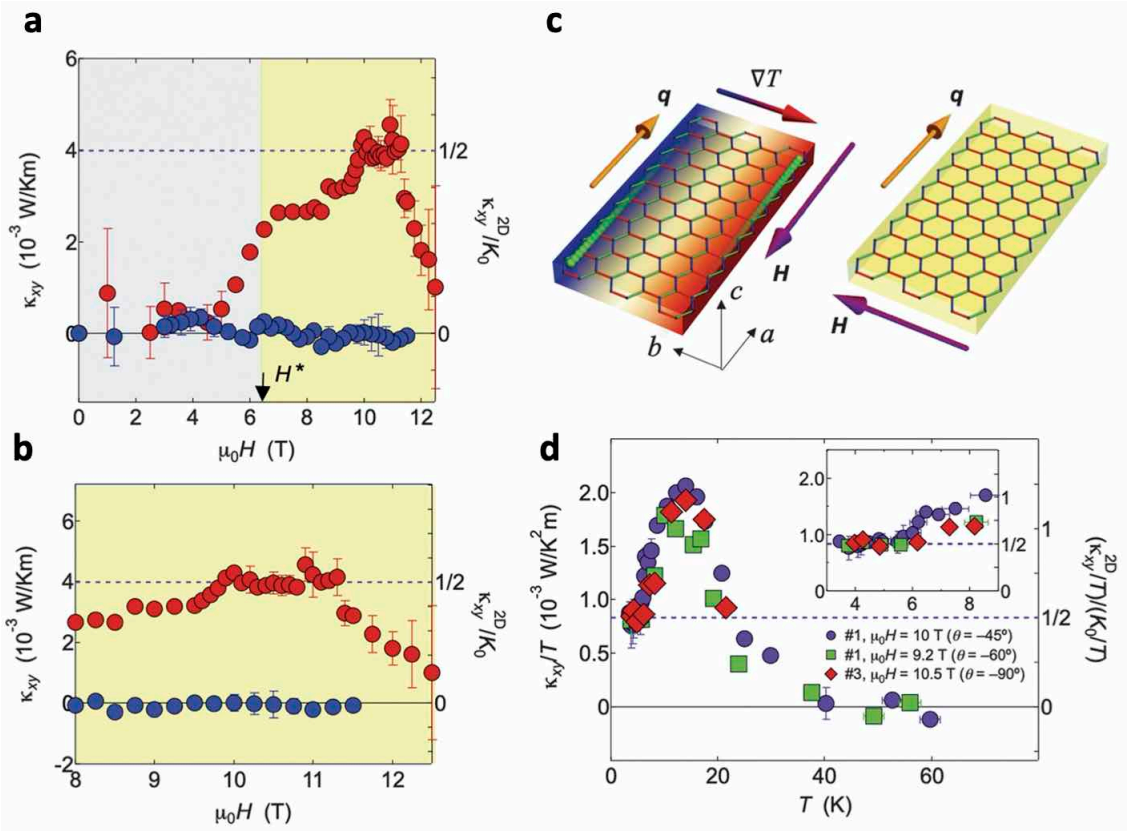

Figure 3.3: Panel (A): Thermal Hall conductivity κ_{xy} vs. B measured at 4.8 K. The measurement is done for both $\mathbf{H} \parallel \mathbf{a}$ (red) and $\mathbf{H} \parallel \mathbf{a}$ (blue). A finite and quantized signal is seen in for the former while no signal is observed for the latter. Panel (B) shows the same data, but focuses only on the narrow field range where a signal is observed. Panel (C): Physical depiction of how the applied $\mathbf{H}$ and heat current $\mathbf{q}$ (as well as the resulting thermal Hall temperature gradient ∇T) are oriented relative to the honeycomb lattice. Panel (D): κ_{xy}/T vs. T for three different $\mathbf{B}$ orientations. The inset focuses only on the narrow T range where quantization is claimed to be observed. This figure is adapted from [107].

inconsistent with a signal derived from fermionic edge states.

One source of skepticism of the alleged quantization is the fact that the Kyoto group only claims to observe quantization within a narrow temperature range around 3-5 K (as shown in Fig. 3.3). κ_{xy}/T increasing beyond its quantized value for $T > 5$ K can be explained by thermal excitation of gapped bulk excitations, but the question of what exactly happens below 3 K is more mysterious. At present, the Kyoto group has shown no κ_{xy} data for $T < 3$ K, which has led the QSL community to believe the signal either vanishes or is no longer quantized at low T. This led two groups of theorists to propose distinct, but ultimately very similar models for why κ_{xy}/T would only exhibit quantization within a narrow temperature window [122] [121]. Fig. 3.4 provides an illustration of the underlying physical picture in these two theories. The key idea is that strong thermal coupling between the spin-derived chiral edge modes and phonon-dominated bulk is necessary for the observation of a half-integer quantized κ_{xy}/T. In fact, the model from which the prediction of quantized κ_{xy}/T appears actually breaks down in real materials due to the presence of bulk phonons. However, the authors find that if the phonons are able to thermally couple to chiral Majorana edge modes, then this quantization is restored. Notably, this restoration only happens if the gapless spin excitations are restricted to exist only at the edge of the sample. If any exist in the bulk, then quantized κ_{xy}/T will not be observed. The reason this model predicts a finite T window where $\kappa_{xy}/T = \frac{1}{2}K_0/T$ is that the strength of the Majorana-phonon thermal coupling should be strongly T-dependent. As T decreases the coupling should eventually become so weak that spins and phonons are no longer able to fully thermalize and the quantization should break down in some nonuniversal sample-dependent fashion. Quantization is lost at high T because the gapped Majorana fermions in the bulk are able

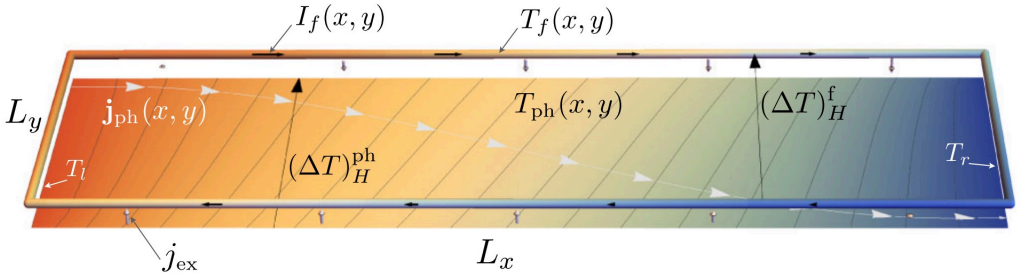

Figure 3.4: Illustration of Ye et al.'s [121] model for spin-phonon coupling-induced quantized thermal Hall effect in bulk Kitaev materials. Heat is allowed to conduct via phonons in the bulk and the chiral Majorana states at the edges. The phonons and Majorana fermions can have different temperatures (labeled T_{ph} and T_f). Quantization should only be observed when the phonons and the fermions fully thermalize. L_x and L_y refer to sample dimensions, I_f is the heat current in the Majorana edge mode at a given point, j_{ph} is the phonon heat current density through the bulk. j_{ex} is the heat current density exchanged between the bulk phonons and edge fermions. T_l and T_r are the temperatures on the left and right sides of the sample depicted here. Figure adapted from [121].

to be thermally excited. We again stress that the low T breakdown has not actually been definitively observed (we disagree with Bruin et al.'s interpretation of their data [85], which will be discussed later). Regardless of whether these theories ultimately prove useful for $RuCl_3$, they do present several important questions regarding spin-phonon thermalisation that have been largely overlooked historically.

3.3 Field-angle Dependence of Thermal Hall Conductivity

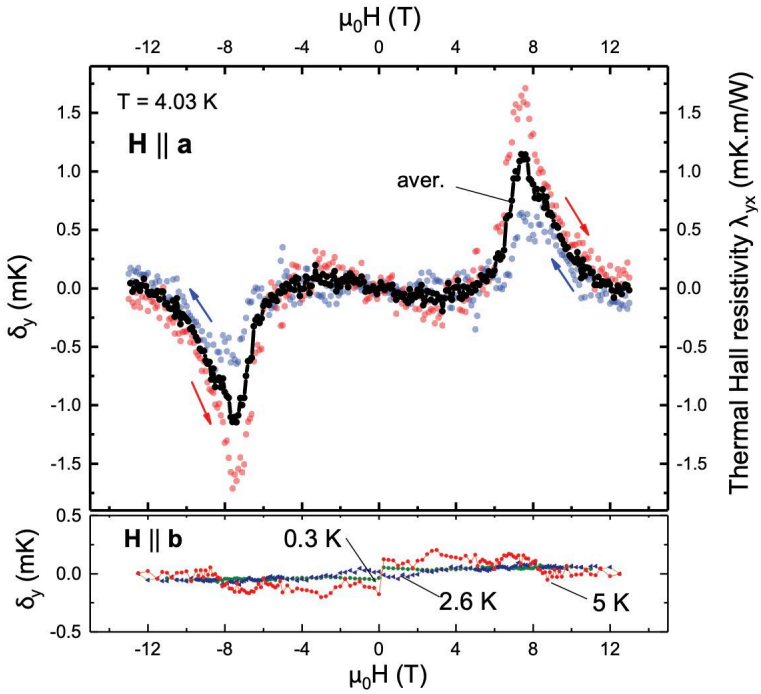

Figure 3.5: The top panel shows the field-antisymmetrized transverse temperature gradient δ_y for a pair of field sweeps measured at $T_{Sample} = 4.03$ K for $\mathbf{H} \parallel \mathbf{a}$. The "upsweep" (negative to positive field) is shown in red, the "downsweep" (positive to negative field) is shown in blue, and their average is shown in black. The difference between the two directions is due to the anomalous field-induced hysteresis seen in thermal transport. The large size of the averaged signal indicates that the effect is a true Hall effect. The appropriate units for thermal Hall resistivity λ_{xy} are shown on the right axis. The bottom panel shows averaged (average of upsweeps and downsweeps) curves at a series of temperatures for $\mathbf{B} \parallel \mathbf{b}$. The δ_y signals are substantially smaller and any finite signal that remains is likely due to experimental error. The observation of a true Hall signal for $\mathbf{H} \parallel \mathbf{a}$, but not for $\mathbf{H} \parallel \mathbf{b}$ is qualitatively consistent with Yokoi et al.'s report [73] as well as the original prediction in Kitaev's model [8]. Figure adapted from [49].

Interestingly, we did observe a qualitatively similar field-angle dependence to that observed by Yokoi et al. We found that a nonzero κ_{xy}/T is observed for $\mathbf{B} \parallel a$, but not for $\mathbf{B} \parallel b$. This (combined with the fact that the effect is observed at all for an entirely in-plane field) was initially interpreted

as a smoking gun for Majorana fermion edge states whose topological characteristics are expected to obey these symmetry rules.

This prediction comes from Kitaev's original paper [8]. In chapter 1, we showed the the Chern number $\mathcal{C}$ in the pure Kitaev model should have the following form:

$$\mathcal{C} = sgn(h_x h_y h_z) \tag{3.4}$$

where h_x, h_y, h_z and refer to the Kitaev axes, not the Cartesian directions. This is in contrast with the typical expectation, which would should have a form such as $\mathcal{C} = sgn(h_x + h_y + h_z)$ where the direction of the out-of-plane component of the applied $\mathbf{H}$ dictates the sign of $\mathcal{C}$. A depiction of how $\mathcal{C}$ varies with the angle of the applied field is shown in Fig. 3.6. $\mathcal{C} = 0$ when the field projection along any of the three Kitaev axes is zero. If $\mathcal{C} = 0$, the Majorana spectrum will remain gapless and

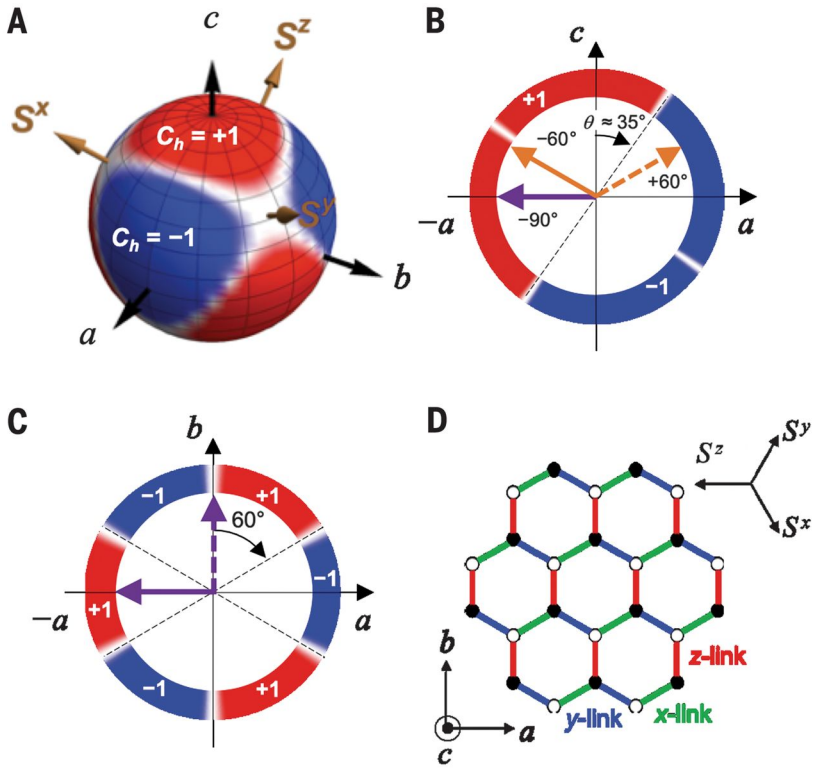

Figure 3.6: Field angle dependence of the Chern number $\mathcal{C}(\mathbf{H})$ in the pure Kitaev model. Panel (A): Spherical graphic showing $\mathcal{C}(\mathbf{H})$ in 3D. The Kitaev spin axes S_x, S_y, and S_z are also shown. If the projection of the field along any one of these three axes is zero, the Chern number will also be zero. Panel (B): $\mathcal{C}$ as a function of field angle within the a-c crystal plane. The $\mathcal{C}$ sign change illustrated here is the reason for the κ_{xy} sign change observed in Fig. 3.7. Panel (C): Field angle-dependence of $\mathcal{C}$ within the a-b plane. Note that $\mathcal{C} = 0$ when $\mathbf{H} \parallel \mathbf{b}$. Panel (D): Illustration of how the a, b, and c axes (and the Kitaev axes S_x, S_y, and S_z) are defined relative to the honeycomb lattice. Note that the Kitaev spin axes are directed partially out-of-plane. Figure adapted from [73].

the system will not acquire the nontrivial topology necessary for producing a thermal Hall effect. The angles for which this is the case are shown in white in Fig. 3.6a where the red and blue regions correspond to angles with $\mathcal{C} \pm 1$. The reason for the anisotropy demonstrated in Fig. 3.5 can be seen more explicitly by reexpressing the monoclinic directions (**a** and **b**) in terms of the Kitaev spin axes. One then finds that the **a** direction is equivalent to the Kitaev [1 1 $\overline{2}$] and the **b** direction is equivalent to the Kitaev [$\overline{1}$ 1 0] (or their symmetry equivalents). In this notation, applying **H** along **b** (the honeycomb armchair direction) will always have a projection value of 0 along one of the Kitaev spin axes ($h_z = 0$ in the example).

One physically intuitive way to understand this is that the finite Chern number (and ultimate) thermal Hall conductivity are fundamentally derived from edge states, not orbital physics as would be the case in the quantum Hall effect. This is why an out-of plane field is not necessary. However, we emphasize that, despite the intuitive physical picture behind this, a true (or Onsager) type planar Hall effect is highly unusual phenomenon. At present, the only other known example of a material capable of exhibiting such a behavior is the topological semimetal $ZrTe_5$ [123] (though in that case it is an electrical rather than thermal Hall effect).

A more rigorous test of the field angle dependence for $\mathcal{C}$ was done by Yokoi et al. [73] and is

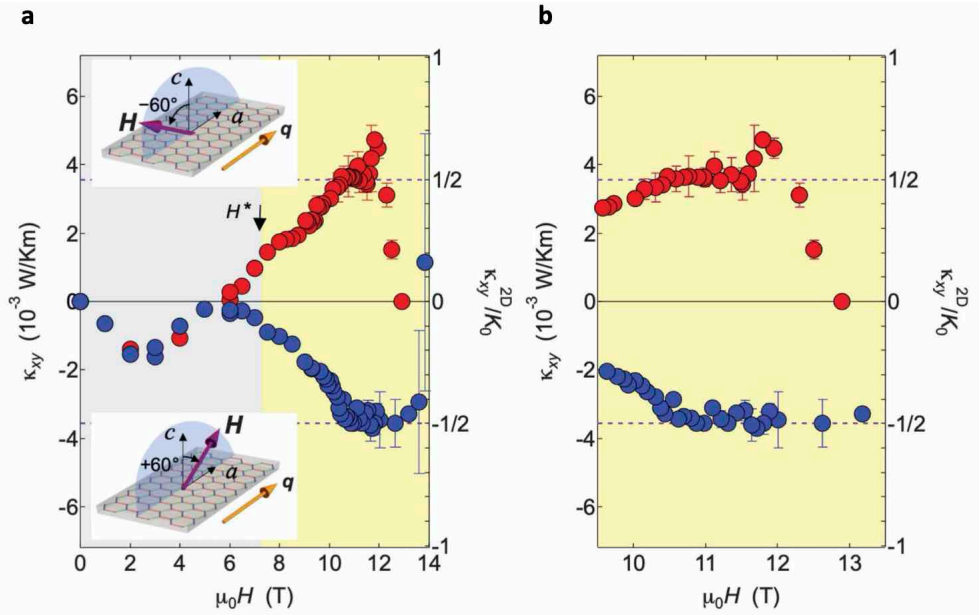

Figure 3.7: Panel (A): thermal Hall conductivity κ_{xy} vs. B for two different field orientations (θ = +60° and θ = -60° relative to the **c** axis). The high field signal changes sign between the two different orientations while the low field signal does not. Panel (B): The high field portion of the data shown in the previous panel is shown in greater detail to emphasize that the value of κ_{xy} in the spin liquid phase is equal to the quantized value (emphasizing that the Chern number $\mathcal{C} = \pm 1/2$). Note that T = 4.3 K and $\mathbf{H}_{\parallel} \parallel \mathbf{a}$. Figure adapted from [73].

shown in Fig. 3.7. According to Eq. 3.4, $\mathcal{C}$ should be able to exhibit a sign change without changing the out-of-plane component of the applied field. For example, if one measures κ_{xy} for **H** directed 60° toward the **a** and then performs the same measurement with **H** instead pointed toward the other **a** axis, then one should observe sign change in the κ_{xy} signal. This is exactly what Yokoi et al. observed. This may initially appear to be a spontaneously broken symmetry as there is no reason to expect that directing **B** 30° above the **a** axis would produce different physics from the application of the field 30° above the -**a** axis. However, this symmetry originates from the ligand geometry (the Cl octahedra) where the difference between these two directions is more obvious (see crystal structure images in Chapter 1).

Yokoi et al. also find that the sign change is only observed at high field. They observe a smaller, non-quantized κ_{xy} signal within the AFM ordered phase that is the same (within error) for both field orientations. The authors claimed that the low field signal must be a conventional magnon thermal Hall effect whereas the high field signal while the high field signal is caused by more exotic Majorana fermion physics.

It was subsequently realized that this particular field angle dependence is actually inherent to the Kitaev-type exchange interaction ($H = \sum_\alpha K_{ij}\sigma_i^\alpha\sigma_j^\alpha$) and is not necessarily a smoking gun

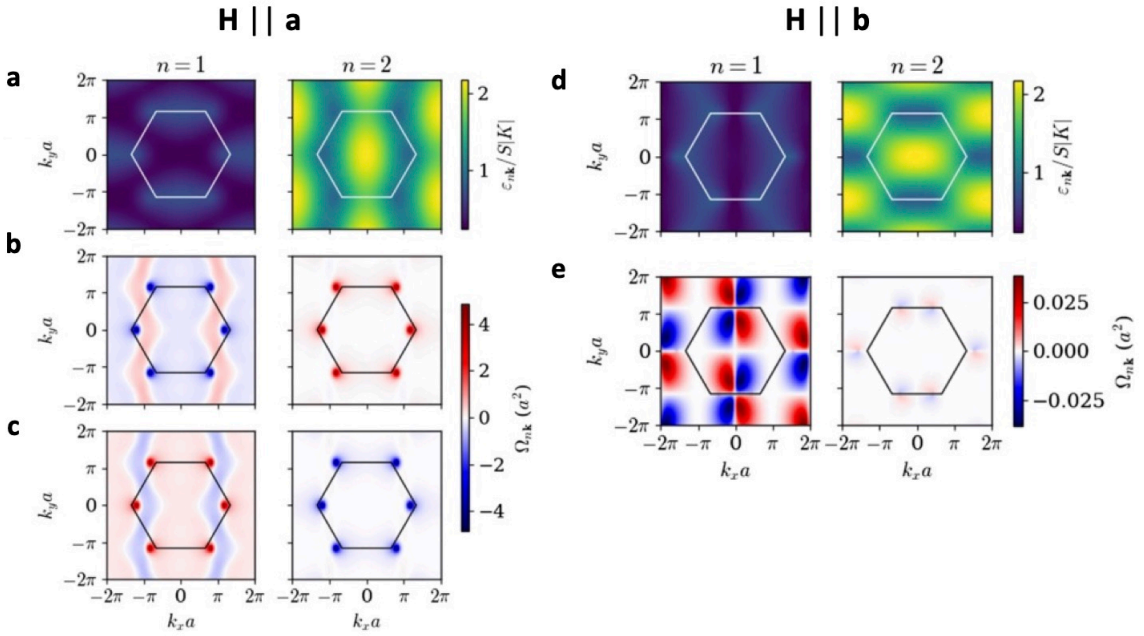

Figure 3.8: Chern et al. calculate the expected magnon bands in the high B spin- polarized phase of $RuCl_3$ as well as the Berry Curvature $\Omega_{n,\mathbf{k}}$. They do this for two different directions of the applied **H**. The left collection of panels shows the results for **H** ∥ **a** while the right set is for **H** ∥ **b**. Figure adapted from [124].

for Majorana fermions [124]. Inspired by our observation of a large, temperature-dependent κ_{xy} signal, Chern et al. [124] (no relation) proposed a magnon-based theory for the PTHE in $RuCl_3$ that should exhibit the same angle-dependence as the Majorana-based signal. Specifically, they showed that that the magnon bands in the spin-polarized phase of a Kitaev magnet should possess $\mathbf{\Omega}_{n,\mathbf{k}}$ with a finite component along $\mathbf{c}$ (even though $\mathbf{B}$ is directed entirely in-plane), and that the resulting κ_{xy} should vanish when $\mathbf{B} \parallel \mathbf{b}$. They then demonstrated this by calculating the magnon spectrum and associated $\Omega_{n,\mathbf{k}}$ for an extended Kitaev Hamiltonian with parameters specific to $RuCl_3$. These calculations are depicted in Fig. 3.8. For a $\mathbf{\Omega}$-induced thermal Hall effect to be seen in an experiment, $\mathbf{\Omega}$ must change sign with $\mathbf{B}$. Otherwise, no signal will remain after performing the antisymmetrization procedure described in Chapter 1. Chern et al.'s calculations demonstrate that this is clearly the case for $\mathbf{B} \parallel \mathbf{a}$. This is illustrated by the reversal of $\mathbf{\Omega}_{n,\mathbf{k}}$ between Fig. 3.8b and Fig. 3.8c. Something different is seen for $\mathbf{B} \parallel \mathbf{b}$ where $\mathbf{\Omega}_{n,\mathbf{k}}$ lacks the asymmetric distribution between bands that would give rise to a finite κ_{xy}.

We would also like to emphasize an important difference between the the Majorana-based model and the magnon system presented in 3.8. Unlike the pure Kitaev model where the excitation spectrum will remain gapless for $\mathbf{B} \parallel \mathbf{b}$, the magnon spectrum will always be gapped due to the Zeeman effect. The gap-opening associated with non-trivial topology instead happens at finite energy (where an avoided crossing occurs for $\mathbf{B} \parallel \mathbf{a}$), away from the chemical potential μ which is fixed at zero. As we will show in the next section, this fact is key in deriving the model that we will use to analyze our data.

An alternative explanation for the absence of a κ_{xy} signal for $\mathbf{B} \parallel \mathbf{b}$ is the underlying mirror symmetry. This is illustrated in Fig. 3.9. A thermal Hall effect is forbidden if mirror symmetry is present. For $RuCl_3$, the relevant mirror plane is that which contains the $\mathbf{b}$ axis. Because $\mathbf{B}$ is an axial vector, it shows the opposite behavior under mirror reflection as a polar vector. Specifically, a field directed perpendicular to the mirror plane will not change sign under reflection. In the present case this means that a finite $\mathbf{B} \parallel \mathbf{b}$ respects the original mirror symmetry of the system. Then, because $\mathbf{J}_Q$ is a polar vector, its sign will reverse under mirror reflection. Mirror symmetry requires that $\mathbf{J}_Q = \mathbf{J}'_Q$ which is only possible if $\mathbf{J}_Q = 0$. Thus, there will be no thermal Hall effect for $\mathbf{B} \parallel \mathbf{b}$.

The drawing on the right side of Fig. 3.9 illustrates why a Hall signal is allowed for $\mathbf{B} \parallel \mathbf{a}$. $\mathbf{B}$ applied parallel to the mirror plane will reverse sign under mirror reflection. Therefore, any finite component of $\mathbf{B}$ applied along this direction is incompatible with mirror symmetry, meaning the field acts to destroy the mirror symmetry that was originally present. Because mirror symmetry is broken, finite $\mathbf{J}_Q$ (and therefore κ_{xy}) are permissible for $\mathbf{B} \parallel \mathbf{a}$.

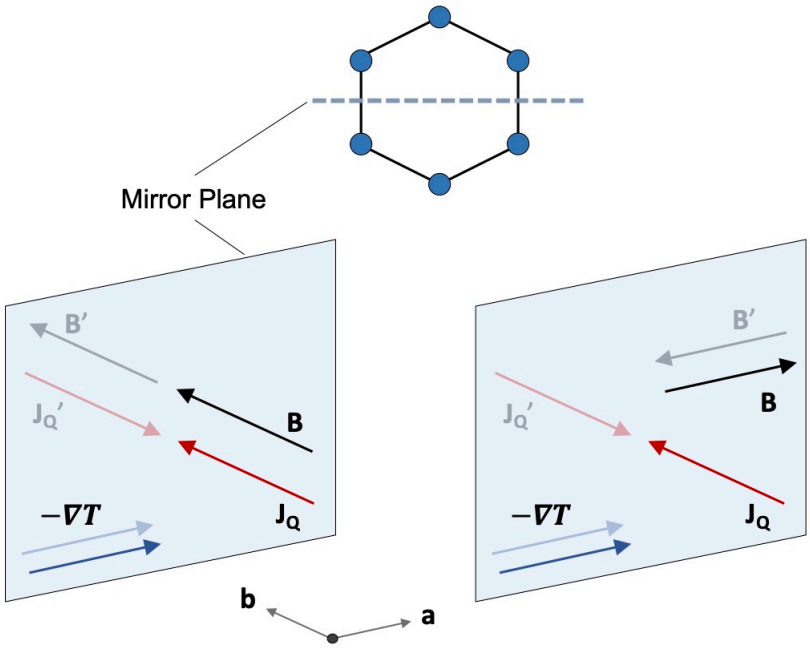

Figure 3.9: This figure illustrates the mirror symmetry of the honeycomb lattice and its effect on $RuCl_3$'s ability to exhibit the thermal Hall effect. Finite κ_{xy} can only be observed if the mirror symmetry is broken. Applying $\mathbf{B} \parallel \mathbf{a}$ breaks the mirror symmetry whereas it remains for $\mathbf{B} \parallel \mathbf{b}$. Note that $-\nabla T$ and $\mathbf{J}_Q$ are polar vectors while $\mathbf{B}$ is an axial vector.

3.4 Results

3.4.1 Thermal Hall Measurements

As stated earlier, in our first report we qualitatively verified the existence of an anomalous planar thermal Hall conductivity in $RuCl_3$, but were unable to reproduce the quantized value. To further investigate the Hall effect, we performed what we believe to be the most high density measurement of the full T- and B- dependence of κ_{xy} in any individual sample to date (and of any compound, not just $RuCl_3$). The technical aspects of how this data was collected are discussed at length in Chapter 1, but we will briefly review the some important details for the reader's convenience. The measurements are done using a field-step procedure. For this specific experiment, B is swept from 13 to -13 T (or vice versa) in 0.2 T steps over approximately 8 hours during which the stage temperature T_{Stage} is fixed at a constant value ($\pm$ 1 mK). At a given step, B is kept fixed for approximately 150 s. B is swept in steps to remove transient artifacts such as Eddy currents and magnetocaloric effects as well as to provide a large averaging window to lower effective statistical noise. For a given T_{Stage}, B must always be swept both down (13 to -13 T) and up (-13 to 13 T) to remove hysteretic artifacts. Note that $\mathbf{B} \parallel \mathbf{J}_q \parallel \mathbf{a}$ for the entire experiment.

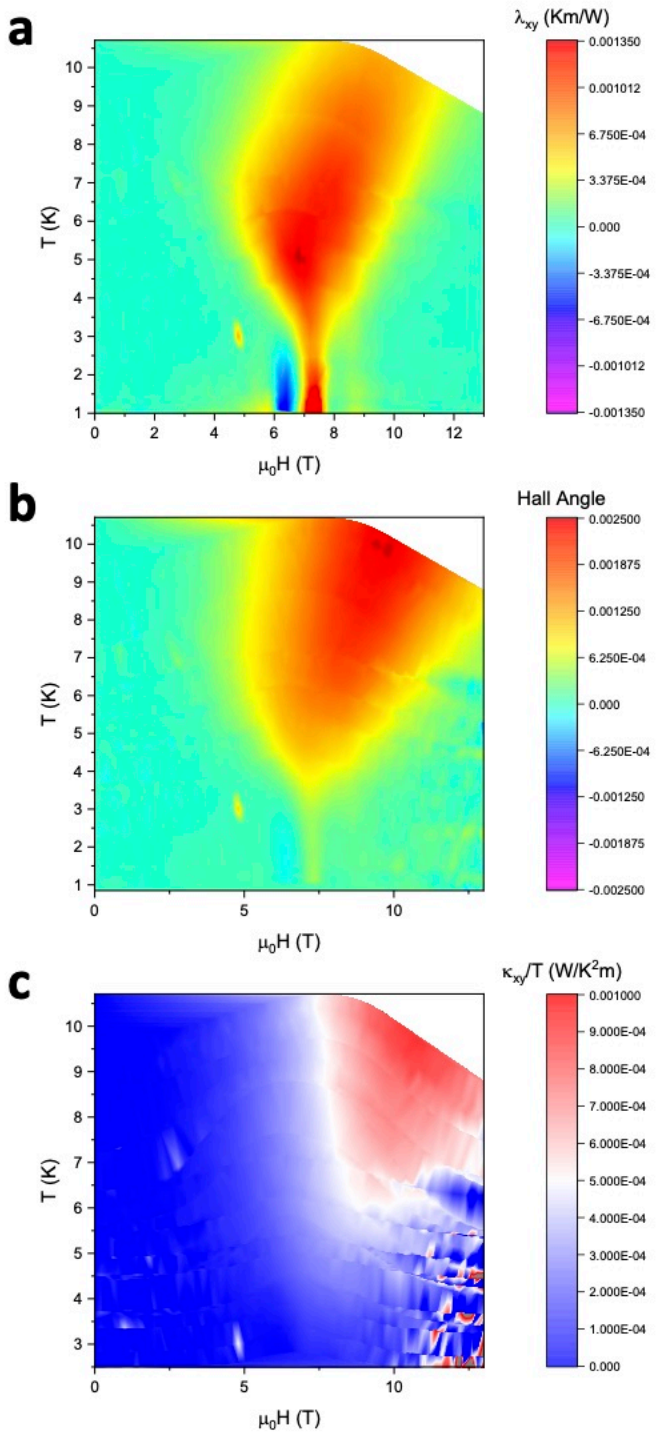

Figure 3.10: Colormaps showing the large quantity of thermal Hall effect data collected for this experiment. The data is presented in three different forms. Panel (A): Thermal Hall resistivity λ_{xy}. Panel (B): Thermal Hall angle (κ_{xy}/κ_{xx}). Panel (C): Panel (C): Thermal Hall conductivity divided by temperature (κ_{xy}/T).

Fig. 3.10 shows the results of this experiment in colormap form. The plotted data is of three separate quantities: the thermal Hall resistivity λ_{xy}, the thermal Hall angle (κ_{xy}/κ_{xx}), and the thermal Hall conductivity (divided by temperature) κ_{xy}/T. We have chosen to present the data so as to provide greater insight into the experimentalist's perspective. Thermal Hall reports typically focus on κ_{xy} as it is generally easier to connect with theory. However, it is actually λ_{xy} that is the more fundamental quantity to the experimentalist. As explained in Chapter 1, what is actually measured is the B-antisymmetric transverse temperature difference ΔT^{AS} and it is λ_{xy} that is directly proportional to this quantity. κ_{xy} is calculated as $\kappa_{xy} \cong \lambda_{xy}\kappa_{xx}^2$. This leads to complications in materials like $RuCl_3$ where κ_{xx} is strongly B-dependent. Specifically, the rapidly increasing κ_{xx} can distort the underlying signal. This is why the noise level is so high in κ_{xy} in the examples shown here.

We can also observe several features whose existence is tied to the fundamental physics of the material, rather than just issues of resolution. The color map provides an overview of how λ_{yx} varies over the B-T plane. The large λ_{yx} region above 4 K (red area) tapers to a thin neck at 7.5 T as T decreases to 1 K. Below 2.5 K, λ_{yx} becomes slightly negative in the small region shown in blue. A representative subset of the field sweeps used to construct the color maps for λ_{xy} and κ_{xy}/T are shown in Fig. 3.11. The evolution of the field profiles of λ_{yx} is shown in Fig. 3.11a. At 9.22 K, the profile features a broad peak that narrows dramatically as $T \to 3.65$ K. At high B (> 10 T), λ_{yx} is strongly suppressed to values below our resolution for $T < 4$ K. Like in our previous experiment, κ_{xy}/T is both large and T-dependent. At high T (9.22 K) κ_{xy}/T at peak is higher than the reported

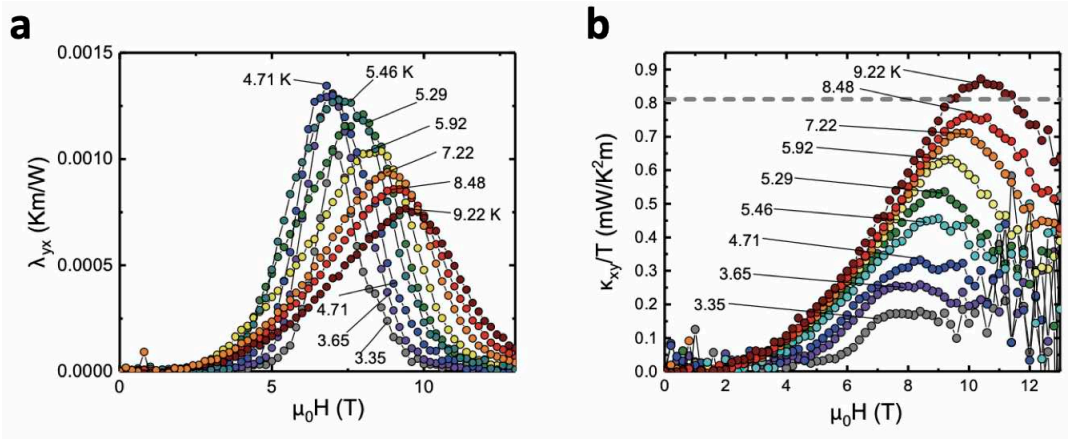

Figure 3.11: Panel (A): the thermal Hall resistivity λ_{xy} vs. field for a series of sweeps taken at fixed T_{Stage}. Panel (B): The calculated κ_{xy}/T values for the same field sweeps as panel (A). The enhanced noise at high B in κ_{xy}/T is caused by the rapidly increasing κ_{xx}. Note that the sweeps displayed here represent only a small subset of the total number that were collected for this project.

quantized value. However, no plateau is observed and most importantly, the κ_{xy}/T vs. B curves do not intersect. We remind the reader that this detail is important because any T-dependence is incompatible with a signal derived from fermionic edge states.

3.4.2 Model for $\kappa_{xy}(T)$

As discussed earlier, the theoretical framework established by Murakami and collaborators provides a way to quantitatively predict the Berry curvature-derived thermal Hall conductivity for spin excitations. These predictions are robust because κ_{xy} should only depend on topological features of the band structure and not on microscopic details such as the excitation's mean free path. For example, Lee et al. [125] were able to construct a model that reproduced many of the features in Hirschberger et al.'s Cu(1-3, bdc) data [108]. Unfortunately, it is generally not possible for the theory to be employed in an inverse fashion and be used to fit experimental data as a typical excitation spectrum will typically be too complex to be described by a small number of fitting parameters. One exception is for the case of topological bands. If the magnon excitation spectrum consists of only two bands and if those bands are sufficiently flat that we can reasonably ignore $\mathbf{k}$-dependence, further simplifications to the above model can be made.

We begin with the general expression for a Berry curvature-derived thermal Hall conductivity (originally presented in Eq. 3.3), but with c_2 now incorporated more explicitly:

$$\frac{\kappa_{xy}}{T} = \frac{1}{\hbar V}\sum_{n,\mathbf{k}} \Omega_{n,z}(\mathbf{k}) \int_{\epsilon_{n,\mathbf{k}}}^{\infty} d\epsilon \frac{(\epsilon-\mu)^2}{T^2}\left(-\frac{d\rho}{d\epsilon}\right) \tag{3.5}$$

where $\hbar$ is the reduced Planck constant, V is the crystal volume, ϵ is the energy, μ is the chemical potential, and ρ is the relevant distribution function (we will use the Bose-Einstein distribution here). We reiterate that while this generalized model is typically associated with bulk bosonic physics, it also reproduces the correct (quantized) Kane-Fisher value [126] for fermionic edge states:

$$\frac{\kappa_{xy}}{T} = \frac{\pi^2}{3}\frac{k_B^2}{h}\nu, \quad (\nu \in Z) \tag{3.6}$$

We now rewrite Eq. 3.5 in a more instructive form:

$$\frac{\mathcal{K}_H}{T} = \frac{\kappa_{xy}/T}{k_B^2/h} = \sum_n \mathcal{C}_n c_2^n(\omega_n, T) \tag{3.7}$$

This new form is now in the units of universal thermal conductance and emphasizes the connection to band topology. $\mathcal{C}_n$ is the Chern number of a given band and the function $c_2^{(n)}(\omega_n, T)$ is defined

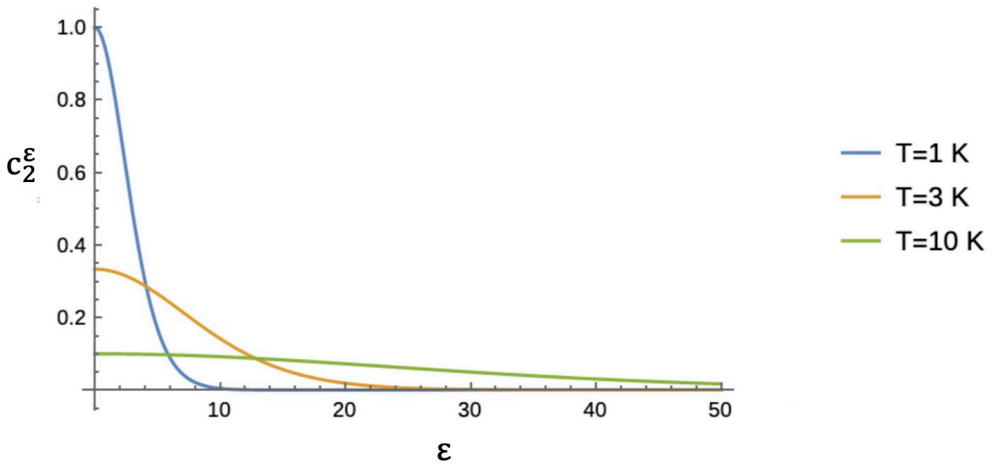

Figure 3.12: Integrand of c_2 function (labeled c_2^ϵ here) plotted for $T = 1$, 3, and 10 K. The function is strongly weighted towards zero at low T, but broadens significantly as T is raised.

as:

$$c_2^{(n)}(\omega_n, T) = \int_{u_{0n}}^{\infty} du u^2(-d\rho/du), \qquad (u_{0n} = \beta\omega_n(\mathbf{k})) \tag{3.8}$$

with $\rho = 1/(e^u - 1)$ and $\beta = 1/(k_B T)$. The integrand of this function is plotted in Fig. 3.12 where it is defined as c_2^ϵ. The function is narrowly localized around $\epsilon = 0$ at low T, but broadens substantially at T is raised. The examples shown in the figure are for $T = 1$, 3, and 10 K.

We also emphasize that c_2^n is defined as the integral of c_2^ϵ between ω_n (the excitation energy) and ∞. This is illustrated in Fig. 3.13 where c_2^n is represented by the area shown in red.

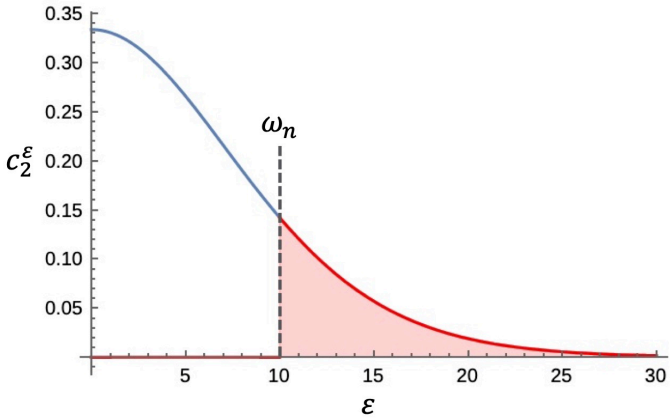

Figure 3.13: c_2^n is obtained by integrating c_2^ϵ between ω_n and ∞. This area is shown in red.

Note that in obtaining Eq. 3.7, we chose to ignore any possible $\mathbf{k}$-dependence to $\epsilon_{n,k}$ (in other words, approximating the band as flat). This was the reason for adopting the variable ω_n which

we will now treat as a single energy associated with a given band n. We have also invoked the winding number association between $\mathcal{C}_n$ and $\Omega_{n,z}$: $2\pi\mathcal{C}_n = \int_{BZ} d^2k\, \Omega_{n,z}(\mathbf{k})$. Finally, if there are only two magnon bands with equal and opposite Chern number ($\mathcal{C}_1 = -\mathcal{C}_2$), we obtain the following expression for $\mathcal{K}_H/T$:

$$\frac{\mathcal{K}_H}{T} = \mathcal{C}_1\left[c_2^{(1)}(\omega_1, T) - c_2^{(2)}(\omega_2, T)\right] \tag{3.9}$$

Also note that while we have used an integral expression for $c_2^{(n)}(\omega_n, T)$ above, but it also has the following explicit analytical form:

$$c_2^n(\omega_n, T) = \frac{\omega_n}{T^2}\left(\frac{\omega_n}{e^{\omega_n/T} - 1} - 2T\ln\left(1 - e^{-\omega_n/T}\right)\right) + 2Li_2\left(e^{-\omega_n/T}\right) \tag{3.10}$$

Fig. 3.14 summarizes the physical picture associated with the model we will use for fitting analysis later in this chapter (Eq. 3.9). There are two well-separated, weakly dispersive bosonic bands with equal and opposite Chern number. This nontrivial topology leads to a chiral edge mode that connects the bands and carries the thermal Hall current. The right panel in the figure shows a possible $\Omega_{n,\mathbf{k}}$ distribution for one of the bands where the intensity is localized to a few specific high symmetry points within the Brillouin zone (likely the K-points).

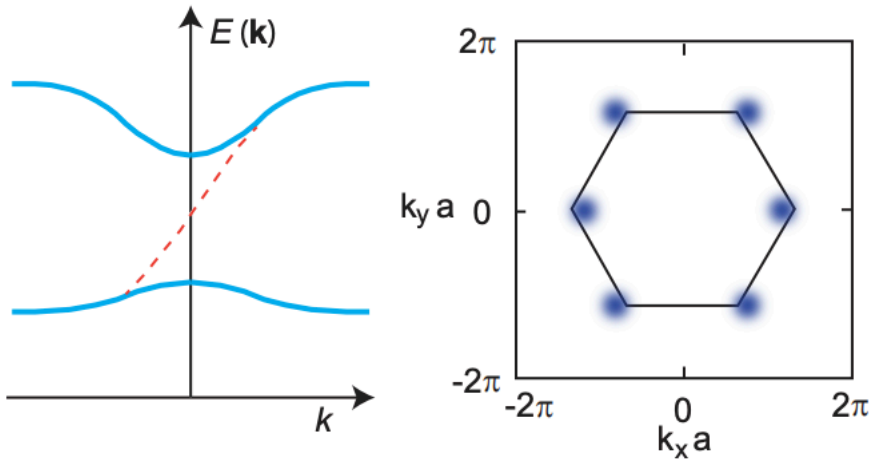

Figure 3.14: Left Panel: Sketch of the two magnon modes (blue curves) with $\omega_1 = 11.6$ K and $\omega_2 \approx 50$ K. With $\mathcal{C} = 1$ in the lowest band, an edge mode traverses the gap (dashed curve). Right Panel: The Berry Curvature $\Omega_{n,\mathbf{k}}$ is likely concentrated at a few high intensity spots in the Brillouin zone for $\mathbf{B} \parallel \mathbf{a}$ (as revealed by calculations in [124]).

3.4.3 Topological Magnons in the Spin-Polarized State of the Kitaev Model

We explain why this bosonic model should be appropriate for $RuCl_3$. First, topological magnons have actually been predicted to exist in Kitaev magnets in the high B spin-polarized phase [127] [128] [124]. The physical reasons for nontrivial topology in this phase are similar to the Majorana case. The Kitaev term (in combination with the applied $\mathbf{B}$) breaks time-reversal symmetry and opens a gap in the excitation spectrum, thereby producing nonzero Chern numbers for the two bands. As we explained in the previous section, the difference here is that the Kitaev exchange creates an avoided crossing in the magnon spectrum at finite energy instead of inducing an energy gap in a previously gapless state. We now sketch out McClarty et al.'s argument for topological magnon states at high field. We begin with the a typical Hamiltonian for the extended Kitaev model on the honeycomb lattice:

$$H = J\sum_{\langle i,j\rangle}\mathbf{S}_i\cdot\mathbf{S}_j + \sum_{\langle i,j\rangle_\gamma}\left[2KS_i^\gamma S_j^\gamma + \Gamma(S_i^\alpha S_j^\beta + S_i^\beta S_j^\alpha)\right] - \mathbf{h}\cdot\sum_i \mathbf{S}_i \tag{3.11}$$

where the $\{\alpha,\beta,\gamma\}$ indices run over the $\{x,y,z\}$ components with the γ component referring to the type of bond (either x, y, or z). This is essentially the same generalized Kitaev Hamiltonian discussed in chapter 1, except we have dropped the Γ' term and added an external magnetic field. At high B, the spins will be polarized along the applied field direction in a collinear fashion. Note that McClarty et al. choose $\mathbf{B} \parallel [111]$ (out-of-plane), but we expect the model to apply to other field directions as well (this was shown explicitly by Chern et al. [124]). We can then solve for the full magnon spectrum by considering the fluctuations about the collinear state using linear spin-wave theory. More specifically, the authors use Holstein-Primakoff bosons [129] to describe these fluctuations:

$$S_i^z = S - a_i^\dagger b_i = S - n_i \tag{3.12}$$

$$S_i^x = \frac{\sqrt{2S-n_i}a_i + a_i^\dagger\sqrt{2S-n_i}}{2} \approx \sqrt{\frac{S}{2}}(a_i + a_i^\dagger) \tag{3.13}$$

$$S_i^y = \frac{\sqrt{2S-n_i}a_i - a_i^\dagger\sqrt{2S-n_i}}{2} \approx -i\sqrt{\frac{S}{2}}(a_i - a_i^\dagger) \tag{3.14}$$

where the bosons satisfy the commutation relations $[a, a^\dagger] = 1$.

After performing the appropriate transformation, we obtain the following quadratic Hamiltonian:

$$H_{LSW} = \sum_{\mathbf{k}} \Upsilon_{\mathbf{k}}^{\dagger} M(\mathbf{k}) \Upsilon_{\mathbf{k}} \tag{3.15}$$

where $\Upsilon = \left(a_{\mathbf{k}}\ b_{\mathbf{k}}\ a_{-\mathbf{k}}^{\dagger}\ b_{-\mathbf{k}}^{\dagger}\right)^{T}$ and a and b are bosonic operators whose labels refer to the two sublattices of the honeycomb lattice. $\mathbf{M}(\mathbf{k})$ is a 4×4 Hamiltonian with the following form:

$$\mathbf{M}(\mathbf{k}) = \begin{pmatrix} A(\mathbf{k}) & B(\mathbf{k}) \\ B^{\dagger}(\mathbf{k}) & A^{T}(\mathbf{k}) \end{pmatrix} \tag{3.16}$$

The A block contains the number-conserving terms (such as $a^{\dagger}a$) and the B block contains number-nonconserving terms (such as $a^{\dagger}a^{\dagger}$). Crucially, the B block is proportional to K, the strength of the Kitaev term. The spin-wave branches can then be solved for by performing a Bogoliubov transformation. It is found that the number-nonconserving terms (which are are derived from the Kitaev-type exchange) are responsible for a gap opening between two spin wave bands at the K point. These terms also break time-reversal symmetry, thereby leading to nonzero Chern numbers for the two magnon bands, or more formally, a topological insulator of class D.

One can also verify explicitly that the obtained spin-wave bands are in fact topologically non-trivial. The magnons are bosons so they must satisfy the commutation relations $[\Upsilon_a, \Upsilon_b^{\dagger}] = \eta_{ab}$ with $\boldsymbol{\eta}$ = diag(1,1,...,-1,-1,...) where there are m ones and m minus ones along the diagonal. One can

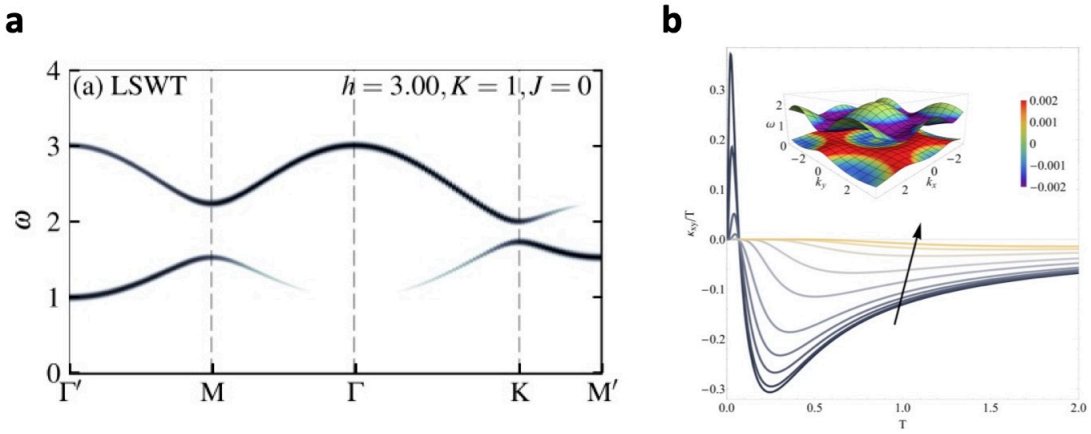

Figure 3.15: Panel (A): Spin Wave Theory (SWT) calculation of the magnon spectrum in the high field, spin-polarized phase of a Kitaev magnet. Panel (B): Thermal Hall conductivity (calculated as κ_{xy}/T here) vs. T for a series of magnetic fields in the high field SWT model. The inset depicts the Berry curvature throughout the magnon bands from which κ_{xy} is calculated. Figure adapted from [127].

then define a diagonalizing transformation that satisfies:

$$\mathbf{U}^{\dagger}(\mathbf{k})\mathbf{M}(\mathbf{k})\mathbf{U}(\mathbf{k}) = \mathbf{\Lambda}(\mathbf{k}) \tag{3.17}$$

$$\mathbf{U}(\mathbf{k})\mathbf{U}^{\dagger}(\mathbf{k}) = \boldsymbol{\eta} \tag{3.18}$$

where $\mathbf{\Lambda}(\mathbf{k})$ is diagonal. To make the connection to topological band theory, we must first define the Berry connection $A_{\nu}^{(n)}(\mathbf{k})$. We consider an eigenstate for band n and multiply it by a phase that is a smooth function of momentum. This has the form $e^{i\theta(\mathbf{k})}$. The Berry connection is then obtained from the formula:

$$A_{\nu}^{(n)}(\mathbf{k}) = i\Big[\boldsymbol{\eta}\mathbf{U}^{\dagger}(\mathbf{k})\boldsymbol{\eta}\partial_{k_\nu}\mathbf{U}(\mathbf{k})\Big]_{nn} \tag{3.19}$$

The Berry connection transforms in the following way under the phase change: $A_{\nu}^{(n)}(\mathbf{k}) \rightarrow A_{\nu}^{(n)}(\mathbf{k}) - \partial_{k_\nu}\theta(\mathbf{k})$. This resembles the way that a similar gauge transformation is implemented for the electromagnetic vector potential in traditional electromagnetism. The Berry curvature $\mathbf{\Omega}_n(\mathbf{k})$ is obtained from $A_{\nu}^{(n)}(\mathbf{k})$ via the curl operation $\mathbf{\Omega}_n(\mathbf{k}) = \nabla \times A_n(\mathbf{k})$. The explicit form for the 2D case is:

$$\Omega_n(\mathbf{k}) = \partial_{k_x}A_y^n(\mathbf{k}) - \partial_{k_y}A_x^n(\mathbf{k}) \tag{3.20}$$

It can be shown via Stokes theorem that the integral of $\Omega_n(\mathbf{k})$ over the whole Brillouin zone (BZ) is zero if $A_{\nu}^{(n)}(\mathbf{k})$ is a smooth function everywhere in the BZ. In this case, the band in question is topologically trivial. If it is impossible for the eigenstate to be parametrized over the whole BZ for a single gauge choice, then the band is topologically nontrivial. Integrating the Berry curvature over the entire BZ will instead yield an integer value:

$$\mathcal{C}^n = \frac{1}{2\pi}\int_{BZ} d^2\mathbf{k}\ \Omega_n(\mathbf{k}) \equiv \mathbb{Z} \tag{3.21}$$

This value is the Chern number $\mathcal{C}$ that we invoked when deriving our fitting model for κ_{xy} above.

3.4.4 Fitting Measured κ_{xy} Data to Model

Before discussing the results of the fitting procedure, we highlight a few points. First, one key assumption that was made when deriving Eq. 3.9 was that the energy scale of an entire band can reduced to a single value ω_i (with i = 1,2 for the upper and lower band respectively). Without this simplification, it would be impossible to obtain such a fitting function. Earlier, we referred to this as a flat band approximation. We mention the above point to clarify that we do not mean to imply

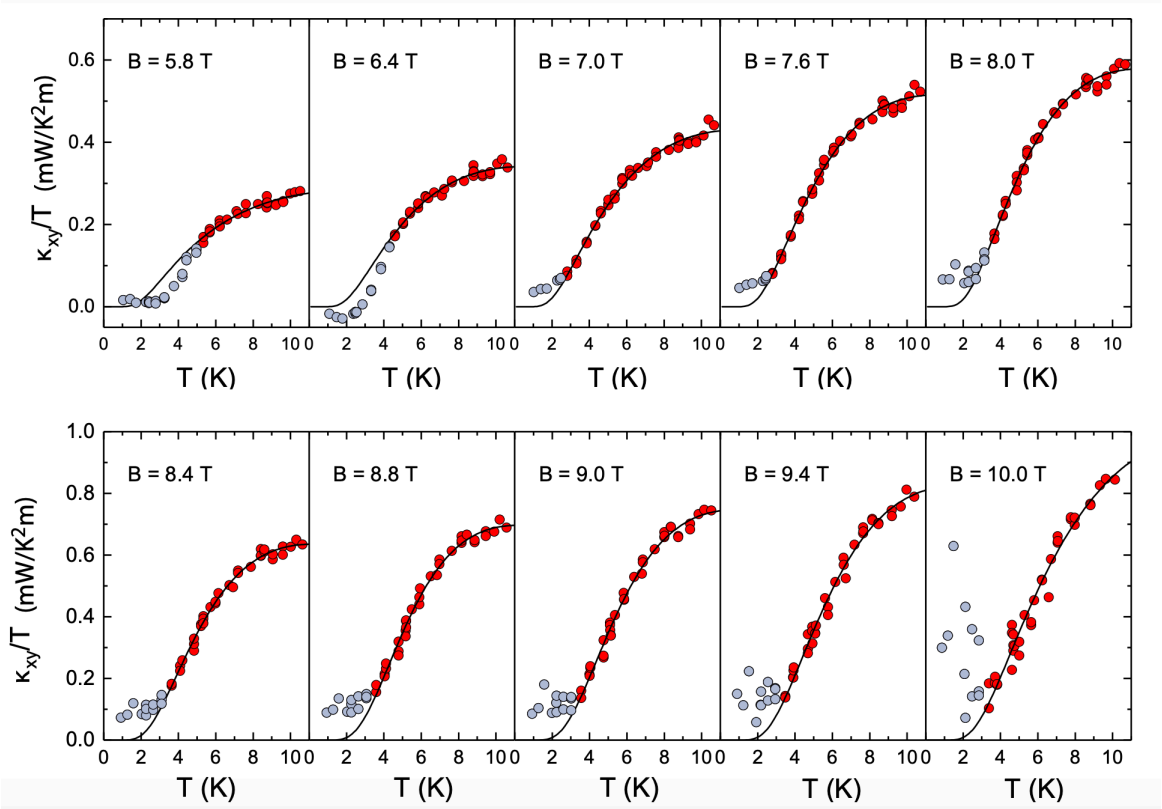

Figure 3.16: A collection of curves showing κ_{xy}/T vs. T at a series of fixed B's (the values of which are indicated in each panel). The data is described well by our fitting model at high temperature (red points), but deviates from the predicted behavior at low temperature (gray points).

that the the model presented here has any relation to other active research areas such as Moire physics. We only mean to say that we assume a sufficiently simple band structure for the bosonic spin excitations (an approximation that seems reasonable for $RuCl_3$). Finally, we emphasize that we have chosen to use a strictly quasi-2D model. While the measurement itself is done on a bulk 3D crystal, the measured values can be converted to the 2D equivalent with the formula: $\kappa_{xy}^{2D} = \kappa_{xy}^{3D} d$ where d is the thickness of an individual crystal layer (5.72 Å for $RuCl_3$).

We may now begin utilizing this model to analyze our κ_{xy} results. Fig. 3.16 shows a series of temperature cuts in our κ_{xy}/T data set and attempts to fit them. It is immediately clear that the model describes the data remarkably well for most T's measured (points in the range where the fitting is successful are shown in red). However, κ_{xy}/T does appear to deviate from the predicted behavior at low T. This deviation seems to generally occur around 3 K though this shifts to higher T at lower B (likely reflecting the dome-like shape of the zig-zag AFM state). We will discuss the possible reasons for these deviations at length in a later section. For now, we emphasize that the model is most effective in describing the high T,B regime, which is where we expect the simple two

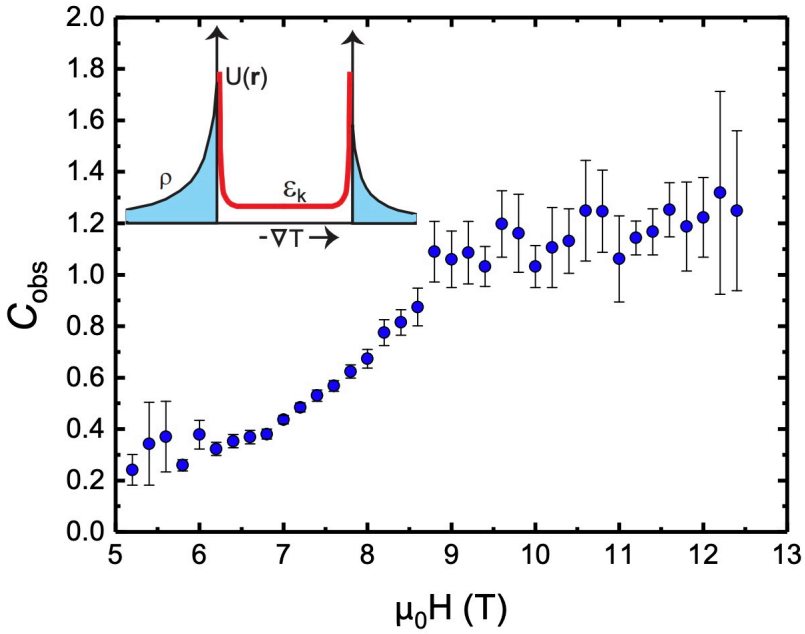

Figure 3.17: The effective Chern number $\mathcal{C}_{obs}$ obtained from our fitting model as a function of B. $\mathcal{C}_{obs}$ saturates at 9 T at a value of 1.0 (within error), as expected for the predicted topological phase. The inset illustrates how κ_{xy} is calculated in the magnon-based model ($U(\mathbf{r})$ is the edge potential that causes the magnon wave packet to circulate around the sample).

band description to be most accurate.

Our model allows us to gain greater insight into $RuCl_3$'s by studying the extracted fitting parameters and how they vary with B. We remind the reader that the leading coefficient in Eq. 3.9 is the effective Chern number $\mathcal{C}_{obs}$ of the bands (with the sign being opposite for the upper and lower ones). In Fig. 3.17 we plot $\mathcal{C}_{obs}$ vs. B and reveal an incredible result. $\mathcal{C}_{obs} \approx 0.3$ around 5 T, but gradually increases with increasing B. It eventually saturates at a value of 1.0 (within experimental resolution) starting at 9 T. This saturation continues up to the highest B at which we are able to fit the data ($\sim$ 12.6 T). Above 12.6 T, the noise level is too high. Notably, 9 T is exactly the same value at which Balz et al. observed the reappearance of sharp magnon-like modes in INS (after vanishing in the intermediate B spin liquid regime) [52]. The inset in Fig. 3.17 is a reminder of how κ_{xy} is calculated in our model. The confining potential encourages the magnon wave packet to circulate around the circumference of the sample. The asymmetry in the effective distribution function between the hot and cold ends of the sample will cause the thermal current carried by the wave packet at each end to differ as well. This asymmetry is what produces the Hall effect.

Our fitting model also allows us to compare our results with other $RuCl_3$ measurements through the ω_1 parameter. ω_1 corresponds to the energy scale of the lowest energy (sharp) spin excitation so

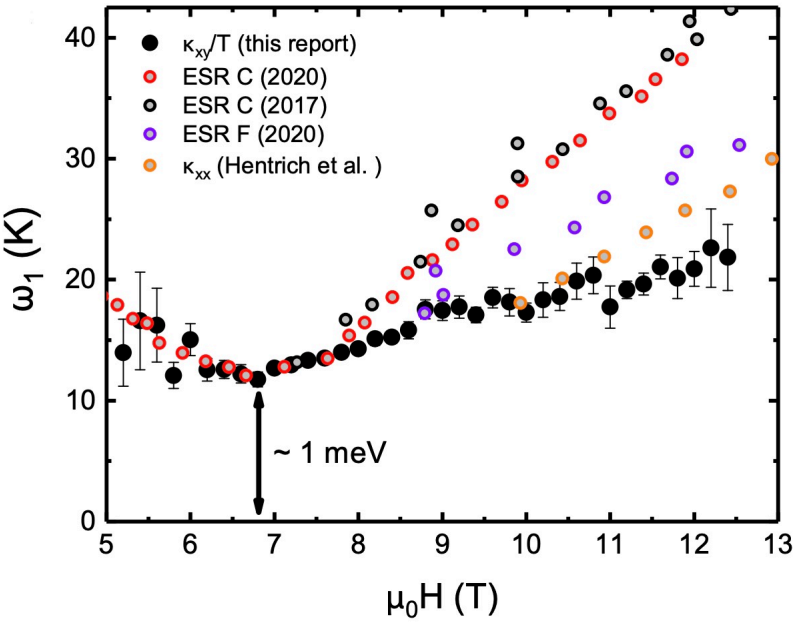

Figure 3.18: The B dependence of the energy level ω_1 derived from the fit of κ_{xy}/T vs. T to Eq. 3.9 at each B. At the minimum (at 6.8 T), ω_1 agrees with the energy of the narrow mode seen in ESR ($\sim$ 1 meV). At large B, ω_1 is slightly lower than the ESR mode, and in better agreement with the energy extracted from κ_{xx} in [68].

should be comparable to earlier measurements of excitation gaps. Our results for the higher band (with energy ω_2) will be discussed in a later section. In Fig. 3.18 we plot our extracted values for ω_1 against previously measured values obtained using electron spin resonance (ESR) [131][130] and κ_{xx} [68] measurements (that are similar to what is seen in neutron scattering [52]). We find that the values all agree remarkably well around 7 T where $\omega_1 \approx 1$ meV. As B increases, ω_1 increases less quickly that the ESR values, but matches the values extracted from the Callaway model fits of κ_{xx}. This discrepancy results from the selection rules inherent to ESR measurements. $RuCl_3$'s ESR spectrum is summarized in Fig. 3.19. ESR primarily probes the energy at Γ. This excitation is called "C" in Ponomaryov's labeling system. A lower energy excitation can be probed via a loophole associated with the folding of the Brillouin zone along the c axis. This lower energy mode is labeled "F". Higher energies can also be seen in ESR measurements via multiparticle excitations. These are labeled "2F", "E", and "2C" and there k-space descriptions are indicated in Fig. 3.19. The M1, M2', and M3' labels refer to excitations seen in Raman scattering [132]. Thermal transport is not limited by these kind of selection rules that only allow for the measurements of energy gaps at specific points in the Brillouin zone. For example, calculations of $\epsilon_{\mathbf{k}}$ for the spin-polarized phase of $RuCl_3$ indicate that the lowest point in the lower magnon band should be at the M point, not

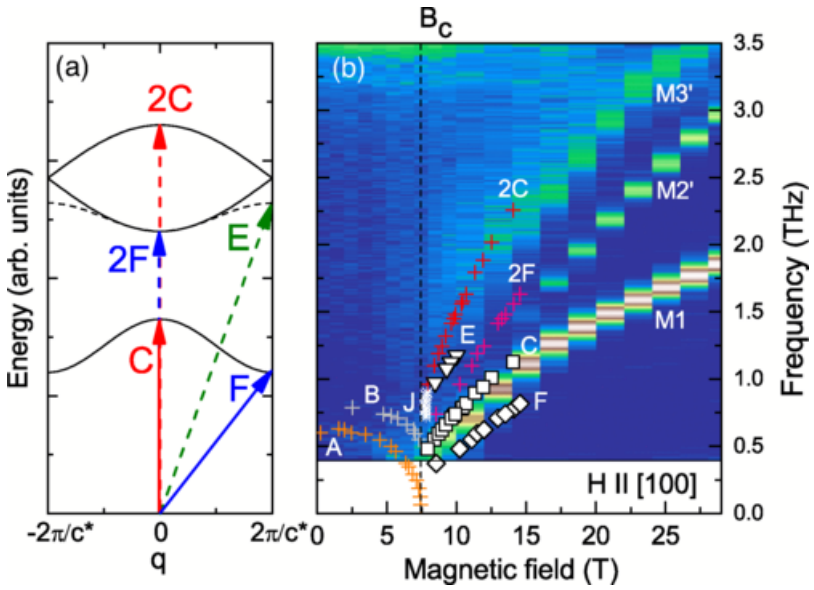

Figure 3.19: Left Panel: Graphic illustrating the momentum space interpretation of $RuCl_3$'s Electron Spin Resonance (ESR) spectrum. Selection rules typically restrict ESR-visible excitations to those with zero momentum. However, band edge excitations (along the **c** axis) can also be seen in $RuCl_3$ due to band-folding. Additionally, multiparticle excitations are observable as well. Right Panel: ESR colormap from which the illustration in the previous panel is derived. Figure adapted from [130].

Γ. It seems likely that the two thermal transport measurements primarily probe these lower energy points in the Brillouin zone.

A highly compelling physical picture emerges from this analysis. The thermal Hall signal is caused by the same sharp magnon-like modes observed in the spin-polarized state in a variety of other probes. The energy bands associated with these excitations are topological (they possess finite Chern numbers). These bands do not intersect in the bulk, but are connected by chiral modes at the edge of the sample. It is these chiral edge states that give rise to the Hall effect. The magnon chemical potential is fixed at $\mu = 0$ while the edge states only exist at finite energy. Therefore, quantized κ_{xy}/T, which is predicted for the Majorana case will not occur. However, the edge states here can still be glimpsed via thermal activation. This thermal activation mechanism will impart a distinct T-dependence to κ_{xy}/T vs. T (which we derived earlier) and that is exactly what we observe here.

We are then left with the question of how one can understand κ_{xy} below 9 T (where $\mathcal{C}$ is not yet quantized). Chern numbers are fixed to integer values so it is notable that our fitting model generally works (the functional form of κ_{xy}/T vs. T matches the data) even when the topological description breaks down. Our measurement is intrinsically global in nature so it is difficult for us

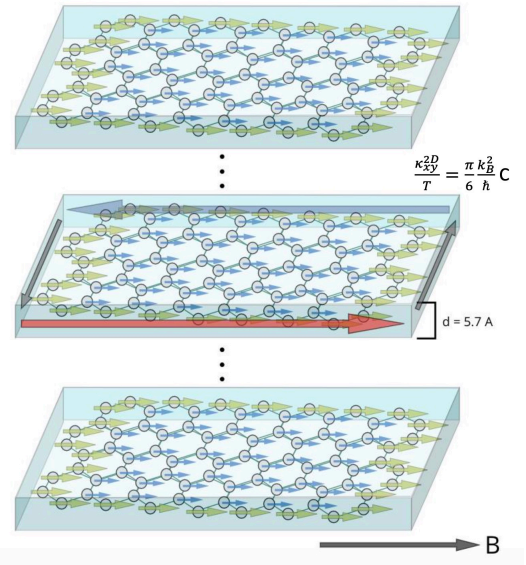

Figure 3.20: Our analysis reveals that the spin-polarized state of $RuCl_3$ behaves like series of decoupled 2D bosonic Chern insulator layers. The center layer in the picture indicates the thermal current carried by the edge states that gives rise to the thermal Hall effect. Note that this description differs from the traditional quantization (the formula for which is given in the figure) as the thermal Hall conductivity is temperature-dependent in our experiment.

to speak precisely about what may be happening more microscopically. However, we can offer a few thoughts on what may be causing this effect. First, the excitation spectrum may just not meet the criteria assumed in our models (two well-separated bands with weak dispersion). It may be that the spectrum at lower fields does not justify this discrepancy and, for whatever reason, the disagreement is more apparent in $\mathcal{C}_{obs}$ than in ω_1. Similarly, the pseudo-ferromagnetic order in the spin polarized state may need to be more complete for the true topological effect to be observed. It could be that the spins are still too strongly fluctuating or that only some regions of the sample show sufficient spin-polarization. Alternatively, the signal (or at least some component of it) could be from a different kind of excitation. Perhaps it originates from the field-induced QSL state. We stress that the ESR measurements we reference pertain only to the sharp excitations. $RuCl_3$'s spin excitation spectrum has also been shown to possess a continuum of scattering states (even at intermediate to high field) [56]. The excitations associated with this continuum could play a role as well. Some degree of coexistence could help explain the fact that $\mathcal{C}_{obs}$ reaches its quantized value at 9 T while the low T κ_{xx} oscillations do not cease until around 11 T. Regardless, this clearly merits more investigation.

3.5 Low Temperature Deviations

3.5.1 Sign Reversal at Low Temperature and Intermediate Field

As shown earlier in the λ_{xy} colormap, the thermal Hall signal exhibits a sign change within a narrow T, B window (roughly $T < 3$ K, $6 < B < 7$ T). Fig. 3.21 shows κ_{xy}/T vs. T for a series of fields within this window. It is clear that the negative signal is most apparent for $B = 6.4$ T. Before discussing possible origins of this effect, we would like to clarify that because **B** is directed entirely in-plane in this experiment, we are unable to define the sign of the signal in the conventional way. We have therefore chosen to define the signal seen throughout most of the phase diagram as positive and the one seen in the narrow window discussed here as negative. As discussed in [73], the true sign of the κ_{xy} signal can potentially be defined by the orientation of **B** with respect to the Kitaev axes, but these axes are not easily identifiable.

We now offer a few possible explanations for the negative signal. First, it may be a property of the field-polarized state, but just not one that fits our simplified description. Such an effect was predicted by McClarty et al. whose calculations showed that there should be substantial $\Omega_{n,z}(k)$ at Γ with a sign opposite that of the rest of the band [127] (as seen in Fig. 3.15b). Second, this

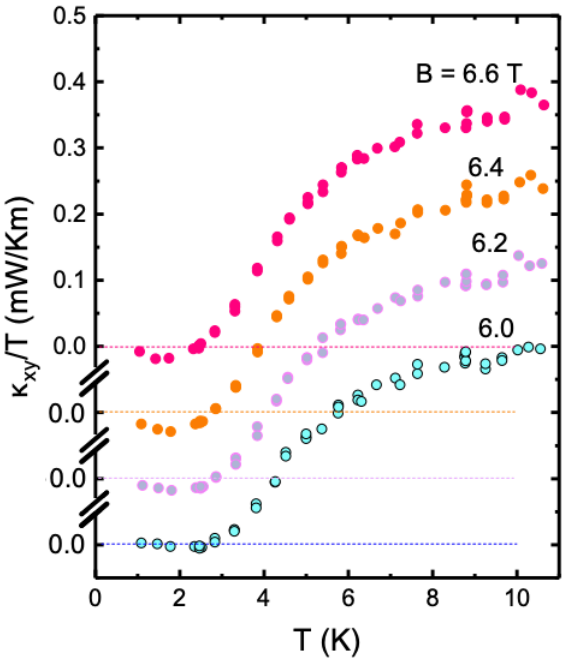

Figure 3.21: Curves of κ_{xy}/T vs. T with B fixed at 6.0, 6.2, 6.4 and 6.6 T (just inside the zig-zag phase). Below 3 K, κ_{xy} displays a weak negative contribution. For clarity, we have shifted successive curves vertically by 0.1 mW/Km.

behavior may be due to the zig-zag ordered phase as predicted by Zhang et al. [133]. The T,B regime where the effect is observed clearly place it within the ordered phase. The zig-zag ordered phase has a unit cell of 6 sites (per layer) and therefore a more complex magnon band structure that does not satisfy the criteria necessary for us to use the fitting model. The bands are likely not well-separated and even non-topological bands can contribute to κ_{xy}. Finally, we propose a third potential explanation that has not been previously predicted. The T,B scales at which the negative signal appears (in addition to other deviations from the high T behavior) are remarkably similar to those of the field-induced ZZ2 phase [52], which we discussed in Chapter 1. This state is even more complex than the zig-zag phase and its more 3D character presents additional complications. Reminder, our κ_{xy} model assumes a quasi-2D character so deviations from this could help explain the reduced value of $\mathcal{C}_{obs}$ at lower B.

Finally, we stress that previous experiments have revealed strong mixing between the various magnetic phases in $RuCl_3$. In addition to the three types of ordered phases (or quasi-ordered in the case of the spin-polarized regime), there also exist possible quantum spin liquid states [60][49] that may coexist with them. Future attempts to model κ_{xy} in the more complex regions of the system's phase diagram will need to account for this.

3.5.2 Low Temperature linear T signal for $7.0 < B < 7.8$ T

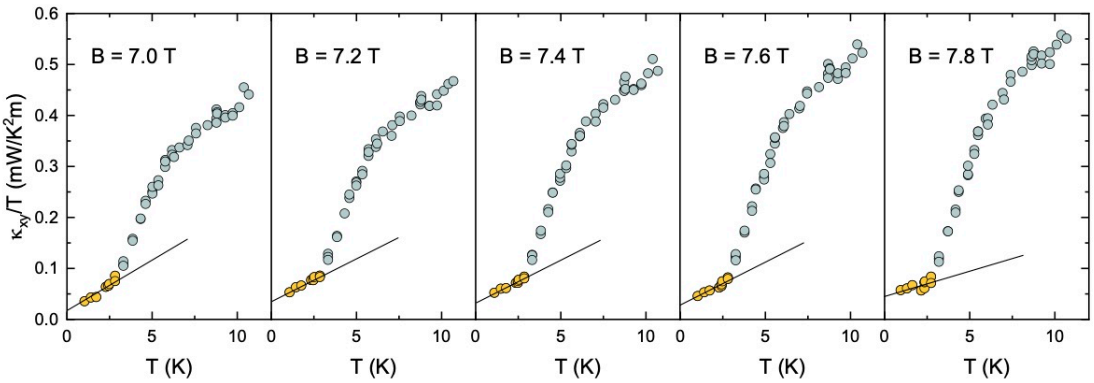

Figure 3.22: Between 7 and 7.8 T, the low T (below 3 K) κ_{xy}/T is approximately linear in T with a finite intercept (yellow points). Above 3 K, the fitting model used for the rest of the phase diagram (at high T) applies.

As shown in Fig. 3.22, the part of the phase diagram defined by $7 < B < 8$ T and $T < 3$ K displays an interesting deviation of the data from the edge mode fit. As T is decreased in fixed B, κ_{xy}/T shows a distinct break-in-slope at 3 K. Below 3 K, κ_{xy}/T displays a T-linear profile (yellow

circles in Fig. 3.22) that extrapolates to a finite intercept in the limit $T \to 0$. In analogy with heat capacity experiments, the finite intercept could suggest a small, residual population of fermionic excitations. However, the T-linear segments lie close to the limits of our present resolution. In the present report, we regard the deviations as tentative; they hint at an interesting regime deserving of further investigation. An alternative explanation is that this behavior is simply a combination of the negative signal seen for $6 < B < 6.8$ T and the low T plateaus seen at higher and lower fields.

3.5.3 Low Temperature Plateau in κ_{xy}/T

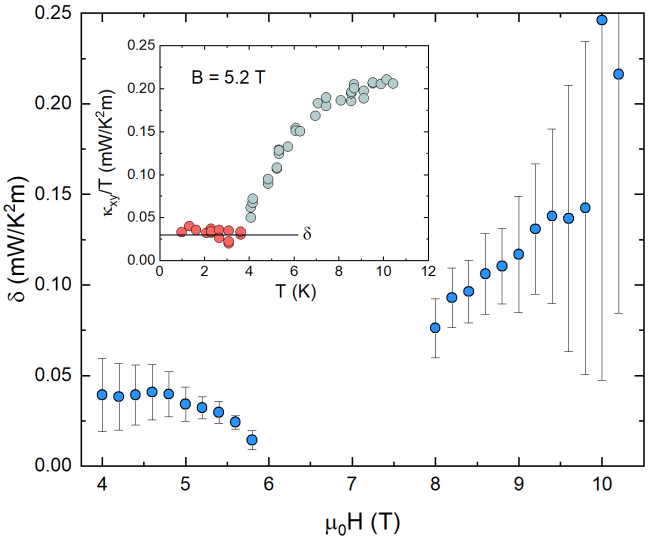

Figure 3.23: Low T intercept (example for $B = 5.2$ T shown in inset) in κ_{xy}/T vs. T. Note that the behavior is observed for $B < 6$ T and $B > 8$ T.

The fitting model fails at the lowest T's (< 3 K), where it appears to plateau at a small, but finite value instead of continuing to 0 as the high T behavior predicts. This behavior is observed at both low and high B (below 6 T and above 8 T) although both the lower and upper bounds are difficult to resolve due to increased noise when κ_{xx} becomes high. The value of this intercept δ as a function of B is shown in Fig. 3.23 (as is a specific example for $B = 5.2$ T in the inset). Different behaviors (which we discussed earlier) occur at intermediate B.

The origin of this low T plateau is unclear, but we are able to offer a few potential explanations. One possibility is that there really is a different phase at low T that produces a separate thermal Hall effect. The potential relation to the oscillations in the κ_{xx} will be discussed later. For now, we just remark that this could be one way of reconciling the gaplessness implied by the oscillations with the

gap-derived (topological) mechanism associated with our model for the thermal Hall conductivity.

Another possibility is that the specific assumptions used in the fitting model break down at low T. Our model is intrinsically two-dimensional in nature and $RuCl_3$ is only quasi-two dimensional. Perhaps the effective dimensionality of the system increases to three spacial dimensions at low T and the 3D dispersion has a substantial effect on the functional form of κ_{xy}/T vs. T. Similarly, Murakami's theoretical framework for boson thermal Hall effects [105] only applies to non-interacting excitations. It is possible that interaction effects between the spin excitations become more relevant at low T and change the effective T-dependence. Another interesting observation is that the value of the low T intercept δ vs. B bears some resemblance to κ_{xx} vs. B. This could suggest a different mechanism for the low T thermal Hall effect that is derived from a bulk-based origin.

3.6 Upper Band Energy

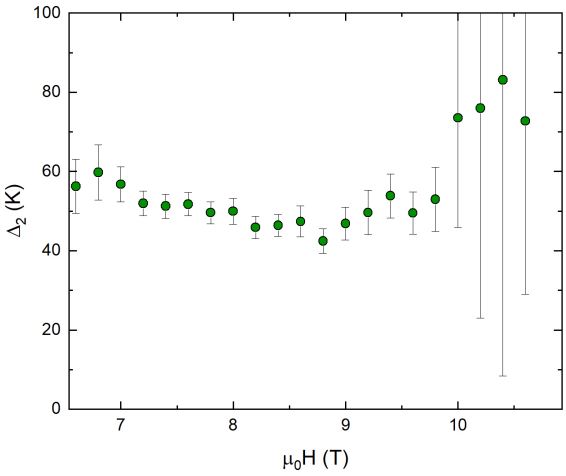

Figure 3.24: The energy scale ω_2 of the higher magnon band extracted from fitting as a function of B.

Another source of novelty for this fitting model is that it allows for the estimation of the energy scale of the upper magnon band. There are few to no experiments that have been able to extract quantitative information about the higher energy band in the spin-polarized phase of $RuCl_3$. There are a few different reasons for this. One is that the energies are simply too high for a significant population to be thermally accessible in a more traditional measurement such as neutron scattering or optical probes. Another source of difficulty is $RuCl_3$'s propensity for multiparticle excitations (with some remaining disagreement regarding precise interpretations) [27][134][130][132].

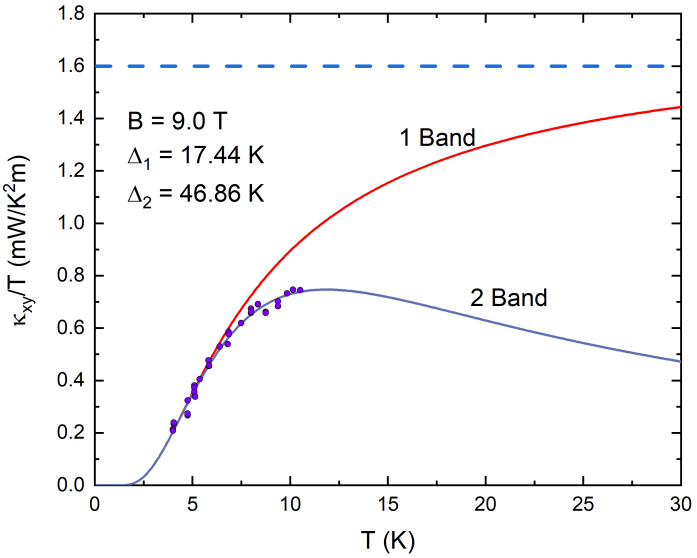

Figure 3.25: Illustration of the importance of the higher band for quantitative descriptions of the thermal Hall conductivity. In addition to being required physically, the inclusion of the second band with energy scale Δ_2 is necessary for obtaining the correct functional form of κ_{xy}/T vs. T. The effect of the second band becomes particularly noticeable around 7 K. The example depicted here is for $B = 9$ T. The blue dotted line indicates the half-quantized conductivity predicted by Kitaev.

I would also like to address a potential criticism of our experiment that pertains to the ω_2 fitting parameter. The second, higher band is necessary physically (Chern numbers must sum to zero) and for capturing the correct functional form of the data. However, the presence of the second band only produces a noticeable impact on κ_{xy}/T vs. T at around 7 K (as shown in Fig. 3.25). One could therefore ask why we did not extend our measurements to higher temperatures. We can offer a few answers to this question. From an experimental point of view, measuring at higher T's presented two distinct difficulties. First, the RX102A thermometers become less sensitive at high T (The R vs. T curve becomes less steep) and 10 K is already approaching the regime where the limited sensitivity would render a thermal Hall measurement impossible. The thin $RuCl_3$ crystal used for this experiment is too fragile for the thermometers to be changed to Cernox-based ones that would be more appropriate at high T. Second, 10 K is also around the maximum temperature that can be reasonably reached (at least stably) in our Janis ^{3}He system. We would have therefore had to switch the crystal to a separate cryostat during which we would risk damaging the sample.

From a theoretical perspective, it is not obvious that we should expect our κ_{xy} model to hold at elevated temperatures. We remind the reader that our model is only intended to describe the spin-polarized phase where a magnon description is appropriate. If we were to increase the temperature further, the system could lose its rigid polarization and alter the functional form of the model.

For example, we find that $\mathcal{C}_{obs} = 1$ at 10 T. However, at high T, the effective Chern number may eventually become non-quantized as we see at lower B in our analysis. This additional T-dependence not accounted for in our model could lead to incorrect values for ω_1 and ω_2. Additionally, it has been suggested that additional T-dependencies may universally appear in κ_{xy} at high T [135]. It would be very difficult to determine how best to incorporate this proposed behavior so it is actually safer to limit our measurements to lower T where the more strictly Berry curvature-oriented description should hold.

3.7 Relation to Apparent Oscillations in κ_{xx}

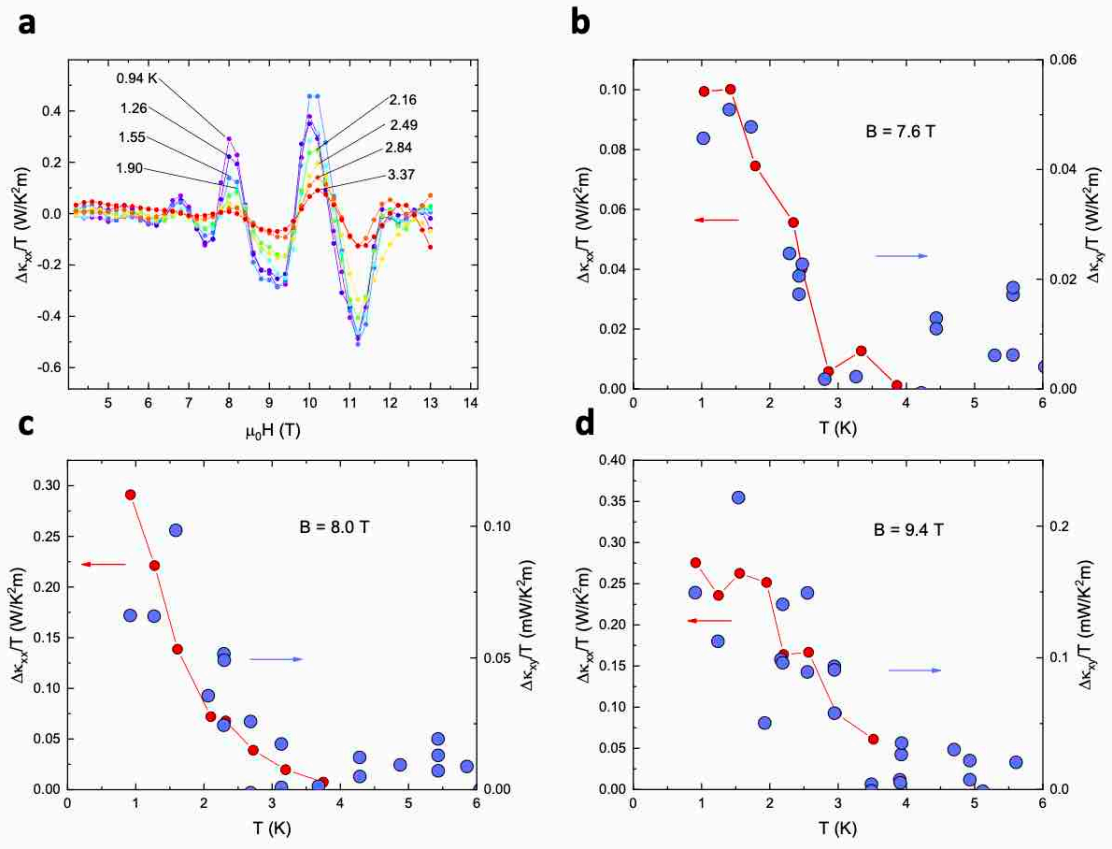

Figure 3.26: Panel (A): κ_{xx} oscillation amplitude (defined as $\Delta\kappa_{xx}/T$ here) for a series of field sweeps at fixed T_{Stage}. Panel (B), Panel (C), and Panel (D) show $\Delta\kappa_{xx}/T$ vs. T (red points and left axis) and the deviation of the thermal Hall conductivity from the high temperature behavior $\Delta\kappa_{xy}/T$ vs. T (purple points and right axis) for 7.6, 8.0, and 9.4 T respectively. The two become noticeable at 3 K and exhibit the same functional form. The strong correlation may imply a similar origin.

In Chapter 2, we discussed our observation of field-induced oscillations in $RuCl_3$'s longitudinal thermal conductivity κ_{xx} [49] and noted that they seemed to be anticorrelated with the planar

thermal Hall effect signal. We observe a similar trend here as well, but can also identify more detail in this new, higher quality data set. As discussed earlier, the measured κ_{xy}/T does not trend toward zero with decreasing temperature as the model and high temperature behavior predicts (Fig. 3.23). It generally reaches a finite low T plateau instead. If we calculate the deviation from the expected value $\Delta\kappa_{xy}/T$ and plot it as a function of T, we observe that it strongly correlates with the oscillation amplitude. This data is shown in Fig. 3.26 for fields of 7.6, 8.0, and 9.4 T. The oscillation amplitude is calculated as $\Delta\kappa_{xx}/T$ to match the units of the Hall conductivity (W/K^{2}m).

$\Delta\kappa_{xy}/T$ and $\Delta\kappa_{xx}/T$ both emerge around 3 K and increase with T with a similar functional form. This strong correlation suggests a common origin. One explanation is that there really is a different phase at low T or at the very least that the thermal transport is dominated by a different set of excitations. This scenario could potentially help reconcile the low T oscillations that imply a gapless phase with the high T thermal Hall effect that is consistent with a gapped topological state.

3.8 Inconsistency with Phonon-based Mechanism

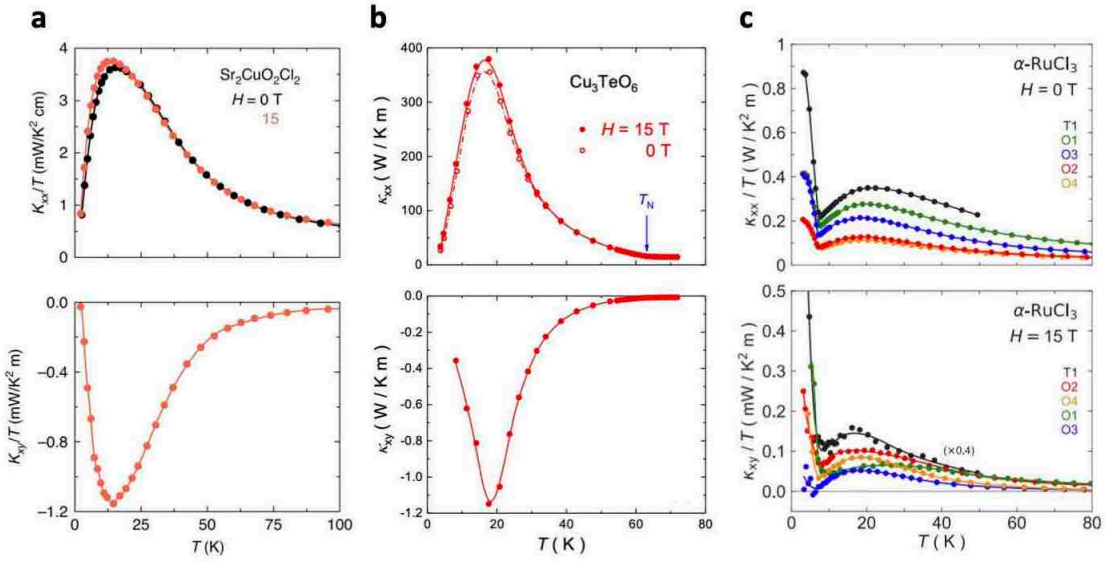

Figure 3.27: It was recently suggested that a large phonon-derived thermal Hall effect may be a relatively common property of magnetic insulators. The signature for this specific mechanism is a clear correlation between κ_{xx} vs. T and κ_{xy} vs. T. This figure presents examples for cuprate compound $Sr_2CuO_2Cl_2$ [136] in Panel (A), trivial magnetic insulator Cu_3TeO_6 [137] in Panel (B), and $RuCl_3$ (for mostly perpendicular field configurations) [113] in Panel (C).

We now comment on the relevance of our results to the recent work on phonon-derived thermal Hall effects in various magnetic insulators from Louis Taillefer's group. Motivated by an intriguing κ_{xy} signal in cuprate superconductors (and related compounds) [138][139], they have studied similar

effects in a variety of magnetic insulators [136][137][113]. The authors argue that the effect is phononic in origin in all of these systems and propose that large phonon thermal Hall effects may actually by a fairly ubiquitous phenomenon in magnetic insulators (as evidenced by its appearance in trivial insulator Cu_3TeO_6). The argument invoked for a phonon thermal Hall effect is the similar temperature profiles of $\kappa_{xx}(T)$ and $\kappa_{xy}(T)$ (see Fig. 3.27). The underlying reasoning is that a phonon's ability to conduct heat in a longitudinal fashion (quantified by κ_{xx}) should translate to its Hall conductivity κ_{xy}. As phonons account for almost all of the bulk heat conduction, changes in κ_{xy} should simply track what is observed in κ_{xx}.

Notably, one of the recent Sherbrooke group experiments involved $RuCl_3$ [113]. Results from this report are shown in Fig. 3.27c. The qualitative correlation between $\kappa_{xx}(T)$ and $\kappa_{xy}(T)$ is clear for all five samples measured. Note that the identification of this correlation is the primary novelty of their report. Similar κ_{xy} data was previously reported by other groups [111][112]. Also note that because **B** is primarily (in all but one experiment) directed entirely out-of-plane, the signal being measured is in the zig-zag AFM ordered phase and not the intermediate to high B regime that is the primary focus of our work. Additionally, it has been suggested that an out-of-plane field component is necessary for the generation of a phonon thermal Hall effect, meaning that this scenario should not be applicable to our results. However, for the sake of completeness, we will now address this alternative mechanism using our data.

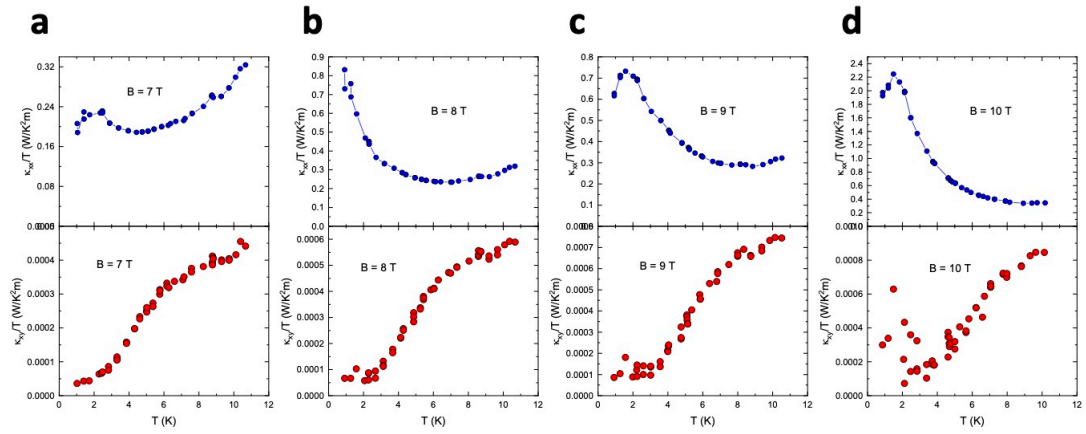

Figure 3.28: Comparison of the temperature-dependencies of the longitudinal κ_{xx} and Hall κ_{xy} thermal conductivities divided by temperature for a selection of magnetic fields. κ_{xy}/T vs. T exhibits the same characteristic T-dependence for all fields shown, but κ_{xx}/T vs. T varies significantly depending on the value of B. Additionally, the T-dependence of κ_{xy}/T differs substantially from κ_{xx}/T. This is inconsistent with the phonon-based phenomenology that has been proposed for other magnetic insulators. Panels (A), (B), (C), and (D) show data collected at 7, 8, 9, and 10 T respectively.

Figure 3.28 shows plots of our κ_{xx}/T and κ_{xy}/T vs. T with B fixed at 7.0, 8.0, 9.0, and 10.0 T. In sharp contrast with the conclusions in Ref. [113], the two quantities clearly have qualitatively distinct T-dependencies. κ_{xy}/T increases with T while κ_{xx}/T generally decreases. Additionally, while the profiles of the longitudinal thermal conductivity κ_{xx}/T vary substantially with B, the profiles for the thermal Hall conductivity κ_{xy}/T show the same general behavior. This clearly demonstrates that the scenario proposed for a phonon-based κ_{xy} in $RuCl_3$ does not apply at least in the planar Hall geometry of interest here.

3.9 Relevance to Alleged Quantization of κ_{xy}/T

As discussed throughout this thesis, $RuCl_3$ is alleged to exhibit a half-integer quantized thermal Hall conductivity κ_{xy}/T that is indicative of chiral Majorana fermion edge modes. However, our measurements consistently reveal a temperature-dependent and non-quantized thermal Hall signal. We now discuss some more recent results from other groups and comment on why these other measurements may differ from ours or how the various claims may be reconciled. We will primarily focus on results from the Kyoto group (led by Yuji Matsuda) [73][140] and the Stuttgart group (led by Hidenori Takagi) [85]. Note that a similar report was published by Yamashita et al. [120] though it is our opinion (as with many members of the community) that the data in this report was too noisy to justify the claims. In particular, the evidence for quantization in their measurements has not been considered convincing. We also acknowledge that these are the same two groups that were the focus of a similar section in the previous chapter. As we have frequently emphasized, the thermal Hall effect is notoriously challenging to measure and there are very few groups in the world with the appropriate expertise. This is the reason that we refer so much to work from just a few other groups.

We first discuss the recent work from the Kyoto group who have studied the sample dependence of $RuCl_3$'s thermal Hall conductivity [73] [140]. We remind the reader that improper synthesis or handling of samples can lead to stacking faults in the material's crystal structure and these imperfections are a likely source of sample variability in various measurements [40]. The authors measure κ_{xy}/T, κ_{xx}, and χ for a series of samples. They find that crystals that exhibit large lattice thermal conductivity peaks around 5 K (with κ_{xx} at peak greater than 4 W/Km) and minimal χ structure above 7 K show quantized κ_{xy}/T while those with smaller κ_{xx} peaks and noticeable features in χ above 7 K exhibit κ_{xy}/T values close to zero. A similar effect (κ_{xy}/T being either quantized or nonexistent) was claimed by Yamashita et al. though their data is far too noisy for

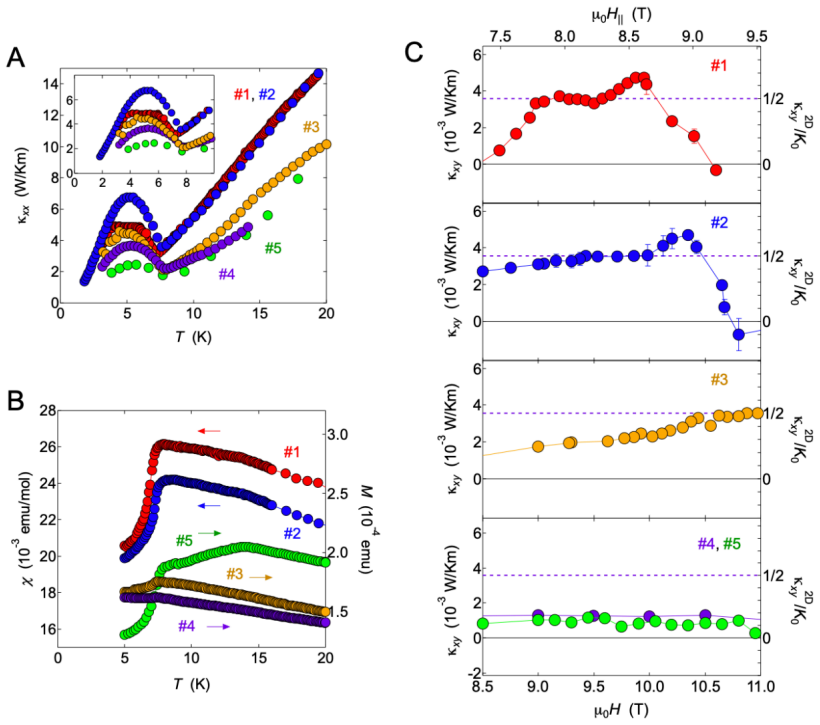

Figure 3.29: Data from Yokoi et al. [73] illustrating the importance of sample quality for the observation of a half-integer quantized thermal Hall conductivity (κ_{xy}/T). The presented data is from five crystals. Panel (A): Longitudinal thermal conductivity vs. temperature. Panel (B): Magnetic susceptibility vs. temperature. Panel (C): thermal Hall conductivity vs. field. The samples of apparent high quality (crystals 1, 2, and 3) exhibit a large, quantized κ_{xy} while the ones of apparent low quality (crystals 4 and 5) show very low κ_{xy} values.

quantization to be convincingly demonstrated [120]. These observations motivate a physical picture where the Majorana edge modes exist in apparently high quality crystals, but are destroyed by crystal defects. We will first address how this picture relates to our data before moving on to some more general commentary on the science behind this claim.

First, the reports from the Kyoto group frequently contain responses to our results and claims. This is particularly true for their most recent report [140]. The crystals measured by their group (as well as those of the Stuttgart group) are grown using a Bridgman method while ours are grown using chemical vapor transport (CVT). The authors hypothesize that their synthesis method must be superior and that is why they observe different thermal Hall conductivities. However, this assertion is simply not supported by the data. As described elsewhere, our crystals pass all of the traditional tests for sample quality. The absence of stacking faults is verified (either for the specific crystal or one from the same batch) using magnetic susceptibility and the high quality is confirmed in-situ during thermal transport experiments using the κ_{xx} values at 0 T and 5 K as well as at the high B

plateau at low T. We can also go even further and point to evidence that our crystals may actually be the better ones. Even the supposedly high quality crystals measured by Yokoi et al. show some structure (even if it is somewhat weak) around 14 K. There is also some evidence in the thermal transport data of our crystals being the superior ones. Our crystals (especially Sample 3) show 5 K κ_{xx} peak values that are as high as (and higher in some cases) than what is seen in crystals from the Kyoto group that do show quantization.

The Kyoto group also employs some measurement procedures that differ from our own and we believe may lead to degradation of crystal quality. First, their experiments are set up in a way that makes them more susceptible to the effects of magnetic torque. $RuCl_3$ is a strongly anisotropic magnet, a property that leads to strong torque when a field is applied ($\tau = \mathbf{M} \times \mathbf{B}$). The Kyoto group also does most of their measurements in a tilted field configuration ($\mathbf{B}$ directed partially out-of-plane), which will produce a much stronger torque than if $\mathbf{B}$ is directed within the honeycomb plane. Additionally, they use very thin crystals (often only 20 μm in thickness) and do not appear to provide them with any mechanical support. In contrast, we primarily perform experiments with the field directed in-plane, use much thicker crystals (50-100 μm thick), and use posts made from low thermal conductivity polymer Delrin to support the otherwise freestanding end of the crystal (see Chapter 1 for details). In fact, the authors themselves admit that the field-induced torque can permanently damage the crystal through mechanical deformation. The possibility of damage to the sample from the strong magnetic field employed in the experiment is another reason that in-situ methods of evaluating crystal quality (such as the thermal transport metrics described here and elsewhere) are so useful.

Another procedural feature employed by the Kyoto group that we believe may potentially be harmful is the fact that they cut their crystals into rectangular shapes for experiments. This step may be necessary for them as the Bridgman-grown crystals may be too large to be measured as-grown. However, as has been mentioned numerous times throughout this thesis, any rough handling can induce stacking faults in $RuCl_3$ crystals. Cutting a crystal is a particularly violent process that has been shown to degrade $RuCl_3$ samples. Regarding the crystals studied in this thesis, Sample 1 was cut while Sample 3 was measured as grown. This is likely why the latter appears to be the higher quality sample (at least as implied by κ_{xx} measurements). For this reason, we believe it is best to measure crystals as grown even if the irregular shapes may introduce geometric complexities and uncertainties.

We now discuss why the thermal Hall effect may be so dependent on crystal quality even though this detail does not appear to explain the discrepancy between our measurements and those of the

Kyoto group. We begin by saying that Yokoi et al.'s assertion that there is a correlation between κ_{xy} and crystal quality does seem to be correct. This is particularly true for their crystal 5 (shown in green in Fig. 3.29), which shows a clear peak in χ at 14 K that suggests that there are so many stacking faults present that two layer AB-type stacking may actually be the dominant structure (as opposed the three layer ABC stacking seen in higher quality crystals). The authors only measure magnetization (not the more sensitive susceptibility) for the other apparently low quality crystal (4, shown in purple) so it is unclear whether the stacking fault population is high in this crystal as well. We note that the effect of stacking faults on κ_{xy} is somewhat surprising. $RuCl_3$ is a typically treated as a quasi-2D system and this fact is especially true for the thermal Hall effect. Both the bosonic model presented in this thesis as well as the Majorana fermion model supported by the Kyoto group assume that the thermal Hall transport can be understood to originate from an array of 1D chiral edge modes from uncoupled 2D crystal layers. In both cases this assumption is then verified in the experiment. As a reminder, quantized transport should generally only be visible for 2D systems. A conversion to 3D units is done using the formula $\kappa_{xy}^{2D} = \kappa_{xy}^{3D} d$ where d is the thickness of an individual crystal layer (5.72 $\mathring{A}$ for $RuCl_3$). Regardless, Yokoi et al.'s observation strongly implies that interlayer exchange interactions are important even if the thermal transport can be understood without them. Perhaps they only act as weak perturbations that stabilize one of multiple possible ground states. This could explain why the κ_{xx} oscillations show similarly strong sample-dependencies.

It is also interesting that any kind of defect (not just stacking faults) would produce such noticeable changes in κ_{xy}. The thermal Hall effect (at least in the absence of a Lorentz force) is an intrinsically topological effect. As discussed earlier, excitation mean free path is not incorporated in theoretical models of κ_{xy}. Only the topological characteristics of the excitation spectrum should matter. This fact should provide a significant degree of protection and robustness to κ_{xy}, but that is clearly not what Yokoi et al. observe. From a purely empirical point of view, one could argue that the nature of the calculation ($\kappa_{xy} = \lambda_{xy}\kappa_{xx}^2$) makes the correlation between κ_{xx} and κ_{xy} unsurprising. However, there are still substantial qualitative (not just quantitative) differences between the two sets of crystals. This likely requires a more substantial explanation.

The effectiveness of our bosonic model makes this effect even more mysterious. One could plausibly argue that the Kitaev spin liquid state is highly fragile and defects may act to break the frustration that stabilizes the entangled state. However, our bosonic fitting model treats the spin-polarized state as the source of the thermal Hall transport. The high field state is highly robust as the Zeeman effect is sample-independent. Every crystal, no matter how full of defects, will eventually

enter a spin-polarized phase. And because the underlying $\Omega_n(\mathbf{k})$-derived thermal Hall effect should not depend on any microscopic characteristics, it is unclear why a crystal would fail to produce any substantial thermal Hall effect.

We also stress that the primary disagreement between the two sets of results is the low T behavior. Above the narrow T window of quantization (3-5 K), the Kyoto group observes a large T-dependent signal, which peaks around 10 K. Qualitatively, this bears some resemblance to our results; the quantitative discrepancies in the absolute values of κ_{xy}/T could occur due to differences in measurement procedures or potentially sample-dependent contributions.

We now discuss the recent thermal Hall measurements from the Stuttgart group [85]. They claim to confirm the robust half-integer quantized κ_{xy}/T, but the evidence presented in their report does not appear to justify the use of the "robust" label. Our reasons for disagreement with this label will be discussed later. Bruin et al.'s [85] experiments are done on a crystal grown using the Bridgman method and obtained from the same source as those used for the Kyoto group's experiments. They perform measurements with **B** directed either entirely in-plane or 20° above the **a** axis. Notably, they find that the observed κ_{xy} values depend only on the in-plane component $H_{\parallel}$. This differs from the observations of Kasahara et al. [60] who found that the quantization field window varied

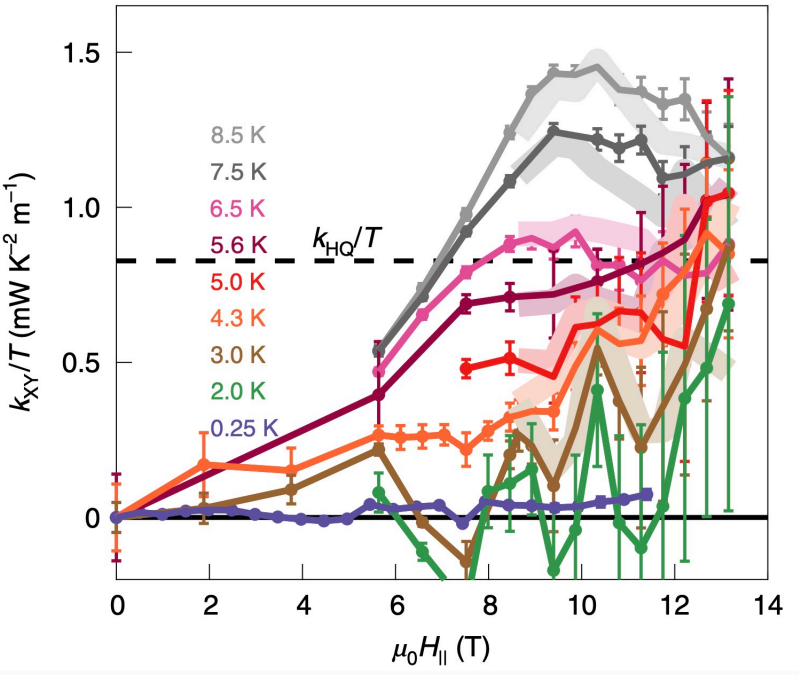

Figure 3.30: Bruin et al.'s measurements of κ_{xy}/T vs. B. Note the round, broadened profile of the curves that more resemble our measurements than those of the Kyoto group. Figure adapted from [85].

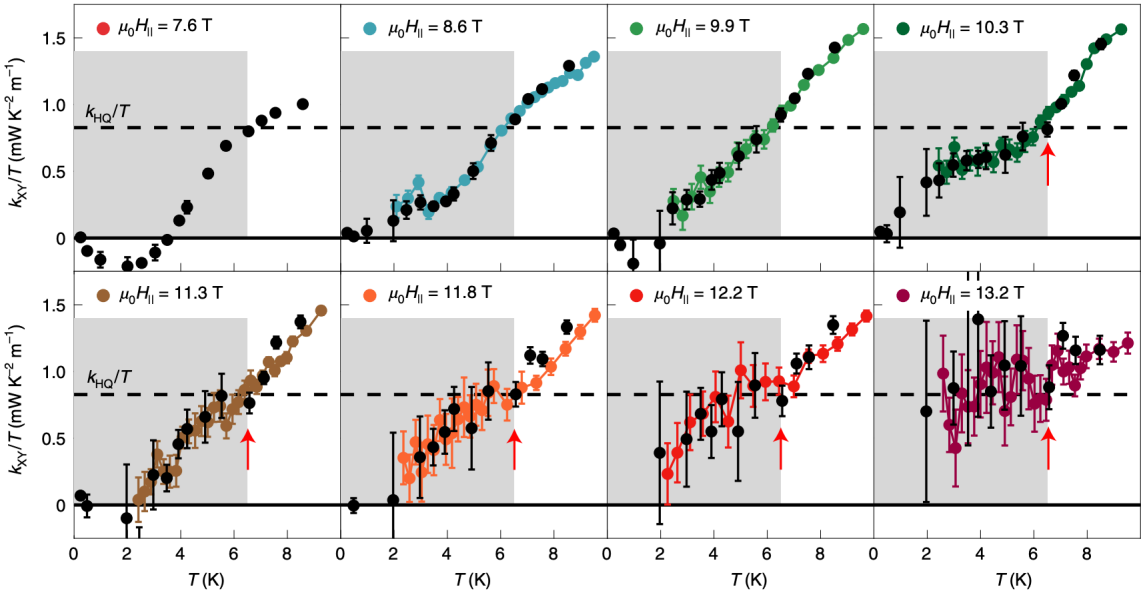

Figure 3.31: Bruin et al.'s measurements of $RuCl_3$'s thermal Hall conductivity divided by temperature. κ_{xy}/T vs. T is plotted for a series of fixed magnetic fields. The authors claim that this data reveals robust half-integer quantization and point to the weak upturn of κ_{xy}/T vs. T seen for 11.8 and 12.2 T and the apparent plateau at 13.2 T. The high noise level seen at high field strongly undercuts their claim of robustness. The black points are taken by sweeping B at fixed T while the colored points are measured by sweeping T. Measurements are done with **B** entirely in-plane or **B** directed 20° out-of-plane (with this data set appearing to contain results for both configurations). Also note that some features like the negative κ_{xy} signal at intermediate field match what we observe in our experiments. Figure adapted from [85].

with the field angle. The data shown in Fig. 3.31 appears to have been collected in both field configurations. Unlike the Kyoto group, they measure down to dilution refrigerator temperatures. They also perform both T sweeps at fixed B and B sweeps at fixed T. Our group as well as the Kyoto group only do the latter.

We will now comment on how these results relate to our own. The first observation one can make is that their data is remarkably similar to ours. In fact, it looks more similar to our results than it does to those obtained by the Kyoto group. This is surprising given that the crystal sources and growth methods are the same as those of the Kyoto group. We now highlight a few specific similarities. First, they observe a signal that is largely T-dependent (see Fig. 3.31) and at least superficially seems to follow a somewhat similar functional form to what we find for κ_{xy} vs. T. However, the Kyoto group generally only reports data within a narrow B range and for $T > 3$ K so at present it is impossible to compare the results directly. The clear T-dependence is also reflected in the rounded profile seen for κ_{xy} vs. B. This is highly reminiscent of our measurements for both Sample 1 and Sample 3 and is in stark contrast with the sharp, square-shaped appearance

reported by Yokoi et al. [73] and Kasahara et al. [60]. A series of κ_{xy}/T vs. B curves from Bruin et. al.'s report that exemplify this are shown in Fig. 3.30. Another notable similarity is the negative low T sign change in κ_{xy} seen at intermediate B. Note that Bruin et al. observe such an effect at 7.6 T, while we found that a sign change was not seen for $B > 7$ T. Potential reasons for this discrepancy include sample differences and the nonzero out-of-plane field component. The clear similarities to our data strongly suggest that sample differences alone are not sufficient to explain the differing results between the various groups. At present, we can only speculate as to what possible experimental procedures may play a role, but some possibilities that appear worthy of exploration include hysteresis removal techniques as well as the thermometry.

We now focus on Bruin et al.'s claim of robustness more directly. In our opinion, the validity of this claim rests on the the interpretation of the data rather than a straightforward viewing of the results. However, it is also our opinion that the authors assessments of their own measurements are highly suspect, overly optimistic, and at times misleading. The optimism is apparent in their high field κ_{xy} vs. T measurements (see Fig. 3.31). The authors summarize their data by saying that κ_{xy}/T shows a kink-like feature in a narrow T window around the expected quantized value and that the size of this window increases with increasing B. At 13.2 T, this plateau extends all the way down to the lowest T measured (though this is only 2 K whereas at other fields the measurements are done down to dilution fridge temperatures). The issue with this particular curve is that the data is far too noisy to even fully justify the identification of a plateau, let alone the claim that it matches the quantized value. The noise level is larger than the signal itself. Similar statements can be made about all curves measured for $B \geq 11.8$ T. We do not intend to criticize the authors' experimental skills. As discussed throughout this thesis, these measurements are incredibly difficult and we are highly impressed by Bruin et al.'s success in successfully performing them without the long experience possessed by our group and Yuji Matsuda's. However, the "robust" label is simply a dishonest way to describe data with such a high noise level.

Another difference seen in the data sets obtained from the two Bridgman crystal-using groups is the differing quantization temperature windows. For example, at 11.8 T, Bruin et al. observe the (possible) plateau-like feature for 5-7 K, very different from the 3-5 K window reported by the Kyoto group. This would seem to imply a difference in bulk Majorana gap and it is not obvious why this would vary between samples. We mention these seemingly small and technical discrepancies to emphasize the numerous reasons that Bruin et al.'s claim to have reproduced the data from the Kyoto group is unjustified. The quantized thermal transport has not yet been conclusively shown and the attempts to attribute our results to poor quality crystals are unwarranted.

We also comment on their physical interpretation of their results. Another key difference between Bruin et al.'s data and that of the Stuttgart group is that the former claims to observe a quantized signal up to much higher fields. A key piece of evidence for the Majorana-based signal in Kasahara et al.'s [60] original report was the fact that the signal vanished abruptly once the system moved from the field-induced spin liquid phase to the spin-polarized phase (around 12 T for the experiment done with $\mathbf{B} \parallel \mathbf{a}$). However, Bruin et al. do not observe a clear drop in κ_{xy} vs. B except in curves taken at high T ($T > 7$ K) and their window of alleged quantization extends to fields as high as 13.2 T where the system should be in the spin-polarized phase, not the field-induced disordered one. Similarly, the authors place significant emphasis on the existence of an "upturn"-like feature at high B and low T. However, as we discussed in an earlier section, such an effect was observed in our measurements as well, but at a highly B-dependent value (though we were not sufficiently comfortable with the resolution in our data to justify reporting the values at fields above 10 T). It seems quite possible that these two effects are similar in origin. We hypothesized that this low T plateau effect is tied to the appearance of κ_{xx} oscillations at the same T, but further study will be needed to determine the cause of this unusual feature. Other possibilities include improper hysteresis subtraction or other physics associated with a potential low T spin liquid state.

These facts point to the true origin of Bruin et al.'s κ_{xy} signal being the spin-polarized state. As with our results, a true topological magnon thermal Hall effect is observed in the high B regime that likely leaks into the lower field regime via less sharp paramagnon excitations (though we emphasize again that some spin liquid contribution cannot be entirely ruled out). At this point, we would like to draw attention to a widely held conception in the debate over $RuCl_3$'s thermal transport physics (and its relation to sample characteristics) that we believe relies on a highly problematic assumption. Specifically, the Majorana and magnon-derived effects are not mutually exclusive. While the assumption of a fragile Majorana-inhabiting KSL state is not unreasonable, the same cannot be said for the magnon-derived effect. The bosonic phenomenology at the heart of our model is highly robust. Every $RuCl_3$ crystal will eventually enter a spin-polarized state no matter how many impurities the crystal may have. And the model that describes our κ_{xy} data has no way to incorporate defects or impurities. This robustness is inherent to the topological nature of the effect. All of this is to say that the signal discussed in our report cannot be removed. The fact that we observe $\mathcal{C}_{obs} = 1$ down to fields as low as 9 T implies that even if a Majorana signal is observed, it will coincide with the magnon one. We are left with the question of where the magnon effect is in these other reports. This fact presents a major challenge for thermal Hall experiments in $RuCl_3$ and will need to be addressed before speculation about possible Majorana fermion excitations can

continue.

We close this section by reiterating that κ_{xy} measurements (and calculations) depend on numerous technical subtleties that can produce sizable erroneous effects in the resulting data. One key detail that we have made a deliberate attempt to emphasize throughout this thesis is that it is actually the thermal Hall resistivity λ_{xy} that is the most fundamental quantity measured in these experiments as it is directly proportional to the tiny B-antisymmetric transverse temperature gradient. κ_{xy} requires more complicated calculation. Despite this, λ_{xy} is rarely reported. We therefore encourage other groups to do as we have done here and show λ_{xy} in future reports.

3.10 Discussion

Most of the discussion so far has been about how these results relate to prior work on $RuCl_3$ and the ongoing debate over its thermal Hall conductivity. I would now like to address the broader significance of the discovery presented in this chapter. First, as discussed earlier, quantitative fitting of thermal Hall data has never been done in this fashion. Our novel analysis technique provides a semi-universal functional form that can readily be applied to a wide variety of two-band topological magnon systems. Generalizations to systems with additional bands also appear straightforward. We have therefore provided a new framework for analyzing existing and future thermal Hall data sets. Additionally, we have brought attention to the fact that the unusual mechanism by which the thermal Hall effect comes about also produces a rather unusual functional form for its T-dependence that is distinctly non Boltzmann (or fermionic or bosonic).

Second, bosonic topological states represent a promising frontier that have been studied very little experimentally. To the best of our knowledge, the experiment presented in this chapter is one of the first observations of such a state in a bulk material. An additional source of novelty is the fact that the relevant signature is visible in a transport experimentally at technologically practical temperatures. This feature makes $RuCl_3$ an attractive platform for future topological magnon experiments that may eventually be of use in spintronics applications [141] [142].

Appendix A

Hysteresis in Thermal Conductivity

As discussed earlier in this thesis, we discovered that $RuCl_3$ exhibits clear field-induced hysteresis. Hysteresis refers to that fact that different κ_{xx} values are measured depending on whether the field is being swept "up" (negative to positive B) or "down" (positive to negative B). Such an effect is quite common in magnetic systems due to the typically first order nature of magnetic phase transitions. What is unique about this observation in $RuCl_3$ is that hysteresis has never been seen in magnetization measurements. We remind the reader that the field-antisymmetric component of a κ_{xx} field sweep is calculated as:

$$\kappa_{xx}^{AS}(H) = \big[\kappa_{xx}(+H) - \kappa_{xx}(-H)\big]/2 \tag{A.1}$$

We expect that the thermal transport hysteresis is purely longitudinal in origin. However, while this contribution may not arise from the Hall effect, the field-asymmetry can look like a Hall effect if the hysteresis is not properly subtracted.

As discussed earlier, we found that the typical profile consists of a broad hump-like feature for $0 < |B| < 5$ T followed by a series of peaks and (almost) zeroes that match the periodicity of the oscillations in κ_{xx}^{SY} (the field-symmetric component). While our highly detailed T,B mapping of $RuCl_3$'s thermal transport properties (discussed in Chapter 3) was primarily aimed at studying the thermal Hall conductivity, the same raw data set can be used to obtain a similar mapping of κ_{xx}^{AS}. The results of this are shown in Fig. A.1. We remind the reader that this data is from Sample 3, not

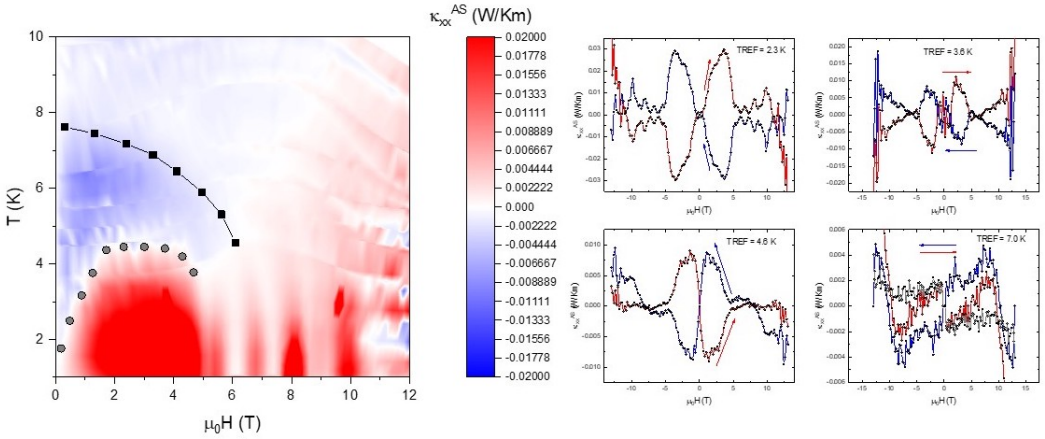

Figure A.1: Temperature, field-mapping of the hysteretic component of $RuCl_3$'s longitudinal thermal conductivity. The left panel shows a color map of κ_{xx}^{AS} while the right panels show a series of examples of κ_{xx}^{AS} redorded for both "up"-sweeps and "down"-sweeps at a series of fixed T_{Stage}'s.

Sample 1. Included in this figure are a color map of κ_{xx}^{AS} as well as a series of examples of individual sweeps from which this map is constructed. The color map reveals a large amount of structure. While much of this simply reflects features in the individual κ_{xx}^{AS} sweeps discussed earlier, some new observations can be made as well.

One example is the sign change that occurs in the low B hump-like feature. We have chosen our sign convention such that for $B \geq 0$, a positive signal in $\kappa_{xx}^{AS,up}$ is taken as positive. However, this is largely an arbitrary choice. Nevertheless, the sign change is a novel and robust feature. An example from an individual sweep can be seen in the right side of the figure in the pair of curves measured at $T_{Stage} = 4.6$ K. The gray points in the color map are used to identify the T, B values at which the sign change occurs. While the precise origin of this effect is unclear, it appears likely that it is associated with the magnetic order. One interestingly possibility is that there is yet another transition within the zig-zag AFM phase that has not been previously observed. Further study of this region of the phase diagram will be needed before any precise claims can be made though.

The association of the hump-like feature with the zig-zag order is also apparent in the fact that $|\kappa_{xx}^{AS}|$ vanishes when the system leaves the ordered phase. More specifically, for $4 < T < 8$ K and $0 < B < 6$ T the T, B values at which $|\kappa_{xx}^{AS}|$ becomes zero (indicated by black points in the figure) clearly trace the lobe-shaped phase boundary for the zig-zag state. For higher fields where the hysteresis consists only of the oscillation-like peaks, the effect vanishes around 4 K (like the oscillations in κ_{xx}^{SY}). These facts point to the hysteresis being a low T effect. However, the fact that it extends to fields beyond H_c means that magnetic order alone likely cannot fully account for this unusual effect.

We also note that the peak-like structures at intermediate field in Fig. A.1 are not quite as clear as they were for Sample 1. This is notable as the oscillations in this crystal were also less obvious (at least superficially). This fact further supports a connection between the two effects.

We emphasize again that this is a highly anomalous effect. The absence of a corresponding signature in magnetization measurements is highly unusual, but we are currently unable to make any definitive statements about a precise mechanism by which the thermal conductivity hysteresis arises. One can speculate about a potential order parameter or additional first order transition that may lead to the asymmetry, but further study will be needed to identify a specific origin.

Note that similar hysteresis effects have since been observed in a few other measurements (though our observation in thermal transport was the first). Two such examples are shown in Fig. A.2. The first is the magnetocaloric effect [143] and is shown in Fig. A.2a. The second example (depicted in Fig. A.2b) is from a magnetic linear dichromism (MLD) measurement. MLD (as well as other quadratic magneto-optical effects) can be used to study antiferromagnetic order. MLD refers to the polarization rotation of the linearly polarized light after being reflected off of the sample. Future studies should attempt to address how these various signatures relate to each other.

As for the reproducibility of our results, the published data is somewhat ambiguous. Fig. A.3 shows one example of an attempt to address this by the Kyoto group. The authors compare κ_{xx} field sweeps measured for "up" and "down" directions. They then claim to observe no difference between the two. However, it does not appear that they haven attempted to antisymmetrize this data, which would likely be necessary given the typically small ratio $\kappa_{xx}^{AS}/\kappa_{xx}^{SY}$ at the temperatures used for the experiment $T > 4$ K. It it thus currently unclear whether the thermal conductivity

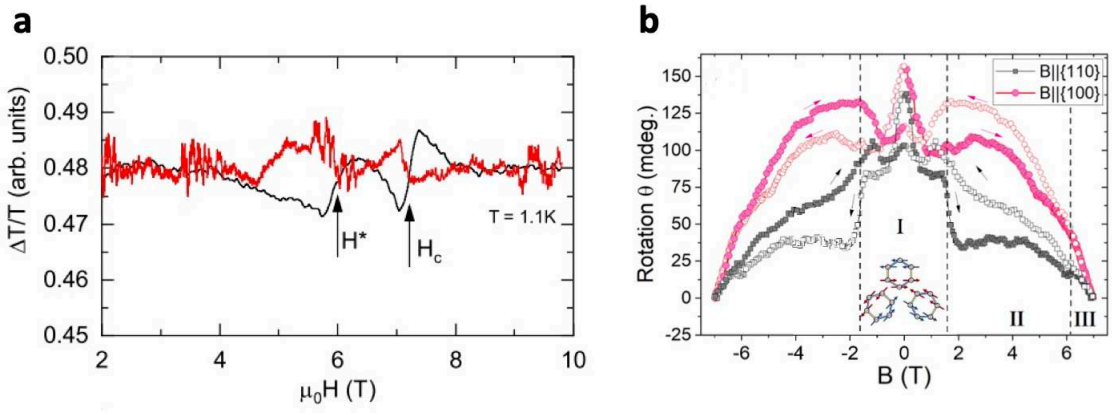

Figure A.2: Other examples of hysteresis-like effects appearing in other measurements on $RuCl_3$. Panel (A) shows the magnetocaloric effect and Panel (B) shows magnetic linear dichromism data. Figures adapted from [143] [144].

hysteresis is reproducible for samples with different growth techniques.

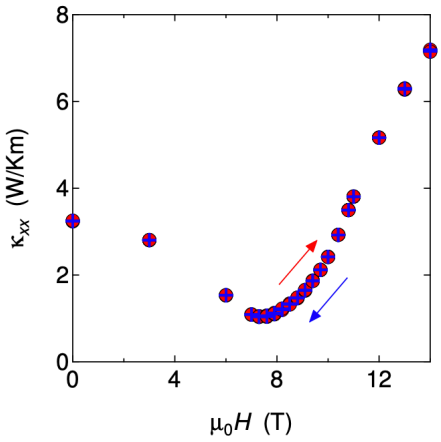

Figure A.3: Yokoi et al. claim to not observe any field-induced hysteresis in their thermal conductivity measurements. Figure adapted from [73].

Appendix B

Extended Discussion of Sample Characteristics and Quality

As we have discussed throughout the main text of this thesis, the frustrated magnetism community has developed a series of tools to identify high and low quality samples of $RuCl_3$. Here, we summarize these criteria and then present a new set of benchmarks that we believe may provide additional information. At present, the two primary indicators are:

1. **$T_N = 7$ K:** Crystals with stacking faults (regions with two-layer instead of the preferred three-layer stacking periodicity) will show additional structure in heat capacity C and magnetic susceptibility χ around 14 K or possibly at temperatures in between 7 and 14 K. High quality crystals will clearly show $T_N = 7$ K in a wide variety of measurements.

2. **High Absolute value of κ_{xx}:** At low T, defects are the primary impediment to phonon transport. Therefore, crystals with generally high κ_{xx} values can be assumed to possess few defects. Again, in $RuCl_3$ stacking faults are the most common (or at least the most discussed) defects. High quality crystals typically show a peak in κ_{xx} around 5 K at zero field. The presence of this clear peak as well as the value of κ_{xx} at the maximum are therefore often used as indicators of sample quality. High quality crystals show $\kappa_{xx} > 5$ W/Km at this peak. This sort of in-situ verification is a highly attractive feature of thermal transport experiments as the they allow us to confirm that the crystal was not damaged during the mounting process. This is not possible with many other probes.

The crystals used for the experiments presented in this thesis meet these criteria. As shown in

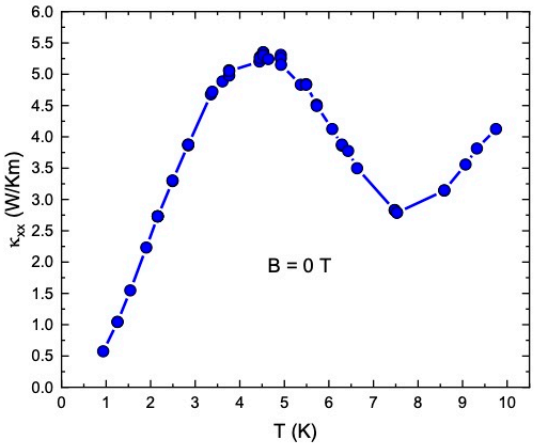

Figure B.1: Thermal conductivity κ_{xx} vs. T at zero B for Sample 3. The large hump is indicative of high crystal quality.

Fig. B.1, κ_{xx} peaks at 5.5 W/Km around 4.5 K before decreasing down to 2.5 W/Km at $T_N = 7$ K. These values and general behavior are consistent with what has been reported in high quality crystals from other groups.

We now discuss additional indicators of sample quality that can be observed in thermal transport experiments. These new benchmarks are arguably more effective than the value of κ_{xx} at 5 K and 0 T.

- **High absolute value of κ_{xx} at the low T, high B plateau:** As described in our previous report [49], κ_{xx} is likely strongly affected by spin-phonon scattering throughout most of the phase diagram. To isolate the pure phonon contribution to κ_{xx}, one must use the value at the high field plateau at low temperature where spins lack the thermal energy necessary to scatter phonons. A high lattice thermal conductivity is a good indicator of crystal quality (or more specifically the absence of defects). We previously used the value of κ_{xx}/T at this plateau at 1 K as a benchmark and obtained a value of 0.7 W/K^2m. For the crystal used in this report, we obtained a value of 4.66 at 1.16 K (see Fig. B.2). We believe that this is likely a better indicator of quality than the value of κ_{xx} at 5 K and 0 T because the phonon transport is closer to the ballistic limit in the spin-polarized phase (and in particular in the regime where κ_{xx} vs. B becomes flat). In the zero field case, magnon-phonon scattering is likely still significant and there are additional complications from competing zig-zag domains and the close proximity to T_N.

  To evaluate the samples studied in this thesis, we specifically use the value of κ_{xx}/T at 1 K. We

find values of 0.7 W/K^{2}m and 4.7 W/K^{2}m for Samples 1 and 3 respectively. This reveals that Sample 3 is the higher quality sample and is why we selected it for the more time-consuming κ_{xy} experiment presented in Chapter 3. We emphasize that we do not mean to imply that Sample 1 is of poor quality. Its lower value of κ_{xx} at the high B plateau is likely due to its having been manually cut into a rectangular shape like the crystals studied by the Kyoto and Stuttgart groups. Non-material quality-related reasons for Sample 3's substantially higher κ_{xy}/T value include its being measured at a slightly higher T as well as its larger size. The latter would be a consequence of the crystal being in the ballistic limit and its phonon mean free paths being set by crystal dimensions.

- **Strong variation in $\kappa_{xx}(B)$:** As stated, κ_{xx} is strongly affected by spin-phonon scattering in $RuCl_3$. In the high-B/ low-T regime; however, κ_{xx} approaches its intrinsic phonon-derived value (as the phonon transport becomes ballistic instead of diffusive). Measurement dimensions used in calculating κ_{xx} often carry substantial uncertainty. For us, this is due to the large contact size (which helps ensure a strong thermal contact) as well as the non-rectangular shapes of as-grown crystals. These difficulties translate into significant uncertainties in the absolute values of the thermal transport quantities. Thus, a quality indicator that is insensitive to absolute values is desirable. A second benchmark that can be used is the ratio between the value of κ_{xx} at the plateau κ_{xx}^{plat} and the minimum value κ_{xx}^{min} observed during a particular field sweep. This ratio R_K is defined as

$$R_K = \kappa_{xx}^{plat}/\kappa_{xx}^{min} \tag{B.1}$$

As illustrated in Fig. B.2 $R_K = 23.5$ for Sample 3 for the sweeps at $T_{\text{Stage}} = 1.16$ K. This degree of variation was also observed in our previous studies of this crystal and is significantly higher than the ratios seen in essentially any insulator (including other crystals of $RuCl_3$).

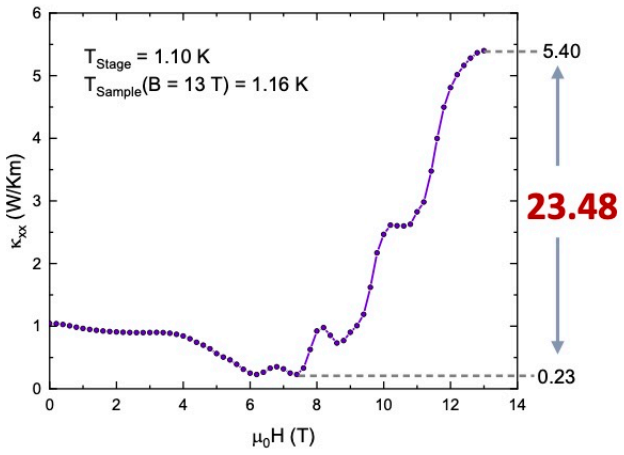

Figure B.2: Field-dependent longitudinal thermal conductivity data taken at $T_{\rm Stage}$= 1.1 K for Sample 3. We note the large value of κ_{xx} attained at B =13 T, and the large enhancement (23.5×) over the minimum value at $B \sim 7.3$ T.

Bibliography

[1] P.W. Anderson. Resonating valence bonds: A new kind of insulator? *Materials Research Bulletin*, 8(2):153–160, 1973.

[2] Philip W Anderson. The resonating valence bond state in la2cuo4 and superconductivity. *science*, 235(4793):1196–1198, 1987.

[3] Ganapathy Baskaran, Z Zou, and Philip W Anderson. The resonating valence bond state and high-tc superconductivity—a mean field theory. *Solid state communications*, 88(11-12):853–856, 1993.

[4] Steven A Kivelson, Daniel S Rokhsar, and James P Sethna. Topology of the resonating valence-bond state: Solitons and high-t c superconductivity. *Physical Review B*, 35(16):8865, 1987.

[5] Lucile Savary and Leon Balents. Quantum spin liquids: a review. *Reports on Progress in Physics*, 80(1):016502, nov 2016.

[6] Yi Zhou, Kazushi Kanoda, and Tai-Kai Ng. Quantum spin liquid states. *Rev. Mod. Phys.*, 89:025003, Apr 2017.

[7] C. Broholm, R. J. Cava, S. A. Kivelson, D. G. Nocera, M. R. Norman, and T. Senthil. Quantum spin liquids. *Science*, 367(6475), 2020.

[8] Alexei Kitaev. Anyons in an exactly solved model and beyond. *Annals of Physics*, 321(1):2–111, 2006. January Special Issue.

[9] Elliott H. Lieb. Flux phase of the half-filled band. *Phys. Rev. Lett.*, 73:2158–2161, Oct 1994.

[10] A Yu Kitaev. Fault-tolerant quantum computation by anyons. *Annals of Physics*, 303(1):2–30, 2003.

[11] F. D. M. Haldane. Model for a quantum hall effect without landau levels: Condensed-matter realization of the "parity anomaly". *Phys. Rev. Lett.*, 61:2015–2018, Oct 1988.

[12] Cui-Zu Chang, Jinsong Zhang, Xiao Feng, Jie Shen, Zuocheng Zhang, Minghua Guo, Kang Li, Yunbo Ou, Pang Wei, Li-Li Wang, et al. Experimental observation of the quantum anomalous hall effect in a magnetic topological insulator. *Science*, 340(6129):167–170, 2013.

[13] Hryhoriy Polshyn, Jihang Zhu, Manish A Kumar, Yuxuan Zhang, Fangyuan Yang, Charles L Tschirhart, Marec Serlin, Kenji Watanabe, Takashi Taniguchi, Allan H MacDonald, et al. Electrical switching of magnetic order in an orbital chern insulator. *Nature*, 588(7836):66–70, 2020.

[14] Simon Burton. A short guide to anyons and modular functors. *arXiv preprint arXiv:1610.05384*, 2016.

[15] Stevan Nadj-Perge, Ilya K Drozdov, Jian Li, Hua Chen, Sangjun Jeon, Jungpil Seo, Allan H MacDonald, B Andrei Bernevig, and Ali Yazdani. Observation of majorana fermions in ferromagnetic atomic chains on a superconductor. *Science*, 346(6209):602–607, 2014.

[16] Vincent Mourik, Kun Zuo, Sergey M Frolov, SR Plissard, Erik PAM Bakkers, and Leo P Kouwenhoven. Signatures of majorana fermions in hybrid superconductor-semiconductor nanowire devices. *Science*, 336(6084):1003–1007, 2012.

[17] Dongfei Wang, Lingyuan Kong, Peng Fan, Hui Chen, Shiyu Zhu, Wenyao Liu, Lu Cao, Yujie Sun, Shixuan Du, John Schneeloch, et al. Evidence for majorana bound states in an iron-based superconductor. *Science*, 362(6412):333–335, 2018.

[18] Stephen M Winter, Alexander A Tsirlin, Maria Daghofer, Jeroen van den Brink, Yogesh Singh, Philipp Gegenwart, and Roser Valentí. Models and materials for generalized kitaev magnetism. *Journal of Physics: Condensed Matter*, 29(49):493002, nov 2017.

[19] Jeffrey G. Rau, Eric Kin-Ho Lee, and Hae-Young Kee. Generic spin model for the honeycomb iridates beyond the kitaev limit. *Phys. Rev. Lett.*, 112:077204, Feb 2014.

[20] Stephen M. Winter, Ying Li, Harald O. Jeschke, and Roser Valentí. Challenges in design of kitaev materials: Magnetic interactions from competing energy scales. *Phys. Rev. B*, 93:214431, Jun 2016.

[21] Giniyat Khaliullin. Orbital Order and Fluctuations in Mott Insulators. *Progress of Theoretical Physics Supplement*, 160:155–202, 06 2005.

[22] G. Jackeli and G. Khaliullin. Mott insulators in the strong spin-orbit coupling limit: From heisenberg to a quantum compass and kitaev models. *Phys. Rev. Lett.*, 102:017205, Jan 2009.

[23] Simon Trebst. Kitaev materials, 2017.

[24] Jeffrey G Rau and Hae-Young Kee. Trigonal distortion in the honeycomb iridates: Proximity of zigzag and spiral phases in na2iro3. *arXiv preprint arXiv:1408.4811*, 2014.

[25] Daichi Takikawa and Satoshi Fujimoto. Impact of off-diagonal exchange interactions on the kitaev spin-liquid state of $\alpha-\mathrm{rucl}_3$. *Phys. Rev. B*, 99:224409, Jun 2019.

[26] Sae Hwan Chun, Jong-Woo Kim, Jungho Kim, H Zheng, Constantinos C Stoumpos, CD Malliakas, JF Mitchell, Kavita Mehlawat, Yogesh Singh, Y Choi, et al. Direct evidence for dominant bond-directional interactions in a honeycomb lattice iridate na2iro3. *Nature Physics*, 11(6):462–466, 2015.

[27] Stephen M Winter, Kira Riedl, Pavel A Maksimov, Alexander L Chernyshev, Andreas Honecker, and Roser Valent. Breakdown of magnons in a strongly spin-orbital coupled magnet. *Nature communications*, 8(1):1–8, 2017.

[28] Andrei Catuneanu, Youhei Yamaji, Gideon Wachtel, Yong Baek Kim, and Hae-Young Kee. Path to stable quantum spin liquids in spin-orbit coupled correlated materials. *npj Quantum Materials*, 3(1):1–6, 2018.

[29] Jacob S Gordon, Andrei Catuneanu, Erik S Sørensen, and Hae-Young Kee. Theory of the field-revealed kitaev spin liquid. *Nature communications*, 10(1):1–8, 2019.

[30] Yogesh Singh and P. Gegenwart. Antiferromagnetic mott insulating state in single crystals of the honeycomb lattice material $\mathrm{na_2iro_3}$. *Phys. Rev. B*, 82:064412, Aug 2010.

[31] Ji ří Chaloupka, George Jackeli, and Giniyat Khaliullin. Kitaev-heisenberg model on a honeycomb lattice: Possible exotic phases in iridium oxides $A_2\mathrm{iro}_3$. *Phys. Rev. Lett.*, 105:027204, Jul 2010.

[32] Yogesh Singh, S. Manni, J. Reuther, T. Berlijn, R. Thomale, W. Ku, S. Trebst, and P. Gegenwart. Relevance of the heisenberg-kitaev model for the honeycomb lattice iridates $A_2\mathrm{iro}_3$. *Phys. Rev. Lett.*, 108:127203, Mar 2012.

[33] S. K. Choi, R. Coldea, A. N. Kolmogorov, T. Lancaster, I. I. Mazin, S. J. Blundell, P. G. Radaelli, Yogesh Singh, P. Gegenwart, K. R. Choi, S.-W. Cheong, P. J. Baker, C. Stock, and J. Taylor. Spin waves and revised crystal structure of honeycomb iridate na_2iro_3. *Phys. Rev. Lett.*, 108:127204, Mar 2012.

[34] K. W. Plumb, J. P. Clancy, L. J. Sandilands, V. Vijay Shankar, Y. F. Hu, K. S. Burch, Hae-Young Kee, and Young-June Kim. $\alpha - rucl_3$: A spin-orbit assisted mott insulator on a honeycomb lattice. *Phys. Rev. B*, 90:041112, Jul 2014.

[35] K Kitagawa, T Takayama, Y Matsumoto, A Kato, R Takano, Y Kishimoto, S Bette, R Dinnebier, G Jackeli, and H Takagi. A spin–orbital-entangled quantum liquid on a honeycomb lattice. *Nature*, 554(7692):341–345, 2018.

[36] Faranak Bahrami, William Lafargue-Dit-Hauret, Oleg I. Lebedev, Roman Movshovich, Hung-Yu Yang, David Broido, Xavier Rocquefelte, and Fazel Tafti. Thermodynamic evidence of proximity to a kitaev spin liquid in $ag_3liir_2o_6$. *Phys. Rev. Lett.*, 123:237203, Dec 2019.

[37] Mykola Abramchuk, Cigdem Ozsoy-Keskinbora, Jason W Krizan, Kenneth R Metz, David C Bell, and Fazel Tafti. Cu2iro3: a new magnetically frustrated honeycomb iridate. *Journal of the American Chemical Society*, 139(43):15371–15376, 2017.

[38] Ruidan Zhong, Tong Gao, Nai Phuan Ong, and Robert J Cava. Weak-field induced nonmagnetic state in a co-based honeycomb. *Science advances*, 6(4):eaay6953, 2020.

[39] M Songvilay, J Robert, S Petit, JA Rodriguez-Rivera, WD Ratcliff, F Damay, V Balédent, M Jiménez-Ruiz, P Lejay, E Pachoud, et al. Kitaev interactions in the co honeycomb antiferromagnets na 3 co 2 sbo 6 and na 2 co 2 teo 6. *Physical Review B*, 102(22):224429, 2020.

[40] H. B. Cao, A. Banerjee, J.-Q. Yan, C. A. Bridges, M. D. Lumsden, D. G. Mandrus, D. A. Tennant, B. C. Chakoumakos, and S. E. Nagler. Low-temperature crystal and magnetic structure of $\alpha - rucl_3$. *Phys. Rev. B*, 93:134423, Apr 2016.

[41] A. Banerjee, C. A. Bridges, J. Q. Yan, A. A. Aczel, L. Li, M. B. Stone, G. E. Granroth, M. D. Lumsden, Y. Yiu, J. Knolle, S. Bhattacharjee, D. L. Kovrizhin, R. Moessner, D. A. Tennant, D. G. Mandrus, and S. E. Nagler. Proximate kitaev quantum spin liquid behaviour in a honeycomb magnet. *Nature Materials*, 15(7):733–740, 2016.

[42] Lukas Janssen, Stefan Koch, and Matthias Vojta. Magnon dispersion and dynamic spin response in three-dimensional spin models for $\alpha-\mathrm{rucl}_3$. *Phys. Rev. B*, 101:174444, May 2020.

[43] Sai Mu, Kiranmayi D. Dixit, Xiaoping Wang, Douglas L. Abernathy, Huibo Cao, Stephen E. Nagler, Jiaqiang Yan, Paula Lampen-Kelley, David Mandrus, Carlos A. Polanco, Liangbo Liang, Gábor B. Halász, Yongqiang Cheng, Arnab Banerjee, and Tom Berlijn. Role of the third dimension in searching for majorana fermions in $\alpha-\mathrm{rucl}_3$ via phonons. *Phys. Rev. Research*, 4:013067, Jan 2022.

[44] Jennifer A Sears, Li Ern Chern, Subin Kim, Pablo J Bereciartua, Sonia Francoual, Yong Baek Kim, and Young-June Kim. Ferromagnetic kitaev interaction and the origin of large magnetic anisotropy in α-rucl3. *Nature physics*, 16(8):837–840, 2020.

[45] Lukas Janssen and Matthias Vojta. Heisenberg–kitaev physics in magnetic fields. *Journal of Physics: Condensed Matter*, 31(42):423002, 2019.

[46] Stephen M. Winter, Kira Riedl, David Kaib, Radu Coldea, and Roser Valentí. Probing $\alpha - \mathrm{rucl}_3$ beyond magnetic order: Effects of temperature and magnetic field. *Phys. Rev. Lett.*, 120:077203, Feb 2018.

[47] A. U. B. Wolter, L. T. Corredor, L. Janssen, K. Nenkov, S. Schönecker, S.-H. Do, K.-Y. Choi, R. Albrecht, J. Hunger, T. Doert, M. Vojta, and B. Büchner. Field-induced quantum criticality in the kitaev system $\alpha - \mathrm{rucl}_3$. *Phys. Rev. B*, 96:041405, Jul 2017.

[48] C. Balz, L. Janssen, P. Lampen-Kelley, A. Banerjee, Y. H. Liu, J.-Q. Yan, D. G. Mandrus, M. Vojta, and S. E. Nagler. Field-induced intermediate ordered phase and anisotropic interlayer interactions in $\alpha-\mathrm{rucl}_3$. *Phys. Rev. B*, 103:174417, May 2021.

[49] Peter Czajka, Tong Gao, Max Hirschberger, Paula Lampen-Kelley, Arnab Banerjee, Jiaqiang Yan, David G. Mandrus, Stephen E. Nagler, and N. P. Ong. Oscillations of the thermal conductivity in the spin-liquid state of -rucl3. *Nature Physics*, 2021.

[50] Xu-Guang Zhou, Han Li, Yasuhiro H Matsuda, Akira Matsuo, Wei Li, Nobuyuki Kurita, Koichi Kindo, and Hidekazu Tanaka. Intermediate quantum spin liquid phase in the kitaev material \α-rucl _3 under high magnetic fields up to 100 t. *arXiv preprint arXiv:2201.04597*, 2022.

[51] J. A. Sears, Y. Zhao, Z. Xu, J. W. Lynn, and Young-June Kim. Phase diagram of $\alpha - \mathrm{rucl}_3$ in an in-plane magnetic field. *Phys. Rev. B*, 95:180411, May 2017.

[52] Christian Balz, Paula Lampen-Kelley, Arnab Banerjee, Jiaqiang Yan, Zhilun Lu, Xinzhe Hu, Swapnil M. Yadav, Yasu Takano, Yaohua Liu, D. Alan Tennant, Mark D. Lumsden, David Mandrus, and Stephen E. Nagler. Finite field regime for a quantum spin liquid in $\alpha-rucl_3$. *Phys. Rev. B*, 100:060405, Aug 2019.

[53] Luke J. Sandilands, Yao Tian, Kemp W. Plumb, Young-June Kim, and Kenneth S. Burch. Scattering continuum and possible fractionalized excitations in $\alpha-rucl_3$. *Phys. Rev. Lett.*, 114:147201, Apr 2015.

[54] J. Nasu, J. Knolle, D. L. Kovrizhin, Y. Motome, and R. Moessner. Fermionic response from fractionalization in an insulating two-dimensional magnet. *Nature Physics*, 12(10):912–915, 2016.

[55] Arnab Banerjee, Jiaqiang Yan, Johannes Knolle, Craig A. Bridges, Matthew B. Stone, Mark D. Lumsden, David G. Mandrus, David A. Tennant, Roderich Moessner, and Stephen E. Nagler. Neutron scattering in the proximate quantum spin liquid -rucl3. *Science*, 356(6342):1055–1059, 2017.

[56] Arnab Banerjee, Paula Lampen-Kelley, Johannes Knolle, Christian Balz, Adam Anthony Aczel, Barry Winn, Yaohua Liu, Daniel Pajerowski, Jiaqiang Yan, Craig A. Bridges, Andrei T. Savici, Bryan C. Chakoumakos, Mark D. Lumsden, David Alan Tennant, Roderich Moessner, David G. Mandrus, and Stephen E. Nagler. Excitations in the field-induced quantum spin liquid state of -rucl3. *npj Quantum Materials*, 3(1):8, 2018.

[57] S.-H. Baek, S.-H. Do, K.-Y. Choi, Y. S. Kwon, A. U. B. Wolter, S. Nishimoto, Jeroen van den Brink, and B. Büchner. Evidence for a field-induced quantum spin liquid in α-$rucl_3$. *Phys. Rev. Lett.*, 119:037201, Jul 2017.

[58] Jiacheng Zheng, Kejing Ran, Tianrun Li, Jinghui Wang, Pengshuai Wang, Bin Liu, Zheng-Xin Liu, B. Normand, Jinsheng Wen, and Weiqiang Yu. Gapless spin excitations in the field-induced quantum spin liquid phase of $\alpha-rucl_3$. *Phys. Rev. Lett.*, 119:227208, Dec 2017.

[59] Zhe Wang, S. Reschke, D. Hüvonen, S.-H. Do, K.-Y. Choi, M. Gensch, U. Nagel, T. Rõ om, and A. Loidl. Magnetic excitations and continuum of a possibly field-induced quantum spin liquid in $\alpha-rucl_3$. *Phys. Rev. Lett.*, 119:227202, Nov 2017.

[60] Y. Kasahara, T. Ohnishi, Y. Mizukami, O. Tanaka, Sixiao Ma, K. Sugii, N. Kurita, H. Tanaka, J. Nasu, Y. Motome, T. Shibauchi, and Y. Matsuda. Majorana quantization and half-integer thermal quantum hall effect in a kitaev spin liquid. *Nature*, 559(7713):227–231, 2018.

[61] Mitali Banerjee, Moty Heiblum, Vladimir Umansky, Dima E. Feldman, Yuval Oreg, and Ady Stern. Observation of half-integer thermal hall conductance. *Nature*, 559(7713):205–210, 2018.

[62] Mitali Banerjee, Moty Heiblum, Amir Rosenblatt, Yuval Oreg, Dima E Feldman, Ady Stern, and Vladimir Umansky. Observed quantization of anyonic heat flow. *Nature*, 545(7652):75–79, 2017.

[63] Chong Wang, Ashvin Vishwanath, and Bertrand I. Halperin. Topological order from disorder and the quantized hall thermal metal: Possible applications to the $\nu = 5/2$ state. *Phys. Rev. B*, 98:045112, Jul 2018.

[64] Biao Lian and Juven Wang. Theory of the disordered $\nu = \frac{5}{2}$ quantum thermal hall state: Emergent symmetry and phase diagram. *Phys. Rev. B*, 97:165124, Apr 2018.

[65] David F. Mross, Yuval Oreg, Ady Stern, Gilad Margalit, and Moty Heiblum. Theory of disorder-induced half-integer thermal hall conductance. *Phys. Rev. Lett.*, 121:026801, Jul 2018.

[66] Maximilian Anton Hirschberger. *Quasiparticle excitations with Berry curvature in insulating magnets and Weyl semimetals*. PhD thesis, Princeton University, 2017.

[67] Ian A. Leahy, Christopher A. Pocs, Peter E. Siegfried, David Graf, S.-H. Do, Kwang-Yong Choi, B. Normand, and Minhyea Lee. Anomalous thermal conductivity and magnetic torque response in the honeycomb magnet $\alpha-rucl_3$. *Phys. Rev. Lett.*, 118:187203, May 2017.

[68] Richard Hentrich, Anja U. B. Wolter, Xenophon Zotos, Wolfram Brenig, Domenic Nowak, Anna Isaeva, Thomas Doert, Arnab Banerjee, Paula Lampen-Kelley, David G. Mandrus, Stephen E. Nagler, Jennifer Sears, Young-June Kim, Bernd Büchner, and Christian Hess. Unusual phonon heat transport in $\alpha-rucl_3$: Strong spin-phonon scattering and field-induced spin gap. *Phys. Rev. Lett.*, 120:117204, Mar 2018.

[69] Y. J. Yu, Y. Xu, K. J. Ran, J. M. Ni, Y. Y. Huang, J. H. Wang, J. S. Wen, and S. Y. Li. Ultralow-temperature thermal conductivity of the kitaev honeycomb magnet $\alpha-rucl_3$ across the field-induced phase transition. *Phys. Rev. Lett.*, 120:067202, Feb 2018.

[70] Joseph Callaway. Model for lattice thermal conductivity at low temperatures. *Phys. Rev.*, 113:1046–1051, Feb 1959.

[71] Joseph Callaway. Low-temperature lattice thermal conductivity. *Phys. Rev.*, 122:787–790, May 1961.

[72] Soobin Sinn, Choong Hyun Kim, Beom Hyun Kim, Kyung Dong Lee, Choong Jae Won, Ji Seop Oh, Moonsup Han, Young Jun Chang, Namjung Hur, Hitoshi Sato, et al. Electronic structure of the kitaev material α-rucl3 probed by photoemission and inverse photoemission spectroscopies. *Scientific reports*, 6(1):1–7, 2016.

[73] T. Yokoi, S. Ma, Y. Kasahara, S. Kasahara, T. Shibauchi, N. Kurita, H. Tanaka, J. Nasu, Y. Motome, C. Hickey, S. Trebst, and Y. Matsuda. Half-integer quantized anomalous thermal hall effect in the kitaev material candidate -rucl3. *Science*, 373(6554):568–572, 2021.

[74] Z. Xiang, Y. Kasahara, T. Asaba, B. Lawson, C. Tinsman, Lu Chen, K. Sugimoto, S. Kawaguchi, Y. Sato, G. Li, S. Yao, Y. L. Chen, F. Iga, John Singleton, Y. Matsuda, and Lu Li. Quantum oscillations of electrical resistivity in an insulator. *Science*, 362(6410):65–69, 2018.

[75] B. S. Tan, Y.-T. Hsu, B. Zeng, M. Ciomaga Hatnean, N. Harrison, Z. Zhu, M. Hartstein, M. Kiourlappou, A. Srivastava, M. D. Johannes, T. P. Murphy, J.-H. Park, L. Balicas, G. G. Lonzarich, G. Balakrishnan, and Suchitra E. Sebastian. Unconventional fermi surface in an insulating state. *Science*, 349(6245):287–290, 2015.

[76] Inti Sodemann, Debanjan Chowdhury, and T. Senthil. Quantum oscillations in insulators with neutral fermi surfaces. *Phys. Rev. B*, 97:045152, Jan 2018.

[77] Olexei I. Motrunich. Orbital magnetic field effects in spin liquid with spinon fermi sea: Possible application to $\kappa-(\mathrm{ET})_2\mathrm{cu}_2(\mathrm{CN})_3$. *Phys. Rev. B*, 73:155115, Apr 2006.

[78] Pengjie Wang, Guo Yu, Yanyu Jia, Michael Onyszczak, F. Alexandre Cevallos, Shiming Lei, Sebastian Klemenz, Kenji Watanabe, Takashi Taniguchi, Robert J. Cava, Leslie M. Schoop, and Sanfeng Wu. Landau quantization and highly mobile fermions in an insulator. *Nature*, 589(7841):225–229, 2021.

[79] Zhongdong Han, Tingxin Li, Long Zhang, Gerard Sullivan, and Rui-Rui Du. Anomalous conductance oscillations in the hybridization gap of InAs/GaSb quantum wells. *Phys. Rev. Lett.*, 123:126803, Sep 2019.

[80] Di Xiao, Chao-Xing Liu, Nitin Samarth, and Lun-Hui Hu. Anomalous quantum oscillations of interacting electron-hole gases in inverted type-ii InAs/GaSb quantum wells. *Phys. Rev. Lett.*, 122:186802, May 2019.

[81] Johannes Knolle and Nigel R Cooper. Excitons in topological kondo insulators: theory of thermodynamic and transport anomalies in smb 6. *Physical review letters*, 118(9):096604, 2017.

[82] Patrick A Lee. Quantum oscillations in the activated conductivity in excitonic insulators: Possible application to monolayer wte 2. *Physical Review B*, 103(4):L041101, 2021.

[83] Huitao Shen and Liang Fu. Quantum oscillation from in-gap states and a non-hermitian landau level problem. *Physical review letters*, 121(2):026403, 2018.

[84] Inti Sodemann Villadiego. Pseudoscalar u(1) spin liquids in $\alpha-\mathrm{rucl}_3$. *Phys. Rev. B*, 104:195149, Nov 2021.

[85] JAN Bruin, RR Claus, Y Matsumoto, N Kurita, H Tanaka, and H Takagi. Robustness of the thermal hall effect close to half-quantization in α-rucl3. *Nature Physics*, pages 1–5, 2022.

[86] Yumi Kubota, Hidekazu Tanaka, Toshio Ono, Yasuo Narumi, and Koichi Kindo. Successive magnetic phase transitions in $\alpha - \mathrm{rucl}_3$: Xy-like frustrated magnet on the honeycomb lattice. *Phys. Rev. B*, 91:094422, Mar 2015.

[87] S. Suetsugu, Y. Ukai, M. Shimomura, M. Kamimura, T. Asaba, Y. Kasahara, N. Kurita, H. Tanaka, T. Shibauchi, J. Nasu, Y. Motome, and Y. Matsuda. Evidence for the first-order topological phase transition in a kitaev spin liquid candidate -rucl_3, 2022.

[88] S. K. Niesen, G. Kolland, M. Seher, O. Breunig, M. Valldor, M. Braden, B. Grenier, and T. Lorenz. Magnetic phase diagrams, domain switching, and quantum phase transition of the quasi-one-dimensional ising-like antiferromagnet $\mathrm{baco_2v_2o_8}$. *Phys. Rev. B*, 87:224413, Jun 2013.

[89] N Li, Q Huang, XY Yue, WJ Chu, Q Chen, ES Choi, X Zhao, HD Zhou, and XF Sun. Possible itinerant excitations and quantum spin state transitions in the effective spin-1/2 triangular-lattice antiferromagnet na2baco (po4) 2. *Nature communications*, 11(1):1–9, 2020.

[90] Wilhelm G. F. Krüger and Lukas Janssen. Nesting instability of gapless u(1) spin liquids with spinon fermi pockets in two dimensions. *Phys. Rev. B*, 104:165133, Oct 2021.

[91] Junsen Xiang, Sile Hu, Zhida Song, Meng Lv, Jiahao Zhang, Lingxiao Zhao, Wei Li, Ziyu Chen, Shuai Zhang, Jian-Tao Wang, Yi-feng Yang, Xi Dai, Frank Steglich, Genfu Chen, and Peijie Sun. Giant magnetic quantum oscillations in the thermal conductivity of taas: Indications of chiral zero sound. *Phys. Rev. X*, 9:031036, Aug 2019.

[92] Zhida Song and Xi Dai. Hear the sound of weyl fermions. *Phys. Rev. X*, 9:021053, Jun 2019.

[93] R Franz and G Wiedemann. Ueber die wärme-leitungsfähigkeit der metalle. *Annalen der Physik*, 165(8):497–531, 1853.

[94] Rajas Chari, Roderich Moessner, and Jeffrey G. Rau. Magnetoelectric generation of a majorana-fermi surface in kitaev's honeycomb model. *Phys. Rev. B*, 103:134444, Apr 2021.

[95] Niravkumar D Patel and Nandini Trivedi. Magnetic field-induced intermediate quantum spin liquid with a spinon fermi surface. *Proceedings of the National Academy of Sciences*, 116(25):12199–12203, 2019.

[96] Ciarán Hickey and Simon Trebst. Emergence of a field-driven u (1) spin liquid in the kitaev honeycomb model. *Nature communications*, 10(1):1–10, 2019.

[97] Shang-Shun Zhang, Gábor B Halász, and Cristian D Batista. Theory of the kitaev model in a [111] magnetic field. *Nature Communications*, 13(1):1–7, 2022.

[98] Stephan Rachel, Lars Fritz, and Matthias Vojta. Landau levels of majorana fermions in a spin liquid. *Phys. Rev. Lett.*, 116:167201, Apr 2016.

[99] Peter Czajka, Tong Gao, Max Hirschberger, Paula Lampen-Kelley, Arnab Banerjee, Nicholas Quirk, David G Mandrus, Stephen E Nagler, and NP Ong. The planar thermal hall conductivity in the kitaev magnet $\{\alpha\}$-rucl3. *arXiv preprint arXiv:2201.07873*, 2022.

[100] Michael Stone. Gravitational anomalies and thermal hall effect in topological insulators. *Phys. Rev. B*, 85:184503, May 2012.

[101] Hosho Katsura, Naoto Nagaosa, and Patrick A. Lee. Theory of the thermal hall effect in quantum magnets. *Phys. Rev. Lett.*, 104:066403, Feb 2010.

[102] Ryo Matsumoto and Shuichi Murakami. Theoretical prediction of a rotating magnon wave packet in ferromagnets. *Phys. Rev. Lett.*, 106:197202, May 2011.

[103] Ryo Matsumoto and Shuichi Murakami. Rotational motion of magnons and the thermal hall effect. *Phys. Rev. B*, 84:184406, Nov 2011.

[104] Ryo Matsumoto, Ryuichi Shindou, and Shuichi Murakami. Thermal hall effect of magnons in magnets with dipolar interaction. *Phys. Rev. B*, 89:054420, Feb 2014.

[105] Shuichi Murakami and Akihiro Okamoto. Thermal hall effect of magnons. *Journal of the Physical Society of Japan*, 86(1):011010, 2017.

[106] Naoto Nagaosa, Jairo Sinova, Shigeki Onoda, A. H. MacDonald, and N. P. Ong. Anomalous hall effect. *Rev. Mod. Phys.*, 82:1539–1592, May 2010.

[107] Y. Onose, T. Ideue, H. Katsura, Y. Shiomi, N. Nagaosa, and Y. Tokura. Observation of the magnon hall effect. *Science*, 329(5989):297–299, 2010.

[108] Max Hirschberger, Robin Chisnell, Young S. Lee, and N. P. Ong. Thermal hall effect of spin excitations in a kagome magnet. *Phys. Rev. Lett.*, 115:106603, Sep 2015.

[109] Max Hirschberger, Jason W. Krizan, R. J. Cava, and N. P. Ong. Large thermal hall conductivity of neutral spin excitations in a frustrated quantum magnet. *Science*, 348(6230):106–109, 2015.

[110] Max Hirschberger, Peter Czajka, SM Koohpayeh, Wudi Wang, and N Phuan Ong. Enhanced thermal hall conductivity below 1 kelvin in the pyrochlore magnet yb _2 ti _2 o _7. *arXiv preprint arXiv:1903.00595*, 2019.

[111] Y. Kasahara, K. Sugii, T. Ohnishi, M. Shimozawa, M. Yamashita, N. Kurita, H. Tanaka, J. Nasu, Y. Motome, T. Shibauchi, and Y. Matsuda. Unusual thermal hall effect in a kitaev spin liquid candidate $\alpha-\mathrm{rucl_3}$. *Phys. Rev. Lett.*, 120:217205, May 2018.

[112] Richard Hentrich, Maria Roslova, Anna Isaeva, Thomas Doert, Wolfram Brenig, Bernd Büchner, and Christian Hess. Large thermal hall effect in $\alpha-\mathrm{rucl_3}$: Evidence for heat transport by kitaev-heisenberg paramagnons. *Phys. Rev. B*, 99:085136, Feb 2019.

[113] É. Lefrançois, G. Grissonnanche, J. Baglo, P. Lampen-Kelley, J.-Q. Yan, C. Balz, D. Mandrus, S. E. Nagler, S. Kim, Young-June Kim, N. Doiron-Leyraud, and Louis Taillefer. Evidence of a phonon hall effect in the kitaev spin liquid candidate $\alpha-\mathrm{rucl_3}$. *Phys. Rev. X*, 12:021025, Apr 2022.

[114] Jonathan Cookmeyer and Joel E. Moore. Spin-wave analysis of the low-temperature thermal hall effect in the candidate kitaev spin liquid $\alpha - RuCl_3$. *Phys. Rev. B*, 98:060412, Aug 2018.

[115] Yong Hao Gao and Gang Chen. Topological thermal hall effect for topological excitations in spin liquid: Emergent lorentz force on the spinons. *SciPost Physics Core*, 2(2):004, 2020.

[116] Takuma Saito, Kou Misaki, Hiroaki Ishizuka, and Naoto Nagaosa. Berry phase of phonons and thermal hall effect in nonmagnetic insulators. *Phys. Rev. Lett.*, 123:255901, Dec 2019.

[117] Jing-Yuan Chen, Steven A. Kivelson, and Xiao-Qi Sun. Enhanced thermal hall effect in nearly ferroelectric insulators. *Phys. Rev. Lett.*, 124:167601, Apr 2020.

[118] Haoyu Guo and Subir Sachdev. Extrinsic phonon thermal hall transport from hall viscosity. *Phys. Rev. B*, 103:205115, May 2021.

[119] L. Sheng, D. N. Sheng, and C. S. Ting. Theory of the phonon hall effect in paramagnetic dielectrics. *Phys. Rev. Lett.*, 96:155901, Apr 2006.

[120] M. Yamashita, J. Gouchi, Y. Uwatoko, N. Kurita, and H. Tanaka. Sample dependence of half-integer quantized thermal hall effect in the kitaev spin-liquid candidate $\alpha-\mathrm{rucl}_3$. *Phys. Rev. B*, 102:220404, Dec 2020.

[121] Mengxing Ye, Gábor B. Halász, Lucile Savary, and Leon Balents. Quantization of the thermal hall conductivity at small hall angles. *Phys. Rev. Lett.*, 121:147201, Oct 2018.

[122] Yuval Vinkler-Aviv and Achim Rosch. Approximately quantized thermal hall effect of chiral liquids coupled to phonons. *Phys. Rev. X*, 8:031032, Aug 2018.

[123] Tian Liang, Jingjing Lin, Quinn Gibson, Satya Kushwaha, Minhao Liu, Wudi Wang, Hongyu Xiong, Jonathan A Sobota, Makoto Hashimoto, Patrick S Kirchmann, et al. Anomalous hall effect in zrte5. *Nature Physics*, 14(5):451–455, 2018.

[124] Li Ern Chern, Emily Z. Zhang, and Yong Baek Kim. Sign structure of thermal hall conductivity and topological magnons for in-plane field polarized kitaev magnets. *Phys. Rev. Lett.*, 126:147201, Apr 2021.

[125] Hyunyong Lee, Jung Hoon Han, and Patrick A. Lee. Thermal hall effect of spins in a paramagnet. *Phys. Rev. B*, 91:125413, Mar 2015.

[126] C. L. Kane and Matthew P. A. Fisher. Quantized thermal transport in the fractional quantum hall effect. *Phys. Rev. B*, 55:15832–15837, Jun 1997.

[127] P. A. McClarty, X.-Y. Dong, M. Gohlke, J. G. Rau, F. Pollmann, R. Moessner, and K. Penc. Topological magnons in kitaev magnets at high fields. *Phys. Rev. B*, 98:060404, Aug 2018.

[128] Darshan G. Joshi. Topological excitations in the ferromagnetic kitaev-heisenberg model. *Phys. Rev. B*, 98:060405, Aug 2018.

[129] T. Holstein and H. Primakoff. Field dependence of the intrinsic domain magnetization of a ferromagnet. *Phys. Rev.*, 58:1098–1113, Dec 1940.

[130] A. N. Ponomaryov, L. Zviagina, J. Wosnitza, P. Lampen-Kelley, A. Banerjee, J.-Q. Yan, C. A. Bridges, D. G. Mandrus, S. E. Nagler, and S. A. Zvyagin. Nature of magnetic excitations in the high-field phase of $\alpha-\mathrm{rucl}_3$. *Phys. Rev. Lett.*, 125:037202, Jul 2020.

[131] A. N. Ponomaryov, E. Schulze, J. Wosnitza, P. Lampen-Kelley, A. Banerjee, J.-Q. Yan, C. A. Bridges, D. G. Mandrus, S. E. Nagler, A. K. Kolezhuk, and S. A. Zvyagin. Unconventional spin dynamics in the honeycomb-lattice material $\alpha-\mathrm{rucl}_3$: High-field electron spin resonance studies. *Phys. Rev. B*, 96:241107, Dec 2017.

[132] Dirk Wulferding, Youngsu Choi, Seung-Hwan Do, Chan Hyeon Lee, Peter Lemmens, Clément Faugeras, Yann Gallais, and Kwang-Yong Choi. Magnon bound states versus anyonic majorana excitations in the kitaev honeycomb magnet α-rucl3. *Nature communications*, 11(1):1–7, 2020.

[133] Emily Z. Zhang, Li Ern Chern, and Yong Baek Kim. Topological magnons for thermal hall transport in frustrated magnets with bond-dependent interactions. *Phys. Rev. B*, 103:174402, May 2021.

[134] A. Sahasrabudhe, D. A. S. Kaib, S. Reschke, R. German, T. C. Koethe, J. Buhot, D. Kamenskyi, C. Hickey, P. Becker, V. Tsurkan, A. Loidl, S. H. Do, K. Y. Choi, M. Grüninger, S. M. Winter, Zhe Wang, R. Valentí, and P. H. M. van Loosdrecht. High-field quantum disordered state in $\alpha - \mathrm{rucl}_3$: Spin flips, bound states, and multiparticle continuum. *Phys. Rev. B*, 101:140410, Apr 2020.

[135] Yi-feng Yang, Guang-Ming Zhang, and Fu-Chun Zhang. Universal behavior of the thermal hall conductivity. *Phys. Rev. Lett.*, 124:186602, May 2020.

[136] Marie-Eve Boulanger, Gaël Grissonnanche, Sven Badoux, Andréanne Allaire, Étienne Lefrançois, Anaëlle Legros, Adrien Gourgout, Maxime Dion, CH Wang, XH Chen, et al. Thermal hall conductivity in the cuprate mott insulators nd2cuo4 and sr2cuo2cl2. *Nature communications*, 11(1):1–9, 2020.

[137] Lu Chen, Marie-Eve Boulanger, Zhi-Cheng Wang, Fazel Tafti, and Louis Taillefer. Large phonon thermal hall conductivity in a simple antiferromagnetic insulator. *arXiv preprint arXiv:2110.13277*, 2021.

[138] Gaël Grissonnanche, Anaëlle Legros, Sven Badoux, Etienne Lefrançois, Victor Zatko, Maude Lizaire, Francis Laliberté, Adrien Gourgout, J-S Zhou, Sunseng Pyon, et al. Giant thermal hall conductivity in the pseudogap phase of cuprate superconductors. *Nature*, 571(7765):376–380, 2019.

[139] G Grissonnanche, S Thériault, A Gourgout, M-E Boulanger, E Lefrançois, A Ataei, F Laliberté, M Dion, J-S Zhou, S Pyon, et al. Chiral phonons in the pseudogap phase of cuprates. *Nature Physics*, 16(11):1108–1111, 2020.

[140] Y Kasahara, S Suetsugu, T Asaba, S Kasahara, T Shibauchi, N Kurita, H Tanaka, and Y Matsuda. Quantized and unquantized thermal hall conductance of kitaev spin-liquid candidate α-rucl$_3$. *arXiv preprint arXiv:2202.11947*, 2022.

[141] XS Wang, HW Zhang, and XR Wang. Topological magnonics: A paradigm for spin-wave manipulation and device design. *Physical Review Applied*, 9(2):024029, 2018.

[142] XS Wang and XR Wang. Topological magnonics. *Journal of Applied Physics*, 129(15):151101, 2021.

[143] Rico Schönemann, Shusaku Imajo, Franziska Weickert, Jiaqiang Yan, David G. Mandrus, Yasumasa Takano, Eric L. Brosha, Priscila F. S. Rosa, Stephen E. Nagler, Koichi Kindo, and Marcelo Jaime. Thermal and magnetoelastic properties of $\alpha - \mathrm{rucl}_3$ in the field-induced low-temperature states. *Phys. Rev. B*, 102:214432, Dec 2020.

[144] Julian Wagner, Anuja Sahasrabudhe, Rolf Versteeg, Lena Wysocki, Zhe Wang, Vladimir Tsurkan, Alois Loidl, Daniel Khomskii, Hamoon Hedayat, Paul HM van Loosdrecht, et al. Magneto-optical study of metamagnetic transitions in the antiferromagnetic phase of \α-rucl _3. *arXiv preprint arXiv:2201.02842*, 2022.